

# Optical Fibre Sensors for Monitoring Prestressed Concrete Structures in Nuclear Power Plants

Marcus K. A. Perry

A thesis submitted for the degree of Doctor of Engineering to  
Institute for Energy and Environment  
Department of Electronic and Electrical Engineering  
University of Strathclyde

June 2013

This thesis is the result of the author's original research. It has been composed by the author and has not been previously submitted for examination which has led to the award of a degree.

The copyright of this thesis belongs to the author under the terms of the United Kingdom Copyright Acts as qualified by University of Strathclyde Regulation 3.50. Due acknowledgement must always be made of the use of any material contained in, or derived from, this thesis.

Signed:

Date:

## Abstract

Lifetime extensions of nuclear fission reactors in the UK are required to satisfy growing demands for electrical power. Many of these reactors are nearing the end of their original design life, so the continued structural integrity, particularly of the reactors' prestressed concrete pressure vessels and containments is of prime concern.

Currently, a lift-off inspection of a 1 % random sample of prestressing tendons is performed at 18 month to 5 year intervals to ensure adequate prestress is present in these structures, but the extended life times are making higher resolution, more frequent and in-depth monitoring techniques more desirable. In this thesis, a method of instrumenting prestressing strands with optical fibre Bragg grating strain sensors is outlined. An all-metal encapsulation and bonding technique is developed to ensure sensor reliability under the radioactive and high-stress environments of fission reactors.

This 'smart strand' is complemented by a specially developed interrogation scheme capable of continuously and automatically monitoring static and dynamic nanoscale changes in Bragg grating strain. High-resolution interrogation was achieved by extending an interferometric demodulation technique into the static measurement regime. By modulating the strain sensitivity using a fast optical switch, strain signals could be recovered independently of noise sources using various signal processing algorithms. The application of this technology could augment the continued monitoring of concrete vessel integrity, reducing both the risks and costs associated with performing lift-off measurements in the current and next generation of nuclear reactors.

# Acknowledgements

Thanks to my supervisors Pawel Niewczas and Michael Johnston for their continual guidance and support throughout this project.

Thanks also to my collaborators over the years — whether you're far-flung, like John Canning and Kevin Cook in Sydney, or in this department, like Gordon Flockhart and John Mackersie. Special thanks to my sensor team mates Philip Orr and Grzegorz Fusiek — I came unstuck a lot of times and you restuck me.

Cheers friends, both old and new for being there and then, more importantly, leaving me alone sometimes when I had to write this book or shave my face.

Super-thanks to my wife, Yu, and also to my parents Adarshika and Douglas Perry for feeding me between the ages of 0 and 26 and for keeping me on the straight and narrow.

If you're reading this then *thank you* for getting this far. Seriously, stick with it — sure, it might be quicker to read the entire Lord of the Rings trilogy, but there's this genuinely life-affirming graph on page 188 that you just have to see.

Thanks thermodynamics — without you, none of this would have been possible.

Oh, and let's not forget the ants. Thanks ants.

Thants.

# Contents

<b>List of Figures</b>	<b>xvi</b>
<b>List of Tables</b>	<b>xvii</b>
<b>Glossary of Abbreviations</b>	<b>xviii</b>
<b>1 Introduction</b>	<b>1</b>
1.1 Research Justification . . . . .	3
1.2 Principal Contributions . . . . .	4
1.3 Thesis Overview . . . . .	6
1.4 Publications . . . . .	8
1.4.1 Journal Articles . . . . .	8
1.4.2 Conference Papers . . . . .	9
<b>2 Nuclear Power Generation</b>	<b>10</b>
2.1 Discovery . . . . .	10
2.2 Fuel Enrichment . . . . .	12
2.3 Basic Reactor Principles . . . . .	12
2.4 Reactor Classification . . . . .	13
2.4.1 Water Cooled . . . . .	14
2.4.2 Gas Cooled . . . . .	14
2.4.3 Liquid Metal Cooled . . . . .	17
2.4.4 Molten Salt . . . . .	19
2.5 Nuclear Safety . . . . .	19
2.5.1 Reactor Safety Systems . . . . .	20

2.5.1.1	Engineered Safety . . . . .	20
2.5.1.2	Passive Safety . . . . .	20
2.5.2	Radiation Levels . . . . .	21
2.5.3	Defence in Depth . . . . .	26
2.5.4	Accident Classification and Case Studies . . . . .	27
2.6	Ageing and Decommissioning . . . . .	29
2.7	Summary . . . . .	30
<b>3</b>	<b>Prestress Losses in Nuclear Concrete Barriers</b>	<b>32</b>
3.1	Concrete Production . . . . .	32
3.1.1	Curing . . . . .	33
3.2	Mechanical Properties . . . . .	33
3.2.1	Elastic Region . . . . .	34
3.2.2	Non-linear Region . . . . .	36
3.2.3	Strain-Softening Region . . . . .	36
3.2.4	Tension and the Poisson Effect . . . . .	37
3.3	Prestressed Concrete Pressure Vessels and Containments . . . . .	37
3.3.1	Prestressing Overview . . . . .	38
3.3.2	Prestressing Steel . . . . .	38
3.3.2.1	Wire Fabrication . . . . .	38
3.3.2.2	Mechanical Properties . . . . .	40
3.3.2.3	Strand Fabrication . . . . .	42
3.3.3	Post-tensioning Method . . . . .	44
3.3.3.1	Tendon Layout . . . . .	45
3.3.3.2	Initial Stressing . . . . .	46
3.4	Prestress Loss . . . . .	51
3.4.1	Elastic Shortening . . . . .	53
3.4.2	Friction and Anchorage Slip . . . . .	53
3.4.3	Shrinkage and Creep . . . . .	56
3.4.3.1	Shrinkage . . . . .	56
3.4.3.2	Creep . . . . .	59

3.4.4	Stress Relaxation . . . . .	60
3.4.4.1	Combination with Other Losses . . . . .	61
3.5	Prestress Inspection Activities . . . . .	63
3.5.1	Lift-Off Measurements . . . . .	63
3.5.1.1	Changes in Lift-Off Force . . . . .	65
3.5.2	Vibrating Wire Strain Gauges . . . . .	65
3.5.3	Load Cells . . . . .	67
3.6	Future Sensor Technology . . . . .	68
3.6.1	Smart Tendons . . . . .	69
3.6.2	Smart Tendon Requirements . . . . .	71
3.6.2.1	Resolution . . . . .	73
3.6.3	Proposal . . . . .	75
3.7	Summary . . . . .	75
<b>4</b>	<b>Optical Fibre Sensing: Fibre Bragg Gratings</b>	<b>77</b>
4.1	Optical Fibres . . . . .	77
4.1.1	Light in Glass . . . . .	77
4.1.2	Wave Guiding . . . . .	78
4.1.3	Fibre Fabrication . . . . .	80
4.1.3.1	Fibre Coating . . . . .	80
4.1.4	Light Losses in Fibres . . . . .	81
4.1.4.1	Bending . . . . .	82
4.1.4.2	Scattering . . . . .	82
4.1.4.3	Intrinsic Absorption . . . . .	82
4.1.4.4	Defect Absorption . . . . .	83
4.2	Radiation Induced Attenuation . . . . .	83
4.2.1	Point Defects . . . . .	83
4.2.1.1	Network Defects . . . . .	85
4.2.1.2	Interstitial Defects . . . . .	85
4.2.1.3	Dangling Bond Defects . . . . .	86
4.2.1.4	Colour Centre Summary . . . . .	86

4.2.2	Compaction . . . . .	89
4.2.2.1	Neutron Compaction . . . . .	89
4.2.2.2	Gamma Compaction . . . . .	90
4.2.2.3	Dose Dependence . . . . .	90
4.2.3	Fibre Coating . . . . .	91
4.2.4	Fibre Dopants . . . . .	92
4.2.5	Direct Comparison . . . . .	94
4.2.6	Radiation Induced Attenuation Summary . . . . .	97
4.3	Fibre Bragg Gratings . . . . .	99
4.3.1	Operation Principle . . . . .	101
4.3.2	Reflection Spectrum . . . . .	102
4.3.3	FBG Fabrication . . . . .	104
4.3.4	Sensing Principles . . . . .	105
4.3.4.1	Temperature Dependence . . . . .	105
4.3.5	Radiation Sensitivity . . . . .	106
4.3.5.1	High Temperature Gratings . . . . .	109
4.3.5.2	Strain Errors . . . . .	110
4.3.5.3	Thermal Properties . . . . .	110
4.3.5.4	Shift Dependence . . . . .	111
4.3.6	Decoupling Strain . . . . .	111
4.3.6.1	Multiplexing . . . . .	112
4.4	Summary . . . . .	113
<b>5</b>	<b>Fibre Sensor Packaging and Attachment</b>	<b>114</b>
5.1	Current State of Technology . . . . .	114
5.1.1	Epoxy Bonding . . . . .	116
5.1.2	Justification for Metal Bonding . . . . .	117
5.2	The Mechanical Role of Fibre Coatings . . . . .	118
5.2.1	Brittle Fracture Mechanics . . . . .	118
5.2.2	Fibre Survival Probability . . . . .	119
5.2.3	Flaw creation . . . . .	121

5.3	Metal Coating Fibres . . . . .	122
5.3.1	Nickel Plating Fibres . . . . .	124
5.3.1.1	Evaporative Deposition . . . . .	124
5.3.1.2	Nickel Electroplating . . . . .	125
5.3.2	Coating Quality . . . . .	125
5.3.3	Discussion of Results . . . . .	128
5.4	Capillary Encapsulation . . . . .	130
5.4.1	Brazing . . . . .	132
5.4.1.1	Brazing Alloys . . . . .	132
5.4.1.2	Atmosphere and Flux . . . . .	133
5.4.1.3	Cleaning Technique . . . . .	133
5.4.1.4	Heating Methods . . . . .	133
5.5	Induction Brazing . . . . .	134
5.5.1	Capillary Material . . . . .	134
5.5.2	Induction Heating Set up . . . . .	135
5.5.3	Induction Heating Theory . . . . .	136
5.5.3.1	Curie Temperature . . . . .	140
5.5.3.2	Hysteresis . . . . .	143
5.5.4	Cooling . . . . .	144
5.5.5	Induction Heating Summary . . . . .	144
5.6	Induction: Temperature Characterisation . . . . .	145
5.6.1	Split Gaussian Algorithm . . . . .	145
5.6.2	Temperature Characterisation: Results . . . . .	148
5.6.2.1	Sole Capillary Heating . . . . .	152
5.6.2.2	Sole Susceptor Heating . . . . .	152
5.6.2.3	Combined Heating . . . . .	154
5.6.2.4	Maximum Temperature Summary . . . . .	157
5.6.3	Application of Results . . . . .	158
5.7	Splice Strength After Heating . . . . .	158
5.7.1	Splicing Process . . . . .	161
5.7.2	Breaking Test Result . . . . .	162

5.7.3	Alternative Approach . . . . .	164
5.8	Metal Welding . . . . .	164
5.8.1	Steel phase diagrams . . . . .	165
5.8.1.1	Consequences for Strand Brazing . . . . .	165
5.8.2	Welding Techniques . . . . .	168
5.8.3	Spot Welding . . . . .	169
5.8.3.1	Method and Theory . . . . .	169
5.8.3.2	Spot Welding: Effect on Strands . . . . .	171
5.9	Spot-Weldable FBG Sensor . . . . .	176
5.9.1	Shim Stamping . . . . .	176
5.9.1.1	Design evolution . . . . .	177
5.10	Smart Strand Characterisation . . . . .	182
5.10.1	Strain Characterisation . . . . .	183
5.10.2	Temperature Compensation . . . . .	188
5.11	Summary . . . . .	191
<b>6</b>	<b>Interrogation Scheme: Passive Interferometric Interrogator</b>	<b>195</b>
6.1	Review of Current Technologies . . . . .	195
6.2	Interrogation System Layout . . . . .	196
6.2.1	Overview . . . . .	196
6.2.2	Mach-Zehnder Interferometer . . . . .	198
6.2.3	Multiple MZI Outputs . . . . .	199
6.2.3.1	Advantages and Limitations . . . . .	203
6.2.4	Signal Acquisition of Multiplexed Sensors . . . . .	204
6.3	Signal Extraction: Fourier Transform . . . . .	207
6.3.1	Sampling and Aliasing . . . . .	209
6.3.2	Frequency, Time and Amplitude Resolution . . . . .	210
6.3.3	FFT Summary . . . . .	211
6.4	Signal Extraction: Lock-in Amplifier . . . . .	214
6.4.1	Basic Theory . . . . .	214
6.4.2	Low Pass Filters . . . . .	215

6.4.2.1	Noise Rejection . . . . .	216
6.4.2.2	Settling Time . . . . .	217
6.4.2.3	FIR vs IIR . . . . .	218
6.4.3	Lock-in Summary . . . . .	219
6.5	System tests . . . . .	219
6.5.1	Signal Extraction Software . . . . .	220
6.5.2	Cut-off Frequency . . . . .	222
6.5.3	Sample Size . . . . .	222
6.5.4	Switching Frequency . . . . .	222
6.5.5	High Frequency Measurements . . . . .	226
6.5.6	Low Frequency Measurements . . . . .	228
6.5.7	Application to Static-Dynamic Strain Measurement . . . . .	228
6.5.8	Long-term Stability . . . . .	230
6.5.8.1	FBG Wavelength Dependence . . . . .	231
6.5.8.2	Relative Photodetector Drift . . . . .	232
6.5.8.3	Source Power Drift . . . . .	234
6.5.8.4	Remnant Polarisation . . . . .	236
6.5.8.5	Optical Path Difference . . . . .	237
6.6	Absolute Wavelength Interrogation . . . . .	240
6.6.1	Phase calibration . . . . .	240
6.6.2	Absolute wavelength . . . . .	242
6.6.3	Simulation . . . . .	243
6.6.4	Laboratory Demonstration . . . . .	244
6.6.5	Initial calibration . . . . .	245
6.6.6	Absolute wavelength resolution . . . . .	245
6.6.7	Dynamic strain measurements . . . . .	249
6.6.8	Static strain measurements . . . . .	250
6.6.9	Absolute Wavelength Discussion . . . . .	251
6.7	Interrogation System Summary . . . . .	254

<b>7</b>	<b>Industrial Application</b>	<b>256</b>
7.1	Smart Strand Installation Procedure . . . . .	256
7.1.1	Anchorage Load Measurements . . . . .	257
7.1.2	Fibre Ingress . . . . .	257
7.1.3	Smart Strand Location . . . . .	259
7.2	Interrogation Scheme Extension . . . . .	259
7.2.1	Number of Measurement Points . . . . .	263
7.2.1.1	Multiple Tendon Monitoring . . . . .	263
7.3	Summary . . . . .	265
<b>8</b>	<b>Conclusions and Further Work</b>	<b>266</b>
8.1	Conclusions . . . . .	266
8.2	Future Work . . . . .	268
8.2.1	Sensor Fabrication and Attachment . . . . .	268
8.2.2	Creep and Stress Corrosion . . . . .	269
8.2.3	Interrogation Stability and Resolution . . . . .	269
8.2.4	Radiation and Temperature Dependencies . . . . .	271
8.2.5	Ingress and Load Cells . . . . .	272
8.2.6	Further Scheme Extension . . . . .	272
8.2.7	Field Trials . . . . .	273
8.2.8	Plant Monitoring . . . . .	273
<b>A</b>		<b>275</b>
A.1	Bragg Peak Shift with Strain . . . . .	275
A.2	Bragg Peak Shift with Temperature . . . . .	276
A.3	Fibre Survival Probability . . . . .	277
A.4	Modelled Induction Heating . . . . .	277
A.4.1	Phase 1 . . . . .	278
A.4.2	Phase 2 . . . . .	280
A.5	Contractor Report: R-tech . . . . .	282
A.6	Strain Transfer Model . . . . .	292
A.7	MZI Interference for Single Output . . . . .	295

A.8 MZI Interference for 2 Outputs . . . . .	300
A.9 MZI Interference for 3 Outputs . . . . .	301
A.10 Optical budget calculation for interrogator . . . . .	303
<b>Bibliography</b>	<b>339</b>

# List of Figures

2.1	Cross section of uranium fission with neutron kinetic energy . . .	11
2.2	Layout of PWR reactor . . . . .	15
2.3	Layout of BWR reactor . . . . .	16
2.4	Layout of AGR reactor . . . . .	18
2.5	Geometry of PCPV and PCC . . . . .	23
2.6	Predicted neutron fluence within the PCPV . . . . .	24
2.7	Predicted dose of gamma rays in the PCPV . . . . .	25
2.8	The INES Scale to classify nuclear accidents . . . . .	28
3.1	The role of stress and strain in cylindrical bodies . . . . .	34
3.2	Stress-strain curve for concrete under compression . . . . .	35
3.3	Crystal structure of untreated pearlite steel . . . . .	39
3.4	Diagram of the cold-drawing process for steel strands . . . . .	40
3.5	Stress-strain curves for prestressing steels . . . . .	41
3.6	Geometry of a 7-wire prestressing steel strand . . . . .	43
3.7	Diagram of prestress transfer in post-tensioning systems . . . . .	44
3.8	Photographs of bearing plates at Torness nuclear power plant . .	45
3.9	Tendon layout within PCPVs at Hinkley Point B and Hunterston B	46
3.10	Tendon layout at Hartlepool and Heysham 1 . . . . .	47
3.11	Tendon layout within the PCC at Sizewell B . . . . .	48
3.12	Photograph of stressing stool slotted over prestressing tendon . .	50
3.13	Strand numbering system for a tendon . . . . .	51
3.14	Intentional angle changes of a strand in a prestressing duct . . . .	54
3.15	Force profile for a strand due to friction . . . . .	55

3.16	Force profile for a 40 m strand due to friction and anchorage slip .	57
3.17	Predictions for stress relaxation over 57 years . . . . .	62
3.18	Jack load against bearing plate deflection during lift-off . . . . .	64
3.19	Force profiles for strands due to anchorage slip . . . . .	66
3.20	Prestress remaining in strands over 35 years in top cap of HPB . .	70
3.21	Change in prestress per day in top cap of HPB . . . . .	74
4.1	Fresnel reflection at a refractive index interface . . . . .	79
4.2	Waveguiding in a multi-mode fibre . . . . .	79
4.3	The molecular composition of silica . . . . .	81
4.4	Network and interstitial defects in silica glass . . . . .	84
4.5	RIA in fibres with and without hydrogen loading . . . . .	87
4.6	Summary of the sources of attenuation in optical fibre . . . . .	88
4.7	Gibbs free energy diagram of the metamict transition . . . . .	89
4.8	RIA due to neutron and gamma radiation . . . . .	92
4.9	Increased RIA due to acrylate coating . . . . .	93
4.10	RIA dependence on dopant concentration . . . . .	94
4.11	Attenuation due to gamma radiation in SMF-28 . . . . .	95
4.12	RIA predictions for SMF-28 fibre in fission reactors . . . . .	96
4.13	Total attenuation of fibres in fission reactors after 10 years . . . .	97
4.14	Diagram of FBG index modulation . . . . .	102
4.15	Reflection spectra from FBGs . . . . .	103
4.16	Bragg peak shifts under gamma irradiation . . . . .	107
5.1	Brittle fracture's dependence on flaw depth . . . . .	119
5.2	Probability of fracture in low and high quality fibres . . . . .	120
5.3	Evaporative deposition of metal onto bare silica fibres . . . . .	126
5.4	Set up for electroplating fibres . . . . .	127
5.5	Electron microscope images of nickel plated fibres . . . . .	129
5.6	Capillary encapsulated FBG layout . . . . .	131
5.7	Capillary encapsulated FBG layout: Cross Section . . . . .	131
5.8	Induction heating set up diagram . . . . .	137

5.9	Induction heating set up photograph . . . . .	138
5.10	Argon atmosphere perspex box diagram . . . . .	139
5.11	Diagram of a Helmholtz coil . . . . .	139
5.12	Magnetic dipole alignment below and above the Curie temperature	141
5.13	Magnetisation vs temperature in a ferromagnet . . . . .	142
5.14	External vs internal magnetic fields in a ferromagnet . . . . .	143
5.15	Bragg wavelength shifts with temperature . . . . .	146
5.16	Induction brazing set up: aerial view . . . . .	146
5.17	Characterisation of induction heating, experimental set up . . . . .	147
5.18	The effects of heating one half of an FBG . . . . .	148
5.19	Split Gaussian algorithm peak detection method . . . . .	149
5.20	Demonstration of split Gaussian algorithm peak detection . . . . .	150
5.21	Temperature evolution in the induction heating set up: overview .	151
5.22	Temperature evolution for sole capillary under induction . . . . .	153
5.23	Modelled vs experimental induction heating . . . . .	154
5.24	Temperature in regular heat susceptors with induction current . .	155
5.25	Photographs of varying heat susceptors . . . . .	155
5.26	Temperatures in various heat susceptors under induction . . . . .	156
5.27	Temperature in capillary end, heated by susceptor . . . . .	157
5.28	Maximum attainable temperatures in the system summary . . . . .	159
5.29	Reflectivity and temperature in a type-I grating during brazing . .	160
5.30	Set up used to test splice strength with temperature exposure . .	161
5.31	Heating profiles for various induction heating times at 200 A current	162
5.32	Distributions of splice breaking strengths after heating . . . . .	163
5.33	Splice strength after heating, summary and fit . . . . .	164
5.34	Steel phase diagram . . . . .	166
5.35	CCT diagram for steel . . . . .	167
5.36	Crystal structures of steel types . . . . .	167
5.37	Resistance spot welding resistance diagram . . . . .	170
5.38	Cross section of prestressing strands . . . . .	172
5.39	Strength of steel specimens after spot welding . . . . .	173

5.40	Photographs of steel strands after welding . . . . .	174
5.41	Cross-sections of steel strands after welding . . . . .	175
5.42	Die and punch used to fabricate strain plate . . . . .	177
5.43	Strain plated design evolution diagram . . . . .	178
5.44	Strain plate: final design . . . . .	179
5.45	Capillary attachment to the strain plate . . . . .	180
5.46	Strain plate stamping and installation: 1 . . . . .	181
5.47	Strain late stamping and installation: 2 . . . . .	182
5.48	Strain plate stamping and installation:3 . . . . .	183
5.49	Strand installed into cantilever stressing rig . . . . .	185
5.50	Epoxied vs welded strain transfer . . . . .	186
5.51	Sandwich method of improving grip angle . . . . .	187
5.52	Improved strain transfer: sensor packaging . . . . .	188
5.53	Epoxied vs welded strain transfer . . . . .	189
5.54	Original vs improved strain transfer . . . . .	190
5.55	Temperature dependence welded FBG sensor . . . . .	192
5.56	Temperature dependence bonded vs unbonded FBG . . . . .	193
6.1	Overview of interferometric interrogation technique . . . . .	197
6.2	Output intensity vs OPD for an MZI . . . . .	200
6.3	MZI modulation of FBG peaks . . . . .	202
6.4	Amplitude noise sources in photodetectors summary . . . . .	205
6.5	Square wave modulation in intensity due to switching . . . . .	206
6.6	An FFT of a noisy signal, demonstration . . . . .	207
6.7	Square wave harmonic composition . . . . .	208
6.8	Sampling of continuous signals and interpolation . . . . .	210
6.9	Aliasing of a waveform . . . . .	211
6.10	Reflection about the Nyquist limit . . . . .	212
6.11	Frequency response of Chebyshev and Butterworth filters . . . . .	216
6.12	Settling time of filters vs frequency . . . . .	218
6.13	Block diagram: steps used to assess system performance . . . . .	221

6.14	Strain noise with lock-in filter cut-off frequency . . . . .	223
6.15	Noise and time lag in the FFT . . . . .	224
6.16	System noise vs switching frequency . . . . .	225
6.17	Secondary FFTs of dynamic strain signals . . . . .	226
6.18	Low frequency dynamic strain profiles . . . . .	227
6.19	Mesh and deformation of a modelled cantilever beam . . . . .	229
6.20	Natural frequency vs strain in a cantilever . . . . .	230
6.21	Strain in colocated FBGs vs temperature . . . . .	231
6.22	Different temperature sensitivities of FBGs . . . . .	232
6.23	Scheme to test relative photodetector gain . . . . .	233
6.24	Photodetector drift with temperature . . . . .	233
6.25	Simulated strain drifts arising from photodetector drift . . . . .	234
6.26	Spectral shape vs output power for broadband light source . . . . .	235
6.27	Strain vs light source power . . . . .	236
6.28	Fast and slow axis after depolarisation . . . . .	237
6.29	Effects of heating the MZI on strain measurement . . . . .	238
6.30	Model of the temperature profile outside and inside an MZI . . . . .	239
6.31	Photodetector voltages during modulation . . . . .	241
6.32	Absolute wavelength simulation histogram . . . . .	243
6.33	Absolute wavelength interrogator set up . . . . .	244
6.34	Absolute wavelength flowchart . . . . .	246
6.35	Resistive heater temperatures in absolute wavelength . . . . .	247
6.36	Absolute wavelength: experimental data . . . . .	248
6.37	Absolute wavelength: experimental histogram . . . . .	249
6.38	Absolute strain measurements of cantilever . . . . .	250
6.39	Absolute static strain measurements . . . . .	252
7.1	Theoretical strain profile from prestress loss . . . . .	258
7.2	Proposed egress point for fibres from the strand . . . . .	260
7.3	Modified anchor barrel to aid fibre egress . . . . .	261
7.4	Fibre egress through detensioning spacer . . . . .	262

7.5	Interrogation system extension with parallel lines . . . . .	264
A.1	2D axisymmetric geometry for heating . . . . .	279
A.2	Heating in the ferrule during modelling . . . . .	281
A.3	3D geometry for cooling model . . . . .	282
A.4	Thermal conductivity of alumina with temperature . . . . .	283
A.5	3D geometry strain transfer . . . . .	293
A.6	Modelling grip angle of the capillary . . . . .	294
A.7	Strain transfer along 25 mm capillary . . . . .	295
A.8	Strain transfer vs grip angle . . . . .	296
A.9	Non-axial stress in capillaries . . . . .	296
A.10	Two dimensional strain transfer modifier . . . . .	297
A.11	Three dimensional strain transfer modifier . . . . .	298
A.12	Modified strain transfer in packaged attached FBG . . . . .	299

# List of Tables

2.1	List of active nuclear power stations owned by EDF in the UK . . .	22
3.1	Properties of 7-wire prestressing strand from BS 5896:1980 . . . . .	42
4.1	Cost and radiation resistance of commercially available fibres . . . . .	99
4.2	Summary of fibre optical sensing types . . . . .	100
5.1	Fibre to structure bonding methods summary . . . . .	115
5.2	Solution composition for nickel electroplating fibres . . . . .	125
5.3	Material properties of ferromagnetic metals . . . . .	135
6.1	Default parameters of the interrogation system . . . . .	220

# Glossary of Abbreviations

AC	Alternating Current
ADC	Analogue-to-Digital Conversion
AGR	Advanced Gas-cooled Reactor
BBS	Broadband Source
BWR	Boiling Water Reactor
CCG	Chemical Composition Grating
CCT	Continuous Cooling Transformation
CVD	Chemical Vapour Deposition
CW	Continuous Wave
CWDM	Course Wavelength Division Multiplexer
DC	Direct Current
DFT	Discrete Fourier Transform
DWDM	Dense Wavelength Division Multiplexing
ED	Evaporative Deposition
EDF	Electricite de France
EMF	Electromotive Force
FBG	Fibre Bragg Grating
FEM	Finite Element Model
FFT	Fast Fourier Transform
FIR	Finite Impulse Response
FOS	Fibre Optic Sensor
FPI	Fabry-Perót Interferometer
FRP	Fibre Reinforced Plastic

FSR	Free Spectral Range
FWHM	Full-Width Half-Maximum
HAZ	Heat Affected Zone
HPB	Hinkley Point B
IIR	Infinite Impulse Response
INES	International Nuclear Event Scale
LOCA	Loss of Coolant Accident
MDL	Minimum Design Load
MM	Multimode
MZI	Mach-Zehnder Interferometer
nε	nanostrains
nm	nanometres (wavelength)
NEP	Noise Effective Power
ODC	Oxygen Deficient Centre
OPD	Optical Path Difference
PCC	Prestressed Concrete Containment
PCF	Photonic Crystal Fibre
PCPV	Prestressed Concrete Pressure Vessel
PD	Photodetector
PM	Polarisation-Maintaining
PSD	Power Spectral Density
PVD	Physical Vapour Deposition
PWR	Pressurised Water Reactor
RG	Regenerated Grating
RIA	Radiation-Induced Attenuation
SM	Singlemode
SNR	Signal-to-Noise Ratio
TDM	Time Division Multiplexing
UK	United Kingdom
UTS	Ultimate Tensile Strength
UV	Ultraviolet

VWSG Vibrating Wire Strain Gauge

WDM Wavelength Division Multiplexing

# Chapter 1

## Introduction

Demand for electrical power has risen sharply with the fast-paced global development of the last decade. Energy shortfalls due to diminishing fossil fuels will become more common in the next 30 years, but problems may arise even sooner in the UK [Uni08, Ofg12]. Nuclear power is already helping to bridge the energy gap in Britain, providing 20 % of our total electrical power in a carbon efficient manner [UK 13, UK 12]. Because new nuclear power plants are still in the planning stage, sustaining these levels of nuclear generation has required careful lifetime extensions of existing plants.

The decision to extend the lifetime of a reactor is not taken lightly. The well-being of the public and environment must be ensured through detailed and conservative safety cases, built on historical and continuing measurements of the state, quality and degradation rate of plant assets. The prestressed concrete pressure vessels (PCPVs) and prestressed concrete containments (PCCs) which surround the reactor are important examples of such assets. These concrete structures shield the reactor from impacts and natural disasters, while simultaneously containing the high-pressures, radiation and heat generated in the core.

The structural integrity of PCPVs and PCCs is ensured, in part, by monitoring their remaining levels of prestress. Current practices include testing the reaction force of a 1 % random sample of the steel tendons used to compress the vessels. These ‘lift-off inspections’, performed every 18 months to 5 years, are an integral part of assuring and predicting the structural health of PCCs

and PCPVs. As the tendons can be mobilised within their ducts, any problems highlighted by an inspection can be rectified through re-stressing, or by replacing the tendons, in whole or in part. Unfortunately, however, lift-off inspections are time consuming, expensive, and due to the high forces involved, represent a safety risk to the personnel conducting the inspection. There is thus a drive to complement lift-off inspections with higher resolution, more frequent, automated measurements—especially as these structures age and slowly tend to their minimum designed prestress allowances.

Automated monitoring can be implemented by converting existing PCPVs and PCCs into ‘smart structures’, augmented with a suite of integrated prestress sensors. Sensor networks, however, are usually designed for and installed during construction, so applying monitoring technologies to existing structures is a unique problem. The challenge is heightened, in this case, by the harsh operating environment—the continuing flux of neutron and gamma radiation, fluctuating temperatures and high stress place unparalleled requirements on sensing technologies.

While many conventional electro-mechanical sensors are unsuitable, optical fibre sensors may provide the solution. Light weight, chemically inert, immune to radiation and electromagnetic interference, and mechanically robust enough to survive some of the harshest environments, fibre sensors detect changes in strain and temperature by measuring the modulated properties of light [Mih12]. Furthermore, optical fibres are small, almost 1-dimensional in nature, making their non-invasive integration into existing structures more convenient than their bulky, electronic or mechanical counterparts.

The aim of this project was to design a fibre-instrumented prestressing tendon and a complementary interrogation scheme, to monitor prestress losses in a surrounding concrete vessel. A method for packaging and attaching a multiplexed array of radiation-resistant fibre strain sensors was developed, along with a demodulation technique capable of resolving sub-newton changes in prestressing force. The ‘smart tendon’ described in this thesis was developed for integration into the tendon ducts of existing PCPVs and PCCs. By verifying and augmenting

health monitoring practices, this technology may improve confidence and safety in not just current, but also future generations of nuclear power plants.

## 1.1 Research Justification

As a product, fibre sensors are still in their early growth phase [Men07]. Annual increasing market shares are driven by innovations in research, but the technology is still not mature enough for habitual deployment within civil engineering. In this project, the requirements of EDF Energy and the nuclear industry were used to drive the development of the smart tendon from its initial conception. This not only encouraged the technology's implementation, but also ensured that the finished product met the high safety standards set out by the industry.

Measuring prestress losses in existing and ageing concrete barriers presents fresh challenges for measurement resolution and stability. Optical fibre sensors, and in particular fibre Bragg grating (FBG) sensors, are able to offer reliable, wavelength-encoded measurements of strain-inducing parameters, that are immune to the interference and intensity fluctuations which plague many conventional electronic transducers [KDP<sup>+</sup>97].

One of the major strengths of FBGs is their ability to form quasi-distributed sensor networks. To take advantage of this, interrogators need to be able to measure and track the reflected peak wavelengths from a multiplexed array. Common methods involve actively scanning wavelength filters to allow the interrogator to map the spectrum, identify and then track peak locations [ZL04]. However, interrogators based on interferometry are usually able to provide a far higher resolution, so it was of interest to develop these schemes further [Byo03]. In this project, a passive, robust, interferometric wavelength-demodulation technique was combined with fast optical pass-band switching to rapidly interrogate a multiplexed FBG array [ON11]. Static and dynamic strain resolutions as high as  $1 \text{ n}\epsilon$  and  $10 \text{ n}\epsilon/\sqrt{\text{Hz}}$  were achieved [PONJ12].

Another often-ignored challenge is the fibre sensors' packaging. This is particularly relevant to the application outlined in this thesis, as the combined radia-

tion, thermal, mechanical and chemical loads on sensors installed within a PCPV or PCC makes sensor survival difficult to ensure. In this work, due consideration was given to fibre packaging to provide the sensors with the robustness and reliability required to function for decades in a harsh environment. The design and manufacture of a fully metallised, encapsulated and spot-weldable fibre strain sensor demonstrates how this technology can begin to break through into more industrial applications in civil engineering.

Scaling the technology up to provide a distributed, continuous measurement of strain over the entire length of at least a small percentage of the thousands of tendons in a PCPV or PCC was also crucial. Because concentrated efforts were made to develop a highly modular system throughout this work, the proposals for scaling up to a real nuclear reactor are in fact very simply addressed. Overall, this research project has produced a proof of concept for a novel optical smart tendon technology, applicable on a wider industrial scale to a real and current industrial problem in the civil and nuclear industries.

## 1.2 Principal Contributions

The principal contributions to the field of optical sensing by this research project are as follows:

- An analysis of prestress loss and its measurement in nuclear concrete structures, capturing the requirements for any smart tendon technology and its interrogation system.
- A detailed literature review of the effects of mixed neutron-gamma radiation on optical fibre sensors, and an estimate for the magnitude of these effects on sensors within a fission reactor environment. This lead into recommendations for the chemistry, coatings and installation procedures for addressing and sensing fibres within a PCPV or PCC.
- The design and application of a nickel re-plating method for bare optical fibres based on evaporative deposition and electroplating.

- The formulation of a fully-metallic capillary-based encapsulation technique for bare fibre Bragg gratings (FBGs), using high-temperature induction brazing. Capillary encapsulation provides superior guidance and protection to bare FBG strain sensors during service.
- Characterisation of the temperature exposure of FBGs during the above encapsulation technique, both empirically and using finite element models. Exploitation of the Curie transition in the kovar capillary was used to physically limit the maximum temperature fibres were exposed to during the induction brazing process.
- Experimental investigation of the influence of high-temperature soldering on fibre sensor reflectivity and fibre splice mechanical strength.
- The design and manufacture of a thin strain plate which could be attached to the capillary and then spot-welded to the prestressing strand.
- Assembly of the capillary-housed FBG and the spot-weldable strain plate, to form a finalised FBG strain sensor for attaching to a prestressing strand.
- Empirical tests of the mechanical properties of prestressing strands and spot-weldable strain sensors after spot-welding.
- Extension of a high-resolution, dynamic interferometric interrogation system into the static regime, without a loss in dynamic performance. The system was combined with signal extraction techniques such as lock-in amplification to provide 1 nanostrain ( $n\varepsilon$ ) resolution measurements of the *relative change* in FBG strain after system initialisation.
- Implementation of interferometer path difference tuning so that the *absolute* initial strain of FBGs could be measured when the system was initialised.
- Experimental demonstration, modelling and discussion of the long-term stability of the above interrogation scheme under fluctuating ambient temperatures.

- Fabrication of prototype smart strands utilising the sensor attachment and interrogation scheme described above. This provided a lab demonstration of temperature-referenced strand strain measurements.
- Descriptions of fibre egress from tendon ducts during smart strand installation in PCPVs and PCCs.
- Proposals for the scaling of the technology to provide distributed, high-resolution measurements of 5 % of the prestressing strands in a PCPV or PCC at a rate of 1 Hz.

### 1.3 Thesis Overview

The thesis begins by outlining the basic operating principles of current and future fission reactors, with a focus on garnering an appreciation of how safety systems and strategies work together to reduce the likelihood and severity of accidents. The roles of crucial passive safety barriers such as the PCPV and PCC are outlined and their radiation shielding properties are discussed.

In the following chapter, the basis and time evolution of the mechanical properties of PCPVs and PCCs are described. The importance of prestressing is highlighted before the short- and long- term mechanisms of prestress loss are reviewed. The current methods used to infer the prestress state of the vessels are then outlined. The rates of prestress loss and the environmental considerations of the previous chapter are used to formulate both a justification and a requirements analysis for newly applied prestress sensor technologies. A fibre-optic instrumented smart tendon is proposed and the requirements for its implementation, installation, measurement performance, mechanical reliability, cost and expandability are outlined.

Chapter 4, begins with an explanation of how optical fibres are fabricated and used to guide light. Light losses arising due to scattering and absorption processes are considered generally, before a detailed literature review of attenuation due to neutron-gamma radiation is presented. Estimates for the radiation-induced

attenuation in fibre systems utilised at different locations within a PCPV are used to provide recommendations on installation locations within the vessels. Following this, the operation, fabrication, thermal/radiation stability and sensing principles of different types of fibre Bragg grating (FBG) are described.

In chapter 5, protection and attachment of FBGs to prestressing strands is considered. Various attachment methods are compared with the requirements of the current application. This is used to justify why metal-embedding of fibre sensors provides unmatched mechanical and radiation resistance. Because metal plated FBGs are not commercially available, a coating process based on evaporative deposition and electroplating is developed. Capillary-encapsulation of bare FBGs using induction brazing is also described and is found to provide superior yields and protection. The influence of high temperatures on the mechanical reliability of fibre splices is experimentally investigated and used to justify a spliceless method of capillary encapsulation. Methods for resistance spot welding the encapsulated FBGs to the steel prestressing strand are outlined and the effects on strand strength are investigated. Finally, cantilever stress tests of instrumented strands are presented and used to characterise the strain transfer of the welded FBGs.

In chapter 6, attention is turned to the interferometric interrogation scheme used to decode strain and temperature signals returning from the FBGs. The system layout is described before the theoretical limitations of its resolution, sensitivity and interrogation speed are outlined. The relative merits and limitations of two signal extraction algorithms are compared—fast Fourier transforming and lock-in amplification. The performance of the interrogator using both of these methods is ascertained for relative changes in both static and dynamic strain signals. The scheme's long-term stability is characterised and proposals for reducing thermal drifts are made. Finally, a method for ascertaining the absolute strain of FBGs during initialisation of the system is described.

In chapter 7, the work from the previous chapters is drawn together and used to propose how the technology can be scaled up and then applied to measure both average and distributed prestress levels in a real PCPV or PCC. Topics

such as FBG characterisation, thermal control of the interrogation system, the optical budget, attachment methodology and fibre egress from the structure are discussed. A method for combining strain measurements of the strand with anchorage load measurements from conventional electronic transducers is described, as this may provide indicators of both average and distributed prestress in the vessel.

Chapter 8 concludes the achievements of the project before suggesting future improvements and applications for this technology. Areas which merit further investigation are highlighted.

## 1.4 Publications

### 1.4.1 Journal Articles

1. M. Perry, P. Niewczas and M. Johnston, ‘Effects of neutron-gamma radiation on fiber Bragg grating sensors: a review’, *IEEE Sensors Journal*, vol 12, no 11, pp 3248–3257, 2012.
2. M. Perry, P. Orr, P. Niewczas and M. Johnston, ‘Nanoscale resolution interrogation scheme for simultaneous static and dynamic fiber Bragg grating strain sensing’, *Journal of Lightwave Technology*, vol 30, no 20, pp 3252–3258, 2012.
3. M. Perry, P. Niewczas, M. Johnston, K. Cook and J. Canning, ‘Induction Brazing of Type-I FBGs into Kovar Ferrules Exploiting Curie Transition’, *IEEE Sensors Journal*, vol 13, no 12, pp 816–823 2012.
4. M. Perry, P. Orr, P. Niewczas and M. Johnston, ‘High-speed interferometric FBG interrogator with dynamic and absolute wavelength measurement capability’, *Journal of Lightwave Technology*, prepublishing, 2013.

### 1.4.2 Conference Papers

1. M. Perry, P. Niewczas, M. Johnston and J. Mackersie, ‘Nickel Plating of FBG strain sensors for nuclear applications’, *21st International Conference on Optical Fiber Sensors*, Ottawa, Canada, 2010.
2. M. Perry, P. Niewczas, M. Johnston, K. Cook and J. Canning, ‘Mechanical strength of silica fiber splices after exposure to extreme temperatures’, *22nd International Conference on Optical Fiber Sensors*, Beijing, China, 2012.
3. P. Orr, M. Perry and P. Niewczas, ‘Solid-State interferometric interrogator and multiplexer for high-speed dynamic and absolute FBG wavelength measurement’, *5th European Workshop on Optical Fibre Sensors*, Krakow, Poland, 2013.

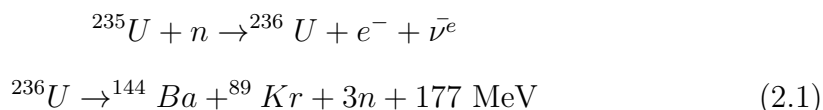
# Chapter 2

## Nuclear Power Generation

### 2.1 Discovery

The early 1900s were an exciting time in nuclear physics. The discovery of the charged constituents of the atom—the proton and the electron—gave scientists an opportunity to explore a new atomic world. Ernest Rutherford first recognised nuclear reactions in 1917, when he discovered that nitrogen transmuted into oxygen under alpha radiation.

In 1932, James Chadwick uncovered a third atomic ingredient—the neutron—and it did not take long for Enrico Fermi to find that these uncharged particles could be used to transmute uranium, somewhat unexpectedly, into lighter elements. Fermi had unwittingly discovered nuclear fission, but it was Lise Meitner who correctly proposed that the neutrons had caused the fissile uranium isotopes to split roughly in two [MF39]:



The energy released from fission can be captured and used to generate electrical power, with the secondary neutrons produced in reaction (2.1) instigating further chain reactions with nearby uranium. Because the likelihood, or ‘cross-

section',  $\sigma_n$ , of a secondary neutron interacting with uranium is energy dependent (as shown in figure 2.1), chain reactions are facilitated by scattering the neutrons from moderators — materials such as water or graphite— to slow them down to thermal energies.

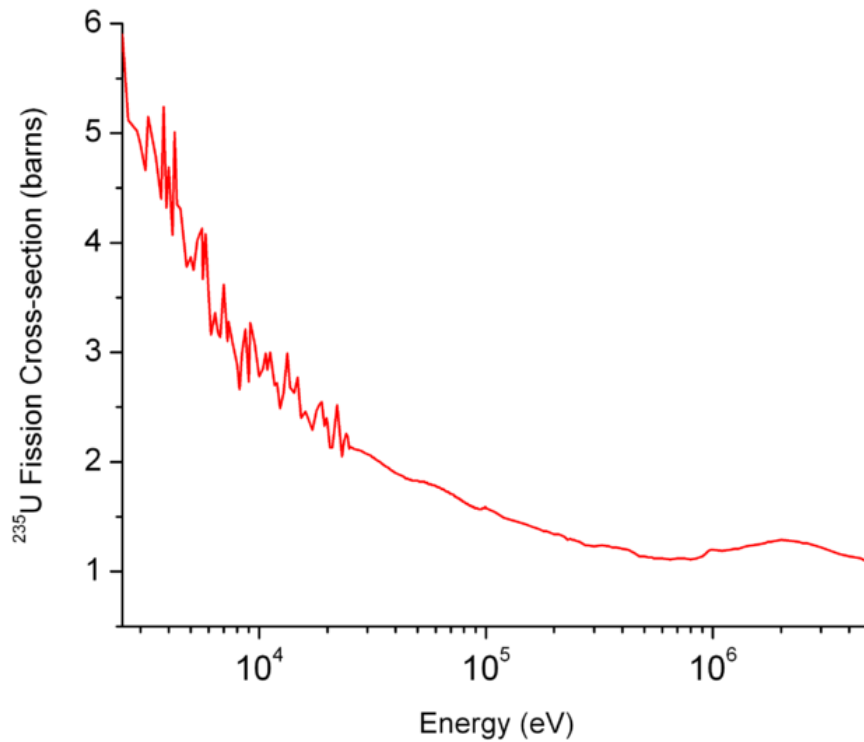


Figure 2.1: The cross-section, or likelihood, of uranium fission as a function of neutron kinetic energy. The likelihood of fast neutrons interacting with the target uranium nucleus is significantly decreased. As such, nuclear chain reactions require that secondary neutrons are slowed by neutron moderators.

It is somewhat apt that the discovery of fission should lead to its very own chain reaction in the global scientific community. Indeed, it was soon realised that this discovery was one of humanity's greatest triumphs of the century, leading somewhat controversially to Hahn alone receiving a Nobel Prize in 1944. A rush to harness the power of the atom (mainly fuelled by an arms race during a turbulent period of history) led to exceptionally rapid advances in the field. By the 1950s, fission chain reactions could be instigated and controlled within a nuclear reactor core. Feasible nuclear power was born.

## 2.2 Fuel Enrichment

Before considering how a modern nuclear reactor sustains a controlled chain reaction, it is worth briefly mentioning how the essential fissile elements are sourced. The only naturally abundant fissile element on Earth is uranium-235. Unfortunately, abundance is a relative term and naturally occurring uranium contains, by mass, less than 1 % of the isotope  $^{235}\text{U}$  and over 99 % of the slightly heavier  $^{238}\text{U}$ , which is not fissile (i.e. cannot be split using thermal neutrons).

To enrich the concentrations of  $^{235}\text{U}$  in any mined uranium, the isotopes are separated by their mass differences, using a variety of techniques such as diffusion, centrifugation, electromagnetic separation and chemical reactions. Needless to say, this is painstaking work and the facilities required to perform enrichment are both complex and expensive. Nevertheless, uranium-235 concentrations can be increased to 4 % for reactor-grade uranium fuel. Any remaining uranium-238 after the enrichment process is then termed ‘depleted’.

## 2.3 Basic Reactor Principles

A supply of fissile uranium fuel and a suitable moderator will allow a nuclear chain reaction to be initiated by a neutron source, termed a ‘neutron howitzer’. The thermal energy, generated within the reactor core is captured and transported to boilers using a circulating liquid or gas coolant. These boilers vaporise water, allowing the steam to drive turbines, generating electrical power.

Heat generation in the core is controlled by limiting the flux of neutrons able to induce fission. The neutron flux is reduced by inserting a series of control rods into the core. These control rods comprise of a neutron poison—a material with a large neutron absorption cross-section which does not undergo fission [Moo71].

At first glance, controlling the chain reaction rate is a daunting task as the time between fission events in the reactor is very short, approximately  $10^{-4}$  seconds. In fact, control is made feasible because a small percentage (0.5%) of secondary neutrons are produced with a naturally occurring delay. While this percentage sounds insignificant, the small number of delayed neutrons is enough to drastically

reduce the rate at which the neutron population in a reactor changes. This allows fission to be fully controlled, over second-long timescales, by control rods and feedback systems.

The pressures, temperatures and radioactive products within the reactor core are extremely harmful to human health. As such, all reactors are housed within biological shielding—often some combination of a steel lining and prestressed concrete.

## 2.4 Reactor Classification

The basic principals above are common to all reactors, but there are many different reactor designs. Nuclear reactors may be classified in any number of convenient ways—a common method is to list them periodically, by their age or generation:

- Generation I: Early prototype reactors.
- Generation II: Commercial reactors built up until 2000. Most reactors currently in operation are generation II, as these are expected to have lifetimes of 30–40 years.
- Generation III: New reactors, at the time of writing, currently under construction. These boast evolutionary improvements to generation II reactors, such as increases in efficiency, safety and cost effectiveness.
- Generation IV: Future reactors currently in a theoretical, research or design stage. All are expected to be constructed post 2030. The main goals of this generation are to reduce both the radioactivity and quantities of waste, while improving energy yields and safety.

Reactors can be further sub-classified by the coolant that they utilise. The choice of coolant is a crucial decision, as the maximum power level any reactor can safely operate at is limited by how quickly heat can be removed from the core. Coolants tend to be held at high pressures, as this improves heat transfer efficiency.

### 2.4.1 Water Cooled

Pressurised water reactors (PWRs) account for approximately half of all commercial reactors globally in generation II. PWRs circulate superheated 320 °C water between the boiler and core under 15 MPa pressure, as shown in figure 2.2. In boiling water reactors (BWRs), the reactor core is flooded with water which acts as both a neutron moderator and coolant and the high core temperatures boil the water directly, as shown in figure 2.3. In both cases, a thick steel shielding contains core pressures. Because steel is expensive and is of limited use as a neutron shield, the radioactive coolant systems, core and boilers are biologically shielded by a secondary concrete layer and a prestressed concrete containment (PCC), which can also contain high pressures and emissions in the event of a core rupture [Mou91].

Decades of experience with water-cooled reactors make them highly reliable and efficient. They are also economical as they use regular water as coolants and moderators. On the other hand, the requirements for specially designed, high-pressure steam turbine technologies can produce major financial and engineering challenges.

While regular water moderates neutrons by scattering, it is also a highly efficient neutron absorber. To improve neutron economy in the core, Canadian deuterium reactors utilise heavy water as a moderator, as its scattering cross-section is some eight-times higher. Unenriched uranium can be used in these reactors, but the need for deuterium production and specialised turbines somewhat offsets the economic advantages.

### 2.4.2 Gas Cooled

More common in the UK, gas-cooled reactors use graphite as a moderator. Now mainly obsolete, generation I Magnox reactors contain gas coolants, such as CO<sub>2</sub> within a pressure vessel. The heated gas is then pumped to external boilers, outside of the PCC [Ner79].

Modern, generation II advanced gas-cooled reactors (AGRs) are an evolution

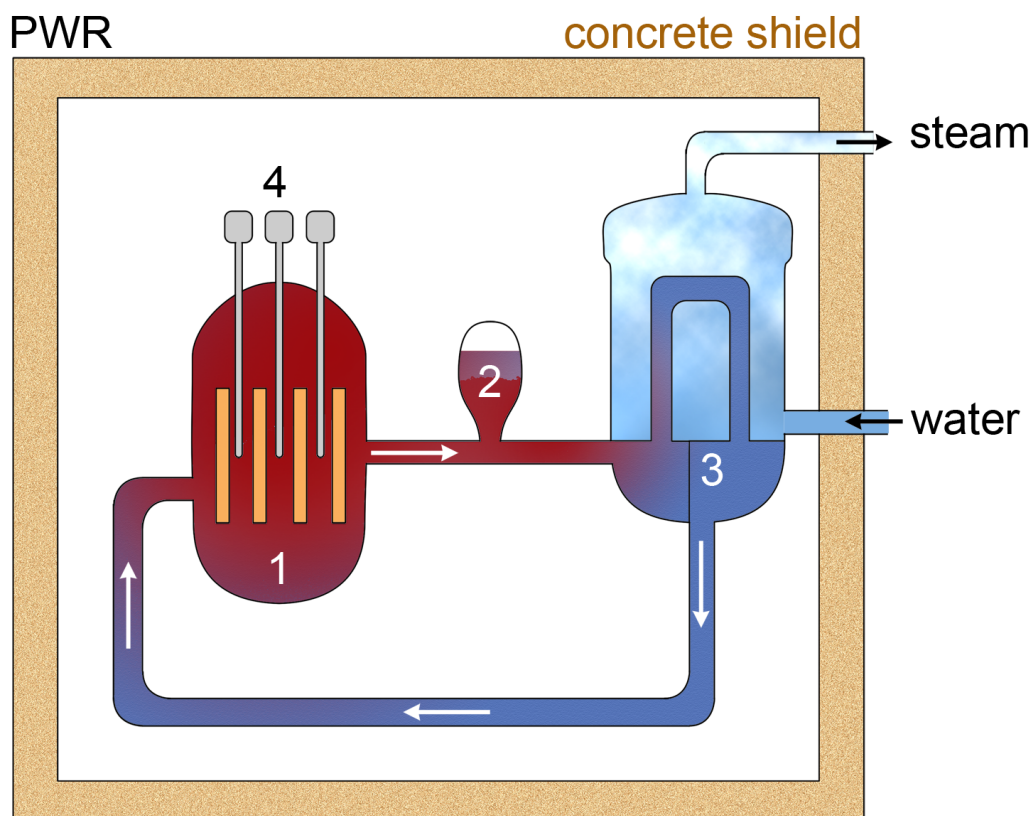


Figure 2.2: The basic layout of a pressurised water reactor (PWR). A pressuriser (2) pressurises water and circulates it between the boiler (3) and reactor core (1). The nuclear reaction is sustained by uranium fuel within a steel liner and controlled using control rods (4). A reinforced or prestressed concrete containment (PCC) surrounds the boiler and reactor.

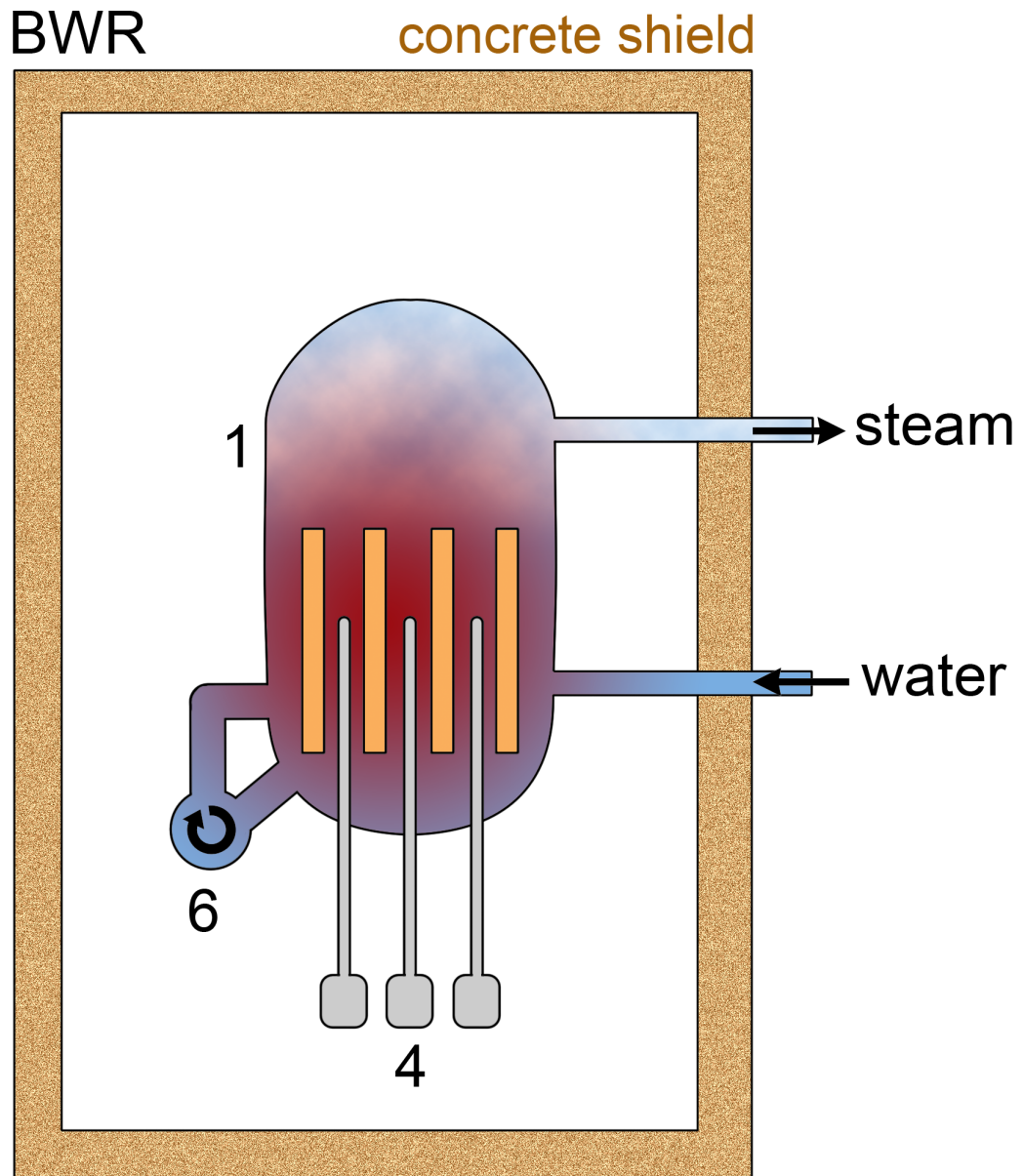


Figure 2.3: The basic layout of a boiling water reactor (BWR). Water is boiled directly within the steel containment vessel and reactor core (1). Pumps circulate the water to ensure heat is distributed evenly (6). The water acts as both a coolant and a neutron moderator. Control rods (4) allow the nuclear reaction rate to be controlled. A reinforced or prestressed concrete containment (PCC) surrounds the reactor, providing biological shielding.

on this principle. As shown in figure 2.4, they provide higher efficiency by using the gas to heat pressurised carbon dioxide *within* the core to a higher temperature. The core and heat exchanging systems are all contained within a steel-lined, 5-metre-thick concrete shield which acts as both a pressure vessel and a radiation shield. This barrier is called a ‘prestressed concrete pressure vessel’ or PCPV. A secondary designated PCC is not required, but the power plant building itself may provide a secondary physical barrier. AGRs present several other advantages over water-cooled reactors. They are safer due to the ability of the graphite core to store excess heat, they use fuel more efficiently and furthermore use conventional superheated steam turbines.

### 2.4.3 Liquid Metal Cooled

Liquid metals, like sodium, are also highly conductive coolants but do not moderate neutrons. This is actually essential for generation III and IV fast breeder reactors, which sustain a fission chain reaction in unenriched uranium-238 using fast neutrons. This process cannot be supported in conventional thermal reactors, as fast neutrons cannot be sustained in the presence of moderators.

Uranium-238 has a further use in this type of reactor as it is ‘fertile’, meaning it can decay into a fissionable element (plutonium-239) after neutron capture. In a fast-breeder reactor, plutonium is ‘bred’ in a uranium blanket which surrounds the reactor core. This blanket not only acts as a highly effective gamma radiation shield, but the plutonium produced can be extracted from the blanket and used to power the reactor later. Fast-breeders therefore transmute their waste into source of power.

While these reactors may be more environmentally friendly from a radioactive waste standpoint, fast neutrons are more difficult to shield. The use of liquid metal coolants, such as sodium, mercury and lead also present appreciable safety, chemical, environmental, engineering and financial challenges for the future.

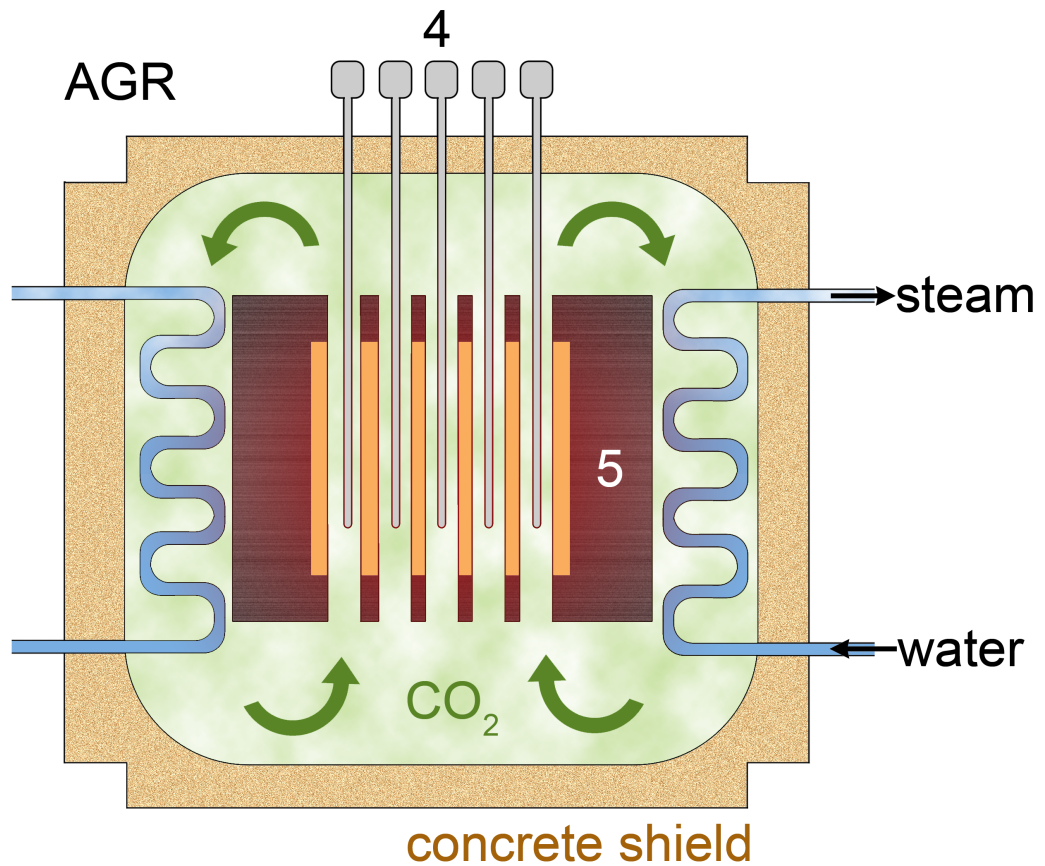


Figure 2.4: The basic layout of an advanced gas-cooled reactor (AGR). Carbon dioxide is circulated around the reactor core transferring heat to a pumped water system. Control rods (4) control the nuclear reaction occurring in the core, which comprises of fuel rods and a graphite moderator (5). A prestressed concrete pressure vessel (PCPV) surrounds the reactor, acting as both a biological shield and a pressure containment vessel.

#### **2.4.4 Molten Salt**

Molten salt reactors (MSRs) utilise coolants and fuels which are molten-salt mixtures. The high operating temperature and heat-transfer efficiency of salt allow these reactors to operate efficiently at lower pressures and with smaller cores. This reduces the mechanical stresses on components in the system, improving safety. There are currently no MSRs in operation as they are all planned for generation IV, but they will undoubtedly require new, tougher regulation and enhanced safety features before being allowed to operate.

### **2.5 Nuclear Safety**

From the descriptions above it is clear that, regardless of their classification, nuclear reactors must operate safely. Nuclear safety is a vast topic, incorporating everything from where and how the reactor is built, to who is permitted to operate it. The discussion in this thesis, however, will focus on the physical and strategic aspects of nuclear safety management.

At a very basic level, reactor systems must ensure that heat generation and transport remain balanced during normal operation. Transient behaviours, such as a failure in the coolant systems (a loss of coolant accident, LOCA) or an uncontrolled chain reaction can lead to excessive core temperatures. The melt down of a reactor is a catastrophic situation, as it may allow harmful radioactive materials to escape the core.

In light of this, the Office for Nuclear Regulation state that reactor safety systems must, as a minimum requirement, be able to permanently shut down the chain reaction and prevent radioactivity from escaping the core during an accident [UK 11]. Ensuring this requires a variety of safety systems and defences, discussed below, which work together to provide cooling and shielding.

## **2.5.1 Reactor Safety Systems**

Safety systems can be classified broadly as either engineered or passive. Engineered components require control, either by plant personnel or electronic systems. Passive or ‘intrinsic’ safety features, on the other hand, are inherent to the physical nature of a reactor component and so do not require any feedback to shut down a reactor safely.

### **2.5.1.1 Engineered Safety**

In the event of an accident, the first priority is termination of the chain reaction. Control rods or neutron poisons such as boron can be injected into the core. Core temperatures are reduced using emergency coolants, which can be injected into the vessel after and even before it is depressurised. The essential service water systems reduce the temperature of heat exchangers and spent fuel rods, while spray systems directly cool the PCC/PCPV. Ventilation systems work to direct radioactive gases into contained areas, away from plant personnel and the wider environment.

Engineered safety systems often rely on electrical power, so multiple emergency electrical back-ups such as diesel generators, flywheels and batteries are utilised with a high level of redundancy to ensure a complete loss of power remains as unlikely as possible.

### **2.5.1.2 Passive Safety**

Passive containment systems also prevent the release of radioactive materials into the environment. Fuel claddings, for example, reduce fuel corrosion and trap gaseous fission products, preventing their diffusion into the coolant systems. Other examples are the thick concrete floor, which resides underneath the reactor core so that in the event of a full meltdown, the molten mixture of reactor components and fuel, dubbed ‘corium’ does not burn through into groundwater systems. Larger containments, such as the steel vessels or PCCs surrounding water-cooled reactors provide biological, mechanical and thermal shielding. The

UK's only PWR, Sizewell B, is housed within a 1.5 m thick PCC with a domed roof, as shown in figure 2.5b. The nuclear power plant building itself acts as a final containment, and may be designed to withstand missile impacts and tsunamis.

As shown in table 2.1, however, the majority of UK reactors are gas-cooled. In an AGR, the reactor vessel and the primary containment are combined into the PCPV (figure 2.5a), which must act to:

- House and support the weight of the reactor and main boilers;
- contain radioactive coolant gas;
- provide a barrier against seismic events, missiles, etc.;
- provide a biological shield against neutrons and high-pressure gas.

As concrete is porous, an insulated steel liner is attached to the inside surface of the PCPV, to contain the reactor gas and protect the concrete from heat and corrosion. In some AGR stations, empty unlined monitoring ducts cast into the concrete are used to monitor the state of the liner and the leakage of carbon dioxide and water from the reactor's cooling systems.

The concrete in PCCs and PCPVs is placed under compression using arrays of steel tendons to improve structural strength. These thick concrete vessels are able to contain high pressures for a fraction of the cost of a steel vessel. Concrete also contains high levels of hydrogen, which has a large neutron absorption cross-section, whereas steel is ineffective as a neutron shield.

## 2.5.2 Radiation Levels

To demonstrate the effectiveness of concrete shielding, the neutron levels in a PCPV at Heysham 1 are shown as an example in figure 2.6. The graph shows predictions for the 10-year integrated neutron flux, or fluence, at four distances from the steel liner [MME81]. Fast neutrons are attenuated dramatically over only a 3 metre distance.

Primary gamma rays arising from the fission reaction terminate immediately at the PCPV's steel side shield [VHW10]. However, secondary gamma rays of

Station Name	Type	Net Output (MW)	No. of reactors	Generation Start	Est. decommissioning date	Operating time (yrs)
Dungeness B	AGR	1040	2	1983	2018	35
Hartlepool	AGR	1190	2	1983	2019	36
Heysham 1	AGR	1160	2	1983	2019	36
Heysham 2	AGR	1210	2	1988	2023	35
Hinkley Point B	AGR	870	2	1976	2016	40
Hunterston B	AGR	890	2	1976	2016	40
Sizewell B	PWR	1191	1	1995	2035	40
Torness	AGR	1205	2	1988	2023	35

Table 2.1: List of the eight active nuclear power stations owned by EDF Energy in the UK [Ene13]. Between them, these nuclear power stations are able to supply electricity to over 17 of the 25 million homes in the UK. Note that since 2006, Hinkley Point B and Hunterston B are both operating at 70% maximum output, as the boilers must be operated at lower temperatures.

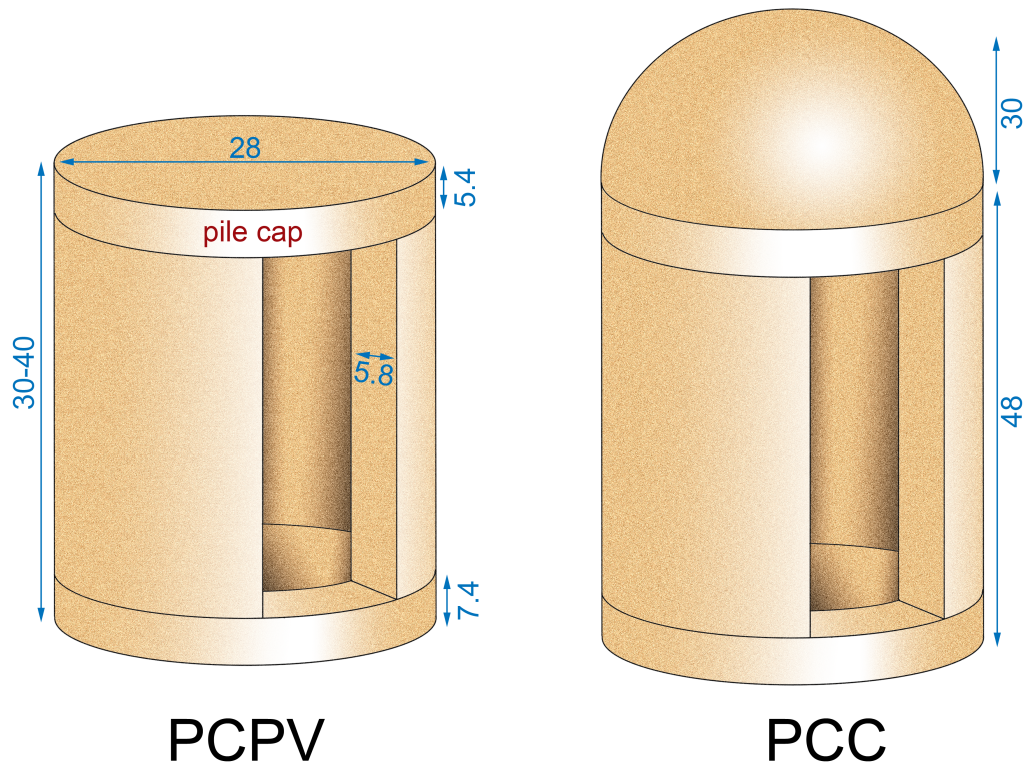


Figure 2.5: Geometry of the prestressed concrete pressure vessel (PCPV) and containment (PCC) with approximate dimensions given in metres. The PCPV geometry is representative of that at Torness, with cutaway showing wall thicknesses. The PCC geometry is representative of Sizewell B.

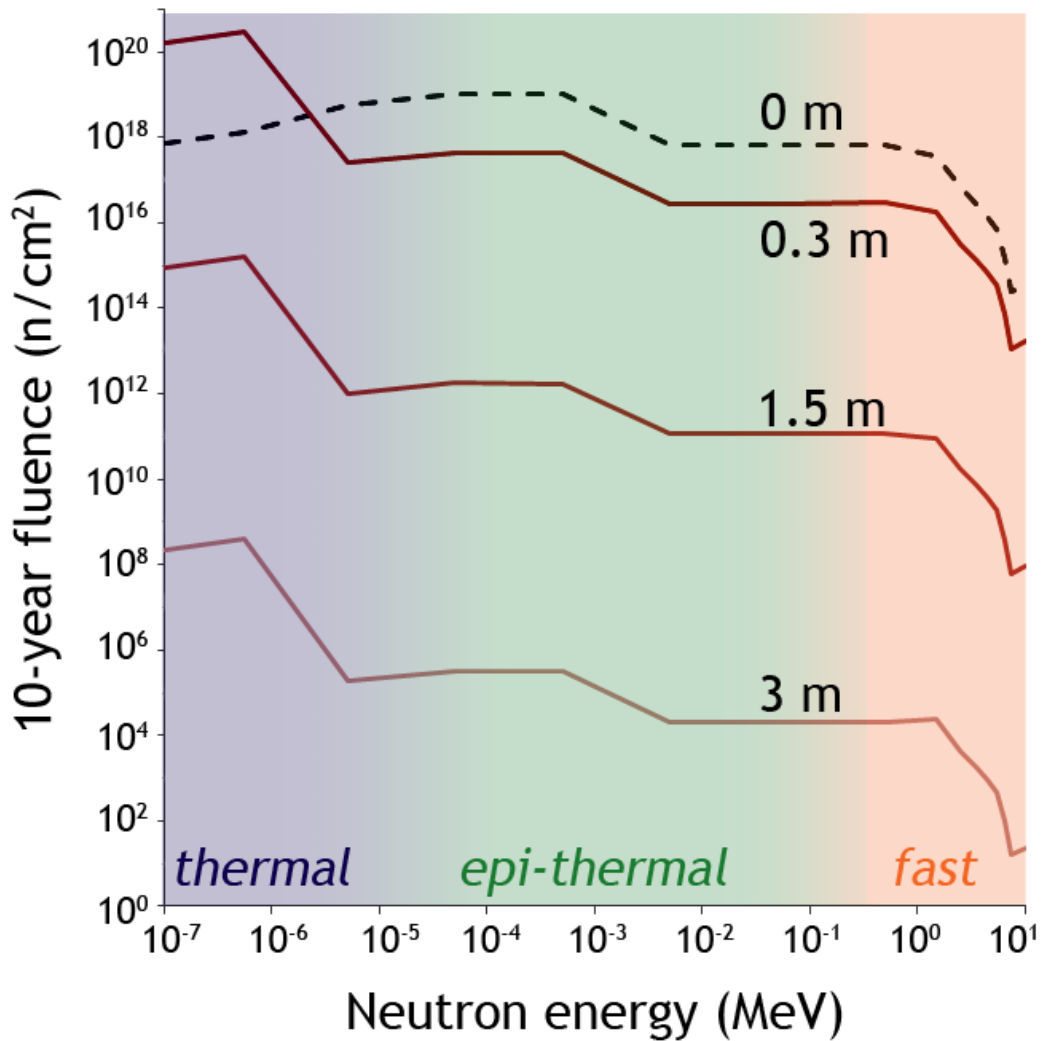


Figure 2.6: Predicted 10-year neutron fluence at four different distances from the reactor core (at  $x = 0$  m, the steel liner, and also  $x = 0.3$ , 1.5 and 3 m). The prediction is for Heysham 1 operating at normal output power. Note the neutron energies are labelled as thermal ( $<1$  eV), epi-thermal (1 eV – 0.5 MeV) and fast ( $>0.5$  MeV). As neutrons are scattered and absorbed from the hydrogen in the concrete, the relative thermal distributions increase. Data is calculated using a model by Ibrahim *et al* [Ibr00]

average energy 1 MeV are produced due to resonances between thermal neutrons and the steel liner. The measured gamma dose rate at the liner of Heysham 1 is 4860 Gy/hr [Daw06] <sup>(1)</sup>. These gamma rays attenuate exponentially through the concrete, leading to the integrated 10-year doses shown in figure 2.7. The dose rate may be slightly higher than this in reality due to the production of more secondary gammas in the concrete, but thick layers of concrete still provide superior shielding against gamma rays.

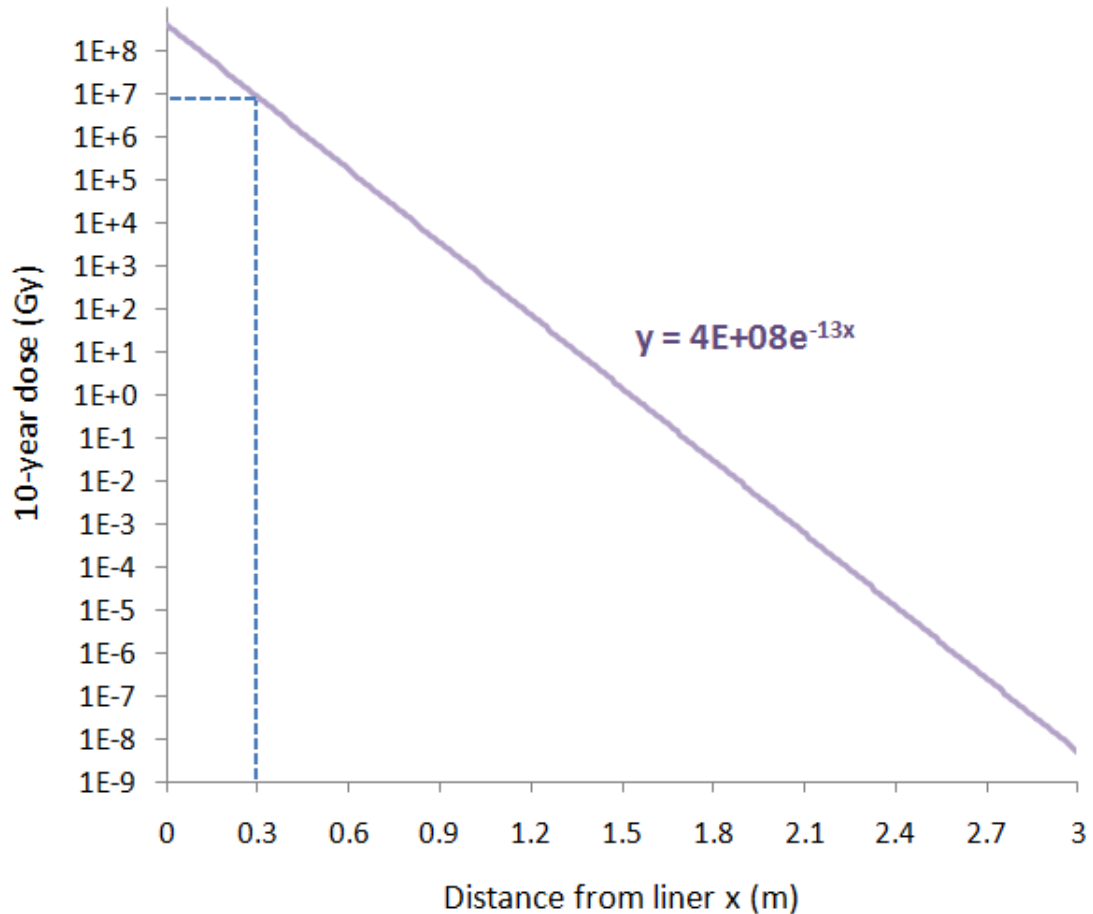


Figure 2.7: The ten-year dose of 1 MeV gamma rays at a distance,  $x$ , from the liner. Concrete's exponential attenuation of gamma rays occurs with the coefficient  $0.13 \text{ cm}^{-1}$  [AN]. The integrated dose thus drops by approximately 5 orders of magnitude every metre.

<sup>(1)</sup>Gamma radiation is often detected by measuring the heat increase per kilogram in an aluminium, water, or silicate glass target, hence dose has units [J/kg] or equivalently [Gy]. The dose a target receives every second is given by  $\dot{D} = \phi \frac{\mu_\gamma}{\rho}$  where  $\phi$  is the gamma ray flux,  $\mu_\gamma$  is the material's attenuation coefficient, describing how well it absorbs gamma rays and  $\rho$  is the target material's density. Conveniently, aluminium, water and glass all have a similar mass-attenuation coefficient,  $\frac{\mu_\gamma}{\rho} = 0.2$ .

### 2.5.3 Defence in Depth

The systems described above supply the physical solution to safety management, but it is also important to formulate a safety strategy. When considering nuclear power plants from a design perspective, it quickly becomes apparent that they operate with a hierarchical ‘defence in depth’ strategy, with multiple conservatively designed fail-safes operating at a very high level of redundancy [INS96]. Each of the five defences, as follows, is designed such that the need for subsequent defences is minimised:

1. *Prevention* — Abnormal operating conditions are defined and then used to decide on plant location, design, construction and operational requirements. Instructions to plant personnel must be clear to prevent accidents from occurring in the first instance. Reactor components are maintained so that they can withstand a prolonged accident.
2. *Operation Control* — Systems to automatically monitor and control abnormal operating transients are implemented. These are used to prevent plant deterioration and to bring the plant back into working order as quickly as possible.
3. *Accident Control* — If an accident condition (such as a LOCA) occurs then systems will prevent the situation from escalating to a severe status, and contain it within barriers, such as the PCPV and PCC. If similar technologies are repeatedly used then their combined failure will be more probable. To avoid these ‘common mode’ failures, several different monitoring and control technologies are chosen to complement and verify each other.
4. *Severe Accident Control* — At this stage the most important objective for accident mitigation is the protection of the reactor confinement. The PCPV or PCC must be cooled and monitored to allow the structure to continue to withstand pressure and contain radioactivity with minimal leakage. Plant operators are trained to utilise systems beyond their originally intended functions to minimise the severity of the accident.

5. *Mitigation of Consequences* — In the unlikely event of a severe accident, this level deals with off-site issues such as radiation exposure of plant personnel and the general public, along with liaison with emergency services and food-chain control.

#### 2.5.4 Accident Classification and Case Studies

Unfortunately, a convincing case for the importance of nuclear safety does not require any imagination. History already holds examples of the consequences of inadequate or poorly designed nuclear safety strategies. From the 1990s, the International Nuclear and Radiological Event Scale (INES) has been used to classify the severity of nuclear accidents, after they have occurred, on a logarithmic scale from 0 to 7, as shown in figure 2.8. To date, there have been only two nuclear accidents classified as major:

- Chernobyl Disaster, 1986 — A sudden surge in reactor power during a test procedure followed by a failure in reactor shut down led to explosive ruptures in reactor containments. Exposure of the reactor’s graphite moderator to the air caused a fire which caused radioactive smoke to propagate and disperse over a large part of Europe. The resulting number of fatalities are disputed, but are often estimated to be in the thousands.
- Fukushima Daiichi Disaster, 2011 — An earthquake caused reactors to shut down and rely on emergency power generation to control cooling systems. The following tsunami, however, caused the reactors to lose their connection to the main power grid, and emergency generator rooms were flooded. These basic design faults resulted in a loss of power and a LOCA, causing reactors to overheat and melt down. The close proximity of the reactors to each other also meant that hydrogen explosions damaged multiple reactor buildings and caused water to drain from spent fuel pools. Future cancer deaths attributable to this accident cannot yet be determined, but some sources estimate the numbers to be as high as one thousand people [VH11].

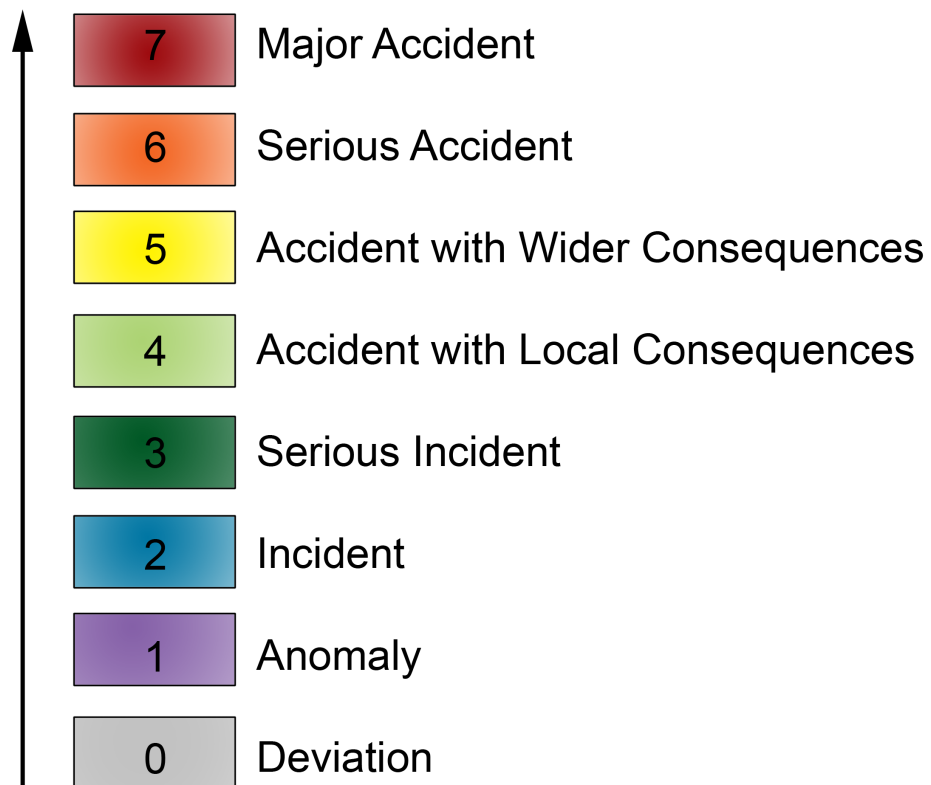


Figure 2.8: INES: The International Nuclear and Radiological Event Scale, used to classify the severity of an accident on a logarithmic scale.

The wider consequences of these disasters are still difficult to ascertain. Ocean currents and local plant and wild life have all provided vectors for radiation dispersal, long after the accidents have occurred [HNO<sup>+</sup>12, PCH12]. Until recently, the Chernobyl disaster of 1986 would have been the only truly significant nuclear disaster since fission generation began. The 2011 Fukushima Daiichi nuclear disaster has provided a poignant reminder of the essential nature of safe nuclear design in the 21st century. The failure of the safety systems at Fukushima, and the fact that the plants had already been operating for 40 years, highlights a problem that this thesis addresses — ensuring the continued safety of an ageing reactor population.

## 2.6 Ageing and Decommissioning

Although originally designed to operate for 20–30 years, it has been found that the lifetime of nuclear reactors in the UK can safely be extended up to 35–40 years. Further lifetime extensions may be planned, provided the plants pass their regular inspection tests. Lifetime extensions are important as they will allow the UK to meet its short-term energy needs while the next generation of reactors are being constructed.

This issue is not special to the UK. As global ageing reactor populations continue to grow, it is important to ensure that safety, particularly passive safety, is never compromised. Many passive safety components in a reactor, such as the graphite core and the PCPV and PCC, degrade with age, so continuous monitoring is becoming more important.

Passive safety barriers may require maintenance even after a reactor has ceased generating power. There is as yet, still no full solution to the difficult problem of decommissioning old generation I reactors. While solutions are continuously being formulated, these reactors still contain hazardous materials, so it is imperative that the passive safety barriers continue to operating adequately.

## 2.7 Summary

The discovery of fission has shaped the modern world by making nuclear power generation not only plausible, but almost commonplace. Moderation of the kinetic energies of the secondary neutrons produced during the fission of uranium-235 allows a nuclear chain reaction to be sustained within enriched uranium fuel. Heat from the chain reaction is transported to boilers by coolants and used to generate steam to drive turbines. Heat generation and transport in the core must remain balanced. The reaction rate can be reduced by limiting the neutron flux using the neutron absorbers contained within control rods.

Water-cooled reactor core pressures and temperatures are contained within a steel pressure vessel. Biological shielding is provided by a passive safety barrier, the prestressed concrete containment (PCC), which surrounds the core and any other radioactive components. Gas-cooled reactors, such as the generation II AGRs more common in the UK, are encapsulated within a steel-lined prestressed concrete pressure vessel (PCPV), which acts as a combined pressure vessel and biological shield. Both the PCC and PCPV act to separate the reactor core from the outside world, especially during accident conditions.

Both engineered and passive nuclear safety systems coincide with a thorough defence in depth safety strategy to provide us with nuclear power plants which operate safely. The Chernobyl and Fukushima disasters provide keen reminders of the devastation which can occur when safety management fails. Fukushima in particular highlights the issues of dealing with an ageing generation II reactor population.

Human or electronic failures may be uncommon, but do happen, so there is a push to improve passive safety in the nuclear industry. Generation III and IV reactors, currently being built or conceived, provide new engineering challenges. These will undoubtedly require evolutions in how plants are monitored and maintained. The task is further complicated by the need to avoid common-mode failures, caused by overusing one type of monitoring technology.

The next chapter focusses on two essential passive safety components—the

PCC and the PCPV. These barriers are essential for at least three parts of the five-step defence in depth strategy and in the case of an accident, may draw the line between a controllable problem and a major disaster. As we will see, the integrity of these safety barriers is not absolute, and concrete structural health monitoring is further complicated by the fact that these supposedly static structures are not as lifeless as they at first seem.

# Chapter 3

## Prestress Losses in Nuclear Concrete Barriers

Prestressed concrete barriers are of prime importance to the safe operation of nuclear power plants. This chapter will follow the manufacture and ageing of PCPVs and PCCs, and justify developments in the technologies used to measure their levels of prestress.

### 3.1 Concrete Production

While the composition varies depending on the application, all concrete is made of the following three constituents:

- *Cement* — Limestone, clay and various other minerals are mixed, heated to 1450 °C and then ground together with gypsum, to produce an ‘ordinary Portland cement’ powder.
- *Water* — This cement powder is mixed with water to form a paste. Too much or too little water can lead to water rejection/bleeding or an unworkable concrete.
- *Aggregate* — Inert, hard particulates such as rocks, gravel, sand and even recycled crushed concrete are mixed with the cement paste to form a concrete mixture. These aggregates, both fine and coarse, form up to 75 % of

the concrete's finished volume. The durabilities, weights, sizes and shapes of aggregates are all carefully selected as they determine many of the mechanical properties of the finished product.

The concrete mixture is poured into a cast and a combination of mechanical impulses, vibration and centrifugation are used to remove entrapped air, reducing porosity [S88]. A set of chemical reactions known as 'hydration' use the water in the paste to create nodes which grow out of the cement particles. These nodes link up to bind the cement and aggregate together into a solid body of concrete.

### 3.1.1 Curing

Water, trapped within sub-micron sized 'gel pores', allows the hydration reaction to continue to fill voids in the concrete matrix, enhancing structural strength. To ensure enough water is provided, the surfaces of the concrete are kept moist via sprinkling, ponding or with wet fabric coverings. Water escape can also be limited by using impermeable plastic sprays and membranes known as curing compounds [oA99].

Up to 95% of concrete's full strength is attained after one month of curing. Reducing water losses also prevents rapid shrinkage, which can lead to cracking. Both hydration and carbon dioxide uptake continue over the years while the concrete is in service, causing it to become harder and stronger as it matures.

## 3.2 Mechanical Properties

As with most materials, the mechanical properties of a concrete member are garnered by measuring its deformation under force, as shown in figure 3.1. The force,  $F$ , acts on internal boundaries of surface area,  $A$ , leading to particle displacement and so a fractional change in the length,  $l$ , of the member. For convenience, the stress,  $\sigma$ , and strain,  $\varepsilon$ , are defined as:

$$\sigma = \frac{F}{A} \quad (3.1)$$

$$\varepsilon = \frac{\Delta l}{l} \quad (3.2)$$

The stress vs strain relationship for a typical concrete member, placed under uniaxial compression, is shown in figure 3.2. The concrete begins to fail at the maximum stress on the graph, at its compressive/breaking strength,  $\sigma'_c \approx 20-100$  MPa.

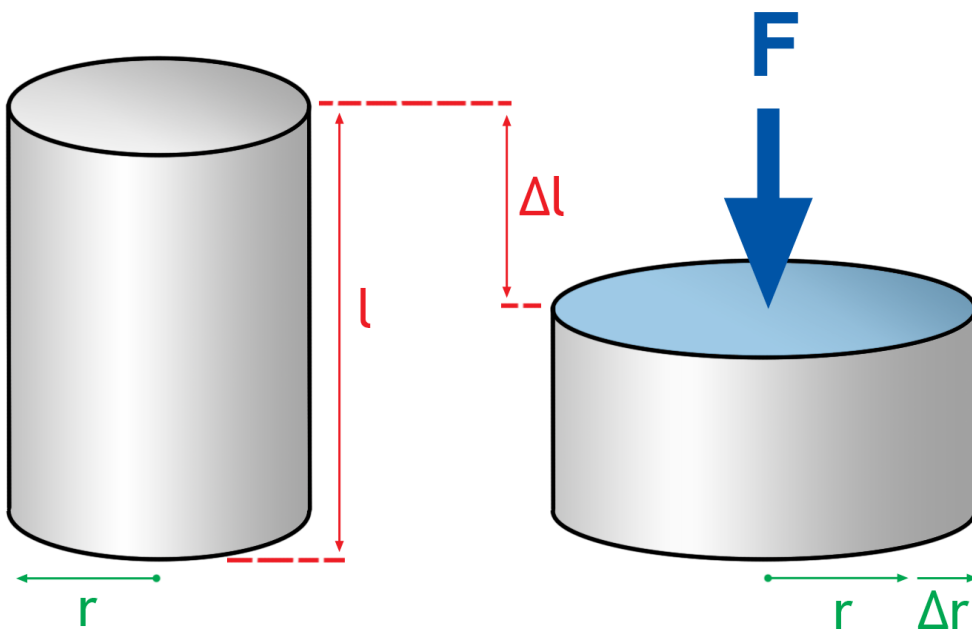


Figure 3.1: A cylindrical body of length,  $l$ , and radius,  $r$ , has its top face placed under compressive force,  $F$ . Elastic deformation causes a reduction in length,  $\Delta l$ , while the Poisson effect leads to a bulging increase in the radius,  $\Delta r$ .

### 3.2.1 Elastic Region

Leading up to failure is an elastic region below  $0.4 \sigma'_c$ , where strain is proportional to the applied stress:

$$\sigma = E_c \varepsilon \quad (3.3)$$

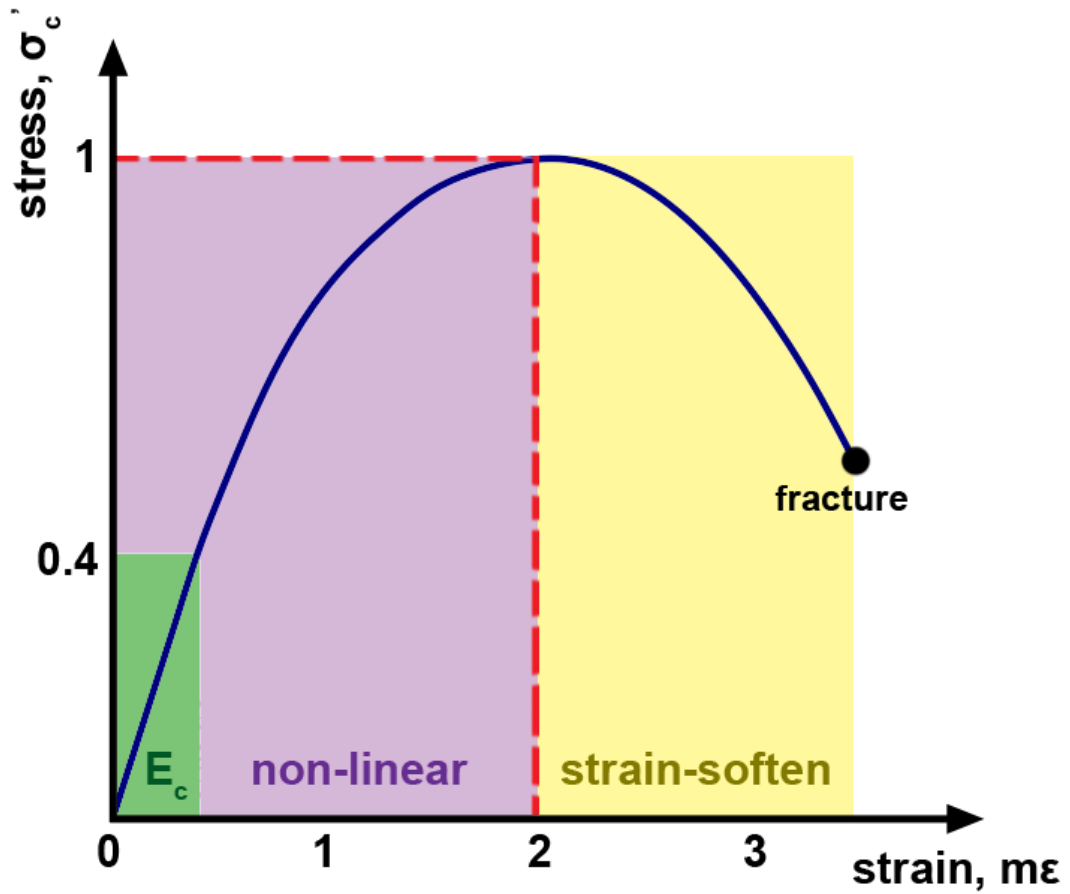


Figure 3.2: A typical stress-strain curve for concrete under compression. The strain in millistrains is measured against the applied stress in units of breaking strength. An elastic region, labelled  $E_c$ , precedes a non-linear region where damage in the form of cracking causes stress-relief. At the breaking strength,  $\sigma'_c$ , real concrete structures will fail. Measurements of the strain-softening region of the graph require stress to be measured under an applied strain instead. Strain-softening demonstrates how heterogeneity leads to the gradual fracture of concrete bodies.

The Young's modulus,  $E_c$ , is a three-dimensional description of the concrete's stiffness or *elasticity*. Concrete's relatively low elasticity of 30 – 50 GPa is dependent on its makeup and age. During the elastic phase, the aggregates within the concrete are forced together, but do not break up or slide over each other. Reducing the stress back to zero at this point will allow the member to return to its original shape <sup>(1)</sup>. This is not the case beyond the elastic region, as permanent damage is introduced [Sta90].

### 3.2.2 Non-linear Region

Concrete cannot remain elastic at higher stresses as it is *heterogeneous*. The Portland cement prevents compositional homogeneity as it is a mixture of several materials, while the variation in aggregates prevent structural uniformity. This means that when uniaxial forces are applied to the concrete, the aggregates typically take up more stress than the cement matrix [Ins68].

Cement nodes are thus placed under more stress at the cement-aggregate interface. The chemical bonds in these areas break first, leading to microcracks in the structure. These small regions of failure release energy, relaxing stress in the entire matrix. This allows the concrete to continue to deform, but under reduced stresses, providing the non-linear region shown in figure 3.2.

### 3.2.3 Strain-Softening Region

As stress is increased up to  $\sigma'_c$  the microcracks coalesce to form a macroscopic crack network which propagates through the structure, leading to failure. At this point, most large structures will collapse under self-weight.

To continue measuring the stress-strain curve beyond failure experimentally, stress becomes the dependent variable while the strain is increased slowly beyond  $2\text{ m}\varepsilon$ . As shown, it gradually requires less force to strain the concrete, demon-

---

<sup>(1)</sup>In reality, there may be no linear region to the concrete's stress-strain curve at all. This occurs because concrete is elastoplastic and almost immediately begins cracking to some extent under force. This can cause problems when attempting to calculate deformations under load, so the elasticity can be estimated via several empirical relationships. One such relationship states that  $E_c = 43\rho_c^{1.5}\sqrt{\sigma'_c}$ , where  $\rho_c$  is the concrete's mass density [kg/m<sup>3</sup>] [IfS08].

strating that fracture is progressive and distributed. This strain-softening effect occurs because the concrete’s heterogeneity allows it to retain havens of structural integrity in low-stress regions [BBC84].

### 3.2.4 Tension and the Poisson Effect

The stress-strain relationship for concrete under tension is conformally very similar to that of compression. Tensile forces, however, are taken up solely by the cement. Hydrated cement has a largely crystalline structure which does not allow much movement to dissipate internal stress. As such, concrete’s tensile strength,  $\sigma'_t$ , is some 10 times lower than  $\sigma'_c$  at only 2 – 5 MPa [22493].

As shown in figure 3.1, tensile stress cannot be eliminated under uni-axial compression, as when the member compressed along the cylinder axis,  $z$ , it will tend to expand radially, along  $r$ . This ‘Poisson effect’ is described by the ratio:

$$\nu = -\frac{d\varepsilon_r}{d\varepsilon_z} \quad (3.4)$$

For concrete, Poisson’s ratio is typically between 0.1 and 0.2. Reducing or eliminating tension in concrete structures thus requires triaxial compression [VMD09].

## 3.3 Prestressed Concrete Pressure Vessels and Containments

Deliberately pre-compressing or ‘pre-stressing’ concrete structures prevents external forces from causing internal tension. Compression also acts to close and prevent the larger cracks which can lead to critical failure<sup>(2)</sup> [dB99]. It is the pre-stressing of concrete containments and pressure vessels that allows them to remain intact while simultaneously containing high pressures, supporting self-weight and resisting missile impacts and natural disasters.

---

<sup>(2)</sup>Small microcracks in the highly tensioned regions of a concrete body may actually be beneficial as cracking dissipates stress. Indeed, the absence of these cracks may be a cause for concern in itself. Small cracks are thus a normal and regularly monitored part of healthy concrete structures.

### 3.3.1 Prestressing Overview

The practical application of prestress requires ductile materials, such as carbon steel, which complement concrete's tensile weakness. There are, broadly speaking, two methods of applying prestress:

- *Pre-tensioning* — The concrete is cast around steel tendons, beams or wires which are held under tension. Hydration causes the cement to bond to the steel so that when tension is released, friction transfers compression to the concrete member. This reliance on friction leads to weaker compression at the extremities of a concrete structure [Raj06]. Pre-tensioned members are also usually fabricated off-site, so logistical issues often limit the structure's size.
- *Post-tensioning* — The concrete is cast around ducts, through which steel tendons are later threaded and tensioned. Compression is transferred to the concrete via anchorages and bearing plates at the tendon ends. As post-tensioning can be performed on site, it is usually the method of choice for large concrete structures such as containment vessels.

### 3.3.2 Prestressing Steel

Prestressing steel preforms consist of iron with a 0–2 % uniformly dispersed carbon content. The carbon inhibits the translation of the iron atoms when the steel is stressed, leading to a higher strength and hardness, at the expense of some ductility. The crystal structure of prestressing steel, dubbed 'pearlite' and shown in figure 3.3, comprises colonies of layered iron ferrite and cementite (a hard iron carbide compound).

#### 3.3.2.1 Wire Fabrication

As the cast steel cools, hot-rolling improves its strength by encouraging uniform thermal-stress relaxation. The solidified preform is then drawn through a series of dies of decreasing aperture at room temperature. This cold-drawing process,

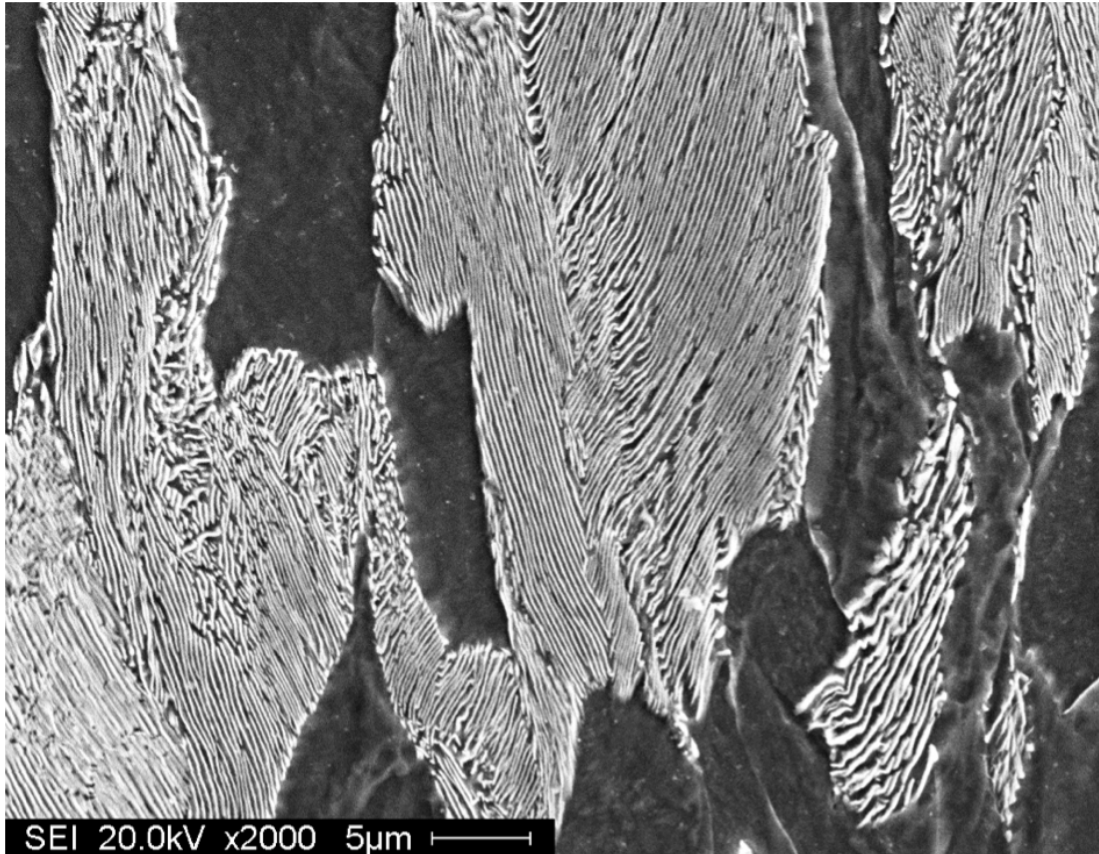


Figure 3.3: The crystal structure of untreated pearlite steel. Layers of iron ferrite and cementite are organised into colonies of similar orientation. A three-dimensional view of each colony would reveal that these 'layers' are in fact all connected, so that each colony is actually only made from two single interpenetrating crystals.

an example of which is shown in figure 3.4, is used to permanently (plastically) deform the preform into a 6 mm diameter wire. This promotes strength by realigning the crystal structure within the steel so that it lines up with the direction of the eventual force application. The steel is also ‘work-hardened’ as the crystal structure becomes saturated with dislocations which further inhibit crystal movement [ID01].

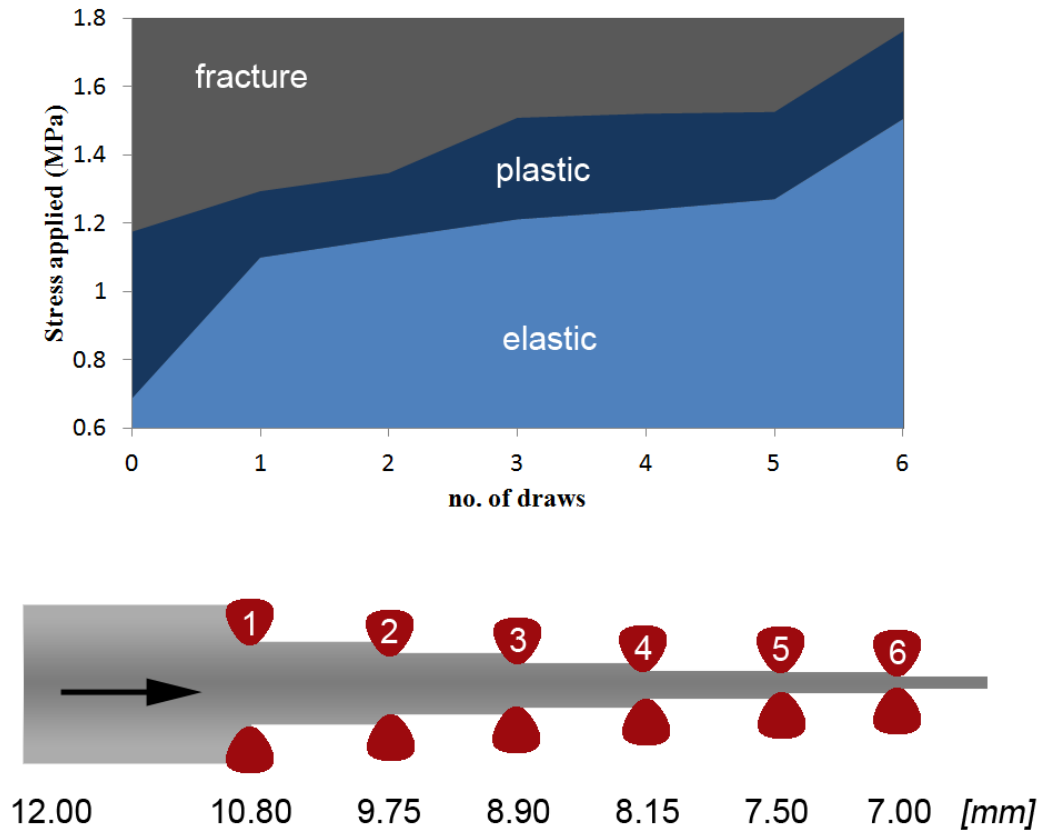


Figure 3.4: An example of cold-drawing. A 12 mm preform is drawn at room temperature through 6, labelled, consecutive dies of decreasing diameter to produce, in this case, a 7 mm wire. The graph shows how each consecutive draw increases the yield and ultimate tensile strength (i.e. both the elastic and plastic limits) of the steel [TO00].

### 3.3.2.2 Mechanical Properties

Typical stress-strain curves for prestressing steels under tension are shown in figure 3.5. The limited carbon content and cold-drawing allow the steel to remain

predominantly linear-elastic, as it undergoes reversible deformation up until the yield strength. Beyond the elastic limit, the steel yields irreversibly under plastic deformation. The sample will finally fail at its ultimate tensile strength (UTS), undergoing necking and shortly afterwards, fracture.

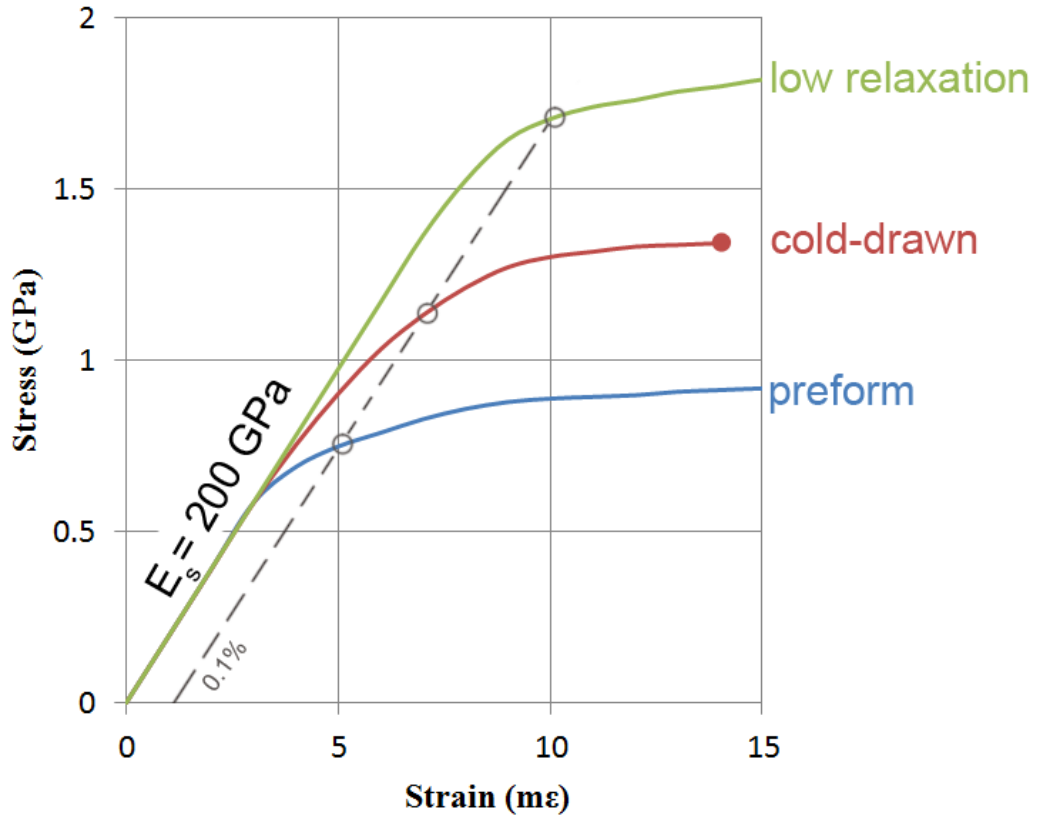


Figure 3.5: Stress-strain curves for prestressing steels. Cold-drawing increases the yield and ultimate tensile strength of preforms, but the increase in hardness causes fracture at lower strain values. Stress relieving increases strength even further, with low relaxation strand remaining elastic almost up until fracture [Hur98]. The stress at which the line labelled 0.1 % intersects with each curve provides the 0.1 % offset yield strength — a number used to define the yield point and the beginning of plastic deformation.

Yielding is undesirable as it reduces the amount of prestressing force applied to the concrete structure. As such, the elastic limit is increased by heating the prestressing wire up to 350 °C. This allows the atoms within the sample to diffuse, relaxing up to 90 % of the internal stresses induced by cold-drawing. The dislocations in the steel may be redistributed or weakened, causing some regeneration of ductility.

Property	Value	Tolerance
Diameter (mm)	18	+0.4, -0.2
Cross-sectional area (mm <sup>2</sup> )	223	+4% -2%
Linear mass density (g/m)	1750	+4% -2%
Elasticity (GPa)	195	± 10
Ultimate tensile strength (MPa/kN)	1700/380	55/12
0.1% offset yield strength (MPa/kN)	1450/323	60/13

Table 3.1: Typical properties of 7-wire, cold-drawn prestressing strand according to BS 5896:1980. The elasticity, yield and ultimate tensile forces (kN) are the most important features as they govern the tendon strand’s ability to deliver prestressing forces.

Another method used to maximise the range of elasticity is strain tempering—the steel wire is again heated but is also placed under tension to further relax dislocations and reduce hardness. The resulting ‘low relaxation’ steel wire is almost entirely elastic up until fracture, as shown in figure 3.5<sup>(3)</sup>.

Because the exact yield points in figure 3.5 are not obvious, engineers often use the offset yield strength to define when the elastic limit has been breached. A line parallel to the elastic region is drawn through a strain of  $1 \text{ m}\epsilon$  (0.1% strain). The stress at which this line intersects the stress-strain curve is designated the 0.1 % offset yield strength [Ros99].

### 3.3.2.3 Strand Fabrication

British Standard BS 5896:1980 offers guidelines for high-tensile-strength steel wires and strands for the prestressing of concrete. Tendon strands typically comprise of six cold-drawn steel wires wound helically around a straight king wire, as shown in figure 3.6. The helical winding ensures that tensile forces are equally distributed between all seven wires. After winding, the strand may be drawn through a final die to compact the wires together and improve integrity.

Table 3.1, lists some of the mechanical properties which BS 5896:1980 states the cold-drawn, 7-wire tendon strands used in PCPV/PCCs in the UK should exhibit [Sta80].

---

<sup>(3)</sup>Low relaxation wire is in fact named because it undergoes less ‘stress relaxation’ than conventional steel, but this is described in more detail in §3.4.4.

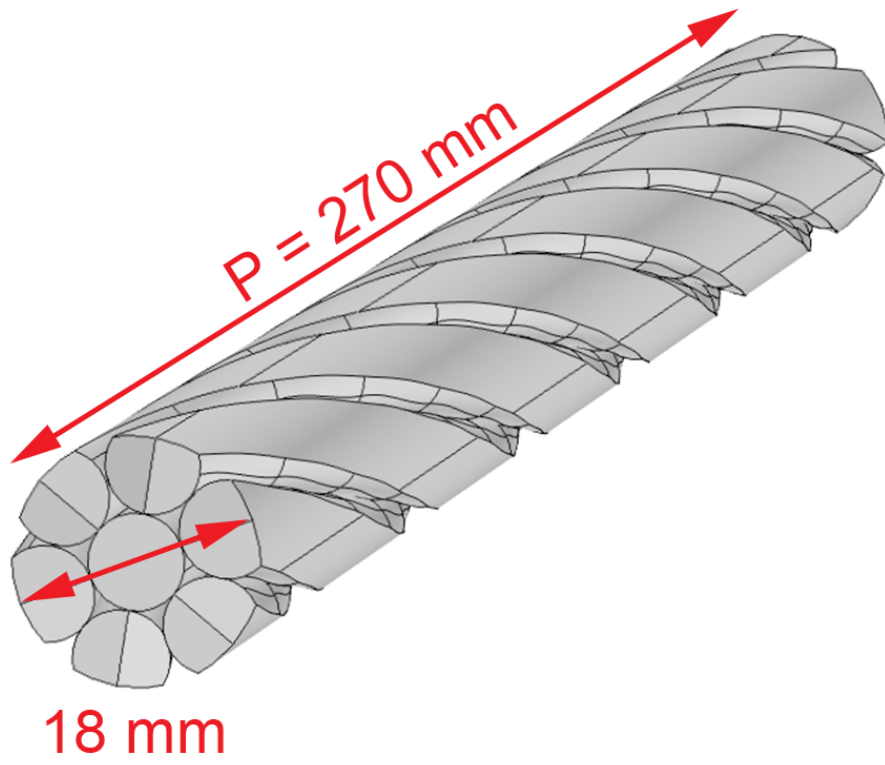


Figure 3.6: The geometry of a section of a typical 7-wire prestressing steel strand. As shown, the pitch of the helical winding is approximately 27cm.

### 3.3.3 Post-tensioning Method

During construction of a PCPV or PCC, the concrete is cast around ducts, through which prestressing strands are later threaded and tensioned using a hydraulic jack. The strands terminate at the edges of the structure, at anchor/grip barrels which transfer stress to bearing plates at the concrete edge, as shown in figure 3.7. Bearing plates can house between 7 and 37 strands, which together form a prestressing tendon, as shown in figure 3.8.

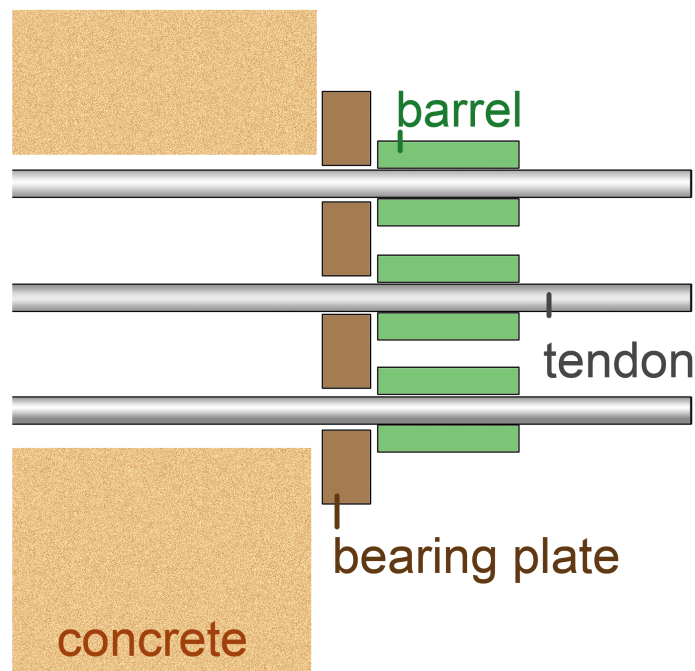


Figure 3.7: Diagram showing how tendons are used to transfer prestress to a concrete structure in a post-tensioned system. Strands are threaded through ducts cast into the concrete and terminate at ‘anchor’ or ‘grip’ barrels. The barrels are used to transfer prestressing forces to a bearing plate, which in turn compresses the concrete structure once the tendons are tensioned.

In unbonded post-tensioning systems, commonly used in the UK, an oil-based lubricant is coated onto the tendons during insertion and/or injected into the tendon ducts. This provides lubrication during installation and also slows the corrosion of the steel in service. In *bonded* post-tensioning systems, the cavity is grouted with Portland cement. Grouting, a method more common globally, prevents corrosion and is thought to form a strong bond between the tendon and

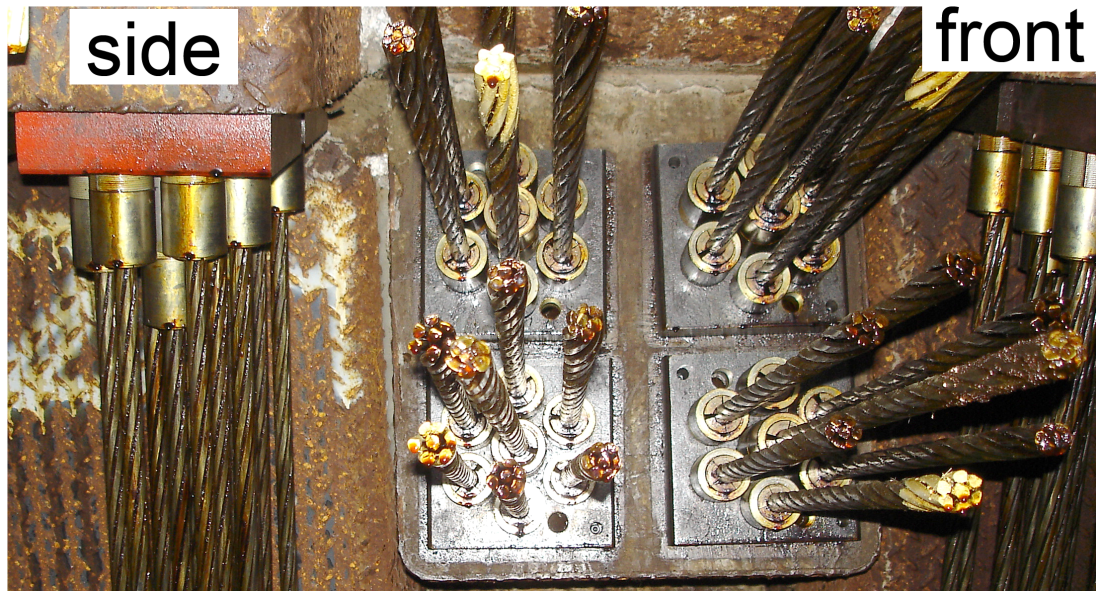


Figure 3.8: Photographs of the bearing plates used in one of Torness nuclear power plant's PCPVs from side and front views. All strands protrude by a minimum of 350 mm beyond the grip barrel to allow prestressing with a jack. While the bearing plates at Torness are square and house 7 strands, bearing plates at Sizewell B are circular and house 37 strands, so there is some variation between plants.

concrete. Unbonded tendons, on the other hand, can be re-tensioned (see §3.5.1) and even replaced at later times, allowing their corrosion and prestress levels to be monitored directly. Partial or full replacement involves de-stressing of the original strand and the welding of a new strand to its end face. As the original strand is pulled out of the duct, the new strand moves in to take its place.

### 3.3.3.1 Tendon Layout

Ensuring triaxial compression in large concrete structures requires some thought about tendon layout. In nuclear concrete barriers, tendons follow paths to avoid the various penetrations, such as boiler penetrations, access holes and monitoring ducts.

Broadly speaking, there are two tendon layouts used in PCPVs. At Torness, Hinkley Point B and Hunterston B, tendons run helically (both left and right-handed) around the circumference of the PCPV in radial rows (see Figure 3.9), providing both circumferential and longitudinal compression. Tendons terminate

in two halls at the top and bottom of the structure called the upper and lower stressing galleries. The PCPVs at Hartlepool and Heysham 1, on the other hand, separate the horizontal and longitudinal prestressing tendons into two groups, as shown in Figure 3.10, with circumferential tendons wound through 120 turns before terminating at cylinder wall faces. The top and bottom caps of PCPVs are typically prestressed using a combination of circumferential, helical and straight tendons.

In the UK's only PCC at Sizewell B, longitudinal prestress is supplied by vertical tendons as shown in figure 3.11. Hoop tendons, each of which span two-thirds of the PCC's circumference are distributed over the height of the containment to supply circumferential compression.

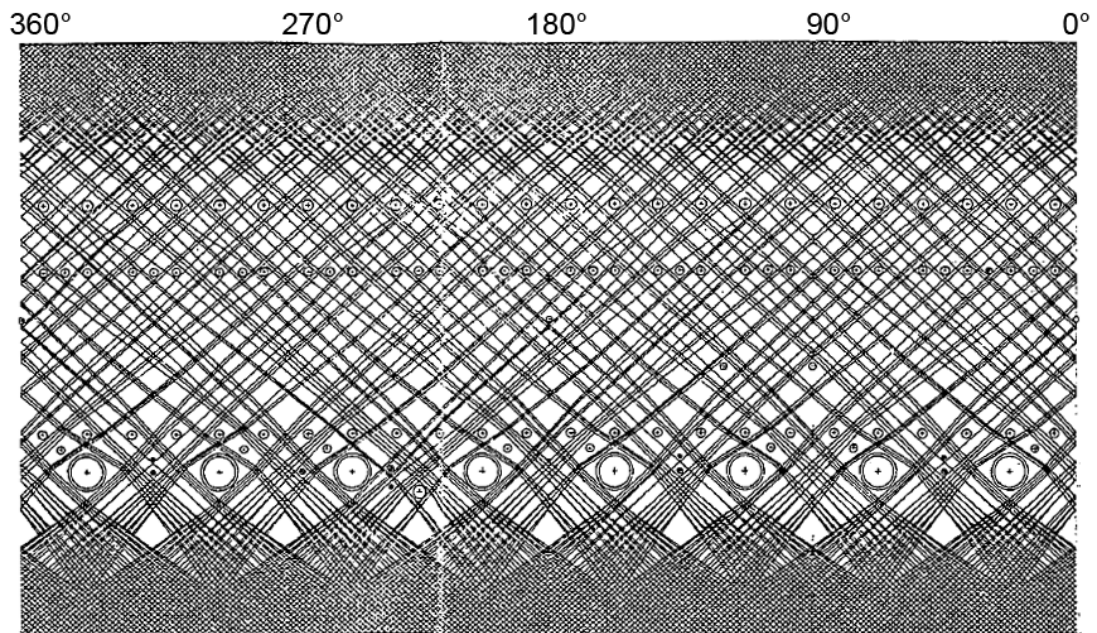


Figure 3.9: Net of the tendon layout at the PCPVs at Hinkley Point B and Hunterston B, showing helically wound tendons. The tendons are inclined at  $36^\circ$  to the horizontal.

### 3.3.3.2 Initial Stressing

The method of initially stressing the tendons varies between power stations, but a general description of the procedure is given as follows:

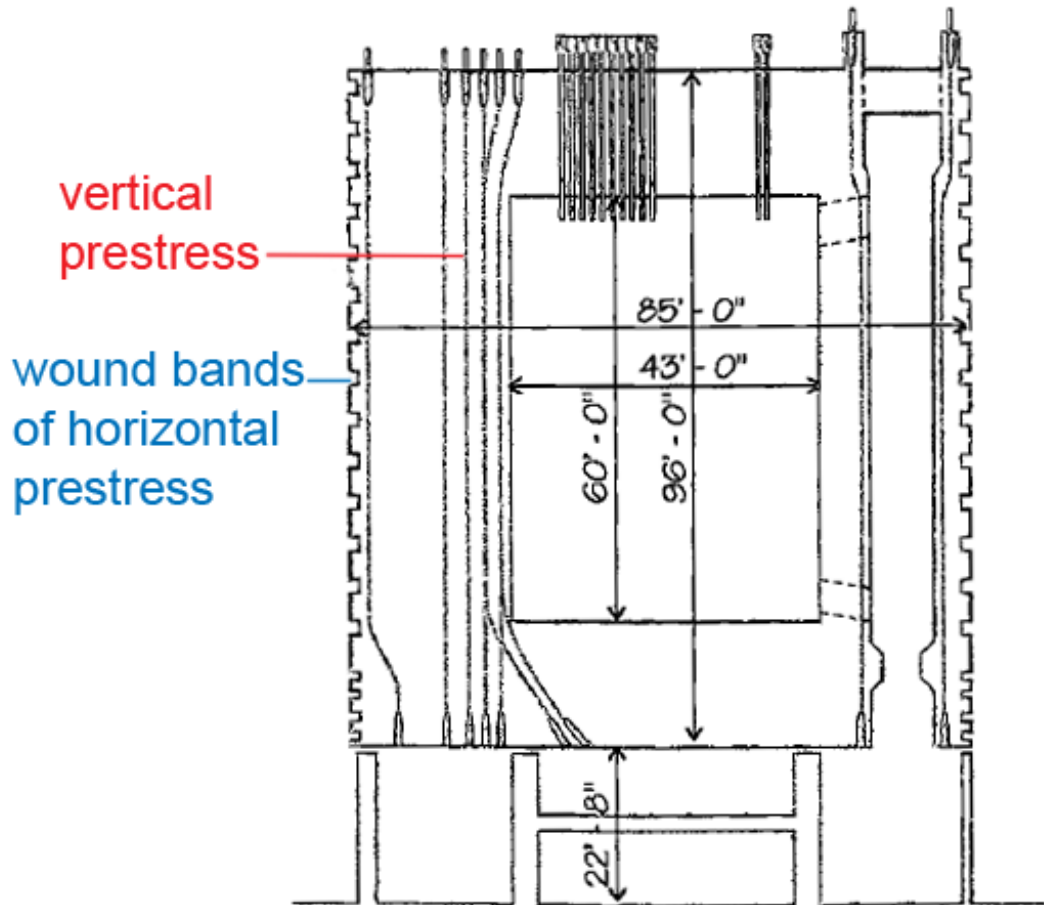


Figure 3.10: Tendon layout at Hartlepool and Heysham 1. Vertical and horizontal prestressing tendons are separate. Also shown are some of the vessel dimensions in feet and inches.

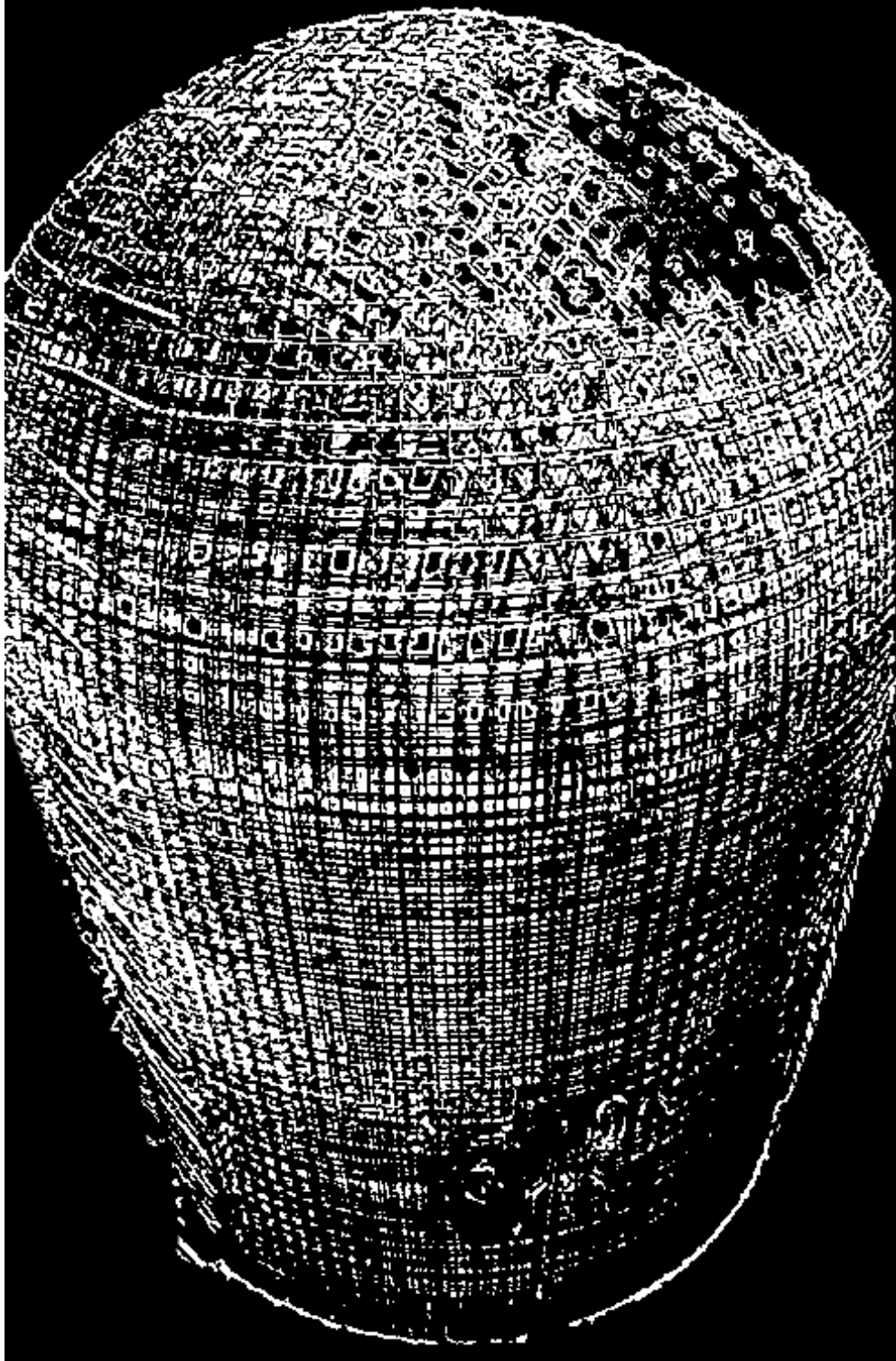


Figure 3.11: Tendon layout within the PCC at Sizewell B. Vertical and horizontal prestressing tendons are separate, with horizontal prestress supplied by circumferential hoop tendons.

1. A stressing stool, shown in figure 3.12, is slotted over the tendon ends. Stressing stools are used to give the prestressing jack a convenient perpendicular face to push against during stressing and to transfer reaction forces to the more robust bearing plate.
2. Calibrated prestressing jacks are fitted onto each end of the centre strand (strand 1 in figure 3.13).
3. The jacks are loaded in stages to 20, 50, 150 and 304 kN<sup>(4)</sup>. The jack force and strand extensions are noted at each sequential stressing stage. Stressing is discontinued and investigated if discrepancies arise between actual and predicted strains. At the final 304 kN stage, pressure and extension readings are taken a second time after 60 seconds, as the load may have to be topped up again.
4. Both jacks are locked-off and then removed simultaneously, allowing the barrels to transfer force to the bearing plate. The final prestressing force applied to the bearing plate is somewhere in the range of 266-304 kN (70-80 % steel UTS) per strand.
5. The calibration of the jacks is checked and the steps above are repeated sequentially on strands 2 to 7, shown in figure 3.13, in sequence.

While strands are usually stressed simultaneously at both upper and lower galleries, in some cases space limitations only allow access to one end of a tendon. As slippage of the strand at the opposite dead-end anchorage could be mistaken for extension, wedges are hammered into barrels before prestressing and the strands are marked and checked for slippage later.

---

<sup>(4)</sup>These forces correspond to approximately 5, 13, 39 and 80 % of the steel's UTS. This should produce strains of 0.4, 1.1, 3.3 and 6.8 millistrains, although actual values may differ as the extension at 20 kN removes slack from the strand and is recorded as a zero extension measurement.

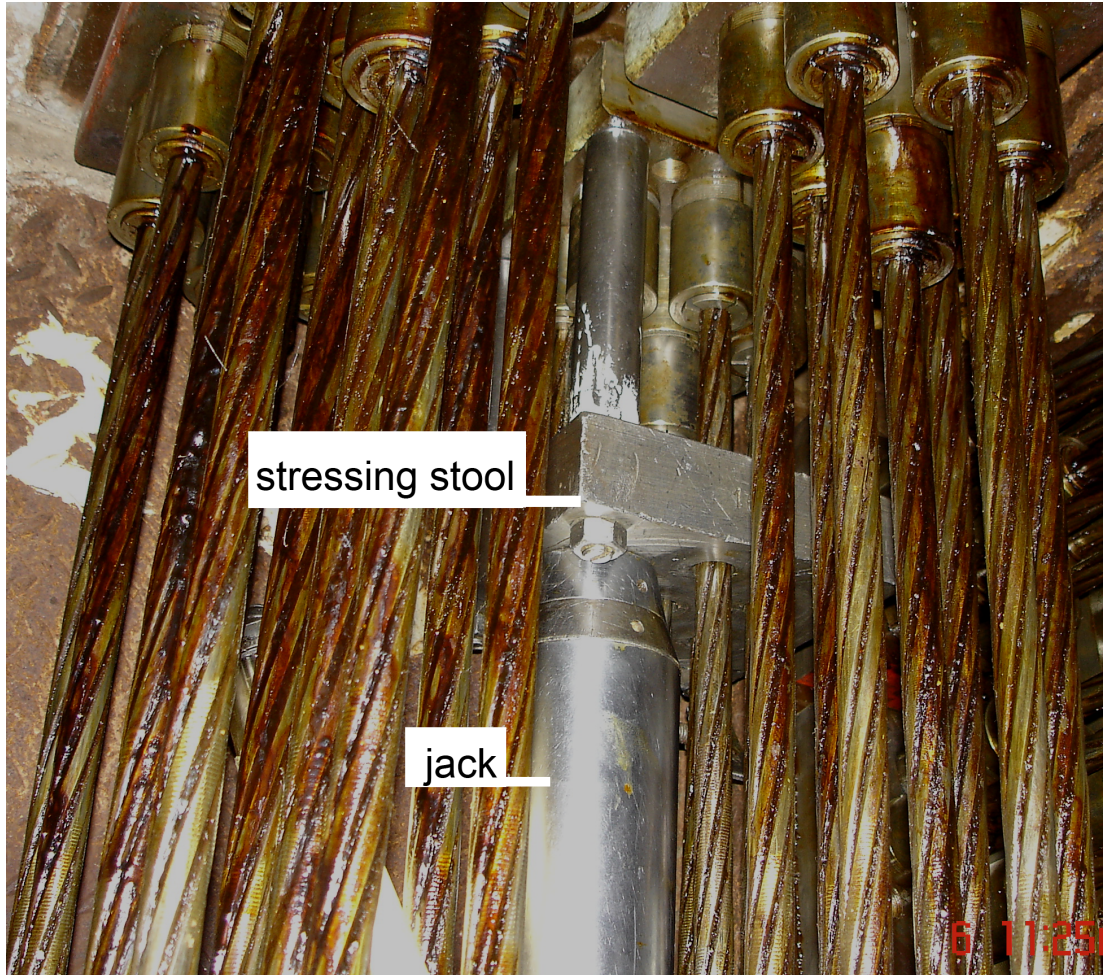


Figure 3.12: A photograph of a stressing stool slotted over 7 strands in the lower stressing gallery at Torness nuclear power station. The stressing stool provides a perpendicular face for the prestressing jack nose to push against during jack loading.

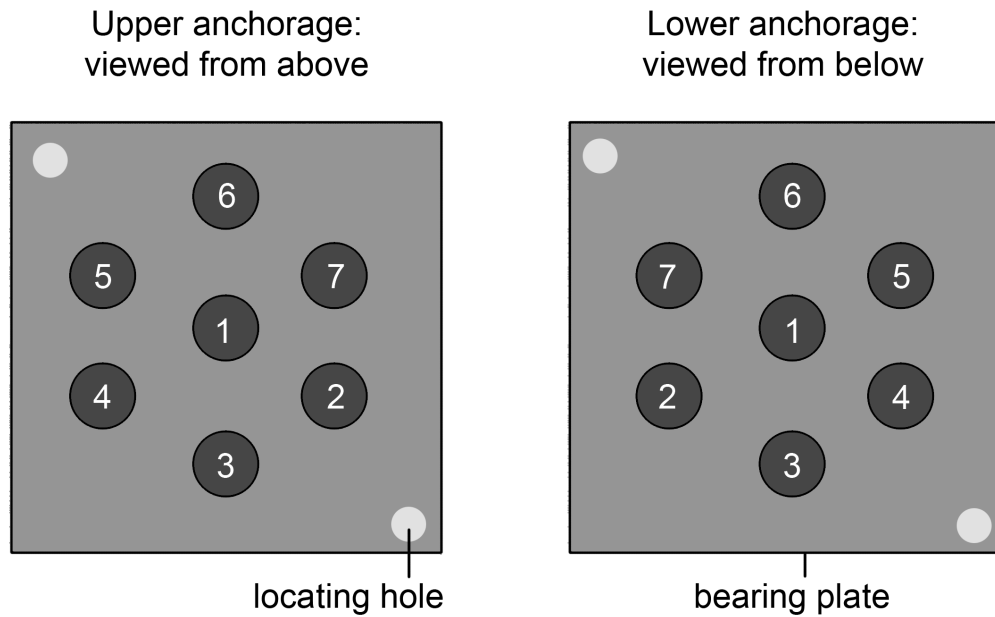


Figure 3.13: The tendon numbering system, following a clockwise sequence when viewed from above in the upper stressing gallery, and an anti-clockwise sequence when viewed from below in the lower stressing gallery. Holes in the bearing plate are used for orientation.

### 3.4 Prestress Loss

Adequate prestress must continue to be transferred to the concrete vessels as they age, as this ensures structural health is not compromised. Short-term prestress losses, effects which reduce prestress as soon as the jacks are locked-off, are compensated for by topping up the force during or within the first month of initial stressing (a process known as ‘reshimming’). The major three short-term prestress losses are:

- *Elastic shortening*,  $\Delta f_{es}$  — Prestress transfer causes immediate elastic compression of the concrete, reducing the force applied by the tendons
- *Anchorage Pull-in/Slip*,  $\Delta f_{an}$  — Barrel wedges and anchorages may slip or be drawn into the concrete as tendon stress is transferred to the bearing plate
- *Friction*,  $\Delta f_{fr}$  — Contact between the strands and the surrounding duct can occur due to unintentional (wobble) and intentional (helical winding or

bending) changes in a strand's angle as it passes through a duct.

Long-term losses of prestress, on the other hand, occur over the course of years or even decades after initial prestressing, so are harder to correct for. These include:

- *Creep*,  $\Delta f_{cr}$  — The slow, permanent deformation of the concrete in response to applied external forces. Creep occurs due to the diffusion of concrete grain boundaries and also due to the load-induced expulsion of water. The rate and magnitude of creep increase with temperature and applied load
- *Shrinkage*,  $\Delta f_{sh}$  — After being cast, water evaporates from the concrete and the structure contracts. Approximately 80 % of shrinkage occurs during the first year after casting
- *Steel Relaxation*,  $\Delta f_{sr}$  — Gradual plastic deformation, or creep, in the steel tendons, will occur as they sustain high loads over time. This causes the tendons to remain the same length, but apply less compression to the structure.

The total prestress loss is simply the sum of these components:

$$\Delta f = (\Delta f_{es} + \Delta f_{an} + \Delta f_{fr}) + (\Delta f_{cr} + \Delta f_{sh} + \Delta f_{sr}) \quad (3.5)$$

As directly measuring the compression state of the concrete is often unfeasible, prestress is ascertained from measurements of the applied tendon force<sup>(5)</sup>. As we shall see, elastic shortening, creep and shrinkage cause a uniform reduction in force over the entire length of a tendon, while the combination of friction, anchorage slip and stress relaxation lead to a much more complicated force profile. Appreciating the somewhat complex interplay between these prestress loss mechanisms requires a further description of how each one propagates over time and distance.

---

<sup>(5)</sup>Nomenclature: Throughout this section, a lower case  $f$  will symbolise the prestressing force of the concrete structure, while a capitalised  $F_i$  is used to symbolise the prestressing force of the  $i^{\text{th}}$  tendon prestressed in the system. The basic assumption, that the concrete reacts to the force supplied by all of the tendons, is thus written mathematically as  $f = \sum F_i$ .

### 3.4.1 Elastic Shortening

Elastic shortening occurs in any concrete structure which is compressed sequentially by multiple strands or tendons. As the strands of one bearing plate are stressed in the sequence shown in figure 3.13, the gradually increasing load on the concrete leads to increasing elastic compression. The stressing of each sequential strand thus reduces the amount of prestress applied by the strand before it. The same is also true on a tendon-by-tendon basis.

In a PCPV comprised of some 3000 tendons, measuring the elastic shortening after every prestressing operation would be prohibitively time consuming. The effect is thus estimated from empirical equations. The simplest of these states that the force lost in each tendon is at least half of that lost by the first one which was stressed,  $\Delta F_0$ . The total force lost due to elastic shortening is thus:

$$\Delta f_{es} \approx \frac{M_{td}}{2} \Delta F_0 \quad (3.6)$$

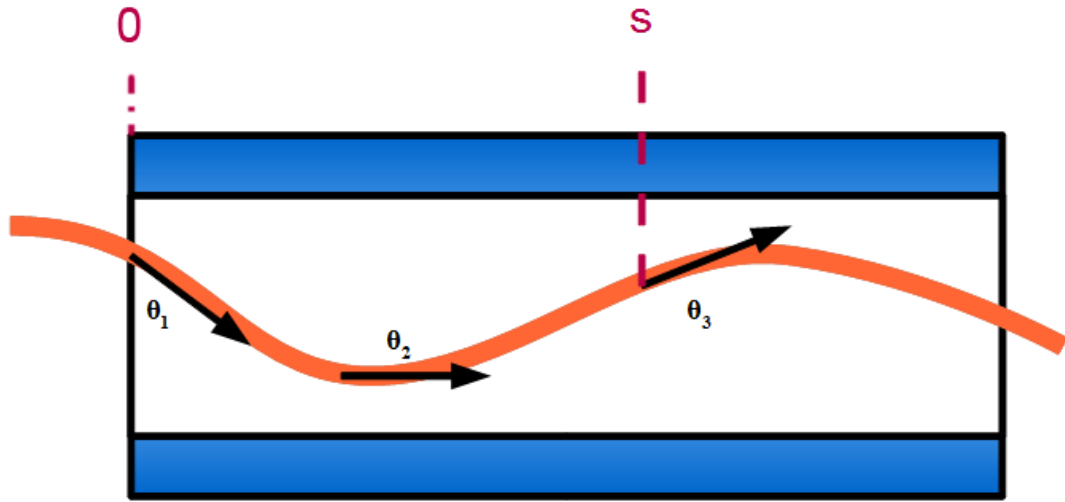
where  $M_{td}$  is the number of tendons in the system. As elastic shortening is an immediate loss, it can be compensated for during initial stressing or reshimming.

### 3.4.2 Friction and Anchorage Slip

Friction and anchorage slip are best described in tandem, as both create a force profile which varies *along the length* of a tendon. Friction occurs when variations in the angle of a strand,  $\theta$ , produce contact with the duct. If the strand-duct coefficient of friction is labelled,  $\mu$  (typically 0.2 for unbonded tendons [Hur98]), then the local force varies as:

$$\frac{\partial F}{\partial \theta} = -\mu F \quad (3.7)$$

If the prestressing force applied at the anchorage,  $F_i(s=0)$ , is known, Cooley's Formula can be used to calculate the force,  $F_i(s)$ , at a distance,  $s$ , along the strand:



$$\alpha = |\theta_1 - \theta_2| + |\theta_2 - \theta_3|$$

Figure 3.14: Calculating the total intentional angle change,  $\alpha$ , for a strand in a duct, by summing the changes in angle by the point,  $s$ .

$$F_i(s) = F_i \exp[-\mu\theta] = F_i \exp[-\mu(\alpha + ks)] \quad (3.8)$$

where  $\alpha$  is the total angle in radians that the strand has *purposefully* been turned through (as a result of helical winding, say) by the time it has reached the point  $s$ , as shown in figure 3.14. The wobble coefficient,  $k$ , on the other hand, describes the average *unintentional* change in strand angle per unit length. Wobble values are typically  $6.6 \times 10^{-4} \text{ rad m}^{-1}$ .

If a strand is stressed from both ends, the force at any point will be given by the same formula, but relative to each anchorage. There will therefore be a discontinuity at the point where the decreasing force profiles meet in the middle. This point of minimum force, called the ‘critical point’, is shown in the line labelled ‘original’ in figure 3.15.

If a prestressing jack is used to subsequently increase the load at one end of the strand only, then there will be a shift in the location of the critical point, as shown by the line labelled ‘increase force’ in the same figure. If, on the other hand, the jack load at one end is reduced from its original value,  $F_B = 1$ , to a new value  $F_A = 0.55$  as shown, then the force profile will instead increase from the

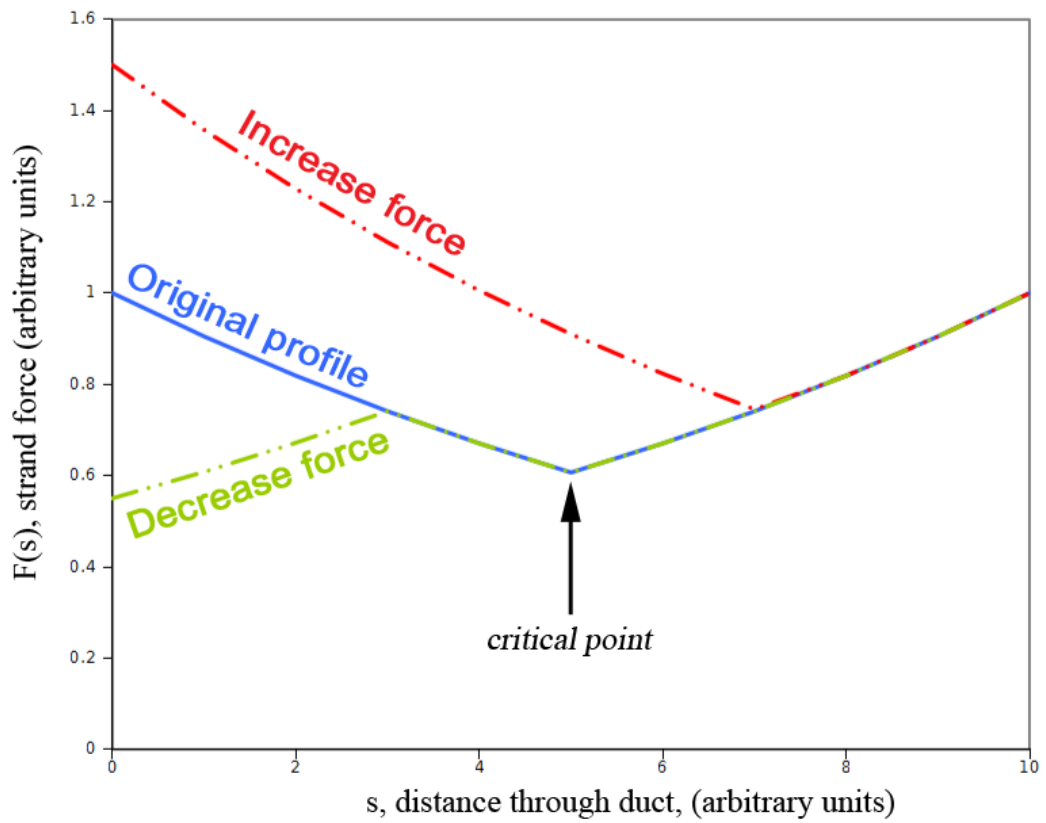


Figure 3.15: Fractional changes in strand force arise due to the presence of friction. In this case, the strand is tensioned at both ends (at  $s = 0$  and 10) and the force decreases with distance through a linearly curved duct for zero wobble. The original force, when the load at both ends is equal is shown, as is the effect of increasing or decreasing the jack force at one end.

anchorage end to meet the original force profile via the inverse Cooley Formula:

$$F(s) = F_A \exp[\mu(\alpha + ks)] \quad (3.9)$$

This ‘reverse friction’ is exactly what is seen during anchorage slip and draw-in [Irv00]. Reverse friction in a post-tensioned system is inevitable, as strands are first stressed to 80% UTS and then locked-off at around 70% UTS to transfer stress to the bearing plate. Anchorage slip at both ends of the strand will thus result in the ‘M’-shaped force profile, shown in figure 3.16, with maximum forces at the shoulders of the ‘M’ given by:

$$F_{max} = \sqrt{F_A F_B} \quad (3.10)$$

While friction and anchorage slip occur immediately during initial prestressing, the force profile along the tendons cannot be corrected for. This means that, unlike elastic shortening, these effects have long-term consequences for the structure.

A real-life measurement of friction would require a distributed measurement of load along a tendon strand. As we shall see in §3.5.1 this is not currently a part of regular inspection activities, due to limitations in the available or applied technologies.

### 3.4.3 Shrinkage and Creep

Long-term prestress losses, such as shrinkage and creep, are difficult to separate both in theory and practice. Engineers are still trying to resolve how macro- and micro-scopic changes in the structure instigate these effects<sup>(6)</sup> [YK07b] [FB03].

#### 3.4.3.1 Shrinkage

Shrinkage is a volume change in concrete due to the loss of water — either to the surrounding environment or to ongoing hydration. The most major causes of

---

<sup>(6)</sup>There are empirically supported models for rough estimates of creep and shrinkage [idb99], but these will not be used as the number of assumptions can make them unsuitable for structures other than those which they were designed for.

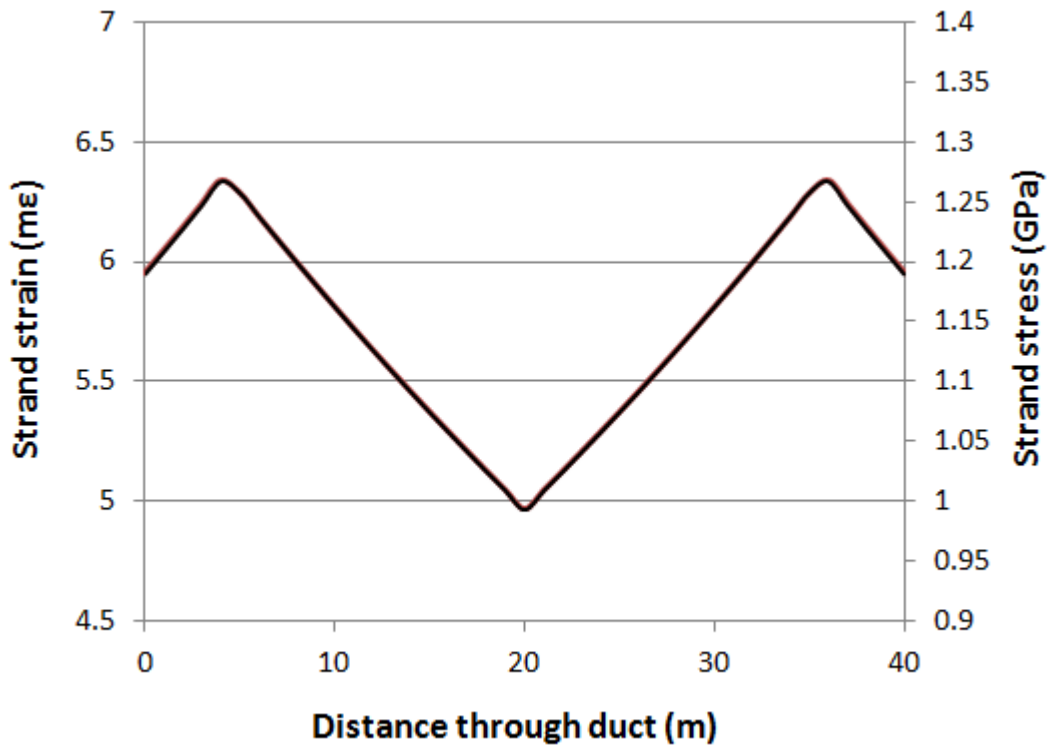


Figure 3.16: Using the net of the tendon layout from figure 3.9, the stress and strain in a tendon strand wound through 180°, passing through a linearly curved, 40 metre duct can be estimated. It is assumed that the strand is tensioned to 80 % UTS before being locked off at 70 % UTS. It is also assumed that there is zero wobble and that the coefficient of friction is 0.2.

shrinkage are:

- *Plastic Shrinkage* — As cast concrete is still in the process of solidifying, moisture is lost to evaporation or due to the aggregates absorbing water. Plastic shrinkage is minimised through proper curing processes.
- *Drying Shrinkage* — Water continues to evaporate from concrete in service. While the evaporation of free water causes little shrinkage, the gel pores within the concrete slowly relinquish their water to the surrounding environment as the concrete matures.
- *Carbonation Shrinkage* — Carbonation of cement compounds leads to a volume loss of water via the mechanism  $Ca(OH)_2 + CO_2 \rightarrow CaCO_3 + H_2O$  [SSV93]. The rate of this effect depends on the mobility of carbon dioxide within the structure and so increases with temperature. As with the other mechanisms above, large exposed surface areas accelerate the water loss rate.
- *Chemical Shrinkage* — As the hydration reaction in the concrete continues over the years, water is used up to form a denser network of cement nodes. As with drying shrinkage, chemical shrinkage increases with temperature as the hydration rate is accelerated.
- *Autogeneous Shrinkage* — This is a consequence of chemical shrinkage. If concentrations of water in the cement are low, then not enough water can be drawn upon to facilitate ongoing hydration. The unmet demand for water creates air voids and capillaries in the concrete, a process known as self-dessication. Because air produces a lower gel pore pressure than water, the concrete shrinks and is placed under microscopic tension [BMC05].

It should be clear that at least some of these effects are inevitable regardless of how much care is taken to eliminate them. The majority of shrinkage occurs in the first 24 hours after casting, with approximately 80% of shrinkage occurring within the first year. This does not make the effect negligible in the long-term,

as during operation the concrete structure is supported by and attached to other solid bodies. Shrinkage will thus not only reduce prestress, but may also lead to tension within the PCC and PCPV or its supports. Over long periods of time this can produce cracking, even in older structures.

### 3.4.3.2 Creep

After concrete's initial elastic shortening, there is an additional gradual yielding over time called creep. Unlike elastic deformation, only a small fraction (typically 20%) of creep deformation can ever be recovered [HAM12]. Creep is quantified by the ratio of the creep strain to the elastic strain in the material [SC11]. Concrete creep has been the focus of over 80 years of concentrated research efforts and can be broken down into a combination of three effects [BGC04]:

- *Basic Creep* — The diffusion and movement of grain boundaries, aggregates and dislocations within the cement matrix. Old, high-strength concretes creep less than those with light, soft aggregates and a poor cement structure.
- *Drying Creep* — Concretes in dry environments creep more than those at high humidity, a phenomenon known as the Pickett effect [Pic42]. Drying creep appears partly because shrinkage leads to microcracks and partly because water loss disrupts the balance in the stress state of the microscopic gel pores. These both lead to slippage in local grain boundaries.
- *Transitional Thermal Creep* — A temporary increase in creep can occur after both sudden increases and decreases in temperature. Again, this occurs due to (thermally induced) microcracking and also because the temperature change disrupts the stress equilibrium in the gel pores. Temperature increases in particular promote creep by increasing the rate of breakage and restoration of chemical bonds.

Creep is known for its decreasing rate as the concrete ages. During the first year of prestressing, the creep rate slows dramatically as hydration converts water

into volumes of load-bearing material (cement nodes are continuously generated and deposited onto capillary walls in a stress-free state) [Baz01, BX95].

After the first year, hydration slows dramatically and further decreases in the creep rate are caused by drying. In young concrete, the microscopic stress in cement bonds is higher because the gel pores are larger and more densely packed. As the concrete dries with age, gel water is lost and the cement bonds are placed under less tensile stress, making them stiffer. Bonds are thus less prone to break, leading to a reduced creep rate [BHSU97].

At a less scientific level, creep can be understood as the concrete structure settling into its new stress state. Moderate creep can therefore be a good thing, as it prevents cracking by allowing for stress relief and/or redistribution. Excessive creep, however, can be responsible for significant deflection, cracking, prestress loss and eventually structural failure, so it is an important variable to monitor.

### 3.4.4 Stress Relaxation

Tendon strands also undergo creep while under prolonged stress as the grains within the steel rearrange themselves to minimise energy. The resulting time-dependent increase in plastic deformation is called stress/steel relaxation. Stress relaxation reduces the prestressing force supplied by the tendons as they permanently relax into their new length state. This in turn means that stress relaxation is the only prestress loss effect which does not lead to a change in strand strain.

As described in §3.3.2.2, strain tempering is used to deliberately induce steel relaxation during the manufacture of low relaxation strands. Forcing the steel to creep before it is used to prestress a vessel minimises the amount of subsequent force loss during operation. Statistical work pioneered by Magura *et al* [MSS64] and improved upon by Ghali and Trevino [GT85] has lead to an empirical equation for the intrinsic stress relaxation,  $\Delta\sigma_{sr}$ , of a steel specimen loaded to an initial stress,  $\sigma_0$ , after  $t$  hours:

$$\frac{\Delta\sigma_{sr}}{\sigma_0} = -J\eta_t \left( \frac{\sigma_0}{\sigma_{UTS}} - 0.4 \right)^2 \quad (3.11)$$

where  $\sigma_{UTS}$  is the ultimate tensile strength of the steel (typically 1.7 GPa) and  $J$  is a constant which is chosen to be 1.5 for stress-relieved strand and 2/3 for low-relaxation strand. The parameter  $\eta_t$  takes the values:

$$\begin{aligned}\eta_t &= \frac{1}{16} \ln \left( \frac{t}{10} + 1 \right) : 1 \leq t < 1000 \\ &= \left( \frac{t}{5 \times 10^5} \right)^{0.2} : 1000 \leq t \leq 5 \times 10^5 \\ &= 1 : t > 5 \times 10^5\end{aligned}\tag{3.12}$$

Theoretical plots for low relaxation and stress-relieved strand, stressed initially to 80% UTS, are shown in figure 3.17. As shown, stress relaxation is actually quite a significant effect, leading to a 10% prestress loss in the first year for stress-relieved strand. Elevated temperatures and higher applied forces can further increase steel grain mobility and hence the stress relaxation rate.

#### 3.4.4.1 Combination with Other Losses

As stress relaxation depends on local forces, it acts to smooth out the ‘M-shaped’ force profile produced by friction and anchorage slip (discussed in §3.4.2). Cooley’s Formula can thus be rewritten to introduce a stress relaxation loss ratio,  $r$ , which reduces the effects of friction:

$$\frac{\partial F}{\partial \theta} = -\mu(1 - r)F\tag{3.13}$$

Furthermore, as a concrete vessel creeps and shrinks over time, the total force sustained by the tendons decreases, reducing the stress relaxation rate. Ghali and Trevino introduced an empirically derived reduction coefficient,  $\chi_r$ , to account for this gradual reduction in applied stress:

$$\chi_r = \exp \left[ \left( -6.7 + 5.3 \frac{\sigma_0}{\sigma_{UTS}} \right) \left( \frac{|\Delta\sigma_{cr} + \Delta\sigma_{sh}|}{\sigma_0} \right) \right]\tag{3.14}$$

where  $\Delta\sigma_{cr}$  and  $\Delta\sigma_{sh}$  are the stress losses in the tendon due to the creep and

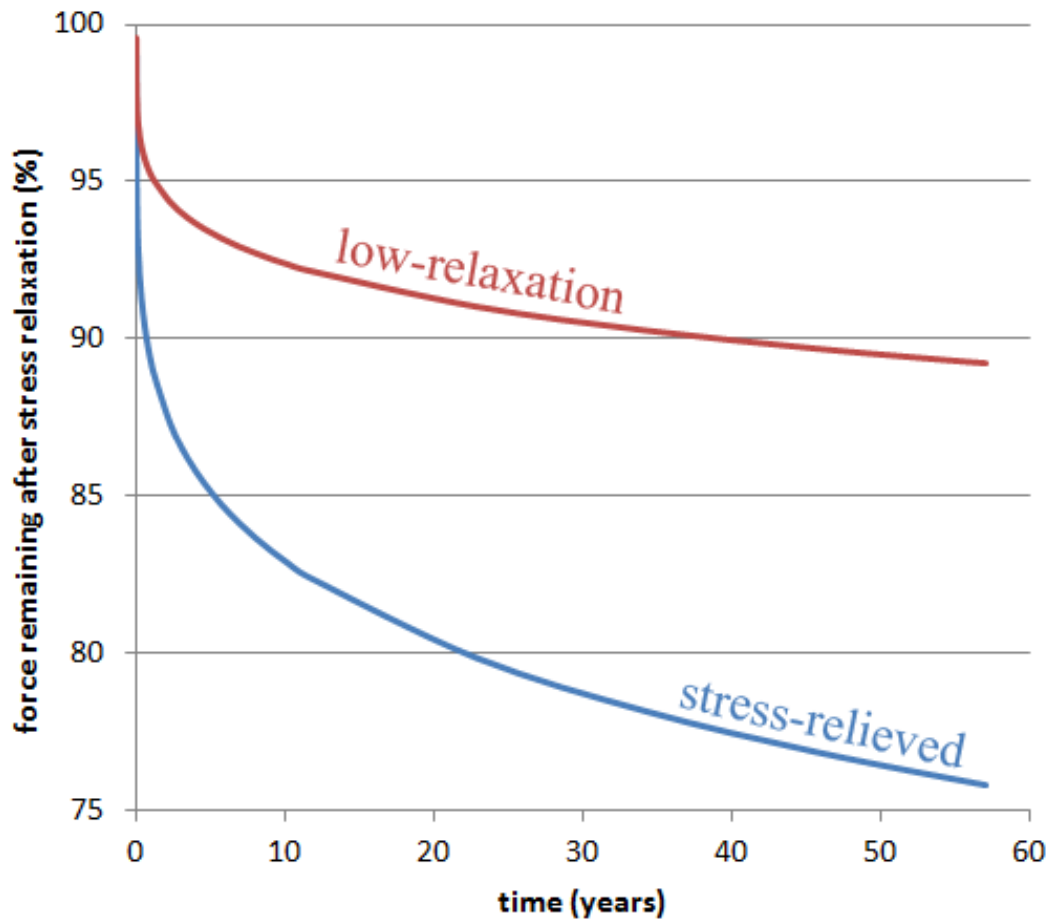


Figure 3.17: Over the years, stress relaxation causes a decrease in the force required to hold a steel strand at a constant strain. Shown are the decreases in the force required (from 100%) for both stress-relieved and low-relaxation strand over a period of 57 years. Graphs are derived from the empirical equation by Ghali and Trevino (3.11).

shrinkage at time  $t$  hours.

This interplay between prestress losses can produce an unpredictable evolution in tendon forces over time and length. It is therefore well-worth obtaining as much information about local and total strand stresses with time, as this allows the prestress state of the concrete vessels to be more accurately gauged and predicted. Unfortunately, as we shall now see, measurements of local tendon load are currently unfeasible in PCPVs and PCCs, due to a lack of suitable technologies.

## 3.5 Prestress Inspection Activities

The tendons in PCPVs and PCCs in the UK are unbonded and this offers key advantages over grouted ducts. Because strands can be mobilised, they can be replaced by welding the ends of new strands to older ones and then pulling them through the duct. Strand mobility also allows the force state of the tendons to be directly monitored, simply by seeing how much force is required to ‘lift-off’ strands from the bearing plate<sup>(7)</sup>.

### 3.5.1 Lift-Off Measurements

To ascertain the prestress levels of PCPVs and PCCs, tendon loads are monitored during the service life of the reactor. The current method typically involves carrying out some variation of a ‘lift-off’ check on a 1 or 2 % random sample (approximately 30) of the prestressing tendons in the structure at 1.5–5 year intervals [Gra09].

In the trap-and-free method, a jack loads one or all of the strands of a tendon

---

<sup>(7)</sup>While this thesis is mainly concerned with monitoring the prestress state of PCCs and PCPVs, it is important to note that prestress measurements are part of a wider array of structural health monitoring activities. There are a host of examinations used to ascertain the structural health of the vessels. Visual inspections of external surfaces are used to locate evidence of leakages or crack propagation. Tendon anchorages are visually examined to check for strand slippage, corrosion, mechanical damage or local cracks in the concrete. Level surveying is used to monitor the settlement and tilt of the vessel, while thermocouples monitor internal temperature fluctuations. Samples of the duct lubricant can also be analysed for acidity, water/impurity content and colour, revealing the presence of anything from corrosive microbes to oxidation [Kha09].

until a thin feeler-gauge can be inserted between the shims or bearing plate. The loads required to trap and free the gauge in several locations are used to calculate the average tendon force. Other tests use potentiometric transducers or instrumented shimming feet to measure the relative movement or force between components in the tendon during lift-off. Cyclic destressing and restressing of the tendons is sometimes performed to characterise strand properties more fully. Not only are all of these practices time consuming, but they also represent a substantial health and safety risk to the personnel performing the inspections. It would therefore obviously be desirable to complement or automate current manual practices.

A typical plot of jack load against bearing plate deflection for a lift-off test is shown in figure 3.18. Lift-off occurs at the intercept between the horizontal and vertical lines in the graph. Extrapolations are used to determine the load at zero displacement, shown as 7200 kN. Loads are reduced by 5 % to account for frictional losses to yield an ‘effective anchorage load’. Statistical analyses of lift-off measurements are then used to ensure that the average prestressing force is not below the minimum design load (MDL).

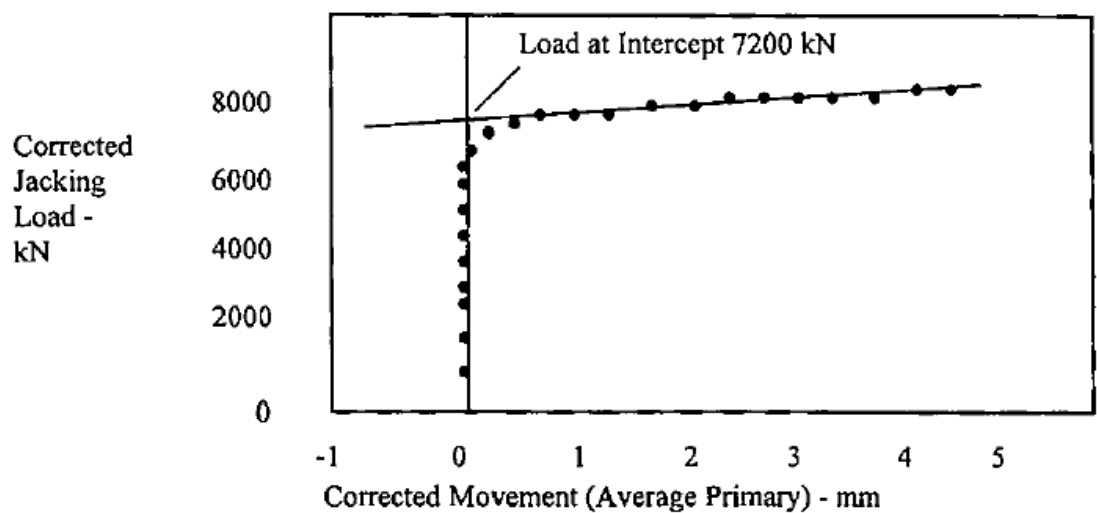


Figure 3.18: Typical plot of jack load against bearing plate deflection used to calculate the lift-off force and hence the prestress load. In the vertical section of the graph, the elastic recovery of the bearing plate as the force is lifted from it has been corrected for. Data taken from Sizewell B [Ltd00].

### 3.5.1.1 Changes in Lift-Off Force

Lift-off measurements are highly dependent on the contact forces a strand is subject to as it travels through a duct. Take for example the typical M-shaped force profile created during initial stressing, as shown in figure 3.19a for  $\mu = 0.2$ . Some years later, if corrosion of the strand causes friction to increase to  $\mu = 0.8$  the force applied during lift-off will decay more rapidly. As the lift-off load does not exceed  $F_{max}$  the tendon cannot be stressed beyond the first shoulder of the M-curve.

As a comparison, figure 3.19b shows the result for a lift-off inspection performed when  $\mu$  increases only to 0.5. As the lift-off force intersects with the M-curve further into the duct, more of the tendon is stressed. This demonstrates that subsequent increases in friction after initial stressing can:

- Increase the decay rate of the applied ‘lift-off’ boundary force
- Cause smaller sections of the tendon to be mobilised

This effect can be beneficial, as it ensures the critical point of a strand is not disturbed. However, it can also make attempts to ascertain the tendon stress state more challenging. In real PCPVs it has been found that the apparent friction of each strand increases from 0.2 to 0.5 immediately after tendons are fully stressed, because there are additional contact forces between adjacent strands. The actual prestress transfer to the vessel, however, is only affected by the friction between the strands and the ducts, *not* inter-strand friction.

Friction tests using conventional load checks are thus problematic. Measurements of the tendon force profile along the length of the tendon would again be hugely beneficial, augmenting the amount of information currently supplied by lift-off checks alone.

### 3.5.2 Vibrating Wire Strain Gauges

In some cases, there are other methods available for monitoring the prestress state of PCPVs. Vibrating wire strain gauges (VWSGs) were embedded into most

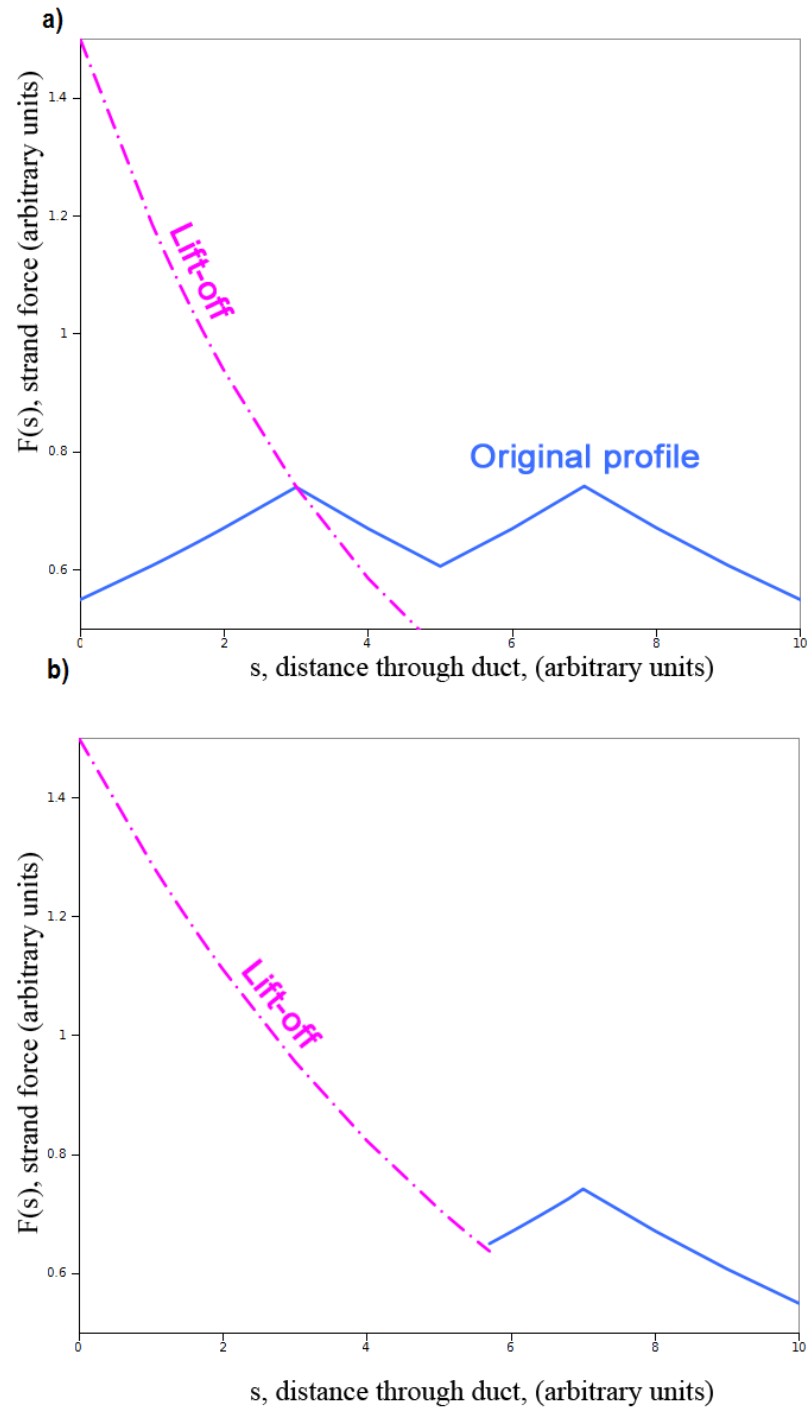


Figure 3.19: The force profiles of strands due to friction and anchorage slip. a) The original force profile after construction and the lift-off force profile a few years later after corrosion has increased the friction to  $\mu = 0.8$ . The strand is not mobilised beyond the first shoulder of the original M-curve. b) When  $\mu = 0.5$ , the lift-off curve intersects the original force-profile further into the duct, allowing more of the tendon to be mobilised.

PCPVs and PCC during construction. They were originally intended to measure vessel strain during the commissioning phase, in particular during pressure tests to demonstrate the structural integrity and load capacity margins of the vessels. Some of these VWSGs, such as at Hinkley Point B and Hunterston B, have survived the last 35 years and are still routinely monitored. Not having been intended for whole-life service, the VWSGs wear out over time, but adequate coverage still currently remains.

The wires span straight ducts, cast within the PCPV at the top cap, bottom cap and side walls. Induction coils are used to measure each wire's electrical resistance and vibrational period as these can be used to ascertain the wire's temperature and strain respectively. The temperature-corrected strain measurements are then used to infer the average vessel prestress over the wire length.

Gradual and continual failure of VWSGs over the years is to be expected, but while they continue to function they are used to support the other measurements taken during regular inspection. Unfortunately, the sensors are installed during construction and are then inaccessible, so there are no methods of repairing or replacing VWSGs. Ideally, new sensor technologies should be installed to reduce the chance of common-mode failures.

### **3.5.3 Load Cells**

Reactors such as Hartlepool and Heysham 1 have changes of load indicators, which detect any changes in inward radial load of circumferential tendons. The forces applied to each load cell are allowed to act on internal strain gauges. The resulting change in the electrical resistance of each strain gauge causes an electrical imbalance in the internal circuitry, leading to a measurable voltage signal.

While load cells are not currently routinely used at tendon anchorages, there are commercially available load cells which can measure up to 450 kN forces with 0.02 % resolution [Mea13]. These would be adequate for measuring large prestress losses such as the stress relaxation in new tendon strands (shown in figure 3.17). Again, this would only provide an average strand force measurement, rather than a distributed one.

## 3.6 Future Sensor Technology

Ideally, prestress sensors need to be planned for and installed prior to concrete casting, while the structure's architecture is still flexible. This has two important consequences for sensing technologies in existing PCPVs/PCCs. Firstly, it is unrealistic to expect force sensors installed 30–40 years ago to remain operational today. This was known at the time and these sensors were never expected to be solely relied upon. The number of operational force sensors in current PCPVs is small and, as they undergo wear with every use, they are deliberately underutilised.

Secondly, as the structures are now old and cannot be accessed conveniently, it is difficult to augment or add to the sensors already installed. New sensor technologies must therefore utilise the existing penetrations in the vessel. The main arguments for implementing new prestress sensor technologies can be summarised as follows [Irv00]:

- *Safety* — The minimum design load (MDL) is 1600 kN per tendon (equivalent to 230 kN or 1025 MPa per strand). No tendon should be allowed to fall below 1495 kN and all tendons within one quadrant of a PCPV should be within 75 kN of the mean. As shown in figure 3.20, a 5 % loss in average strand stress would be enough to bring the prestress below acceptable levels. While prestress losses have slowed dramatically as these structures age (forecasts predict less than a 2 % loss over the next 19 years), it is preferable from a safety perspective to closely monitor these variables rather than predict them.
- *Reliability* — By complementing lift-off inspections with other techniques, measurements can be cross-checked, verified and combined. This leads to a better statistical assessment of the current prestress state and avoids common mode failures.
- *Resolution* — The lift-off method does not supply any spatial resolution as it is an average force measurement of the mobilised part of a strand.

A full understanding of prestress transfer and time-evolution requires force measurements at several locations along the strand. These measurements are not just a point of academic interest—extra information would be of real industrial use as prestress nears the MDL [Gro08].

- *Costs* — While lift-off measurements are providing reliable and accurate data for forecasting, they are time consuming, expensive and (due to the high forces) pose a safety-risk to the personnel conducting the inspections. In some cases, it can take an entire week of plant outage to check only 1 % of the prestressing tendons, with the job itself costing well over £100k. This does not include the associated costs, such as the reactor outage time. These factors mean that it is currently only feasible to conduct lift-off measurements between every 18 months to 5 years.

### 3.6.1 Smart Tendons

A convenient access point for new sensors in the current ageing population of PCPVs and PCCs is the tendon ducts. As they are ungrouted in the UK, strands can be removed, allowing for the installation of sensor networks. Removing prestressing tendons en-masse and replacing them with sensors such as VWSGs, is not feasible however, as this reduces the prestress applied to the vessel. As such, the ideal solution is to instrument the tendons themselves, so that they can both upkeep and monitor prestress levels simultaneously.

The design and installation of ‘smart tendons’ may allow prestress losses to be quantified more accurately and frequently. Smart tendons would allow prestress inspections to be taken without disturbing the strands and without the safety and financial costs associated with lift-off inspections. The strands of a smart tendon may be instrumented with on-board strain and force monitoring technologies which, ideally, could be monitored remotely. Distributed strain measurements could provide local stress information, with force sensors at the anchorages providing measurements of strainless prestress losses such as stress relaxation. This

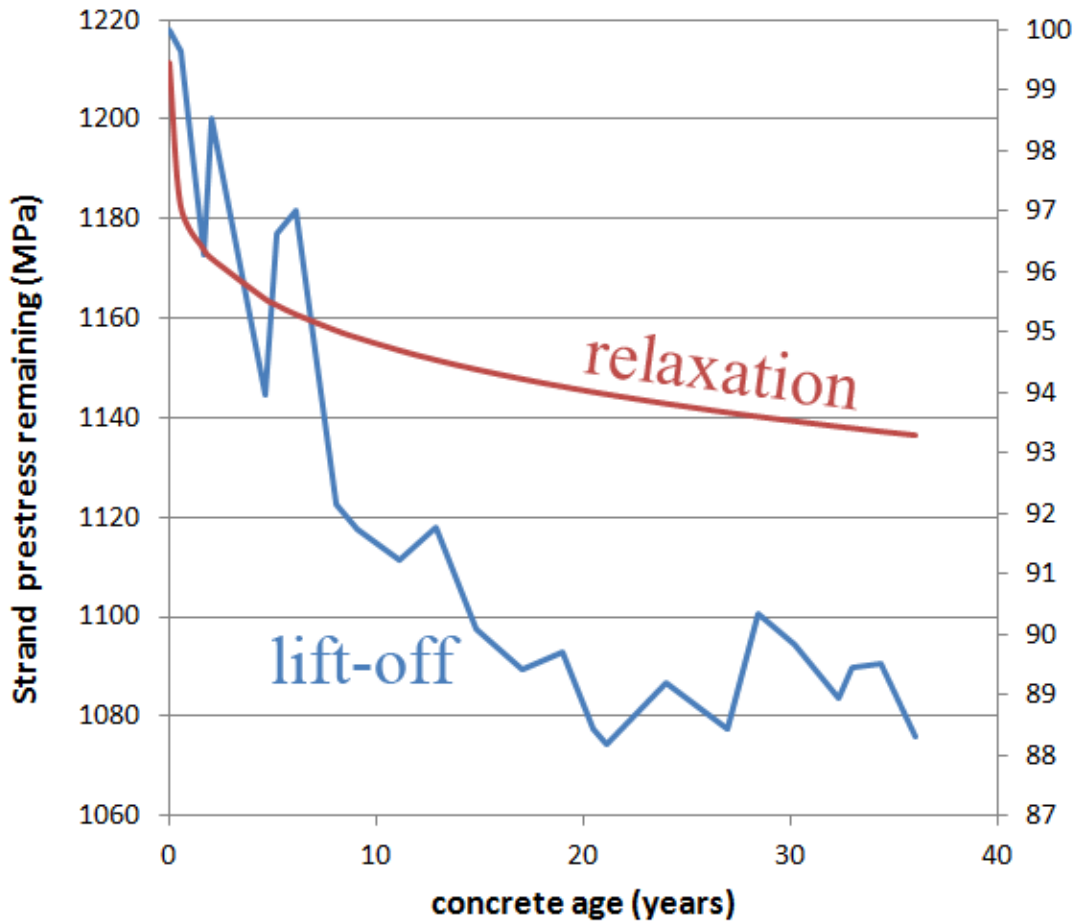


Figure 3.20: The prestress remaining in an average tendon strand over 35 years in the top cap of a PCPV at HPB [Kha09]. The stress inferred from the lift-off data is shown along with the stress-relaxation estimated from equation 3.11. The difference between the two lines is a rough indicator of the amount of creep and shrinkage in the top cap [Kha09].

combined measurement technique would provide a full description of the prestress applied and lost by each strand in the tendon.

Apart from measurements of prestress loss, there are other situations where smart tendons might be beneficial:

- *Strand Slippage* — Measurements of strand extension during initial stressing would rapidly highlight elastic anomalies or slippage, saving time and allowing for more convenient investigations.
- *Access issues* — Prestress measurements could be taken even when tendon end-access is limited.
- *Early Warning* — Lift-off checks have sometimes revealed prestresses lower than those anticipated during the design stage. Frequently monitored smart tendons may allow personnel to become aware of these unforeseen issues much sooner.

### 3.6.2 Smart Tendon Requirements

If the smart tendon is going to be used to monitor prestress losses in a PCC or PCPV, it must meet some stringent minimum design requirements, summarised as follows<sup>(8)</sup>:

- *Durability* — The instrumented tendon and its sensors should be durable. A smart tendon strand should operate and behave similarly to one without instrumentation. This includes its reaction to force, temperature, radiation and chemicals. Leakage of carbon dioxide from the reactor core could allow duct temperatures to range up to 500 °C. This is a rare occurrence however, and because the structures are cooled, temperatures around 30 °C are more typical. Local substances include water, iron oxides and the oil-based lubricant. The maximum strain in a tendon at 80 % UTS is around 7 mε, so the sensors must operate at least within this limit.

---

<sup>(8)</sup>These requirements and all future discussions of prestress monitoring are based on the prestressing systems at Hinkley Point B, Hunterston B, Torness and Heysham 2. While the technologies described in this thesis are applicable to other stations, the focus on PCPVs with seven-strand, helically wound tendons provides a consistent framework.

- *Environmental Stability* — The prestress measurement itself should also remain independent of radiation dose, temperature and chemical attack.
- *Implementation* — The new technology needs to be convenient to implement in existing plants. It should couple seamlessly to existing strand-replacement and plant-operation practices.
- *Non-invasive* — Taking a prestress measurement should not disturb the prestress levels. The strand's sensors should not interfere with the normal operation of that strand and the smart tendons themselves should not interfere with plant operation.
- *Measurement Frequency* — Prestress measurements may need to be taken much more frequently, on a larger number of tendon strands than is currently possible with lift-off inspections.
- *Resolution* — The resolution of the sensors needs to be high enough to capture the smallest losses of prestress in the vessel. In older vessels, this will likely be concrete creep and shrinkage. The spatial resolution of the sensors needs to be able to capture the strand force profile arising from friction and anchorage slip.
- *Accuracy* — Engineers need to be confident that the prestress data that the smart tendon strand is collecting accurately describes the true levels of prestress.
- *Reliability* — Due to the almost static nature of these structures, short- and long- term stability of the sensors is essential. The period of operation could include not only the remaining operational lifetimes of the reactors, but also the decommissioning stage (periods of 10 – 20 years). Sensors should remain active and mechanically reliable as they age.
- *Cost* — The smart tendons should be financially competitive against current practices. If they represent an insurmountable financial hurdle then they are less likely to be implemented.

- *Expandability* — The smart tendons and their network should be scalable. There should be minimal constraints on the number or length of smart tendons which can operate within one structure.
- *Modularity* — The smart tendon system should ideally be modular, so that future advances in technology can be incorporated conveniently.
- *Installation* — The sensors need to be installed onto finished tendon strands. As EDF Energy have no access to the tendons before they are a completed product, the sensors cannot be incorporated at the strand manufacturing stage.

### 3.6.2.1 Resolution

One of the most stringent requirements in the list above is the resolution requirement. Lift-off measurements do not have a spatial resolution as they are a point measurement of average tendon strain. Measurements of the turning points in the spatial profile of tendon strain in figure 3.16 would require a minimum of 5 sensors along the strand. Only sub-millistrain resolution would be required.

Sensors capable of measuring creep and shrinkage, on the other hand, would require a much higher strain resolution. The line labelled ‘lift-off’ in figure 3.20 shows the average stress remaining in the strands from the top cap of a PCPV at HPB<sup>(9)</sup>. The stress-relaxation is also shown, inferred from the equations by Ghali and Trevino (3.11). The difference between these lines is an estimate of the prestress losses due to shrinkage and creep. After correcting for stress-relaxation, the average change in strand strain per day can be estimated as between 10 and 100 nanostrains, as shown in figure 3.21. While these estimates may not be representative of all strands, in all locations, every day, they form a conservative requirement for the strain resolution of any smart tendon technology.

---

<sup>(9)</sup>The average lift-off force on a random sample of strands from the top cap of this PCPV has been measured every two years for over 35 years. Apart from these lift-off measurements, the top cap has remained largely undisturbed and so the data obtained from these measurements can be used to reliably infer the prestress remaining over the reactor’s lifetime. When converting strand lift-off force to average strand stress, it is assumed that the strands have a cross-sectional area and elasticity given in BS5896:1980 (shown in table 3.1).

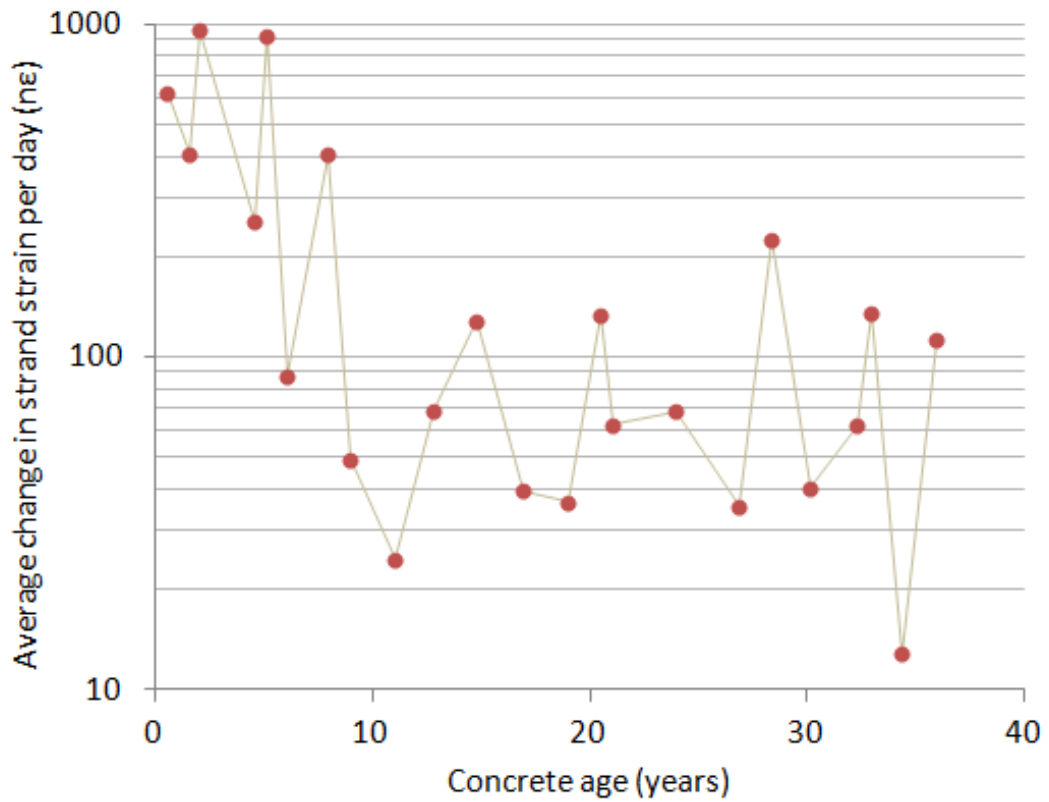


Figure 3.21: The change in prestress per day in the top cap of a PCPV at HPB, measured in units of tendon strand strain. Note that the data has been corrected using the estimated stress relaxation from figure 3.20, as stress relaxation does not induce a strain change. As shown, an average strain change between 10 and 100 nanostrains per day is observed. Note that as it is an average, this strain may not be representative of all days.

### 3.6.3 Proposal

The requirements above are both numerous and stringent, but they are not insurmountable. While many conventional electronic and mechanical sensors would be unsuitable for strand instrumentation (mainly due to their size and low resolution) recent advances in optical sensing technology are making smart tendons a distinct possibility.

Optical fibre strain sensors are very well suited to strand instrumentation due to their non-invasive small size and similar 1-dimensional nature. As we shall see in chapters 4 and 5, fibre strain sensors are also surprisingly durable and economical. They are also often highly modular and easy to scale up. Fibre sensors can be interrogated using light, providing several discrete strain measurements along a length of fibre. Once attached to a strand, fibre strain sensors could be used to infer the force profiles arising from friction and anchorage slip. As we shall see in chapter 6, a nanostrain static resolution is actually attainable from these sensors, so they may also be used to measure long-term prestress losses such as creep and shrinkage.

As stress-relaxation does not induce strain in a strand, the proposal is to combine strain sensing with conventional load cells at the anchorages of the tendon (see §3.5.3). Fibre pressure sensors or standard electronic load cells placed at the shims, bearing plates or barrels may allow total tendon loads to be monitored remotely. Instrumenting enough strands in this manner could provide real-time knowledge of the prestress state of PCPVs or PCCs, without the need for lift-off inspections.

## 3.7 Summary

Concrete is a composite material made up of aggregates suspended in a hydrated cement matrix. Compressive external forces act on these aggregates, while tensile forces act on the weaker cement filler. This makes concrete significantly stronger under compression, so prestressing is used to compress concrete structures before service. Highly elastic steel strands, fabricated through a combination of cold-

drawing and stress-relaxation, are stressed to 70-80 % UTS and used to post-tension PCPVs and PCCs. Seven steel strands pass through an oiled duct and terminate at a set of anchor barrels. These anchor barrels press up against bearing plates at either end of the structure, forming a prestressing tendon.

The prestress initially applied by the tendon is reduced due to elastic compression of the concrete, friction between the strands and the ducts, and slippage at the anchorages. The latter two effects result in an ‘M-shaped’ force profile along each strand. Prestress is also lost gradually over decades as the concrete shrinks and creeps. The tendons also undergo stress relaxation, reducing the prestress that they apply.

Typically, the force applied by a random selection of 1 % of the tendons in a PCPV or PCC is monitored every 1.5–5 years. The average force required to lift a strand’s anchorage away from the bearing plate is used to infer the vessel’s prestress state. In some cases, the results may be cross-checked with those obtained from vibrating wire strain gauges or load cells, but this is gradually becoming more difficult as these sensors fail over time.

There is currently a drive to improve safety, reduce costs, avoid common mode failures and augment the prestress measurements made using lift-off checks. Instrumenting a selection of strands with optical fibre strain sensors and measuring the total force at the anchorages using load cells may provide a clearer picture of the evolution of prestress losses, without the need for lift-off inspections. This is particularly important as the prestress in old PCPVs and PCCs nears the minimum design load.

The remainder of this thesis will outline how smart tendons meeting the requirements outlined in §3.6.2 can be manufactured, interrogated and most importantly, used to monitor prestress losses in nuclear concrete structures. In the next chapter, we will look at how fibre strain sensors work and consider how their strengths and weaknesses can be fully utilised or compensated for. This will provide clues as to how these fibre sensors can be packaged and attached to tendon strands, so that they can continue to operate reliably for decades.

# Chapter 4

## Optical Fibre Sensing: Fibre Bragg Gratings

In the proposed instrumented tendon, glass optical fibres are used to both address and act as strain sensors. This chapter will discuss how lightwave guiding is implemented and how the wavelength reflected by a fibre Bragg grating can be used as an indicator of local strain. As the technology is going to be applied in a nuclear environment, there will also be in-depth discussions of how neutron and gamma radiation affect a fibre-sensor network's signal quality and accuracy.

### 4.1 Optical Fibres

#### 4.1.1 Light in Glass

When light of wavelength,  $\lambda$ , travels through a glass, electron interactions reduce its speed,  $c$ , by a factor of  $n(\lambda)$ , known as the refractive index, while its intensity is reduced by an exponential absorption coefficient,  $\mu(\lambda)$ <sup>(1)</sup>. The Lorentz-Lorenz equation describes how refractive index varies with the number density,  $N$ , and polarisability,  $\alpha_p$ , of the molecules in the glass [Kit04, Fox10]:

---

<sup>(1)</sup>Light oscillates local electrons, causing them to radiate a secondary electromagnetic wave with a phase delay of between 90 and 180 °. The resulting light wave in the glass, described by a superposition of the original and induced waves, therefore travels more slowly due to the 90 ° phase delays (refraction) and with a lower intensity due to destructive interference of the 180 ° phase delays (absorption).

$$\frac{n^2 - 1}{n^2 + 2} = \frac{4\pi}{3} N\alpha_p \quad (4.1)$$

while the absorption coefficient,  $\mu$ , is found from the Kramers-Kronig relations<sup>(2)</sup>:

$$n(\omega) = 1 + \frac{c}{\pi} \mathcal{P} \int_0^\infty \frac{\mu(\Omega)}{\Omega^2 - \omega^2} d\Omega \quad (4.2)$$

where  $\omega = \frac{2\pi c}{\lambda}$  is the light's angular frequency.

### 4.1.2 Wave Guiding

Optical fibres consist of a cylindrical dielectric core of refractive index,  $n_1$ , surrounded by a cladding of lower index,  $n_2$ . Figure 4.1 shows that when light from the core attempts to enter the cladding at an angle  $\theta_i$ , some of it is reflected at an angle,  $\theta_r = \theta_i$ . The amount of reflection is described by the Fresnel equation:

$$R = \left| \frac{n_1 \cos \theta_i - n_2 \cos \theta_t}{n_1 \cos \theta_i + n_2 \cos \theta_t} \right|^2 \quad (4.3)$$

where Snell's law gives the transmitted angle:

$$\sin \theta_t = \frac{n_1}{n_2} \sin \theta_i \quad (4.4)$$

In an optical fibre,  $n_1 > n_2$ , so there are angles where  $\sin \theta_t > 1$  and Snell's law cannot be satisfied. In these cases, there is no transmission and the light is guided along the core via total internal reflection, as shown in figure 4.2. As shown, multi-mode (MM) fibres, with a core diameter  $> 10 \lambda$ , allow several paths or *modes* of light to propagate.

Cross-interference between modes reduces the propagation length of light along MM fibres. By reducing the core-cladding index difference to 0.4 % and the core diameter down to approximately  $5 \lambda$ , fibres can be made to carry a single mode of light along the centre<sup>(3)</sup>. Single mode (SM) fibres, used for the work in

---

<sup>(2)</sup>Because there is a singularity in the integral when  $\Omega = \omega$ , the Kramers-Kronig relations are solved using contour integration. The Cauchy principal value  $\mathcal{P}$  is used to solve the integral around the singularity.

<sup>(3)</sup>The core diameter is now comparable to the light's wavelength, so the geometrical description of optics is no longer valid. Solutions for light propagation in single-mode fibres must

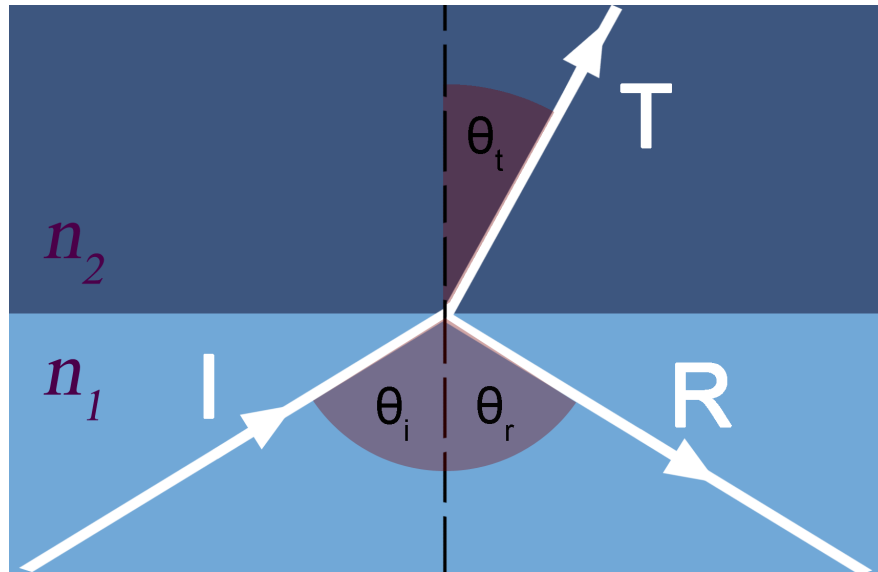


Figure 4.1: Diagram showing a ray of light (I) in a material of index  $n_1$ , travelling at an angle  $\theta_i$  into a material of index  $n_2$ . Because there is a mismatch in how dipoles oscillate at the interface, only some of the light can be coupled and transmitted (T) into the new medium at an angle  $\theta_t$ . The rest is reflected back (R) at an angle  $\theta_r = \theta_i$ .

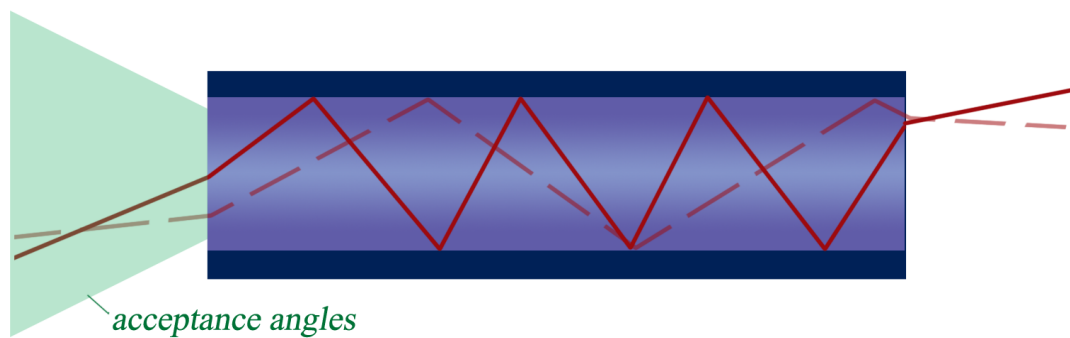


Figure 4.2: Waveguiding along a multi-mode fibre. Rays within the acceptance cone are totally internally reflected along the fibre's length, while those without are rejected.

this thesis, suffer from less attenuation and carry a significant fraction (20 %) of their light in the fibre cladding as an evanescent wave[MS01].

### 4.1.3 Fibre Fabrication

Optical fibres are commonly made from amorphous (also known as vitreous, glassy or fused) silica — a disordered network of rigid  $\text{SiO}_4$  tetrahedron units (shown in figure 4.3a). When the melted end of a glass preform is pulled to produce a thin strand, the fibre supercools and solidifies at the fictive temperature,  $T_f \approx 1700$  °C, before it can crystallise [DLK01]. The tetrahedra share oxygen atoms to form a network of ring-like structures of between 3 and 10 Si-O linkages as shown in Figure 4.3b. Overall, the inter-tetrahedral angles (Si-O-Si) in the glass follow a continuous distribution  $120 \rightarrow 180$  °, with a mean value of 145 °.

The surfaces or ‘cladding’ of the fibre snap-freeze first at a low density ( $\rho_{gla} = 2.2$  g/cm<sup>3</sup>), placing local bonds under enormous residual tensile stresses of around 9 MPa. Strain is particularly high in rings consisting of only 3 Si-O units. Because of the tension in the cladding, the core is placed under compression of around 6 MPa leading to a higher density, a lower polarisability and hence an increased refractive index [MGD06, Sch80].

The refractive index difference can be manipulated further through doping. Common dopants include germanium (Ge) and phosphorous (P) to raise the refractive index, or fluorine (F) and boron (B) to lower it [FAGL84]. Note that many dopants also raise the fictive temperature of the glass, leading to increased intrinsic strains at room temperature.

#### 4.1.3.1 Fibre Coating

To protect the fibres from mechanical, chemical and thermal damage, they are coated immediately after drawing. Typical coating materials include flexible polymers such as acrylate, polyimide and ormocer. Water-tight (hermetic) carbon coatings can also be plated over with metals such as nickel, gold and aluminium

---

instead be derived from Maxwell’s equations [GT98]. The derivation is outside of the scope of this thesis, but more information can be found in the cited reference.

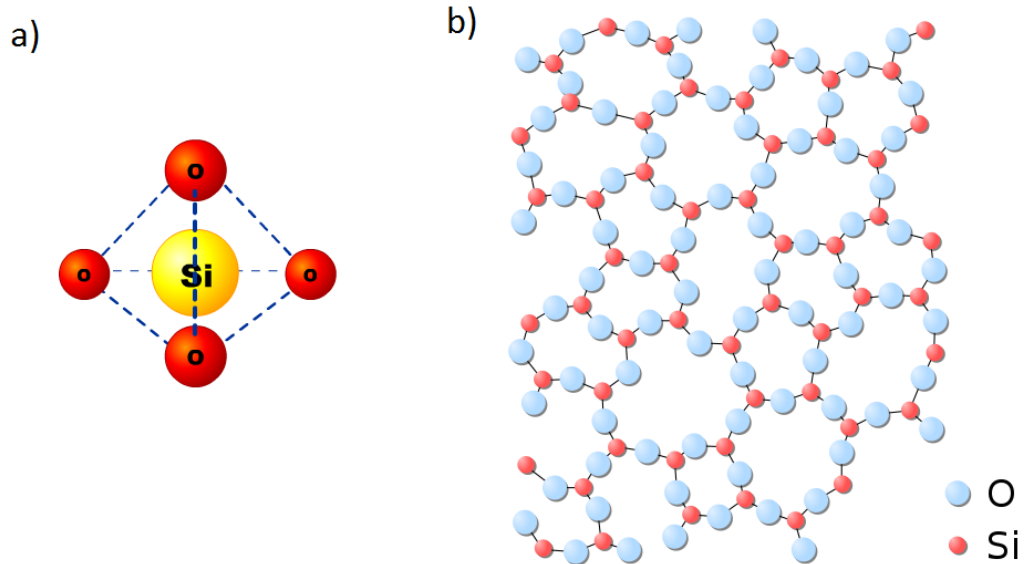


Figure 4.3: a) Single, rigid SiO<sub>4</sub> tetrahedra (angle O-Si-O=109.5±4°) are the building blocks of fused silica. These units are joined, sharing oxygen atoms to form the disordered glassy structure shown in b). The third dimension of the network (coming out of the page) has not been drawn for clarity.

to provide high-performance fibres for harsh environments. Acrylate- or nickel-coated, single-mode SMF-28 and Cu1300 fibres are used for much of the work in this thesis [Cor13, IVG13].

#### 4.1.4 Light Losses in Fibres

The optical power,  $P_2$ , at any point,  $L$  [km], along a fibre depends on the power launched into the fibre,  $P_1$ , and the attenuation [dB/km]:

$$\alpha_{att} = \frac{10}{L} \log_{10} \frac{P_1}{P_2} \quad (4.5)$$

While power loss is dependent on a variety of issues, the typical attenuation in optical fibre (0.2 dB/km at 1550 nanometres) is often lower than the losses in electrical wiring (200 dB/km) [Cor13, Bel13]. Optical systems are, however, more sensitive to bending, scattering and absorption. As such, more care needs to be taken to characterise and understand the effects of mechanical, chemical

and radiation exposure on fibre sensor networks.

#### **4.1.4.1 Bending**

Macroscopic bending of SMF-28 fibre around a 3 cm diameter loop can lead to a 10 % loss in optical power. Microscopic curves at the core-cladding interface termed ‘microbends’ can also lead to attenuation. Microbends typically occur when two fibre ends are melted and ‘spliced’ together to achieve an optical connection. Indeed, microbends are created during most operations which introduce misalignment or mechanical stress, such as fibre coating and heating.

#### **4.1.4.2 Scattering**

Losses of the evanescent field can occur as light scatters from radius or refractive index imperfections at the core-cladding interface (Mie scattering). Light can also scatter from molecular vibrations (Raman scattering) or from non-linearities in the fibre (Brillouin scattering), producing acoustic waves [Bra12]. These effects cause base-line attenuation across the spectrum.

The largest source of attenuation in most optical fibres stems from the Rayleigh scattering of light from molecular irregularities in the glass’ density. Because Rayleigh scattering is more pronounced when the wavelength of the guided light matches the size of the defect, ultraviolet ( $\lambda < 400$  nm) wavelengths are most affected.

#### **4.1.4.3 Intrinsic Absorption**

All materials, including silica, have intrinsic absorption characteristics corresponding to electronic and vibrational resonances. The atoms in glass absorb ultraviolet (UV) light, while infra-red photons are absorbed by the network, inducing vibrational states in the molecular bonds. These excitations eventually decay, re-emitting diffuse and isotropic light. As we will see in §4.2.2, incident neutron and gamma radiation can increase intrinsic absorption by increasing the fibre’s density.

#### 4.1.4.4 Defect Absorption

Point defects in glass produce narrow, strong absorption bands which can lead to dramatic darkening of a fibre at particular wavelengths, or colour centers. As neutron and gamma radiation can produce these defects in stark numbers, radiation point defects are also highly relevant to fibre networks in nuclear environments.

## 4.2 Radiation Induced Attenuation

Radiation induced attenuation (RIA) in fibres is a consequence of the point defect generation and increases in density arising from neutron and gamma exposure. This section will review the mechanisms of RIA and compaction in an attempt to quantify how much of an effect this will have on light losses in the proposed fibre sensor network.

### 4.2.1 Point Defects

The molecular structure of 11 naturally occurring point defects in silica glass are shown in figure 4.4 [SHHK05, Wan05, Neu94, Dev92]. The absorption strength of each is described by the ‘oscillator strength’,  $f_{osc}$ . This quantifies how much light is attenuated by a defect, independently of its concentration<sup>(4)</sup>.

Some of these defects are caused by chemical contamination, but this is usually mitigated by using suitable fibre coatings (an issue dealt with in more detail in §5.2.3). More difficult to avoid are the defects produced by neutron and gamma particles with energies  $>1$  MeV, as this radiation is difficult to shield against. The resulting atomic displacements and bond breakages can lead to an array of network, interstitial and dangling bond defects [BBF<sup>+</sup>01].

---

<sup>(4)</sup>The oscillator strength can be understood as being governed by the probability of a defect making a transition from a low energy state to a high energy state after absorption of a photon. It can be mathematically related to the absorption cross-section via  $\sigma_{abs} = \frac{\pi e^2}{m_e c} f_{osc}$ , where  $c$  is the speed of light and  $m_e$  and  $e$  are the mass and charge of an electron.

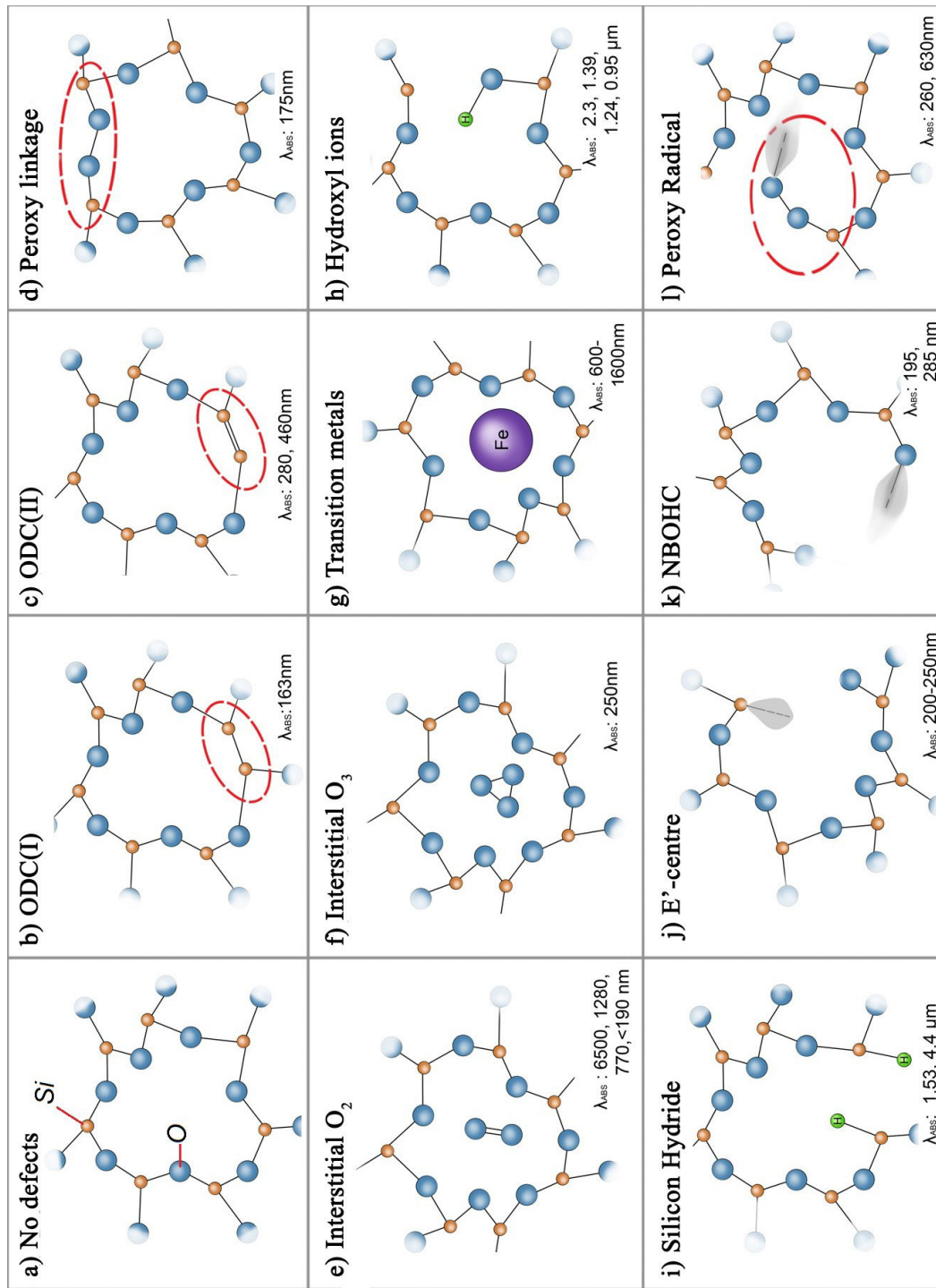


Figure 4.4: Network and interstitial defects based on silicon, oxygen, hydrogen and transition metals. Also shown are the three forms of dangling-bond defect and the 'no defects' case for comparison.

#### 4.2.1.1 Network Defects

Oxygen deficient centres, ODC(I), and divalent bonded silicon atoms, ODC(II), shown in figure 4.4b and c, are created when neutrons ‘knock-out’ the bridging oxygen atoms in the network, or under MGy doses of gamma radiation. ODC(I) defects produce some of the strongest absorption peaks in the UV at 160 nm ( $f_{osc} = 0.2$ ), while ODC(II) defects are at least 100 times weaker [SHHK05, Neu94].

Hydroxyl (Si-OH and Si-O-OH) groups are introduced when fibres are contaminated by water or hydrogen (figure 4.4h). OH ions have a strong vibrational resonance at  $2.3 \mu\text{m}$ , with harmonics at  $1.39\mu\text{m}$ ,  $1.24\mu\text{m}$  and  $0.95\mu\text{m}$  [BTB<sup>+</sup>07]. The harmonic at 1385 nm, the ‘water peak’, is one of the most common and substantial features in the infra-red absorption spectrum. Because OH concentrations of only 150 ppm can induce 0.6 dB/m attenuation at the water peak [BLBH90], commercially available fibres are supplied ‘dry’, with OH ion concentrations reduced to  $<0.15$  ppm.

Under gamma irradiation, hydrogen trapped interstitially may react with ODC(I) defects, producing silicon-hydride (Si-H) groups which absorb at 1530 nm (figure 4.4i). In hydrogen-loaded fibres, this defect can produce attenuation comparable with the water peak [Eva88].

#### 4.2.1.2 Interstitial Defects

As shown in figures 4.4e and f, oxygen, freed from the network by neutron-gamma radiation, can sit interstitially and weakly absorb in the 100 – 300 nm region ( $f_{osc} = 10^{-8}$ ) [SG96]. Interstitial transition metals also attenuate light in the 600 – 1600 nm range (figure 4.4g), but this is rare in highly-pure modern fibres. Even in plated fibres, it is uncommon for metal atoms to diffuse into the cladding at temperatures  $<400$  °C due to their relatively large size [Sem93, BKBK89, BDB<sup>+</sup>97].

### 4.2.1.3 Dangling Bond Defects

Dangling bond defects tend to dominate irradiated silica networks, producing some of the widest and strongest absorption features. Dangling oxygen bonds (figure 4.4k), formed when gamma radiation cleaves silanol (Si-O-H) groups, attenuate light at around 200 nm ( $f_{osc} \approx 0.1$ ). Dangling silicon bonds, or so-called ‘E’-centres’ shown in figure 4.4j, formed under mixed neutron-gamma radiation, dominate the absorption spectrum in the 200 – 250 nm range [MSDP95]. Reaction of E’-centres with interstitial O<sub>2</sub> can also lead to peroxy radicals ( $\equiv Si-O-O-$ , shown in figure 4.4l), which absorb in the visible and UV with  $f_{osc} \approx 0.05$ .

To reduce UV attenuation, some manufacturers allow mobile, molecular hydrogen or fluorine to diffuse through the fibre, saturating Si or O bonds to create stable silanol groups [SSO12]. However, as figure 4.5 shows, hydrogen loading comes at the cost of introducing hydrogen defects at 1300 – 1500 nm [BFOB07]. As a side-effect, both hydrogen and fluorine loading also induce breakage and relaxation of thermally-strained network rings made up of only 3 Si-O linkages. Relaxing the glass in this manner increases its gamma-hardness, preventing bonds from being broken by subsequent ionising irradiation.

### 4.2.1.4 Colour Centre Summary

A summary of the wavelengths affected by radiation-induced point defects, along with the theoretical summed effects of absorption, scattering and leakage are shown in figure 4.6. Because UV and visible wavelengths are plagued by both Rayleigh scattering and RIA, optical fibre systems in radioactive environments should aim to operate in the X, C and/or S bands (1400 – 1600 nm). The components at these wavelengths are also in fact cheaper due to their traditional use in communication systems.

It is worth noting that darkened color centers can be photobleached to regain some transmission. Long-term recovery of RIA may indeed be a natural consequence of the light used to interrogate an optical sensor [FAGL84]. This dynamic behaviour in RIA highlights why it is important to avoid using intensity-based optical sensing techniques in radioactive environments.

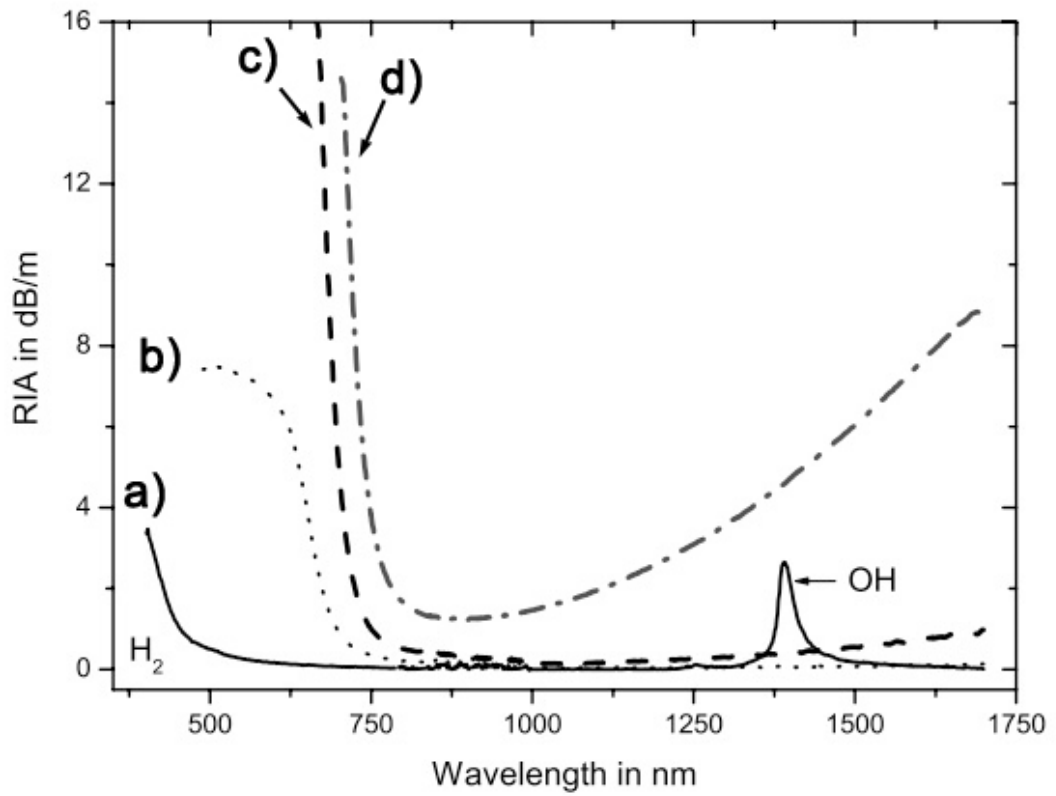


Figure 4.5: A comparison of the RIA in a fibre a) with and b-d) without hydrogen loading for increasing doses of gamma and neutron radiation. Gamma doses, neutron fluences are a) and b) 1 MGy,  $10^{15}$  n  $\text{cm}^{-2}$  c) 28 MGy,  $10^{17}$  n  $\text{cm}^{-2}$ , d) 3 GGy,  $10^{19}$  n  $\text{cm}^{-2}$ . Note that hydrogen loading has reduced the RIA in the visible, but increased RIA in the infra-red due to the formation of the water-peak [BFOB07]

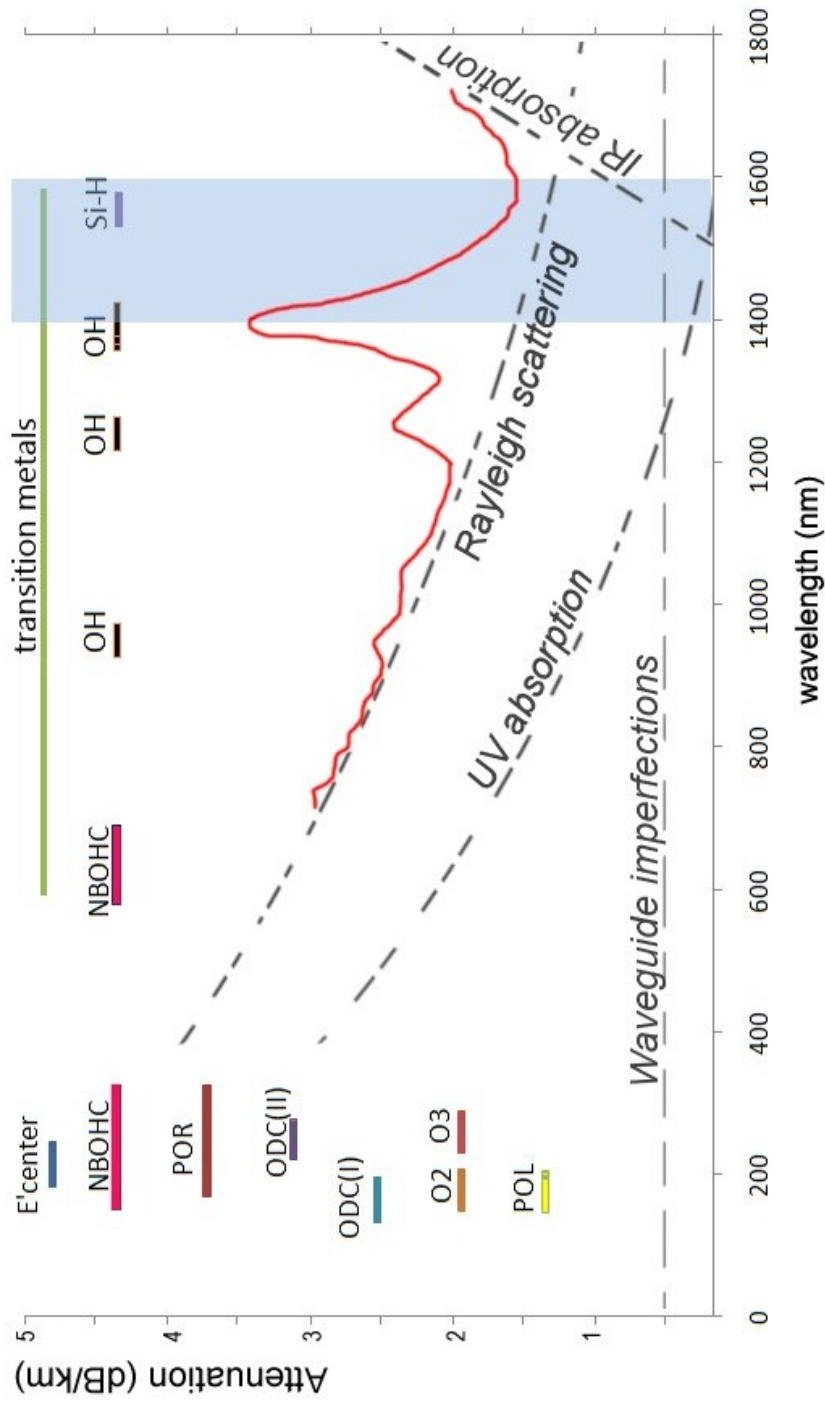


Figure 4.6: Summary of the sources of attenuation in silica optical fibres for wavelengths  $< 1800$  nm, with a plot of a typical example loss spectrum for partially-irradiated SMF-28 fibre. While waveguide imperfections provide constant attenuation over the spectrum, Rayleigh scattering and UV absorption increase drastically at low wavelengths. Exposure of fibres to neutron-gamma radiation will increase the attenuation of features such as the water peak, centered at 1385 nm. The wavelengths affected by the point defects shown in Figure 4.4, are also labelled and arranged for clarity. The shaded area represents the X, C and S bands (1400-1600nm) which are conventionally used for optical fibre communication systems.

## 4.2.2 Compaction

Neutron and gamma radiation can also induce silica compaction, a fractional increase in density, which in turn increase the refractive index and absorption coefficient. Under normal conditions, the inter-tetrahedral angles in the glass (Si-O-Si), shown in figure 4.4a, follow a continuous distribution  $120 \rightarrow 180^\circ$ . The most probable angle,  $\beta = \beta_A = 145^\circ$ , represents the Gibbs free energy minimum of the system, shown graphically in figure 4.7.

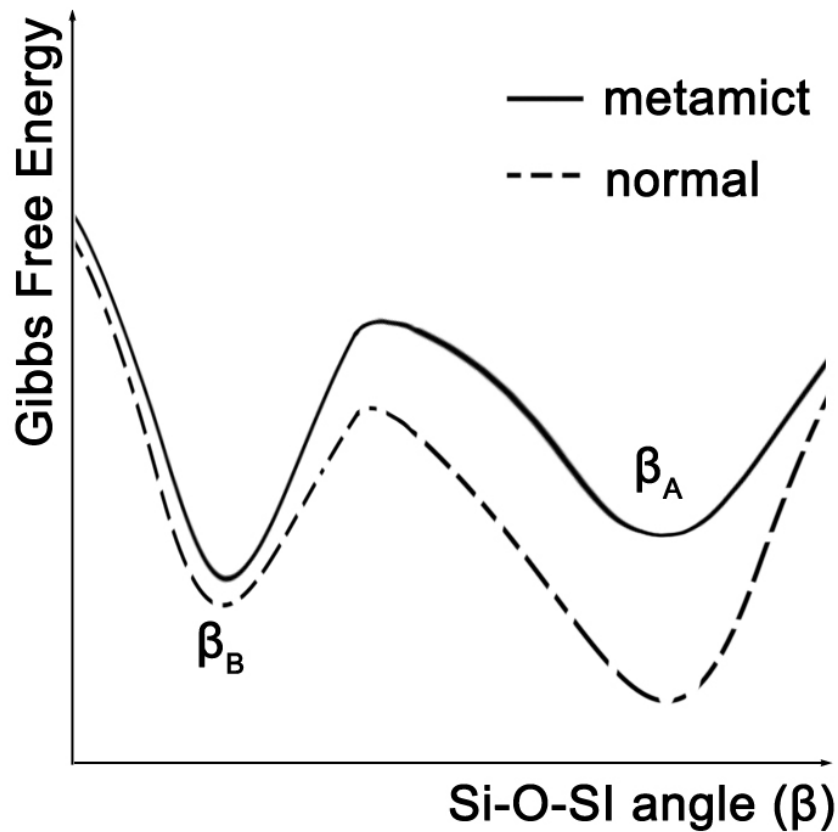


Figure 4.7: Gibbs free energy as a function of the Si-O-Si angle,  $\beta$ , in the silica network. The normal energy minimum of the system is at  $145^\circ$ , but after an increase in temperature or pressure, the Gibbs function shifts to the metamict phase with a new minimum at  $135^\circ$ .

### 4.2.2.1 Neutron Compaction

Large shifts in temperature,  $T$ , and/or pressure,  $P$ , can shift the position of the Gibbs energy minimum to lie at  $\beta = \beta_B = 135^\circ$ , shown again in figure 4.7

[POH00b, POH00a]. The reduced separation between atoms allows the glass to exist in the denser, experimentally confirmed, ‘metamict phase’ [MH88]. It is thought that in the vicinity of neutron or ion bombardment,  $10^4$  atoms are subject to  $T=5000 - 10,000$  °C combined with  $P=0.3 - 0.7$  GPa [Pri57], providing the perfect conditions for the phase change and a mechanism for neutron-compaction. As the number of heated atoms is small, the volume is rapidly quenched, but the energy minimum allows the phase to remain.

Incident neutrons can gradually convert small sections of a fibre to the metamict phase, eventually saturating the entire sample, resulting in a 2 – 3 %, linear densification. It is important to note that this is lower than the 20 % densification produced by non-radiative processes, which suggests neutron bombardment also creates many voids.

#### 4.2.2.2 Gamma Compaction

Gamma induced compaction works under an entirely different principle. In reality, inter-tetrahedral angles (Si-O-Si) are biased to be larger than  $\beta_A$  due to the glass’ intrinsic thermal strain. When incident gamma particles break intermolecular bonds, there is a slight relaxation in the entire network and a subsequent increase in density. As such, gamma compaction is temperature dependent, with an increase in ambient temperature causing a linear reduction in attenuation via  $10^{-3}$  dB km<sup>-1</sup>°C<sup>-1</sup> [VBN+00].

It has also been found that gamma radiation can cause dilation (negative compaction) of pre-compacted silica glasses [PE62]. This occurs because ionising radiation facilitates the rearrangement of long-range overlapping strain fields across the fibre, releasing the compaction induced by other processes, such as neutron bombardment [PK69]. Dilation and compaction may thus occur simultaneously, but the latter is usually the dominant effect [Pri68].

#### 4.2.2.3 Dose Dependence

The dependence of compaction with radiation dose,  $D$ , in vitreous silica follows a power law:

$$\frac{\Delta\rho}{\rho} = AD^c \quad (4.6)$$

where  $A$  is a dose constant and  $c=1$  or  $2/3$  for neutron or gamma radiation respectively. Note that while the effects of neutron bombardment vary little from fibre-to-fibre, the  $c=2/3$  power law for gamma radiation depends on the intrinsic glass strain. This can vary substantially with differing fibre dopants and thermal history [VBN<sup>+</sup>00, Tro98].

The Lorentz-Lorenz equation (4.1), or the empirically derived equation by Cheymol *et al* below can be used to quantify how the refractive index responds to these increases in density,  $\rho_g$  [CLVB08]:

$$\frac{dn}{d\rho_g} = 0.19 \quad (4.7)$$

and the Kramers-kronig relations can then relate these changes to absorption. By separating the effects of neutron- and gamma- induced attenuation in Ge+P doped fibres, Henschel *et al* experimentally confirmed the power-law dependence of compaction [HKL<sup>+</sup>98]. Their results, presented in figure 4.8, show that gamma-induced attenuation dominates at low doses before saturating. Conversely, neutron damage only begins to cause significant attenuation when the damage scale becomes comparable to the scale of the fibre's dopant distribution.

### 4.2.3 Fibre Coating

In fast-neutron environments, the degradation of optical fibres is also strongly influenced by their coating material. Using Monte-carlo simulations, Siebert *et al* predicted that under 14 MeV neutron irradiation, a fibre with a hydrogen-rich coat would receive 21% more radiation from recoil protons than an uncoated fibre [SH98]. This effect was experimentally confirmed by Brichard *et al*, who irradiated both polymer- and aluminium- coated fibres and compared RIA in the 400–1700 nm range [BBF<sup>+</sup>01]. Their results, shown in figure 4.9, display increased attenuation at the water peak for polymer coated fibres — a sure sign of hydrogen contamination [FBB<sup>+</sup>01]. This attenuation continued to increase

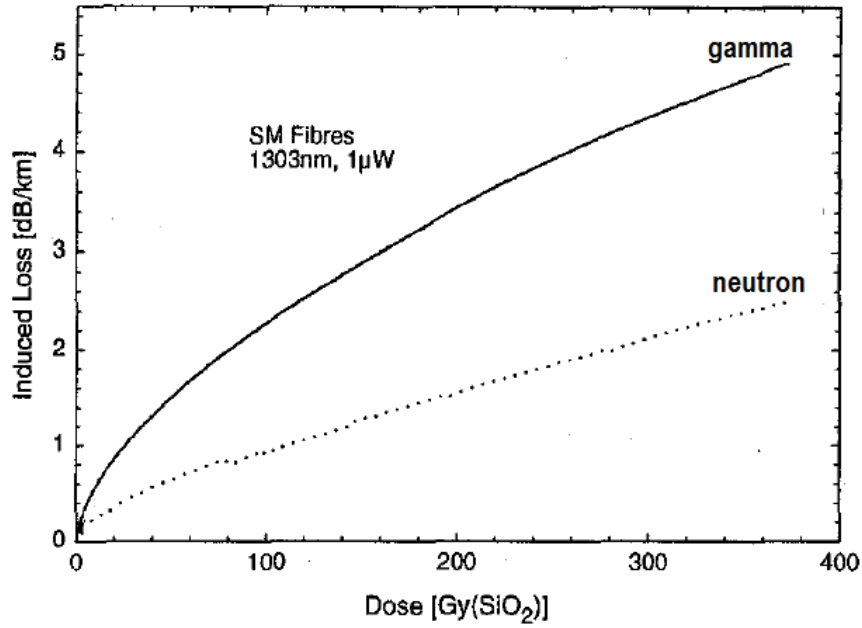


Figure 4.8: Comparison between the RIA at 1303 nm due to neutron + proton (dotted line) and gamma irradiation of fibres up to the same equivalent dose at the same dose rate [HKL<sup>+</sup>98].

even after irradiation had ceased, suggesting that recoil protons implanted in the polymer coat were slowly diffusing into the core. This highlights the importance of using a hydrogen-poor polymer or metal coating in neutron-rich environments<sup>(5)</sup>.

#### 4.2.4 Fibre Dopants

Many dopants reduce the hardness of a fibre to gamma radiation, in part because they raise the fictive temperature of the glass, leading to increased intrinsic bond strain. Dopant atoms are also defect centers — Ge doping, for example, can lead to the creation of Ge-based E'-centers and Ge-based NBOHC defects [BBF<sup>+</sup>06].

Friebele *et al* studied gamma-induced attenuation in Ge doped fibres, co-doped with differing quantities of B and P [FSG80]. They found that RIA increased permanently and linearly with the quantity of P doping, while B doping led to a transient darkening, which recovered when the fibre was removed from the radiation field.

<sup>(5)</sup>Note that it is thought that compaction may be responsible for the increased attenuation in the infra-red shown by metal-coated fibres in figure 4.9, but there has been no further work testing this hypothesis at the time of writing

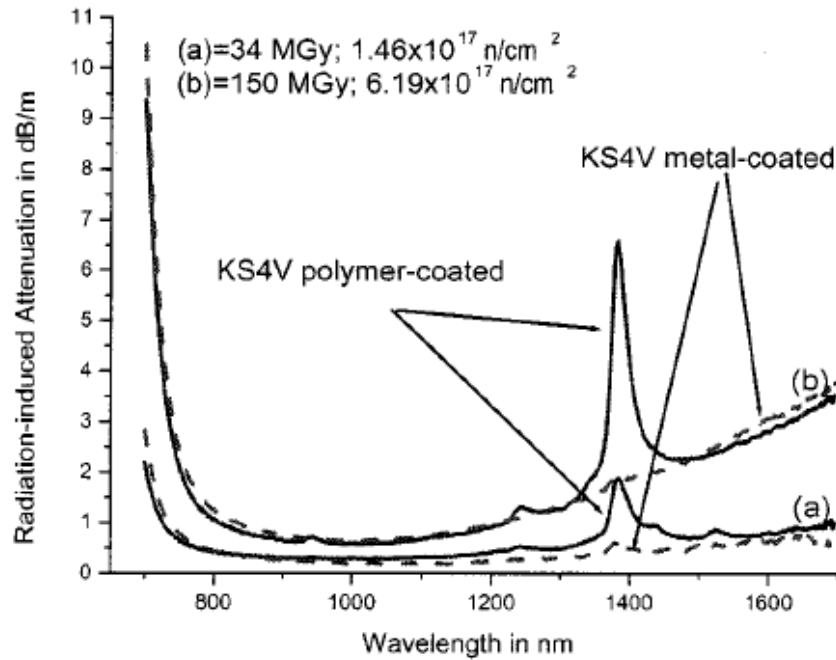


Figure 4.9: Comparison of RIA for acrylate-coated KS4V (pure silica) fibre and its aluminium-coated counterpart. Gamma doses and neutron fluences are shown [BBF<sup>+</sup>01].

Recovery, or annealing, occurs because of the slow, diffusion-limited recombination of defects such as interstitials and vacancies [BBF<sup>+</sup>06]. This re-organisation allows the fibre to recover some of its original properties. RIA is thus more pronounced at higher radiation dose *rates*, as defect centers are not given the opportunity to thermally decay — a hypothesis backed up by experimental studies<sup>(6)</sup> [Eva88, VBN<sup>+</sup>00].

Many other studies have compared the RIA of doped optical fibres under both gamma and neutron irradiation [Gil97, VBN<sup>+</sup>00, BBF<sup>+</sup>06, LPS<sup>+</sup>12]. The results from these studies, one such shown in figure 4.10, repeatedly confirm that germanium, erbium and phosphorous doping are detrimental to radiation hardness. Fibres with undoped, ultra-pure SiO<sub>2</sub> or fluorine-doped cores display unmatched radiation resistance [WDK<sup>+</sup>08]. Fibre claddings can be fluorine loaded to lower

<sup>(6)</sup>While Gill *et al* similarly found post-irradiation recovery behaviour for pure-silica fibres, these fibres immediately regained their original attenuation after reintroduction to a gamma field [Gil97]. They warn that apparent recovery to transmission may sometimes only be temporary, suggesting that the current understanding of recovery mechanisms may be incomplete.

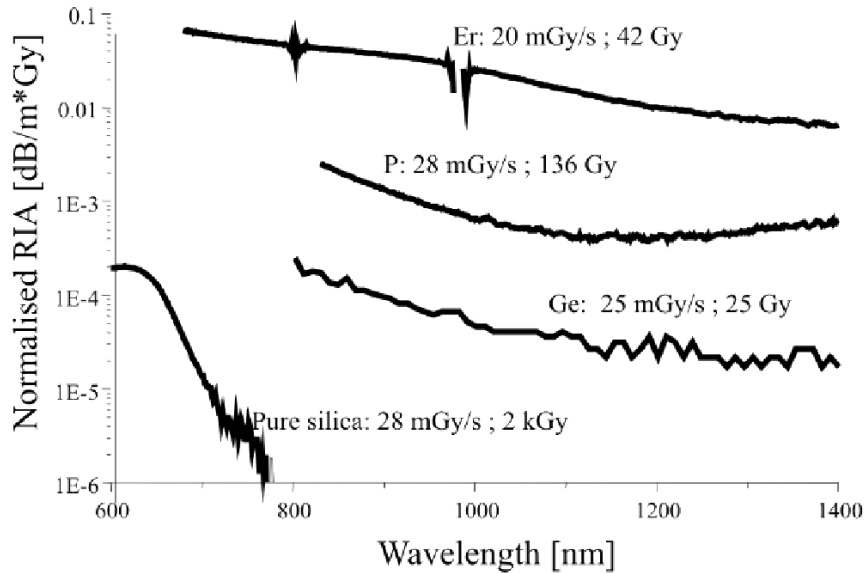


Figure 4.10: Comparison of RIA in fibres with different dopants. RIA is normalised to a 1 Gy gamma dose. The ambient temperature was 28°C. This shows pure silica fibres outperformed the doped fibres across the visible and infra-red [BBF<sup>+</sup>06].

the refractive index, as this also relaxes intrinsic strain, increasing gamma resistance further. This is particularly important for SM fibres which carry a large proportion of their optical power in the cladding. As a side note, MM fibres are generally unsuited to gamma-rich environments, as the dopant concentrations required to attain the core-cladding refractive index difference are large.

#### 4.2.5 Direct Comparison

Using the radiation levels predicted in §2.5.2, an estimate of the RIA for SMF-28 fibre within PCPV and PCC environments can be made. Empirically derived equations state that RIA [dB/m] scales linearly with neutron fluence  $\Phi_n$  and with a power law for gamma dose  $D_\gamma$  [MGy] [FBB<sup>+</sup>01, HKL<sup>+</sup>98]:

$$RIA = X_n \Phi_n + X_\gamma D_\gamma^c \quad (4.8)$$

where  $X_n$  and  $X_\gamma$  are fibre-dependent constants. Data from gamma-radiation studies, shown in figure 4.11, illustrate that  $X_\gamma = 0.18$  and  $c = 0.43$  for SMF-28 fibre [VBN<sup>+</sup>00, Nuf, Tro98]. Note also that attenuation saturates at around 0.5

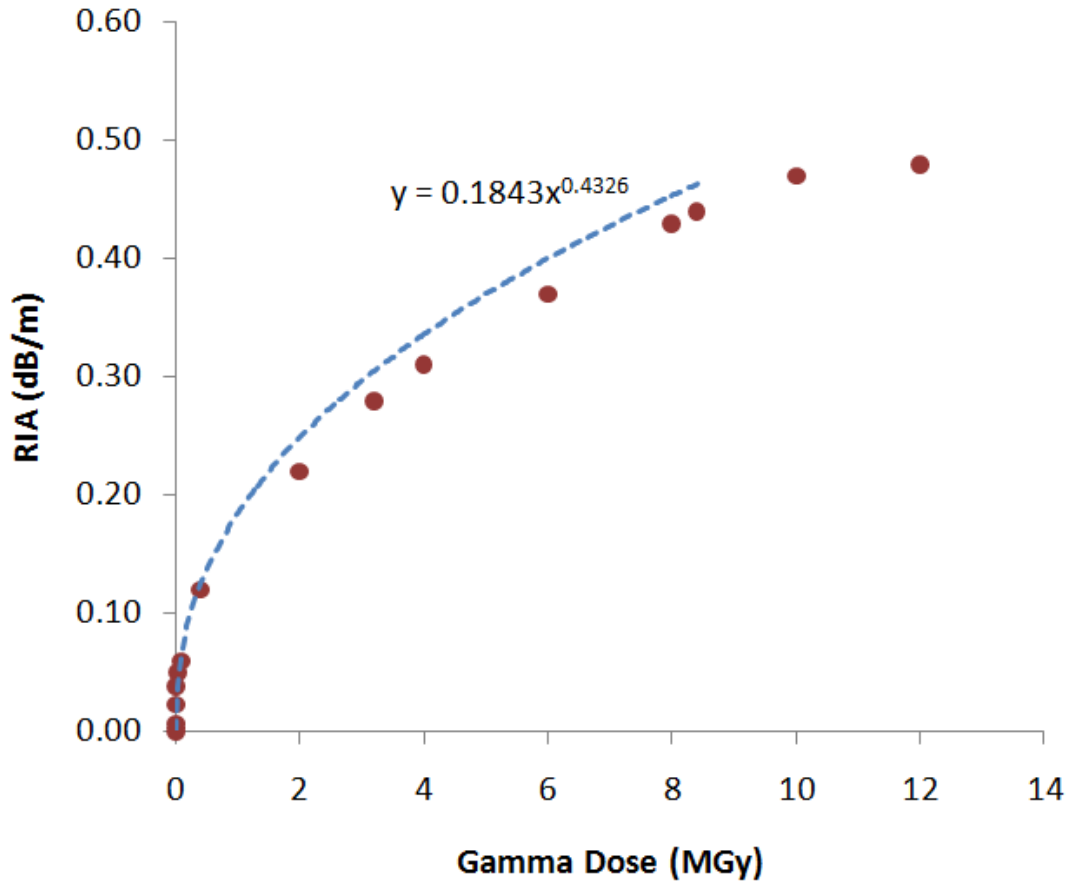


Figure 4.11: Attenuation vs gamma dose rate for SMF-28 fibre at 1550nm, taken from three sources, [VBN<sup>+</sup>00] [Nuf] [Tro98]. Note saturation of the GIA for SMF-28 at around 0.5dB/m. The dashed line shows a power law fit to the data points.

dB/m after a 10 MGy gamma dose. Uffelen *et al* found that when  $D_\gamma = 225$  MGy and  $\Phi_n = 10^{18} \text{ cm}^{-2}$ , RIA was 6 dB/m [FBB<sup>+</sup>01]. The fit predicts that 0.5 dB/m of this attenuation was gamma-induced, implying that  $X_n \approx 10^{-18}$  for SMF-28 fibre.

Using these values for  $X_n$  and  $X_\gamma$  and the radiation levels predicted in §2.5.2 the 10 year RIA for SMF-28 fibre is plotted as a function of distance from the reactor in figure 4.12. The largest radiation dose the fibres receive in the proposed application is at the tendon duct closest to the reactor at  $x = 0.3$  m, leading to attenuation of  $<1$  dB/m after 10 years.

Fibres will be used to instrument 30–60 metre long prestressing strands in the proposed application. The estimated total attenuation after 10 years for a 60

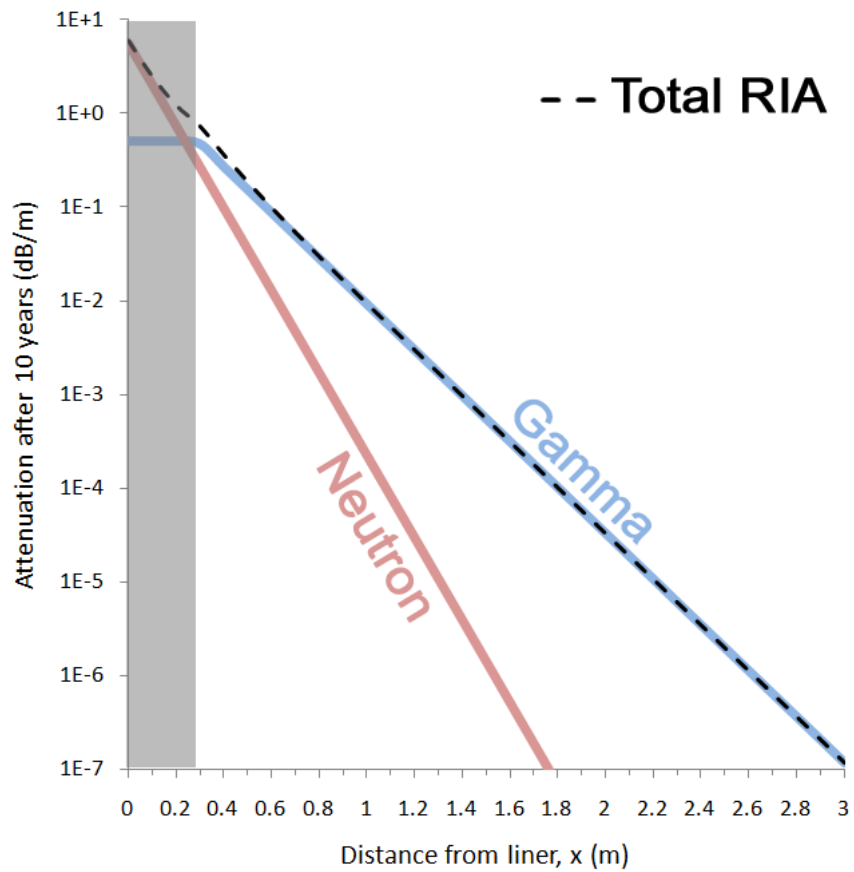


Figure 4.12: Predictions for the gamma-induced, neutron-induced and total RIA in SMF-28 fibre as a function of distance from the reactor liner  $x$ , for Heysham 1 reactor. Note the intrinsic attenuation of these fibres before irradiation is  $10^{-4}$  dB/m.

metre-long fibre system with 40 splices is plotted as a function of distance from the reactor liner in Figure 4.13 <sup>(7)</sup> The figure shows that SMF-28 fibre instrumenting the first tendon helical layer (at  $x = 0.3$  m) would be subject 50 dB attenuation after 10 years. By  $x = 1$  m, however, attenuation is only dependent on the number of splices in the fibre.

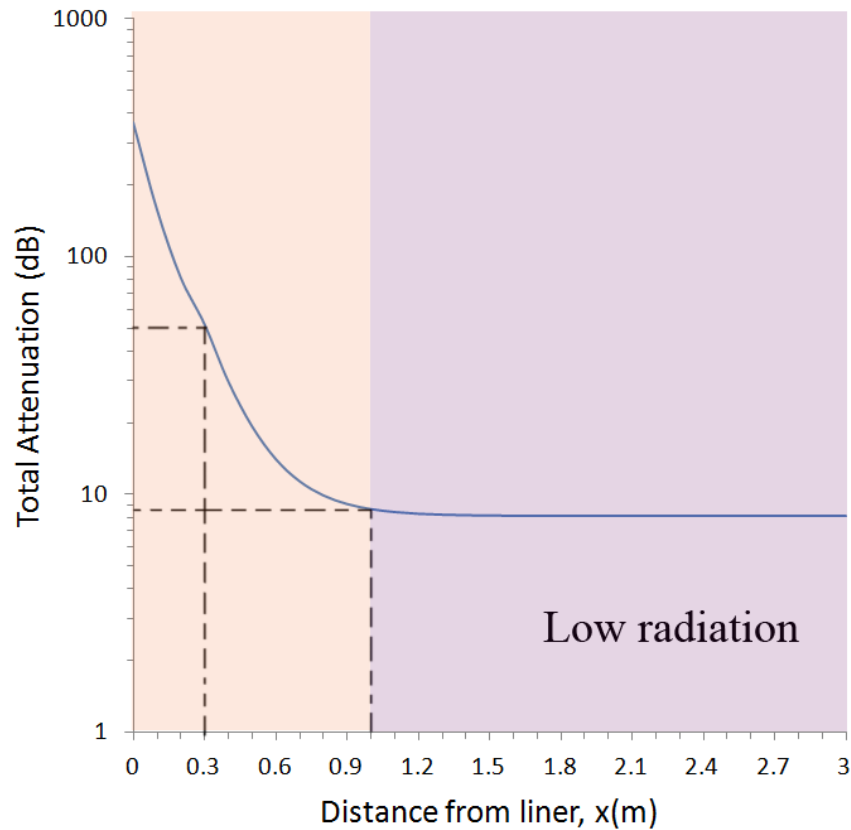


Figure 4.13: The total attenuation in 60 m of optical fibre after 10 years of radiation from a Heysham 1, as a function of distance from the reactor liner. Interrogating fibre sensors attached to the first helical tendon layer at  $x=0.3$  m may require a system capable of coping with up to 50 dB of attenuation. Beyond 1 metre from the liner, radiation levels are so low that the 8 dB losses all arise from splicing.

#### 4.2.6 Radiation Induced Attenuation Summary

There were several simplifying assumptions used to predict RIA for the proposed application, all of which have likely lead to an overestimate:

<sup>(7)</sup>Note that radiation induced attenuation is only one contributing factor to the total optical losses in the system. The largest losses often arise from the 0.2 dB attenuation introduced by microbending for each splice [Bje89].

- *The entire 60 m of fibre is irradiated by a uniform neutron-gamma field* — this may not be the case due to helical winding of tendons in the PCPV/PCC. It is also worth noting that not all fibre sensors will be 60 m away from the light source.
- *RIA is dose-rate independent* — Some of the data used in the calculation was based on an experiment for a fusion application, where dose rates are much higher. This is a necessity due to the very limited and conflicting literature currently available on the topic.
- *Gammas and neutrons work independently to densify silica* — there is an interplay between neutron compaction and gamma dilation, but again, the topic has not yet been explored in enough detail to propose a model.
- *Neutron-induced attenuation does not saturate* — This is likely a sensible assumption for the relatively low neutron fluences in fission reactors
- *RIA is independent of point defects* — Because recoil protons from an acrylate coat contribute to the water peak, it is sensible to use metal coated SMF-28 fibres. As such the treatment above only looked at compaction-based mechanisms for RIA.

Attempting to find a more accurate and realistic result would either require accepted models (which do not currently exist due to a lack of in-depth understanding about the mechanisms of RIA) or future experimentation with SMF-28 fibres in an environment which is more representative of a radiated PCPV tendon duct.

If there are concerns about RIA in SMF-28, then there are also specialist radiation-resistant fibres available. These consist of a high-purity silica core and a fluorine-doped cladding to improve gamma hardness [WDK<sup>+</sup>08, BGT08]. Photonic crystal fibres, which utilise the photonic bandgap effect to guide light through an air-core, also display RIA which is hundreds of times lower than that of Ge-doped fibre [Rus03, GBL05, HKW05, CLVB08]. As table 4.1 shows, how-

Fibre	Rad Res	Cost (£/m)
SMF28	Low	0.3
PSC	High	10-20
Hollow PCF	Excellent	84

Table 4.1: Cost (£per meter) and radiation resistance comparison of commercially available fibres.

ever, these benefits come at a financial cost, as radiation-resistant and photonic crystal fibres are substantially more expensive than SMF-28.

Nevertheless, even with conservative estimates, the literature suggests that RIA will not be an issue beyond 1 metre from the reactor liner, as the rapid attenuation of radiation through concrete makes these environments less harsh. Most of the current work in this area concentrates on the larger neutron-gamma doses and dose-rates found near the cores of fusion reactors, where RIA is likely to be much more of an issue.

Now that the operation and radiation-resistance of the addressing fibre in the system is understood, it is time to consider the fibre strain sensors themselves. The dynamic behaviour of RIA has demonstrated that intensity-based optical strain sensors should be avoided, so the next section will compare sensors which encode strain information into their reflected wavelength.

### 4.3 Fibre Bragg Gratings

There is a vast and growing body of fibre optic sensors (FOSs) available today, but they can all be categorised as either point, quasi-distributed or distributed sensors. While the operation principles of most of these FOSs are outside of the scope of this thesis, a brief comparison of their measurement performance is used to justify the one most suitable for smart tendon monitoring. Because RIA and microbending make intensity-based sensors unviable, only FOSs which encode their strain state into wavelength are considered:

- *Point Sensors* — These focus on accurately measuring a single (1–20 mm long) region along a fibre. Examples include Fabry-Perot interferometers

(FPIs), which resonate light between two partially reflective in-fibre mirrors to reflect a wavelength pattern which is dependent on local strain or temperature. FPIs are sensitive and can be very cheap to manufacture, making them highly suitable as disposable temperature probes [ZKRC10]. FPIs are also capable of providing a superior measurement range (up to 120  $m\epsilon$ ) compared to other FOS technologies [HWZ<sup>+</sup>10].

- *Quasi-Distributed Sensors* — These are point sensors which can be placed in a serial array along one fibre (multiplexed). An array of FOSs which reflect different, narrow wavelength patterns, such as fibre Bragg gratings (FBGs), can be used to garner strain information at several discrete (1–20 mm long) regions along a fibre. While they are affordable (£20 per FBG) and very sensitive to changes in strain, their measurement range is limited to around 7  $m\epsilon$ , depending on processing [HTS<sup>+</sup>98]. This strain range, however, is adequate for most structural health monitoring applications [Zho03].
- *Distributed Sensors* — Some interrogators can turn kilometres of normal fibre into a sensing medium, providing a distributed measurement of strain. Brillouin sensors, for example, measure the strain-dependent frequency reflected from acoustic waves in the fibre. The main issue is that there is a trade off between strain and spatial resolution. While the 2.5 mm spatial resolution of state of the art Brillouin sensors is comparable to that of FPIs and FBGs, the strain resolution of such a system would be hundreds of times lower [BC11]. Furthermore, while the fibre requires no processing, the £30,000 base cost of setting up a Brillouin interrogation system makes it more viable for long-haul sensing projects [OzO13].

<b>FOS Type</b>	<b>Typ. strain res.</b>	<b>Max strain range</b>	<b>Typ. spatial res.</b>	<b>Cost</b>
Point (FPIs)	1 $\mu\epsilon$	120 $m\epsilon$	10 mm	Low
Quasi-Distributed (FBGs)	1 $\mu\epsilon$	7–8 $m\epsilon$	10 mm	Med
Distributed (Brillouin)	10 $\mu\epsilon$	7–8 $m\epsilon$	1 m	High

Table 4.2: Summary of FOS types, with typical resolutions and ranges.

A summary of FOS types is shown in table 4.2. Recall that fabrication of a smart tendon requires that the strain at several points along a prestressing strand are measured up to  $6.8 \text{ m}\varepsilon$  (§3.6.2). While both quasi- and fully- distributed sensors are capable of this, FBGs have been chosen for this project as they are able to offer a better strain and spatial resolution at a much more competitive price. As we shall see in future sections, FBGs display further advantages over other FOSs within this application:

- They are a lower risk solution as they are an established sensor type,
- their behavior under radiation is better understood than other FOSs,
- they are modular, highly customisable, and easily multiplexable,
- each FBG is a point sensor and so only requires attachment at the sensor location,
- their interrogation systems react faster than those for Brillouin sensing

In the following sections, we will outline how different types of FBGs are fabricated, how FBGs convert strain into a reflected wavelength signal and also consider their sensitivity to other environmental variables such as temperature and radiation.

### 4.3.1 Operation Principle

A fibre Bragg grating (FBG) is a periodic modulation of the refractive index in the core and cladding of an optical fibre, as shown in Figure 4.14. When guided light meets the sudden increases or decreases in refractive index, there is partial Fresnel reflection with a  $\pi$  or zero phase shift respectively:

$$R_{\perp} = \left( \frac{n_1 - n_2}{n_1 + n_2} \right)^2 \quad (4.9)$$

The period of the index modulation  $\Lambda$  and the average effective index of the grating,  $n_{eff}$ , allow the reflected peaks and troughs of a narrow set of wavelengths

to match up and constructively interfere. The central value of the reflected *Bragg* wavelength is given by [HM97]:

$$\lambda_B = 2n_{eff}\Lambda \quad (4.10)$$

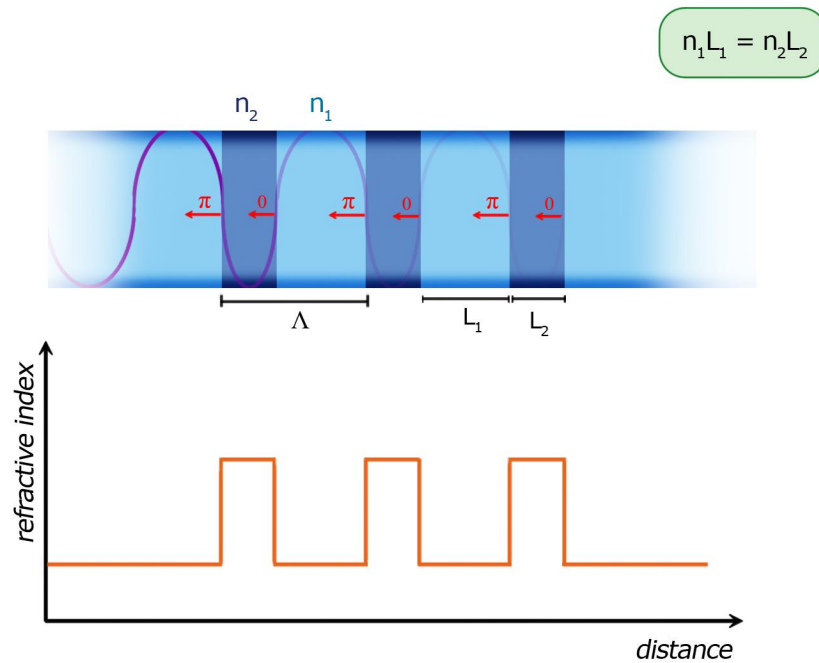


Figure 4.14: A fibre Bragg grating is a modulation in the refractive index of the fibre’s core and cladding, as shown. Broadband light, guided through the fibre, is reflected at the interface of each increase or decrease in refractive index with a  $\pi$  or  $0$  phase shift respectively. This leads to constructive interference of the Bragg wavelength, the value of which depends on the period of the grating  $\Lambda$  and the average refractive index. Note that constructive interference can only occur if the grating is designed so that the optical pathlength ( $nL$ ) of light is the same in high and low index parts.

### 4.3.2 Reflection Spectrum

Figure 4.15a) shows a typical Bragg reflection for a uniform grating (the refractive index modulation is shown inset). The primary reflection at  $\lambda_B$  is flanked by side bands which correspond to other harmonic wavelengths which are able to

constructively interfere in reflection<sup>(8)</sup> [Erd97]. As shown in figure 4.15b), the strength of these side bands can be reduced by apodising the index modulation of the grating. This can prevent side band cross-talk between Bragg gratings which are written at similar wavelengths.

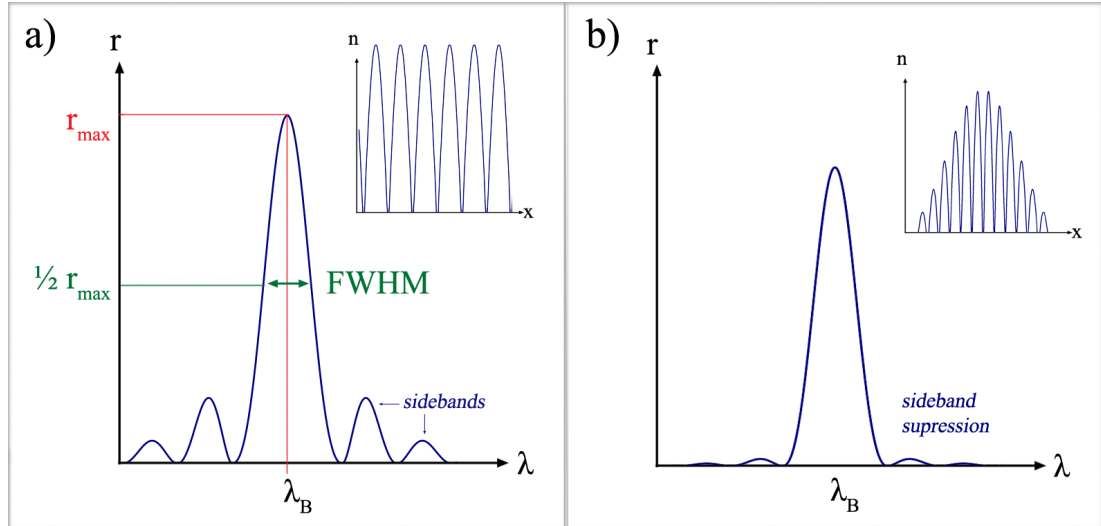


Figure 4.15: Reflection spectra of FBGs with and without Gaussian apodisation. a) The primary Bragg peak at  $\lambda_B$  is flanked by sidebands which may be suppressed through apodisation, shown in b). The index modulations along the grating are shown inset. The width of the primary peak is measured at half the maximum reflectivity,  $r_{max}$ .

The Bragg peak's full width at half maximum (FWHM) is also shown. Peaks are broader for more severe grating index modulations because the increased Fresnel reflection allows the grating to act as a mirror for a wider range of wavelengths. The side bands of highly reflective FBGs are also more difficult to suppress through apodisation. For a grating of fixed physical length, there are thus trade offs between achieving a high grating strength, a narrow peak and side-band suppression. The majority of the FBGs used for the work in this thesis are 10 mm long, apodised, with a FWHM of 0.1–0.3 nm and a reflectivity in the range of 50–60%.

<sup>(8)</sup>These harmonics arise from the weaker constructive interference of wavelengths over multiples or fractions of the grating period.

### 4.3.3 FBG Fabrication

The wavelength-specific mirroring of an FBG relies on the fabrication of the index modulation. A phase mask or interference pattern is used to selectively-illuminate a fibre from the side with a continuous-wave UV laser. In germanium-doped fibres, such as SMF-28, UV absorption by oxygen-deficient centre (ODC) point defects causes changes in the refractive index due to [Can08]:

- Alteration of the electron distribution (hence polarisability) of defects,
- gamma-induced compaction,
- increases in internal stress.

To improve the index modulation (and grating strength) further, fibres can be hydrogen loaded to temporarily introduce even more UV-absorbing defects. Because the index modulation of standard (type I) FBGs is reliant on the *introduction* of internal stress, heating these gratings up to 320 °C leads to stress-relaxation and erasure of the grating. Type II gratings with improved thermal resistance can be written (even in pure-silica glass) by pulsing the writing laser to increase its energy output so that it fractures the glass. Because the core of an optical fibre is naturally under a state of compression after fabrication (§4.1.3), fracturing allows index changes to be introduced through stress-relief. Because type II gratings are created through the *removal* of internal stress, they are harder to erase through annealing, and so survive beyond 1000 °C.

Another method used to improve thermal resistance is grating regeneration. Type I gratings are hydrogen (or helium) loaded after fabrication and then annealed at high temperature<sup>(9)</sup>. The original type I grating is erased, but the mechanical outward pressure of the hydrogen allows a second mechanical grating to regenerate in its place. Regenerated gratings are, like type II gratings, formed through stress-relief and as such are temperature stable up to and beyond 1300 °C, the softening point of the glass core [ACFT10, CCS12].

---

<sup>(9)</sup>The hydrogen penetrates the glass matrix. Upon heating the fibre to >500 °C, the hydrogen increases the glass' internal pressure, essentially forcing the core of the fibre to dilate and reduce tensile stress in the cladding.

Regardless of how the gratings are formed, they now reflect a Bragg wavelength which is dependent on the grating's periodicity and refractive index. As such, operations which change either of these parameters are able to induce shifts in the Bragg wavelength. This sensitivity is both a fundamental strength and weakness of FBG sensors.

#### 4.3.4 Sensing Principles

Application of axial strain to an FBG,  $\varepsilon_z$ , leads to stretching and an increase in the grating's periodicity,  $\Lambda$ . While this is tempered somewhat by a decrease in the refractive index, there is an overall linear relationship between fractional changes in the Bragg wavelength and the applied strain<sup>(10)</sup>:

$$\frac{\Delta\lambda_B}{\lambda_B} = (1 - p_e)\varepsilon_z \quad (4.11)$$

where  $p_e = 0.22$ , the strain-optic coefficient, accounts for the effect strain has on the grating's index. Fractional changes in  $\lambda_B$  can be converted to axial strain using this formula, allowing the FBG to act as a strain sensor. Indeed FBGs can sense anything which induces longitudinal strain. While this means that they can be converted into a variety of magnetic, acceleration and chemical sensors using suitable set ups, they are also naturally sensitive to temperature fluctuations.

##### 4.3.4.1 Temperature Dependence

Increases in temperature cause thermal expansion, in turn affecting periodicity and index. This means (4.11) must be expanded to:

$$\frac{\Delta\lambda_B}{\lambda_B} = (1 - p_e)\varepsilon_z + (\alpha_\Lambda + \alpha_n)\Delta T \quad (4.12)$$

where  $\alpha_\Lambda = 5.5 \times 10^{-7} \text{ }^\circ\text{C}^{-1}$  and  $\alpha_n = 8.3 \times 10^{-6} \text{ }^\circ\text{C}^{-1}$  are the thermal-expansion and thermo-optic coefficients for silica<sup>(11)</sup>. Temperature response is usually dominated by refractive index changes, unless the FBG is bonded to a material with

---

<sup>(10)</sup>A full derivation of this relationship is available in appendix A.1

<sup>(11)</sup>A full derivation of this relationship is available in appendix A.2

a high thermal expansion coefficient, such as steel ( $\alpha_{st} = 10.8 \times 10^{-6} \text{ }^\circ\text{C}^{-1}$ ).

### 4.3.5 Radiation Sensitivity

As sensitization to UV light during the FBG writing process can be permanent, gamma radiation in nuclear environments can continue to alter FBGs. Gamma-compaction and normalisation of the index modulation can lead to red-shifts and decreases in the Bragg reflection [Neu94, GFV<sup>+</sup>02, GBF<sup>+</sup>00]. From (4.10) we can see that while infra-red Bragg wavelengths are more sensitive to changes in refractive index (hence strain and temperature), they similarly show increased red-shifts under radiation-induced compaction [KHW06].

However, it has been confirmed that red-shifting of Ge-doped gratings saturates at 20 pm after a gamma dose of 80 kGy, with doses up to 1.5 MGy causing no further shifts, changes in the FWHM or temperature sensitivity of the Bragg peak [FBB<sup>+</sup>01, GVM<sup>+</sup>07, FBBD02]. While most FBGs display saturation behavior regardless of their fabrication method, we can see from Fig. 4.16 that the magnitude of the shift depends on the chemical composition of the FBG [GBF<sup>+</sup>00]. While hydrogen-loaded fibres show large shifts, lower red-shifts have been found in FBGs written in untreated, photosensitive Ge-doped fibre, possibly due to the reduced oscillator strength of Ge-based defects [FBBD02]. Various experiments, summarised in [HGH<sup>+</sup>11], have aimed to characterize the gamma-induced peak shifts of FBGs written in fibres with assorted dopants. The lowest shifts yet (<5 pm under a 1 MGy dose) are found in type II gratings, written via UV femtosecond laser pulses into fluorine-doped fibre cores.

Due to its dependence on glass relaxation, the magnitude of the Bragg-shift is temperature dependent, with shifts doubled at -50 °C compared to those at room temperature [HGH<sup>+</sup>11]. Defect annealing also means peak shifts are dose rate dependent, with dose rates of 1 to 25 kGy/hr causing shifts of 20 to 80 pm in Ge-doped fibre [FBBD02]. Removal of an FBG from a radiation field sometimes allows it to recover, with the peak blue-shifting to its original wavelength. The amount of annealing is again dependent on the dose rate, with faster doses reducing overall recovery [FBB<sup>+</sup>02]. All of these factors can lead to varying errors in

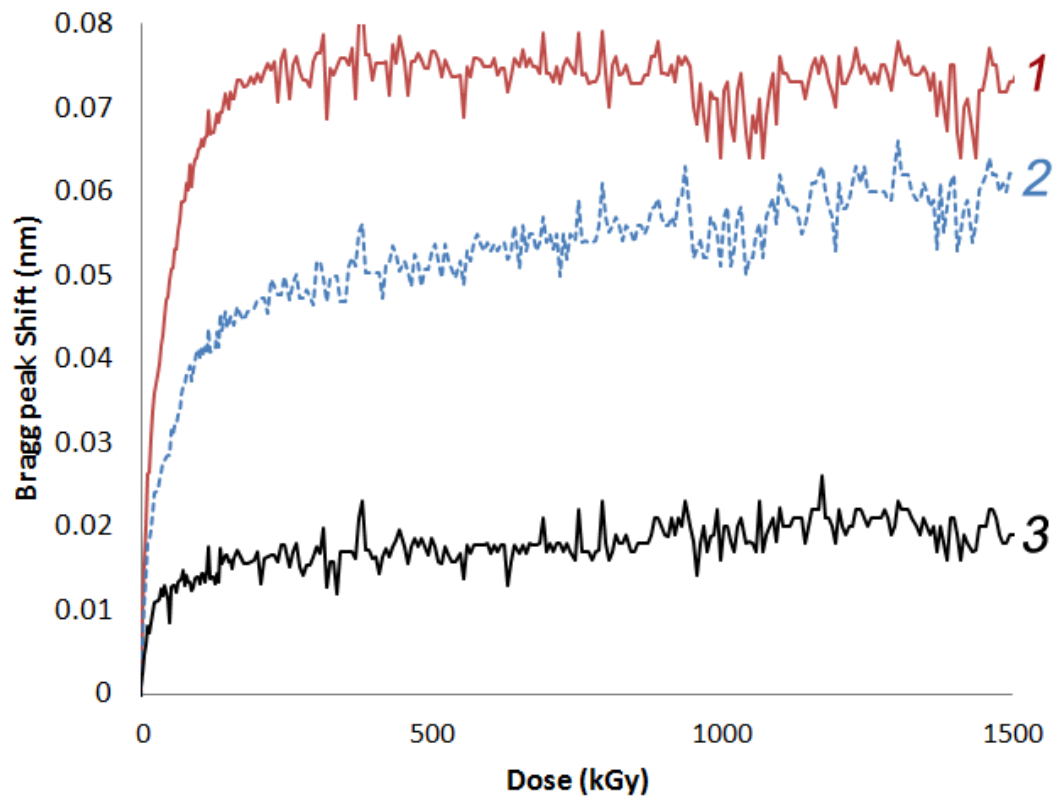


Figure 4.16: Comparison of Bragg peak shift under gamma irradiation for hydrogen loaded (1 and 2) and Ge-doped (3) fibres. Dose rate is 3 kGy/hr. [GBF<sup>+</sup>00]

strain or temperature measurements if FBGs are left uncharacterised. Note, however, that it is possible to take advantage of saturation by gamma pre-irradiating FBGs at a low dose rate, converting defect centers to induce a controlled shift which does not worsen when the FBGs are installed in a radioactive environment [LSJ<sup>+</sup>11, FGB<sup>+</sup>02].

It has also been found that gamma radiation can cause swelling of polymer coatings, leading to constriction of housed FBGs. For a 40 kGy dose, the resulting strains induced FBG shifts of 50, 20 and 10 pm in ormocer-, polyimide- and uncoated Ge-doped fibres respectively [GCM<sup>+</sup>08]. As such, it may be advisable to avoid polymer coatings when accurate or long-term measurements are required. Neutron irradiation can also induce silica compaction, leading to a shift in the average refractive index and hence the Bragg peak. However, neutron-induced shifts show no recovery under ambient conditions [Gus10].

It is also important to consider long-term effects at low dose rates. Over a period of 8 years, Gusarov *et al* exposed a variety of Ge-doped and hydrogen-loaded FBGs to a fast neutron fluence of  $10^{17}$  cm<sup>-2</sup> and a gamma dose of 10 MGy [Gus10]. While all tested fibres showed identical 60 pm neutron-induced shifts, gamma-induced shifts were chemical-composition dependent. The lowest overall peak shifts of 50 pm were found in non-aged, non-hydrogen-loaded, pre-irradiated FBGs. These also showed a 0.09 dB reduction in peak amplitude. The best performance from a hydrogen-loaded fibre was from pre-irradiated and pre-aged FBGs. These showed peak shifts of 0.12 nm and 0.97 dB attenuation in peak amplitude. While hydrogen contamination likely led to increased peak-shifts and losses, ageing may have allowed hydrogen to diffuse from the fibres, reducing its detrimental effects.

While there may be some dependence of FBG shifts on ambient temperature during irradiation [FBB<sup>+</sup>02], there has not been any work which examines this at the time of writing. Non-rigorous definition of environmental variables makes comparing data across independent studies difficult, so future work should aim to characterize temperature dependence in one study.

### 4.3.5.1 High Temperature Gratings

In some applications, such as monitoring fusion reactors, FBGs must be capable of withstanding both radiation and temperatures up to 800 °C [ITE99]. While conventional Ge-doped gratings and even novel hydrogen-loaded gratings are erased between 300-600 °C [LCB<sup>+</sup>09a, LCB<sup>+</sup>09b, BRBG97, ACSC10], regenerated gratings (RGs) have shown stability at temperatures over 1500 °C [CBS<sup>+</sup>09, ACFT10, ACC<sup>+</sup>12].

Historically, regenerated gratings were originally referred to as ‘chemical composition gratings’ (CCGs) [Fok04]. This term, now outdated, is used in this context to distinguish early RGs from their modern counterparts. While CCGs were stable up to 800 °C, their radiation-induced Bragg-shifts were found to be large due to a hydrogen sensitization step. When Fernandez *et al* tested the effects of neutron-gamma radiation on CCGs, they reported a linear, non-saturating drift in the wavelength (5 pm per 1 MGy gamma / 10<sup>16</sup> cm<sup>-2</sup> neutrons), FWHM and reflectivity of the Bragg peak [FBB<sup>+</sup>06]. However, as fibres were polymer coated, gradual hydrogen contamination could have caused these drifts via the reported core dilation of  $\frac{\Delta\rho}{\rho} = -10^{-4}$ .

Modern alternatives, such as regenerated gratings and FBGs written in sapphire fibre are able to withstand temperatures over 1500 °C [GMSD04]. While these gratings have not, at the time of writing, been tested for Bragg-peak shift sensitivity, the conventional hydrogen loading of RGs could be an indicator of increased drift. Lindner *et al* have recently written type II gratings in non-hydrogen-loaded, Ge-doped fibre using nanosecond laser pulses [LCC<sup>+</sup>11]. These gratings are both hydrogen-free and stable up to 1000 °C, potentially making them highly suited to sensing in high-temperature, radioactive environments. We are, however, merely speculating at this stage — recent discoveries showing boron co-doped type IIa gratings display *blue*-shifting have highlighted that the behavior of chemically complex gratings can be unpredictable [MMB05]. Further studies on bare or metal-coated RGs and sapphire FBGs may therefore be necessary to fully characterize radiation resistance and behavior.

#### 4.3.5.2 Strain Errors

Changes to fibre elasticity could lead to anomalous conversions between Bragg peak shift, fibre strain and stress. Elasticity stems from microscopic factors such as bond strength and conformation, so it is undoubtedly affected by radiation-induced compaction and viscous flow [ASC07]. At the time of writing, the dependence of elasticity on neutron-irradiation has not been studied, but FBG strain sensitivity has been shown to be increased by up to 5% by 400 kGy gamma radiation [HGH<sup>+</sup>11]. This could be a direct consequence of stiffness changes or alterations to breaking strength [HFS<sup>+</sup>88].

It has also been shown that an increased OH ion content reduces the elasticity of silica glasses, with a more pronounced effect at higher temperatures [PLP<sup>+</sup>08]. Thus while we should expect hydrogen contamination from neutron knock-out to increase the stiffness of polymer-coated fibres, there have been no studies explicitly studying this relationship at the time of writing.

Fibres bonded to a fixed substrate will also be subject to tensile stresses as their length and cross section is reduced under compaction. Radiation-induced compaction of 3% has been shown to induce 1  $m\varepsilon$  strains in silica samples [Pri82]. It is therefore important to counteract or characterize the effects of radiation on a bonded FBG transducer when attempting to obtain accurate measurements in highly radioactive environments.

#### 4.3.5.3 Thermal Properties

It has been demonstrated that at low temperature, ionizing radiation reduces silica's coefficient of thermal expansion [HFS<sup>+</sup>88]. This could lead to errors in an FBG temperature transducer. Thermal expansion under mixed neutron-gamma radiation at high temperatures has not yet been investigated at the time of writing. The largest contributor to FBG thermal sensitivity is the thermo-optic coefficient, a refractive-index based factor. We would expect this to be altered by compaction, but strangely, FBG studies have shown no overall effect of radiation on Bragg peak temperature sensitivity [FBBD02].

#### 4.3.5.4 Shift Dependence

To an external observer, a wavelength shift in the Bragg peak caused by neutron-gamma radiation will appear identical to one caused by an analogous temperature change,  $\Delta T$ . Radiation shifts can thus be characterised by the time-dependent equation:

$$\Delta T_{rad}(t) = B(1 - \exp(-t/\tau)) \quad (4.13)$$

Where  $B$  and  $\tau$  are dose- and fibre- dependent parameters for a constant dose rate [GFV<sup>+</sup>02]. This equation satisfactorily describes the peak-shift behaviour within both low and high dose-rate environments, but the *relative magnitudes* of the shifts in these respective environments are not adequately accounted for. At the time of writing, there are no models describing peak shifts as a function of dose rate, once again due to a lack of knowledge of the underlying damage mechanisms [Fie04].

Regardless, as equation (4.13) shows, radiation-induced shifts can be seen as apparent shifts in the temperature term in equation (4.12). This is especially true in the current application as the fibre chemistry and dose-rate generally remain constant. As such, equation (4.12) can be rewritten as:

$$\frac{\Delta\lambda_B}{\lambda_B} = (1 - p_e)\varepsilon_z + (\alpha_\Lambda + \alpha_n)(\Delta T_r) \quad (4.14)$$

where  $\Delta T_r$  captures the shifts due to temperature changes *and* radiation.

#### 4.3.6 Decoupling Strain

Equation (4.14) fully describes the FBG shifts which are expected to arise in a nuclear smart-tendon monitoring scenario. The strain of the tendon strands is the only term of real interest, however. There are a variety of methods used to decouple an FBG's strain response [Oth99], such as using co-located FBGs at different wavelengths and with different temperature and strain sensitivities.

The most common and convenient method, especially when radiation is present,

is to introduce redundancy. Subjecting two FBGs to the same temperature and radiation conditions, while only one is subjected to strain, allows the relative wavelength shifts to provide a strain measurement. It is either assumed that the thermal and radiation responses of the co-located FBGs is the same, or these properties can be characterised prior to use.

#### 4.3.6.1 Multiplexing

There are several multiplexing architectures available to increase redundancy in the sensing network and allow quasi-distributed measurements along a fibre:

- *Wavelength division multiplexing (WDM)* — The thin spectral reflection of an apodised FBG allows several strain sensors (and their temperature/radiation compensators) to be written at different wavelengths and multiplexed along a single fibre line. A broadband light source is used to illuminate the FBG array and then separate each reflected peak by its central wavelength. WDM requires FBGs to be spectrally spaced to ensure that there is no overlap between reflection peaks, especially after large strain or temperature changes.
- *Time division multiplexing (TDM)* — If a denser array of sensors is required, the readings from subsequent FBGs in the array can be separated in time. In TDM schemes, the order of the reflection sequence of a pulse of light is recorded. Because the reflections are separated by only a fraction of the time of flight of the light pulse, TDM requires extremely fast optical and electronic technologies and may not even be viable in short fibre arrays unless artificial delay lines are implemented.
- *Spatial division multiplexing (SDM)* — The simplest scheme of all, SDM requires switching between parallel lines of optical fibre. This increases sensor redundancy in one region by utilising several fibre lines.

The number of sensors which can be supported by these schemes depends on the magnitude of the Bragg shifts and the method of interrogation, but in a typical system, each fibre line can support around 10 multiplexed sensors in WDM or TDM [LLS04].

## 4.4 Summary

Intrinsic stress and dopant gradients between the core and cladding of an optical fibre set up refractive index differences which support light wave guiding through total internal reflection. While optical losses from bending, scattering and glass absorption occur in any fibre system, neutron-gamma radiation can introduce densification of the glass and a variety of point defects which absorb strongly at particular colour centres. Radiation-induced attenuation affecting infra-red wavelengths (the X, C and S bands) can be controlled to some extent by selecting pure-silica core optical fibres with a fluorine doped cladding and metallic coat. Nevertheless, due to the effectiveness of concrete as a neutron-gamma barrier, metal-plated Ge-doped fibres, such as SMF-28, are suitable for the current application in tendon ducts beyond 1 metre from the reactor vessel's liner.

The intensity fluctuations caused by radiation-induced attenuation make only wavelength-based fibre optic sensors a viable solution in nuclear environments. An economical, high-resolution and quasi-distributed measurement of strand strain can be made through attaching an array of wavelength-division multiplexed fibre Bragg grating sensors along the length of each strand. The Bragg peak shifts caused by radiation and temperature can be compensated for by allowing each strain sensor to have a local 'temperature reference' grating.

Armed with an in-depth understanding of this project's motivation and proposed solution, we can now begin to consider two major problems in the following chapters. Firstly, that of how to package and attach FBG sensors to a steel prestressing strand, so that the smart tendon is robust enough to measure temperature-compensated strand strain over decades of use. Secondly, we must consider the optical interrogation method used to provide the nanostrain resolution required to monitor prestress losses such as creep and shrinkage in existing PCCs and PCPVs.

# Chapter 5

## Fibre Sensor Packaging and Attachment

The first hurdle in fabricating the proposed smart tendon is the attachment of fibre sensors to the prestressing strand. In this chapter, state-of-the-art methods in fibre protection and attachment are evaluated and characterised. The aim is to reduce the mechanical and thermal damage to both the fibre sensors and the prestressing strands during processing. Prestressing strands displaying defects are discarded if they do not pass inspection, while high-quality sensors are essential for ensuring long-term reliability.

### 5.1 Current State of Technology

Optical fibre sensors have a history of monitoring strain within civil structures such as bridges, tunnels and dams [MGK<sup>+</sup>08, Ans97, MKF96, Zho03]. An overview of the most common methods used to bond fibre sensors to concrete and steel is given in table 5.1.

The application of fibre sensors to existing PCPVs and PCCs, however, presents fresh challenges:

- The structures already exist and so cannot be designed to incorporate sensors conveniently

Description	Advantages	Disadvantages	Ref.
Epoxy bonding fibres to the surfaces of steel strands or bars	Simple, can be low temperature, low pressure. Epoxies are well understood	Long-term stability of epoxies may be low. Bonding is usually performed <i>after</i> some prestress is applied, as epoxies cannot withstand full prestress	[MN93, SAO <sup>+</sup> 98, MAM <sup>+</sup> 97, MAM <sup>+</sup> 95, CYT <sup>+</sup> 06, MBST05]
Embedding or bonding to fibre reinforced plastic (FRP) composite strand	Easier to integrate fibres into FRPs as plastic embedding techniques are well tested	FRPs are strong enough to support prestressing, but lack the shear, chemical and radiation strength required by the application. FRP strands may not be representative of steel	[ZC93, TMR <sup>+</sup> 01, GLB <sup>+</sup> 05, KWB <sup>+</sup> 07, MAM <sup>+</sup> 97]
Incorporating fibre into the cement before drying, or into ducts before grouting	Can measure shrinkage and faults during curing	Ducts in UK power plants are ungrouted. Achieving a strong bond between fibre and cement is difficult. Cement is alkaline and so corrodes silica glass	[MCM <sup>+</sup> 97, HH94, LCCW04]
Surface mounting fibres onto concrete walls	Convenient for existing structures. Can also measure crack propagation.	Surface area of the walls is large, so this method is more suited to distributed sensing schemes. Cannot measure prestress levels within the structure.	[SCUS00, WAC02, IBCYMY02]
Brazing or soldering fibres directly into steel	Ensures good strain transfer between the strand and fibre, with reduced creep	High temperature processing can damage both the fibre and steel structure	[FZL09, LPS01a]
Spot welding fibre sensor packages to steel structures	Less damage compared to brazing, but requires careful design and manufacture of a sensor package	Fibre sensor packages are usually spot welded to large structures such as bridge beams. The packaging is typically too large and cumbersome to apply to a prestressing strand	[BCF <sup>+</sup> 08, She99]

Table 5.1: Methods currently used to bond fibres to civil structures, complete with the advantages and disadvantages for the current application and a selection of relevant references.

- Prestressing places the sensors under higher loads than in other applications
- The structures are over 30 years old, so tend to be more static than new builds. Plotting a trend in prestress loss may require years of high-resolution, accurate measurements
- The sensors' local environment is radioactive, warm and potentially humid
- The nuclear industry's high safety standards make it less flexible, so new technologies must be non-invasive and complement existing practices

Only some of the techniques listed in table 5.1 are viable. Embedding fibres into the concrete, for example, is unfeasible as the structures are already solid and drilling would be unacceptable from a safety perspective. Surface mounting fibres onto the walls of PCPVs or PCCs may be a sensible option for crack monitoring, but it would not provide direct measurements of prestress inside the vessel.

Utilising fibre-reinforced plastic (FRP) prestressing strands would circumvent many challenges. The softness of FRP allows fibres to be glued or embedded more conveniently [LZW<sup>+</sup>99, ZS02]. FRP strands, however, display different mechanical, thermal and radiation properties and a lower stress relaxation than steel, making them unrepresentative of existing strands<sup>(1)</sup> [SAS98]. The remaining option is to monitor the strain in steel strands. As these strands cannot be accessed during manufacture, the fibres must be bonded or embedded into the finished product.

### 5.1.1 Epoxy Bonding

Glueing the fibres to the strand is an obvious and common solution. Most conventional epoxies are unsuitable for high stress applications as they solidify in a brittle state and this makes them susceptible to surface damage [AY88]. Special high-strength epoxies include additives such as rubber or inorganic particles to improve tensile strength to up to  $8\text{ m}\epsilon$  [Sim13]. While this is within the  $7\text{ m}\epsilon$  limit

---

<sup>(1)</sup>Of course, replacing all 3000 tendons in an existing PCPV would be unfeasibly expensive and time consuming. The weak shear strength of FRPs and their degradation under irradiation, moisture, temperature and acidity also make this practice unlikely [CNA97].

of the prestressing application, achieving a high bond strength also requires that strands be cleaned and abraded using concentrated acid and mechanical roughening [BZ02]. The nuclear industry is understandably hesitant about such caustic pretreatments, as even temporary removal of the strand's lubricating grease, or residual acids may lead to corrosion of the steel in service.

Mechanical creep is also a major problem once epoxies are stressed to beyond 50 % of their tensile strength, and this can reduce a strain sensors' accuracy [FR77, MS09] <sup>(2)</sup>. Furthermore, because epoxies contain a lot of hydrogen, neutron-gamma radiation can cause significant degradation and hydrogen diffusion. Novel epoxies able to withstand radiation have been developed, but these display an unacceptably weak mechanical strength [PHM<sup>+</sup>07, PHM<sup>+</sup>09].

### 5.1.2 Justification for Metal Bonding

The only promising solution left for fibre attachment is metal bonding. Achieving a glass-to-metal bond is by no means straightforward, as it almost inevitably involves temperatures and pressures high enough to damage a glass fibre irreversibly. These challenges make metal bonding an unattractive prospect at first, but it may provide the thermal, mechanical and radiation resistance and diminished creep essential for this application [BRT<sup>+</sup>01, PI01, MME92, TL96, SGC01] <sup>(3)</sup>.

---

<sup>(2)</sup>After 1000 hours of loading at room temperature, it has been found that the ratio of the creep strain to elastic strain (i.e. the creep coefficient) of epoxies is typically between 1.5 and 3 [CB12, MCT09]. Epoxies are polymer based and it is link-breakages within or between polymer chains which lead to creep. Reinforcing these polymers with carbon nanotubes has been shown to reduce polymer chain mobility, in turn reducing the creep at lower stresses [SBM<sup>+</sup>12]. While this work is still at the research and development stage, it is worth noting that epoxies should still not be permanently discounted, as they may eventually become more applicable to high stress applications in future.

<sup>(3)</sup>For completeness, it is worth mentioning one other alternative, that of solder-glass bonding. Solder-glasses are metal-oxide preforms which melt and undergo a glass transition at around 300 °C. They are commonly used in optomechanical packaging, but unfortunately lack the mechanical strength to cope with high loads and impacts [Jin03, HP90].

## 5.2 The Mechanical Role of Fibre Coatings

The first challenge is finding a coating material capable of withstanding and protecting the fibre from high temperatures and pressures both during bonding and after deployment. This role is essential, as the brittle nature of a glass fibre makes it highly sensitive to surface damage.

### 5.2.1 Brittle Fracture Mechanics

The tensile strength of an optical fibre is driven by the condition of the cladding's surface and its internal stresses [Mau75]. Internal compression increases strength by smoothing cracks, while internal tension reduces the external force required to reach breaking strength. The intrinsic tensile strength of pristine fibres is 5.5 GPa, but they will often fracture before this, due to the presence of surface flaws [KGB10]. When a fibre is placed under tension, as shown in figure 5.1, the stress at fracture,  $\sigma_f$  is related to the size of the deepest flaw,  $a$ :

$$\sigma_f \propto a^{-\frac{1}{2}} \quad (5.1)$$

When the fibre fractures, there is crack growth and two new surfaces are exposed to the air. The total energy dissipated,  $G$ , is defined by the total surface energy released:

$$G = 2\gamma_S \quad (5.2)$$

and the constant of proportionality in equation (5.1) is dependent on this energy factor:

$$\sigma_f = \sqrt{\frac{EG}{\pi a}} \quad (5.3)$$

where  $E$  is the Young's modulus of the glass. Meanwhile, the stress field at the tip of the crack just before fracture can be expressed:

$$K_{IC} = \sqrt{EG} = \sigma_f \sqrt{\pi a} \quad (5.4)$$

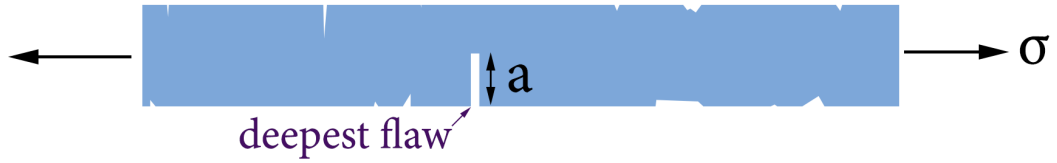


Figure 5.1: Under a tensile load, the stress at fracture will depend on the depth  $a$  of the deepest flaw in the fibre.

These equations show that the maximum stress within a crack (and hence the likelihood of fracture) is highly dependent on the flaw depth.

### 5.2.2 Fibre Survival Probability

The probability,  $S$ , that a fibre of length,  $L$ , will survive a stress  $\sigma$ , depends on the number and depth of flaws in the fibre [OM76]:

$$S = \exp[-LN(\sigma)] \quad (5.5)$$

where  $N(\sigma)$  is the cumulative number of flaws with a strength  $< \sigma$  per unit length<sup>(4)</sup>. The flaws in a freshly drawn fibre typically follow a ‘Weibull distribution’, defined by:

$$N(\sigma) = \left( \frac{\sigma}{\sigma_0} \right)^m \quad (5.6)$$

where the reference stress  $\sigma_0$  and the parameter  $m$  are used to define the shape of the distribution. Values of  $N(\sigma)$  are plotted in figure 5.2 for  $\sigma_0 = 1$  and varying  $m$ -values. If a length of fibre displays  $m < 5$  then this implies the fibre has a large distribution of flaw sizes, suggesting a low-quality surface. Large  $m$ -values ( $> 40$ ), meanwhile, imply an almost perfect flaw-free fibre [KP83].

<sup>(4)</sup>A full derivation of this equation is given in Appendix A.3

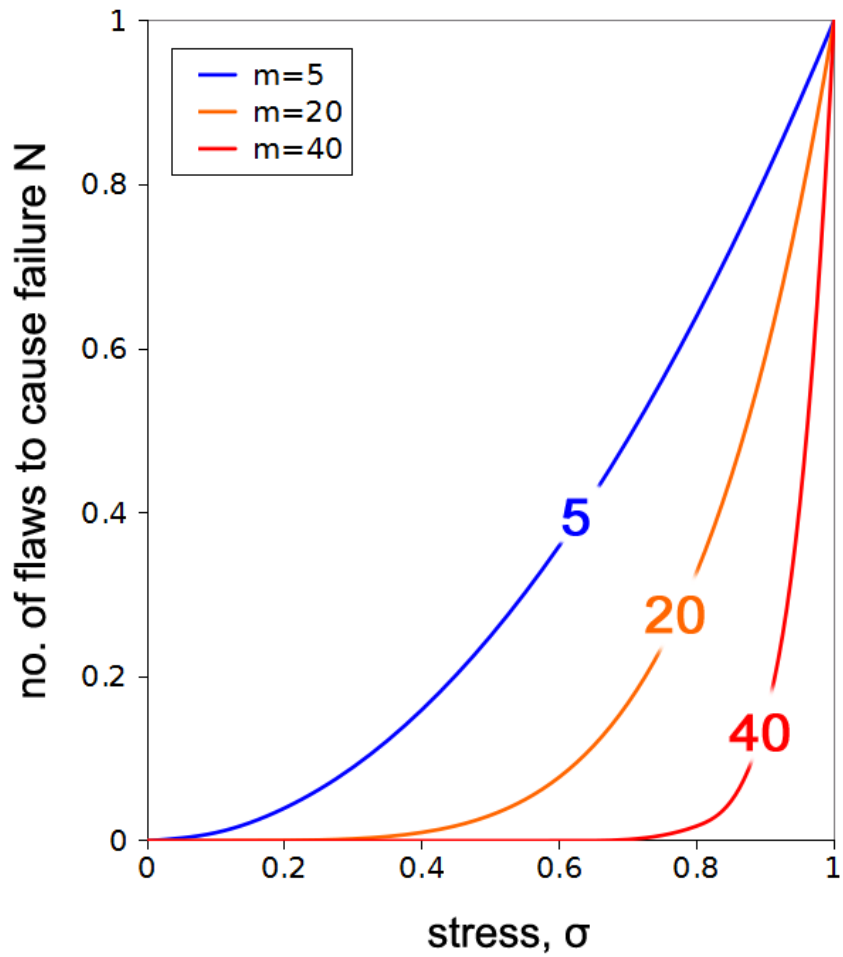


Figure 5.2: The cumulative number of fibre flaws which are stressed enough to fail increases with the amount of stress applied. Lower m-values enhance the chance of fibre failure at low stress values, while high m-values represent pristine, high-quality fibre which will likely fail only once it has reached a stress of  $\sigma_0 = 1$ . Note that distributions are normalised in this graph.

### 5.2.3 Flaw creation

The high strength of modern optical fibres is currently limited by the tiny fluctuations in fibre diameter introduced during drawing. Commercially available fibres such as SMF-28 display m-values as high as 45 [APPF97], but this baseline or intrinsic strength will only decrease once extra flaws are introduced [KGB10].

Flaws may be introduced during handling and metal embedding through the following mechanisms<sup>(5)</sup>:

- *Abrasion* — Mechanical abrasion causes surface flaws, so care must be taken during fibre handling [FRK<sup>+</sup>97, APPF97].
- *Water Damage* — Water hydrolyses silica, breaking bonds and increasing the depth of any microscopic surface flaws already present [RY91b]. Polymer fibre-coatings are not truly hermetic, and so cannot prevent water damage in the long term [ARPS].
- *Metal-silica interactions* — Metal coats are near-hermetic, fibre strength can be reduced as the metal layer places the cladding under tension [KKM89]. An intermediate amorphous carbon underlayer can be deposited between the silica and metal to prevent this, provided long-term ambient temperatures are <400 °C [Sem93, BKBK89, BDB<sup>+</sup>97]. The carbon layer also ensures true hermeticity.
- *Alkalinity* — Alkaline solutions reduce fibre strength dramatically, due to chemical etching which increases surface flaw depth [MK88]. Acidic solutions, on the other hand, have little or no effect on fibre strength [MKH97, RM94].
- *Radiation* — Fluorine leeching from some polymer coats can drastically reduce the strength of fibres after gamma ray exposure, as the fluorine attacks

---

<sup>(5)</sup>For completeness, it is worth noting that FBG writing itself may also have an impact on fibre strength [APPF97, BR03]. The literature suggests the effect seems to depend more on the energy output of the writing laser than the wavelength, but there are also variations between laser types. Further research will be required in this area in future, but the decreases in strength are thought to be minimal compared to other effects listed [YK07a].

the silica surface [SBKaS98]. More commonly, hydrogen atoms are knocked out of polymer coatings by incoming neutrons [SH98]. The subsequent proton collisions with the silica can result in atomic displacements, inducing plastic flows and softening in the glass [Pri64, SWP95, MCH94]. Higher energy (MeV) protons can also cause non-uniform stresses, surface cracking and hydrogen embrittlement<sup>(6)</sup> [MCH94, Pri64, RY91a, ARPS, SO97].

The points above show that while polymer coatings prevent the damage caused through handling, dust and weakly corrosive chemicals, they are not water- or radiation- resistant. The forces and temperatures inherent to metal bonding are also high enough to strip or melt even the most ruggedised polymers. Some nickel, gold, and copper-alloy coatings, on the other hand, are able to withstand metal embedding processes. The carbon-underlayer supplied with these coatings also guarantees hermeticity. Furthermore, having an external metal interface for the fibre can improve the bond strength to other nearby metals [LHYG09, SKRS06].

### 5.3 Metal Coating Fibres

High purity optical fibres, with an amorphous carbon underlayer and a 20 – 50  $\mu\text{m}$  thick copper-nickel alloy plating are already commercially available [IVG13]. The fibres are mechanically robust, radiation resistant and able to withstand temperatures up to 700 °C. Metal-coated FBGs, however, have not been commercially available throughout the lifetime of this project. Metals and polymers strongly absorb in the UV, shielding the fibre from the FBG writing laser, so FBGs must be side-written into bare fibres. While polymer recoating is a simple and common process, there are no readily available facilities for metal recoating fibres.

The methods previously used in research to metallise bare fibres are summarised as follows:

---

<sup>(6)</sup>Over all, polymer coats could be rejected simply based on the evidence of radiation damage. The voids, damage-trails and hydrogen contamination introduced by  $10^{13} \text{ cm}^{-2}$  neutrons can decrease fibre strengths by 4% [HKL<sup>+</sup>98]. While glass relaxation can allow a 1 MGy gamma dose to *increase* average fibre strengths by up to 10% [HSE<sup>+</sup>94, Hen94] doses of between 1 and 10 MGy can decrease strength by over 60% [NNT90]. Any apparent positive effects thus saturate extremely quickly.

- *Physical Vapour Deposition (PVD)* — Metal substrates are evaporated at low pressure, or sputtered with electrons to allow the metal particles to travel to and condense on a nearby fibre surface. Sputtering is sometimes favoured over evaporative deposition as the higher particle energy allows better adhesion to the fibre, but the resulting temperature gradients can lead to microbending and microcracks [DPL07, Li01]. Because it is time consuming, PVD typically only allows for thin,  $<1 \mu\text{m}$  thick, metal coats to be deposited as a precursor for electroplating.
- *Chemical Vapour Deposition (CVD)* — The fibre surface is exposed to an aerosol of volatile precursor chemicals, which react to form a metallic deposit on the fibre, layer-by-layer [HKMS99, CHS02]. CVD is versatile, economical and consistent, but it is also slow, with a  $1 \mu\text{m}$  coating taking hours to deposit [Wil08].
- *Electroless Plating* — Fibres may be dipped into several alkaline chemical baths so that a set of autocatalytic reactions can form a  $1 \mu\text{m}$  thick metal coating on the surface after a few minutes [LHYG09]. While electroless plating was attempted during this project, the coats were found to have a very low adhesion to the fibre and the use of alkaline solutions made the fibres brittle.
- *Electroplating* — Substrates must be electrically conductive for this technique to work, so it is used to increase the thickness of the metal seed-coatings described above. The fibre (cathode) and bulk metal (anode) are immersed in a conductive bath of metal salts. When current is passed through the solution, metal oxides produced at the anode are reduced at the cathode, depositing the metal onto the fibre. Electroplating can produce smooth, uniform, compact nickel coatings with thicknesses between 2 and  $340 \mu\text{m}$  within 2 – 4 hours [LHYG09, SKRS06, Bla08].
- *Thermal Spraying* — Molten metal particles can also be sprayed at fibres directly. The method is quick, well-established in industry and couples

easily to a production line, but it has been found that the coats produced on fibres are brittle, porous and induce a lot of thermal stress [Dan94].

In this project a combination of evaporative deposition and electroplating were used to nickel plate bare fibres<sup>(7)</sup>. Electroplating has the advantages of being an economical, low-temperature and well-understood method, but as an electrically conductive seed layer was required, fibres were first metallised in a 1  $\mu\text{m}$  thick chrome-gold bilayer using evaporative deposition.

### 5.3.1 Nickel Plating Fibres

#### 5.3.1.1 Evaporative Deposition

Evaporative deposition can produce high-quality, well-bonded metal coats [DPL07, VHM95, LL01]. Unlike electroless plating methods, it does not expose the fibres to water, alkaline solutions or hydrogen fluoride, all of which can cause substantial strength degradation [JXH<sup>+</sup>09].

Of the metals which can be evaporated, chrome combines the advantages of low-temperature deposition with a high stiffness and a strong adhesion to silica<sup>(8)</sup>. However, because chrome oxidises when exposed to ambient conditions, gold is plated over it without breaking vacuum. Gold is inert so does not bond well to silica, but it does form strong metallic bonds to the unoxidised chrome bridge, forming an electrically conductive outer layer suitable for electroplating [SH96].

A clean, bare fibre surface was required for deposition. Lengths of acrylate-coated SMF-28 fibre were immersed in acetone for 20 minutes until the coats could be removed by gentle sweeping with an alcohol-soaked tissue. Fibres were then rinsed briefly in ethanol and distilled water, before drying in warm air<sup>(9)</sup>.

The bare fibres were suspended vertically above a chrome source in the deposition chamber as shown in figure 5.3. The fibres were plasma cleaned, by

---

<sup>(7)</sup>Nickel was chosen because the electroplating solutions are convenient to work with. Nickel's stiffness is highly compatible with that of the steel strand, allowing for optimised strain transfer to the FBG

<sup>(8)</sup>Chrome is chemically active, breaking Si-O bonds on the fibre surface and forming Cr-O and Cr-Si bonds. The similarity of the bond types leads to a high interfacial bond strength.

<sup>(9)</sup>While introducing the fibre to water was not ideal, the time scales were short and the residues of the alcohol had to be removed to ensure strong bonding of the metallic seed layers.

Nickel Sulphate Hexahydrate $\text{NiSO}_4 \cdot 6\text{H}_2\text{O}$	300 g/L
Nickel Chloride Hexa/Hepta-Hydrate $\text{NiCl}_2 \cdot 6/7\text{H}_2\text{O}$	20 g/L
Boric Acid $\text{H}_3\text{BO}_3$	40 g/L
Sodium Dodecyl Sulphate $\text{C}_{12}\text{H}_{25}\text{SO}_4\text{Na}$	0.36 g/L

Table 5.2: Solution composition for electroplating fibres with nickel

applying a high voltage to produce a gas discharge current of 10 mA for 10 mins. The chamber was evacuated to a pressure of  $<10^{-4}$  Pa, to allow deposition of the chrome and gold. Ambient chrome gas raps residual water vapour and oxygen in the chamber, reducing the likelihood of coating defects and fibre embrittlement.

### 5.3.1.2 Nickel Electroplating

The chrome-gold bilayer plated fibres were suspended in an electroplating nickel solution as shown in figure 5.4. The electroplating solution composition used is given in table 5.2. A nickel foil cylinder surrounded the fibre to ensure uniform coating around its circumference. When electrical power was switched on, the nickel in the foil cylinder was oxidised, forming nickel-based ions with a positive charge. These associated with negative ions in the electroplating solution. The ion-pair travelled to the fibre and when they came into contact with its negative charge, they were reduced and deposited in a metallic state on the gold surface.

A weight attached to the bottom end of the fibre was used to hold it under tension, removing slack and preventing the fibre from bending and short-circuiting with the nickel cylinder. Fibres were plated at a current density of  $1 - 10 \text{ A/dm}^2$  at a temperature of  $50 - 70 \text{ }^\circ\text{C}$  for 10 minutes.

### 5.3.2 Coating Quality

Scanning electron microscope images of the fibres after electroplating are shown in figure 5.5. Figure 5.5a shows that plating at a low current density ( $1 \text{ A/dm}^2$ ) resulted in smooth, highly uniform,  $5-10 \mu\text{m}$  thick coat with few defects. Increasing the current density to  $10 \text{ A/dm}^2$  increased the deposition rate, but at the cost of coat uniformity, producing a more rugged,  $50-100 \mu\text{m}$  thick coats with several

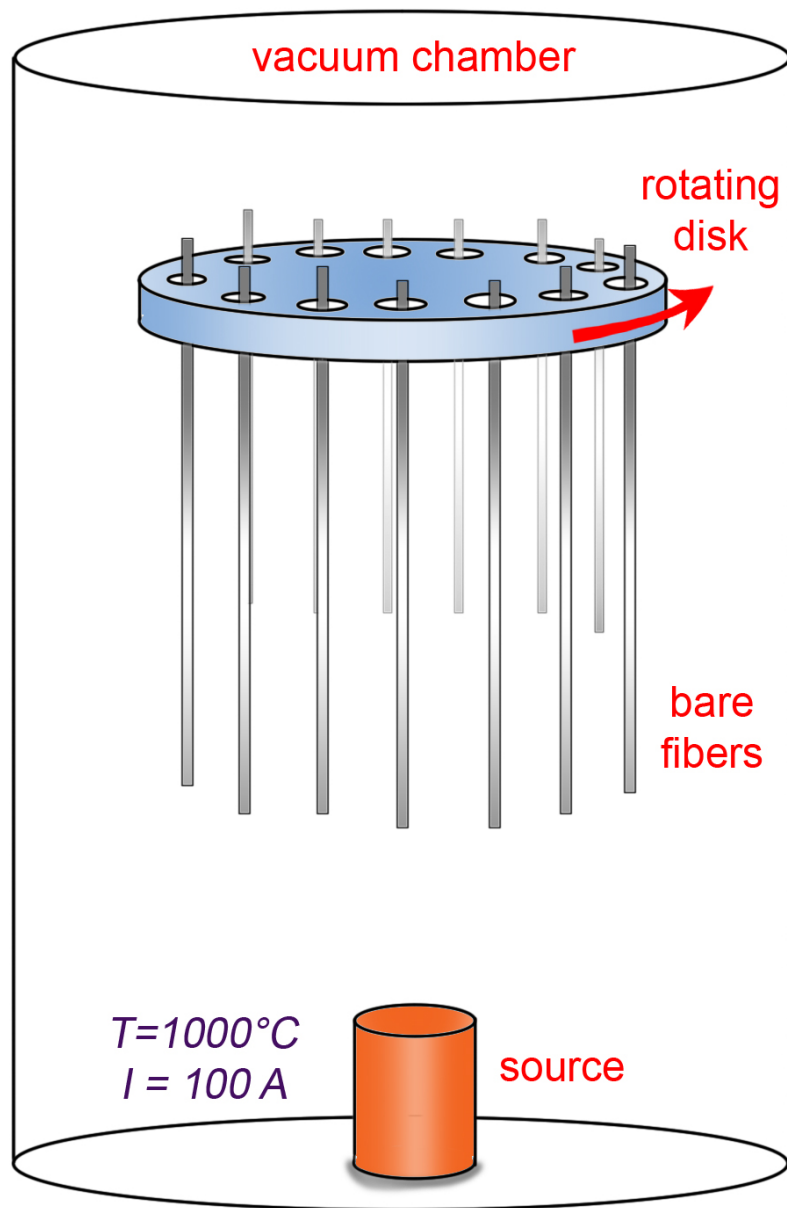


Figure 5.3: Bare fibres were fixed to a steel disk above the chromium and gold source in the evaporation chamber. Rotation of the disk ( $0.4\text{ rad s}^{-1}$ ) aided uniform deposition. The deposition rate was  $20\text{ nm s}^{-1}$  at a current of  $100\text{ A}$  and temperature of  $1000^{\circ}\text{C}$ .

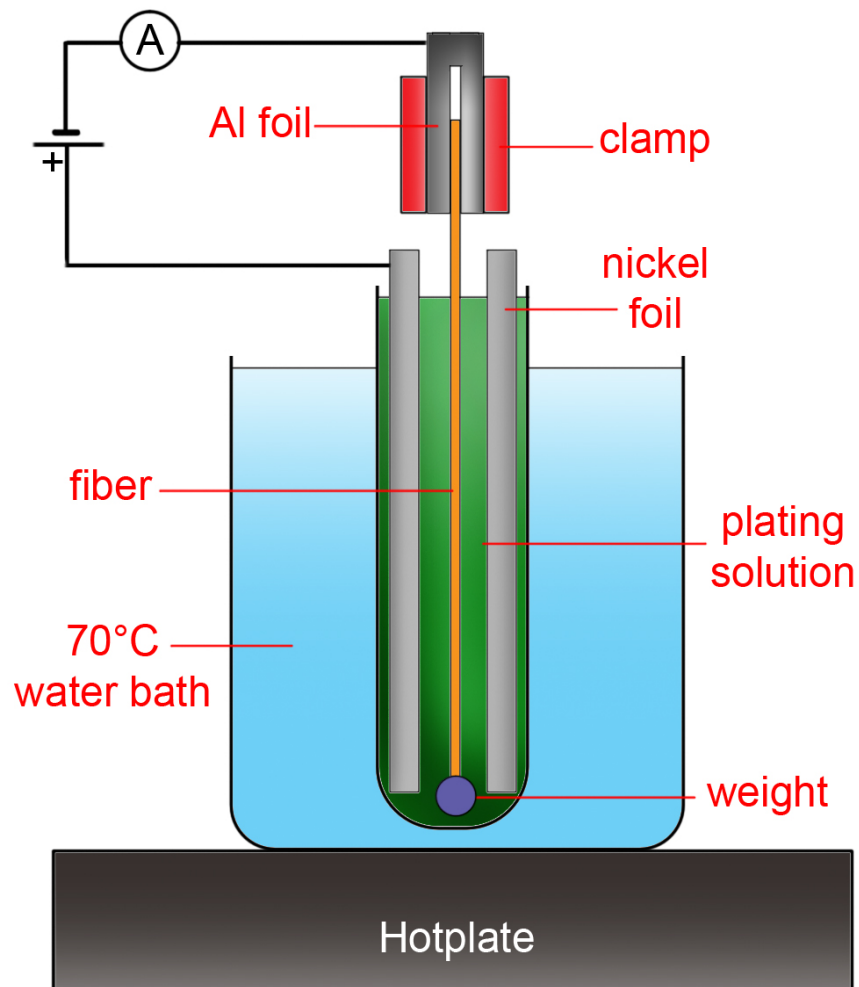


Figure 5.4: Chrome-gold coated fibres (cathode) were suspended in the plating solution and surrounded by a nickel anode. Temperature was held constant by a water bath and current density was measured by an ammeter.

visible defects, shown in figure 5.5b. Both sets of plated fibres were soldered and placed under tension as part of a pull-out test. Neither coat failed before the fibre and this suggested that even the non-uniform coat was strongly bonded.

### 5.3.3 Discussion of Results

Unfortunately, there were several problems with the plating method which made it too time consuming, expensive and unreliable to be suited to mass production. The most major issue was that reproducibility was unacceptably low — the yield of successfully metal-plated fibres was less than 20 %. Often the fibres would be too brittle to use after electroplating, or the coatings were non-uniform and porous. The reason for low yields may have been due to:

- *Overhandling* — While every effort was made to handle the fibres as little as possible, the large number of steps in the process presented several opportunities for flaws to be introduced to the cladding surface, either through abrasion or water damage.
- *Imperfect-hermeticity* — Even shallow scratches in the 1  $\mu\text{m}$  thick chrome-gold bilayer would allow the caustic alkaline electroplating solution to come into contact with the fibre,
- *Evaporative deposition* — The adhesion of the chrome-gold bilayer depended on the fibre's location in the deposition chamber. Those hanging directly above the source received a thicker and more even coat than those at the periphery.
- *Nickel anode* — The conformation of the nickel anode around the fibre needed to be perfectly cylindrical to encourage even plating. This could not be ensured with the set up used, so the uneven build up of the metal coat may have led to fibre bending and stress.
- *Chemistry* — There are often large tolerances in quoted electroplating solution concentrations to account for the size, shape and electrode vicinity

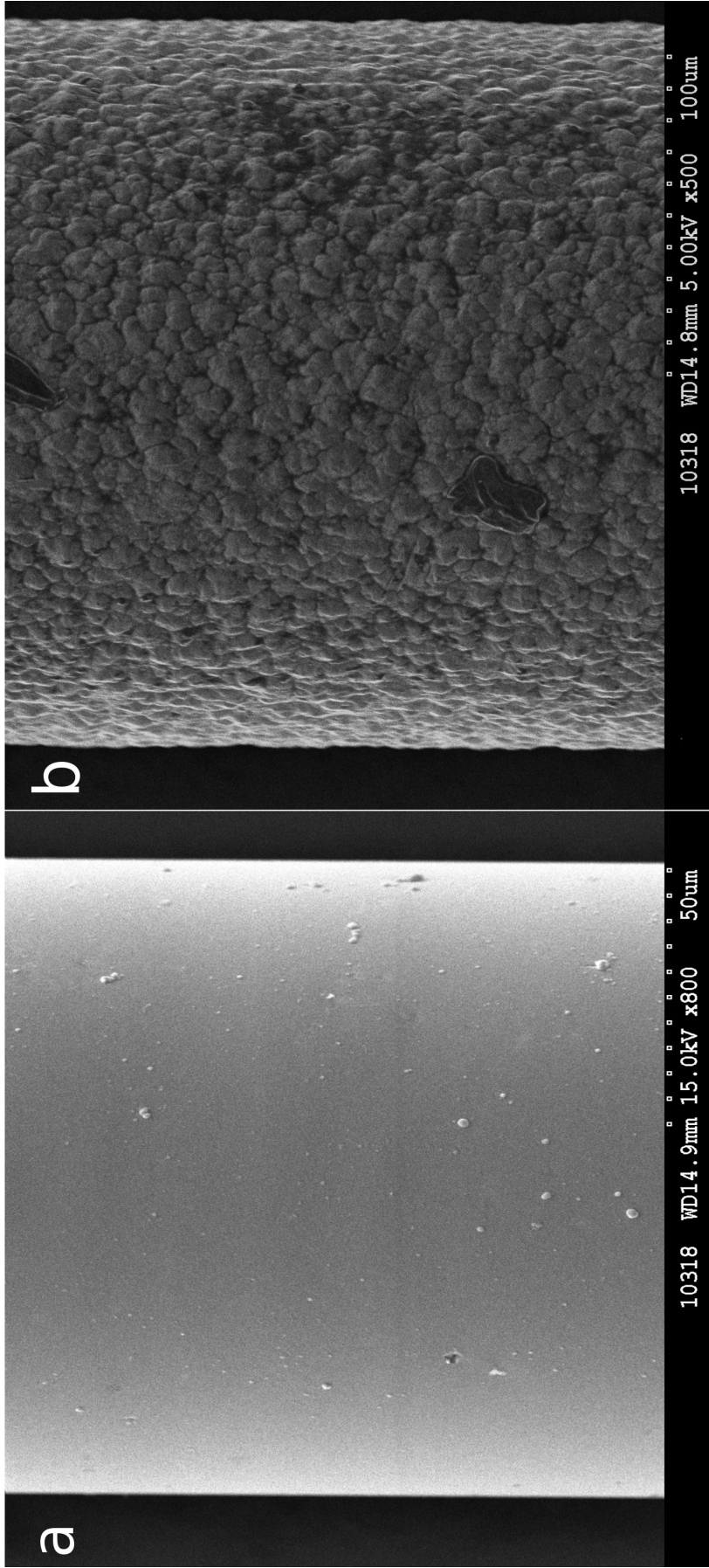


Figure 5.5: Electron microscope images of nickel plated fibres. a) Fibre plated for 10 minutes at 1 A/dm<sup>2</sup> displaying a very smooth but thin (5–10 µm) nickel coat. b) Fibre plated for 10 minutes at 10 A/dm<sup>2</sup>, note the coat is far less smooth but is thicker at 50–100 µm.

of the set up. Following the steps in some literature sources did not always provide acceptable results, so finding the correct concentrations for this application was very much a process of trial and error.

- *Cleanliness* — Oil or contaminants introduced to the gold surface after removal from the evaporative deposition chamber may have reduced the adhesion of the nickel coat. While solvents could be used to clean the fibres, it was difficult to clean such a thin layer of metal without removing it from the fibre.
- *Smoothness* — Achieving good coating adhesion on a smooth fibre surface was challenging. Some literature sources suggest surface roughening of fibres with hydrogen fluoride, but this has a profound impact on fibre strength [JXH<sup>+</sup>09].

Addressing the points above may allow future yields to be improved. True hermeticity could be achieved by depositing an amorphous carbon underlayer onto the fibre in a dedicated carbon deposition chamber. Sputtering the coatings onto the fibres, rather than evaporating them, may also improve adhesion [TTQ12]. None of these facilities were available at the time and there were some concerns that even a thick-metal coating would not provide enough thermal shielding for the FBG during subsequent metal bonding. As such, it was decided that time would be better invested in developing an altogether different method of encapsulating bare FBGs.

## 5.4 Capillary Encapsulation

The 10 mm long bare fibre section containing an FBG can be encapsulated within a 25 mm long capillary (also called a ferrule). As shown in figures 5.6 and 5.7, the capillary is joined to the plated sections of fibre using metal solder. This allows strain transfer from the capillary to the FBG, while it remains protected from damage<sup>(10)</sup>.

---

<sup>(10)</sup>In this project, the designed ferrule's inner and outer diameters were 300 and 700  $\mu\text{m}$  respectively as this allowed it to contain the 200  $\mu\text{m}$  diameter metalised fibre with a very small

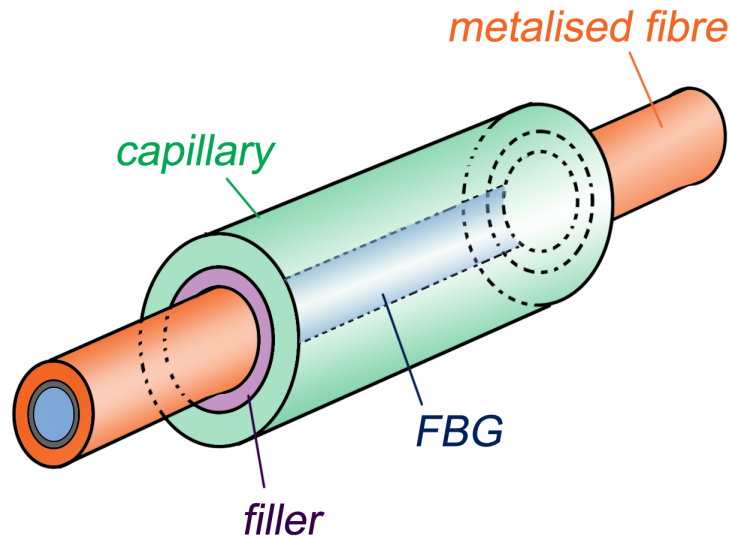


Figure 5.6: Diagram of a capillary-encapsulated bare FBG. A bare section of fibre housing an FBG is slotted through a metal capillary. The ends of capillary are bonded to the metalised section of the fibre using solder. The fibre is protected and length changes in the capillary are allowed to act upon the FBG.

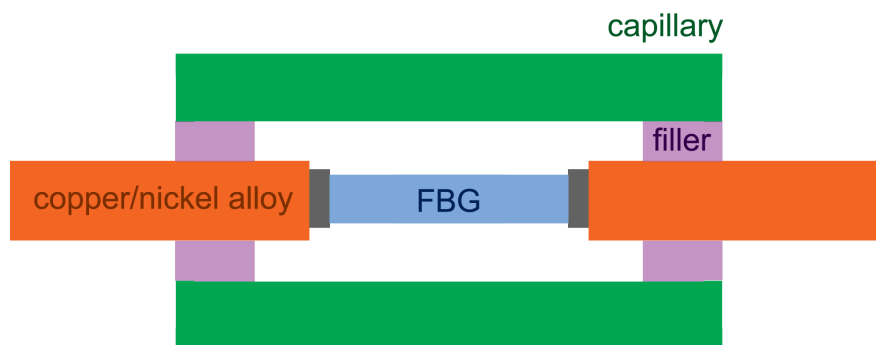


Figure 5.7: Cross-section of the capillary encapsulated FBG. This diagram shows more clearly how the filler material is bonded to the metalised part of the fibre, closing off the ends of the housing (providing hermeticity) and allowing strain transfer between the capillary and the FBG.

Because capillaries are more rigid than plated fibres, they are often used to lend fibre sensors extra mechanical strength [BCF<sup>+</sup>08, OZZ03]. The ferrule can also provide guidance under compression, retaining its shape under forces which would bend or snap a lone fibre [MSZ<sup>+</sup>04, ZZGF03]. The method does rely on the development of a suitable soldering technique, however. In this project, high-temperature soldering (otherwise known as brazing) was investigated, as it provides a high mechanical integrity with diminished creep (§5.1.2).

### 5.4.1 Brazing

Brazing alloys are melted to allow them to flow into the spaces between adjacent metals through capillary attraction, where they then re-solidify upon cooling. Brazing has been previously used to embed plated fibres into metal structures [SH03, LHYG09], but the success of the method is highly dependent on the choice of a suitable technique, alloy, atmosphere and heating method.

#### 5.4.1.1 Brazing Alloys

Brazing alloys come in a variety of forms from pastes and creams to wires, solid preforms and even powders. They are typically a mixture of two or three metals in concentrations which are chosen to manipulate the following properties:

- *Wetting* — The viscosity and chemical composition of the alloy in its liquid state affect its flow rate.
- *Solid Behaviour* — The finished joint's resistance to corrosion, its hardness, shear strength, elasticity and creep.
- *Melting Point* — If the base workpieces are sensitive to high temperature, then low melting point alloys are used. Alloys with a low melting point (400 °C) tend to be softer, more elastic and prone to creep than those of a high melting point (1000 °C) [MME92].

---

clearance. The clearance was minimised (taking account for thermal expansion) to allow the solder to distribute itself evenly over adjacent surfaces.

- *Reactivity* — The application may require chemical or radiation inertness.

Brazing in this project was mainly performed with a 42% silver alloy. It was chosen for its high flow rate and low melting point of 620 °C).

#### 5.4.1.2 Atmosphere and Flux

Ambient oxygen creates an oxide barrier on metals and this leads to weaker joints with the brazing alloy. Brazing within a vacuum, or within inert or reducing atmospheres such as argon, nitrogen and hydrogen can reduce oxidation. Argon was used in the work described here as it does not react with any of the base metals or solders. In the absence of a pure atmosphere, flux is used to shield the workpieces from the air and dissolve residual oxides. The chemically corrosive flux is displaced by the molten alloy, but as residues can weaken a joint, flux must be removed by quenching or abrading the workpiece after brazing.

#### 5.4.1.3 Cleaning Technique

Oil and grease can prevent capillary action and repel flux, leaving bare metal exposed during heating, so workpieces are degreased and cleaned with ethanol. Heavy oxidation is removed mechanically, or by acid pickling and brazing is performed immediately after cleaning <sup>(11)</sup>.

#### 5.4.1.4 Heating Methods

The method used to melt the alloy must be suitable for the small and thin fibre and ferrule. The following methods have been used for fibre brazing in previous research:

- *Torch* — Directly applying a flame to a fibre is not recommended, but brazing alloys can be melted within a crucible and then poured onto the workpieces [LGA<sup>+</sup>91, TL93]. Controlling the flow of the molten alloy can be

---

<sup>(11)</sup> Acid pickling is not applied to the prestressing strands — the oxides on these are thin and easily removed through light abrasion with fine grain sandpaper. Removing steel-based oxides from other components requires low concentration acetic acid (common vinegar) solutions.

cumbersome as capillary action is inhibited by the fact that the workpieces are not pre-heated [Sch95].

- *Thermal Spraying* — Thermal spraying has been used to embed metallised fibres into titanium composites, but the lack of control over the heating and cooling of the brazing alloy can lead to porosity and oxidisation [BTS90].
- *Induction* — Induction coils induce heating in nearby ferromagnetic metals. Careful design and selection of coil conformity, current and frequency allows for more control over heating schedules [FNB11, NM11].
- *Furnace* — Furnace heating, particularly in a vacuum, is a common method of brazing fibres as it is simple, easily controlled and safely confined [SH03, LHYG09]. Furnace heating is quite slow, however, and this can coarsen the microstructure of the alloy leading to brittle joints [Sch95, YLS05].
- *Laser/Electron* — Pulsed lasers or electron beams can melt metal powders layer-by-layer over a fibre [AT11, LPS01b]. This method allows for a great degree of spatial control but the high costs for these methods are a barrier to their widespread use.

Induction brazing was chosen for this work because variation of the coil's parameters allowed a great degree of flexibility and control over workpiece temperatures. Brazing small parts using induction takes seconds, rather than minutes, and there are natural mechanisms (§5.5.3.1) which can be used to ensure workpiece temperatures do not exceed specified limits.

## 5.5 Induction Brazing

### 5.5.1 Capillary Material

The magnetic field generated by an induction coil heats nearby ferromagnetic metals. Ferromagnetism, however, only occurs within a limited temperature range. Beyond the Curie temperature,  $C_T$ , ferromagnetism ceases and induction heating

	Silica	Steel	Nickel	Kovar	Invar 42
Yield Strength (MPa)	-	415	210	345	276
Tensile strength (MPa)	-	540	520	517	517
Young's modulus (GPa)	72	200	170	159	148
Poisson's Ratio	0.17	0.29	0.3	0.32	0.3
Thermal conductivity (W/mK)	1.3	65.2	70	17.3	10.7
Thermal expansion ( $\mu\text{m}/^\circ\text{C}$ )	0.55	11.5	13.3	5.5	4.7
Curie Transition ( $^\circ\text{C}$ )	-	750	360	435	380

Table 5.3: A comparison of the mechanical, thermal and magnetic properties (at room temperature) of potential capillary materials. These properties are dependent on chemical composition, tempering and heat treatments. Actual Curie temperatures may vary with material composition [RS75].

is dramatically reduced. In this project, this effect was exploited as it reduced the heat exposure of the fibre within the capillary. Based on this, several suitable candidates for capillary materials are compared to silica glass in table 5.3.

The mechanical and thermal properties of steel and nickel are a good match for the prestressing strand, but they do not couple well to silica. Large discrepancies between thermal expansion coefficients can place the brazing alloy and fibre under considerable stress. Iron-nickel alloys such as kovar and invar display lower thermal expansion, but it is kovar which exhibits the high yield strength required to withstand prestress. Kovar's Curie temperature of around  $430^\circ\text{C}$  also allows for good wetting during brazing and minimal thermal damage to the encapsulated FBG.

### 5.5.2 Induction Heating Set up

The induction heating set up is shown in figures 5.8 and 5.9 [NF11]. The fibre was slotted through the ferrule and fixed to translation stages by magnets at either end. Ferrule ends were coated in brazing paste and 4 mm thick steel heat susceptors enveloped the brazing points. The higher Curie temperature and larger volume of the susceptors allows them to reach up to  $1300^\circ\text{C}$  under induction, so that local heating of the capillary ends melts the brazing alloy.

The setup was placed within an airtight perspex box as shown in figure 5.10. The box was evacuated via a 50 mm diameter tube, while argon gas was fed into

the chamber at the opposite end at a rate of 510 litres per hour<sup>(12)</sup>.

### 5.5.3 Induction Heating Theory

As shown in figure 5.11, electric current flowing through the induction coil produces a magnetic field,  $\mathbf{B}$ , which points along the helix axis. The local magnetic flux at any point on a nearby conductor's surface is given by:

$$\Phi_m = \iint_S \mathbf{B} \cdot d\mathbf{S} \quad (5.7)$$

Rapidly alternating the current direction in the coil with a frequency,  $\omega$ , induces an electromotive force (emf) in the conductor, which opposes the current in the coil:

$$\varepsilon_{emf} = \frac{d\Phi_m}{dt} \quad (5.8)$$

The electrical resistance of the conductor,  $R$ , leads to Joule heating with a total power:

$$P = I^2 R \quad (5.9)$$

The current distribution in the conductor, however, is not uniform. The current density,  $J$ , decreases exponentially with distance,  $d$ , from a maximum value at the conductor edges:

$$J = J_0 e^{-\frac{d}{\delta}} \quad (5.10)$$

with approximately 63 % retained within the skin-depth:

$$\delta = \sqrt{\frac{2\rho_r}{\omega\mu_r\mu_0}} \quad (5.11)$$

where  $\rho_r$  and  $\mu_r$  are the resistivity and relative magnetic permeability of the conductor and  $\mu_0 = 4\pi \times 10^{-7} \text{ Hm}^{-1}$  is the permeability of free space. Relative

---

<sup>(12)</sup>This flow rate is equivalent to  $0.51 \text{ m}^3/\text{hr}$ . Dividing this by the cross-sectional area of the box gives the air velocity within the box as  $v_i = 0.51/(0.2^2) \text{ m/hr} = 0.004 \text{ m/s}$

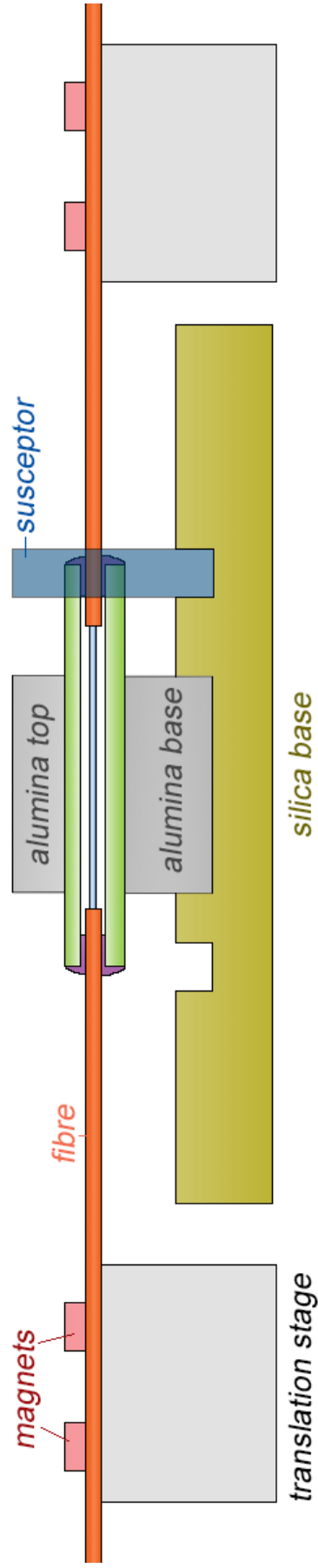


Figure 5.8: Diagram of the induction heating set up. The fibre is held using magnets to two translation stages. The bare section of the fibre (containing the FBG) passes through a kovar capillary, which is itself held within an alumina ceramic holder. The top part of the holder is optional and can be left removed without much of an effect on the experiment. Because the kovar cannot be heated beyond its relatively low Curie transition temperature, a steel heat susceptor envelops one or both ends of the capillary. The susceptor is used to radiate heat to the brazing alloy paste at the capillary ends. A 2-turn induction coil, not shown for clarity, surrounds the heat susceptor.

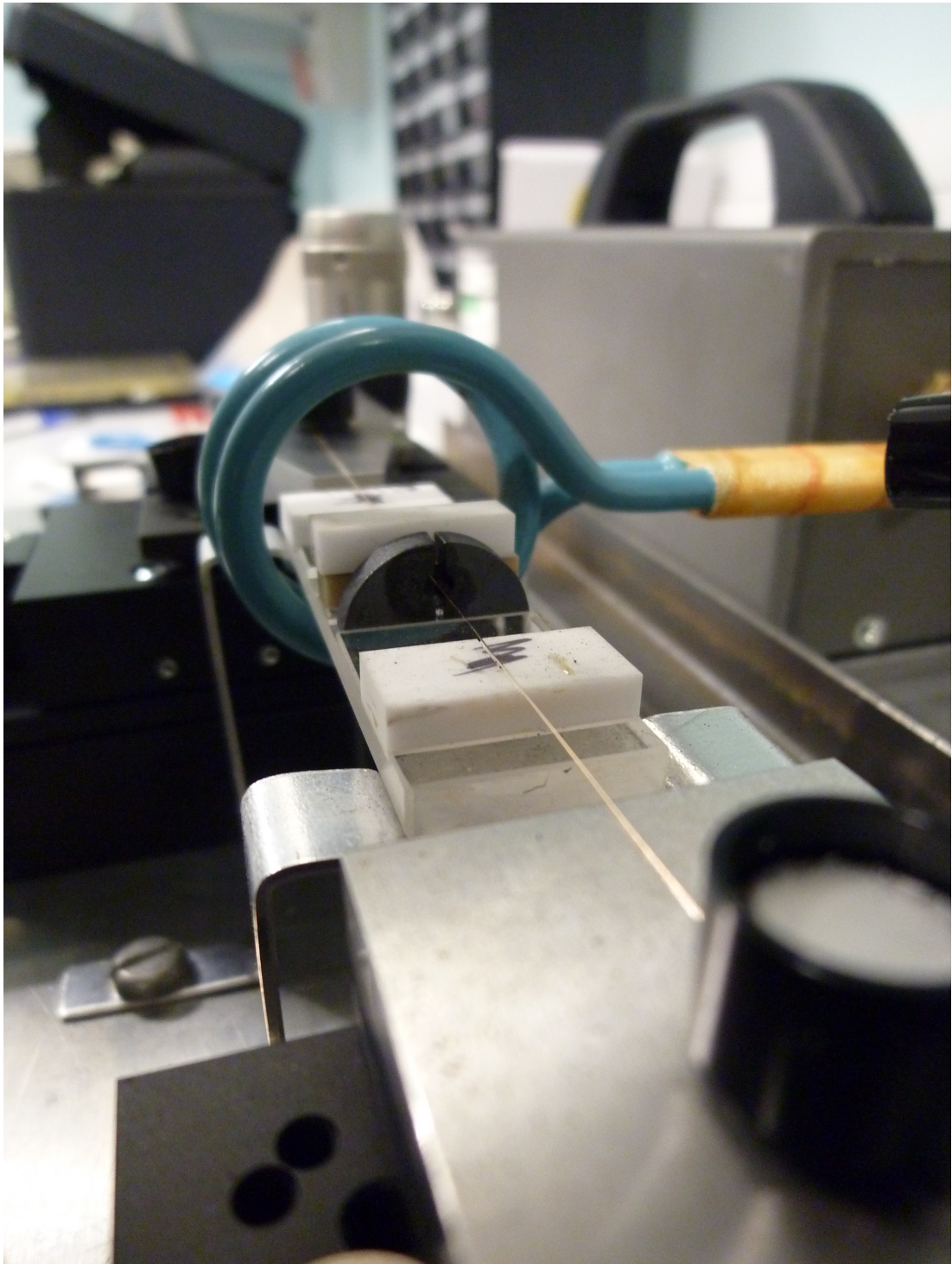


Figure 5.9: Photograph of the brazing rig set up. Visible items from the foreground include a translation stage, a magnet holding the plated fibre, the ceramic alumina and silica holders, a steel heat susceptor and the induction coil.

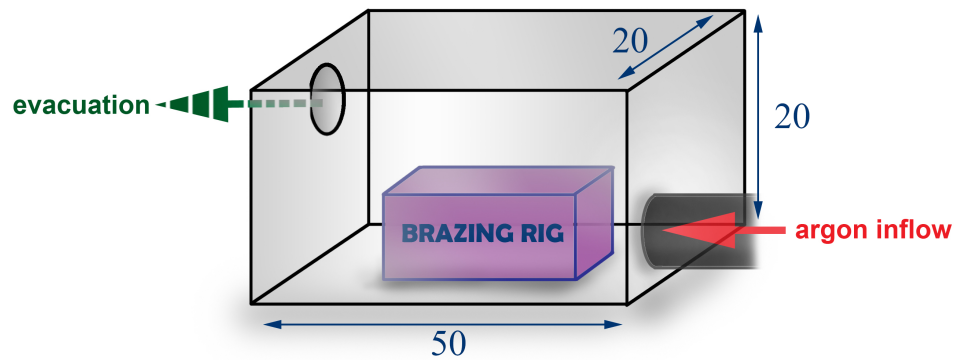


Figure 5.10: Set up of the airtight, argon-filled perspex box used to reduce oxidation of metallic parts during brazing.

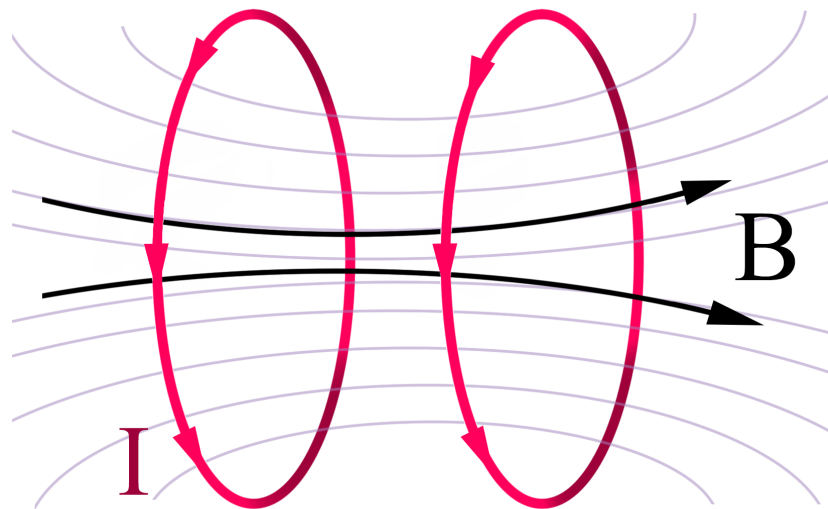


Figure 5.11: A Helmholtz coil. The current flows anticlockwise through  $N$  coils producing a magnetic field vector which points to the right in the diagram.

permeability is a measure of how well the conductor's internal magnetic field,  $\mathbf{M}$ , can be manipulated by the external field from the induction coil,  $\mathbf{H}$ . The susceptibility to magnetisation is given by:

$$\chi_v = \mu_r - 1 \quad (5.12)$$

Equation (5.11) demonstrates that large values for permeability and coil frequency reduce the skin depth, confining current to a smaller cross-sectional area,  $A$ . For a conductor of axial length,  $h$ , the overall resistance to current is:

$$R = \rho_r \frac{h}{A} \quad (5.13)$$

Confinement therefore leads to increased resistance, and hence more Joule heating. Combining the equations above yields a general form for induction heating power:

$$P = GH^2 \sqrt{\rho_r \omega \mu_r \mu_0} \quad (5.14)$$

where  $G$  is constant for a given conductor geometry and  $H$  is the magnetic field intensity at its surface<sup>(13)</sup>.

### 5.5.3.1 Curie Temperature

The kovar ferrule is ferromagnetic and is thus highly susceptible to magnetisation ( $\chi_v > 1000$ ). Magnetisation arises from an excess of electrons with spin components biased in one direction, as shown in figure 5.12. The spin and charge of each electron results in a small magnetic dipole moment, the summation of which produces an overall internal magnetic field  $\mathbf{M}$ . The dipoles in the ferromagnet align with external  $\mathbf{H}$  fields to minimise energy and retain their alignment even when

---

<sup>(13)</sup>Permeability is often assumed to be independent of the location within the ferromagnet and the strength of the applied field strength, but this is actually a poor assumption. Ferromagnets contain microscopic domains, each with a distinct permeability [PB58]. Applied fields can therefore cause very sudden, step-like flips for dipoles in each domain independently. The result is that the overall magnetisation has step-like and extremely rapid changes [CG09]. These rapid changes enhance the skin effect, yielding Eddy currents which are stronger than those predicted with classical formula. Small ferromagnet samples with large domains in particular can thus have their induction heating rates underestimated.

the external field is switched off.

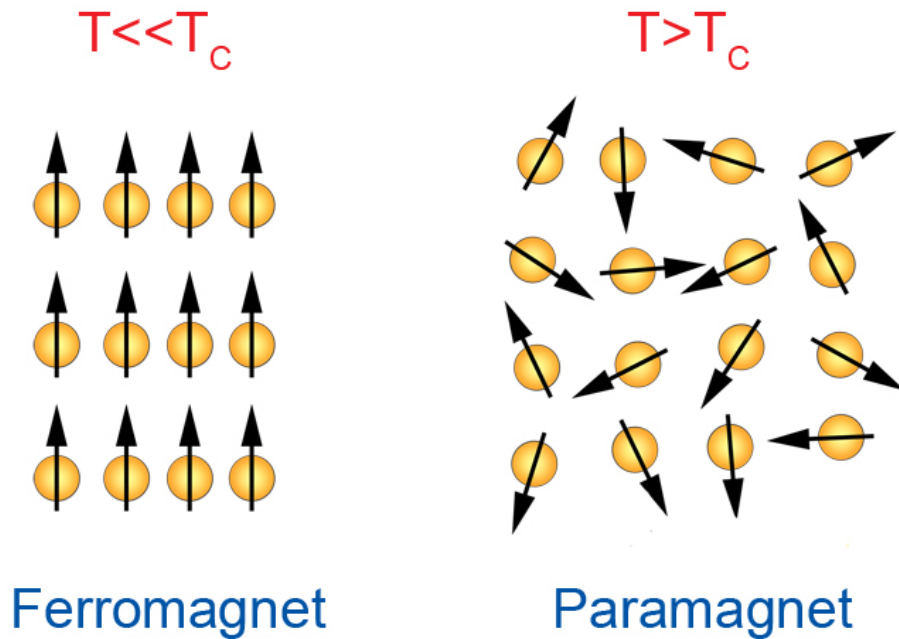


Figure 5.12: Diagram showing aligned magnetic dipole moments in a ferromagnet (below the Curie temperature) and the disordered arrangement of dipole moments in a paramagnet (above the Curie temperature).

Heating reduces electron spin alignment, as shown in Figure 5.12. As illustrated in figure 5.13, magnetisation in the ferromagnet reduces gradually as it is heated and  $\chi_v \rightarrow 10^{-5}$ . Above the Curie temperature,  $T_C$ , dipole moments are disordered, and the material becomes paramagnetic.  $\mathbf{H}$  fields can still induce dipole alignment, but it is only temporary. Ferromagnetism can be reinstated by cooling the material to below  $T_C$ .

This reduction in magnetic permeability by an order of  $10^3$  causes a 30-fold increase in the conductor's skin depth. This increases the volume in which the electrons can flow, drastically reducing Joule heating and in turn making it difficult to heat the ferromagnet beyond  $T_C$ <sup>(14)</sup>.

<sup>(14)</sup>While it is true that there are also thermally induced changes in a ferrule's geometry and resistivity, these are of the order  $10^{-6}$  and  $10^{-8}$  over a 1000 °C range respectively. It is the  $10^3$  change in permeability at the Curie temperature which causes the greatest change in power dissipation.

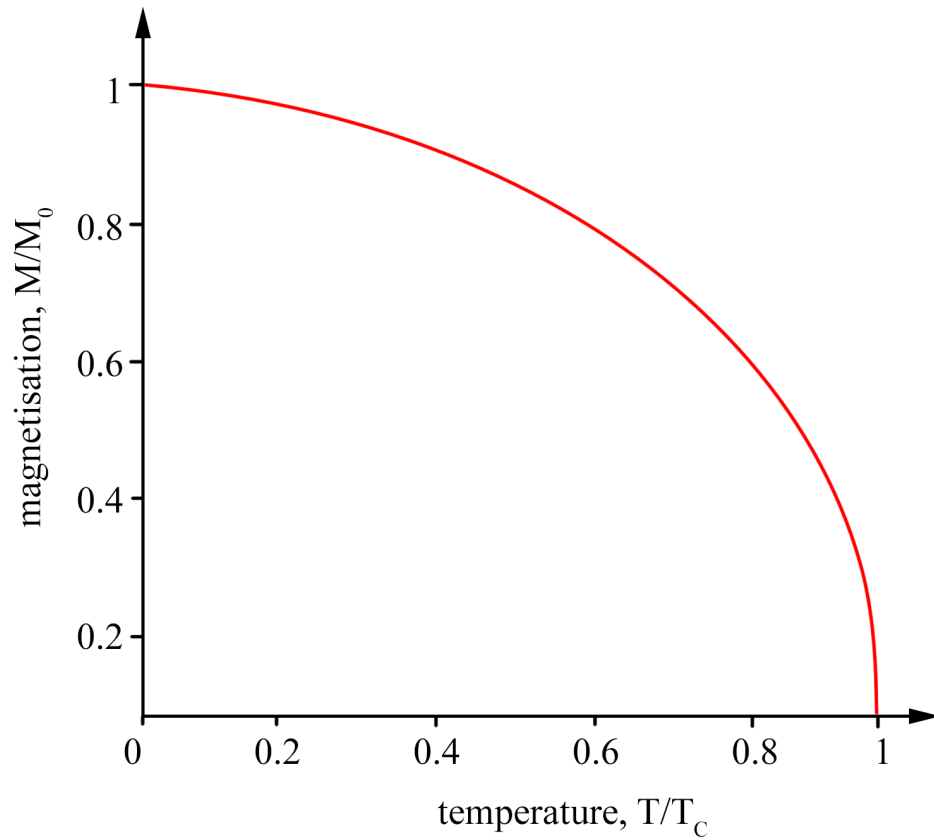


Figure 5.13: Plot of the magnetisation (relative to that at 0 °C) vs temperature (relative to  $T_C$ ) for a typical ferromagnet. Note that the loss of magnetisation is gradual, but at the Curie temperature, magnetisation is drastically reduced as the material becomes fully paramagnetic.

### 5.5.3.2 Hysteresis

Extra induction heating effects occur because a ferromagnet's magnetisation,  $\mathbf{M}$ , scales non-linearly with the external field,  $\mathbf{H}$ . In figure 5.14 a 1-dimensional case is illustrated. Gradually changing the direction of the external field results in a remanent magnetisation,  $m_{rs}$ , or coercivity  $h_c$ , at  $H=0$ . Both of these parameters, hence the amount of hysteresis, scale with permeability.

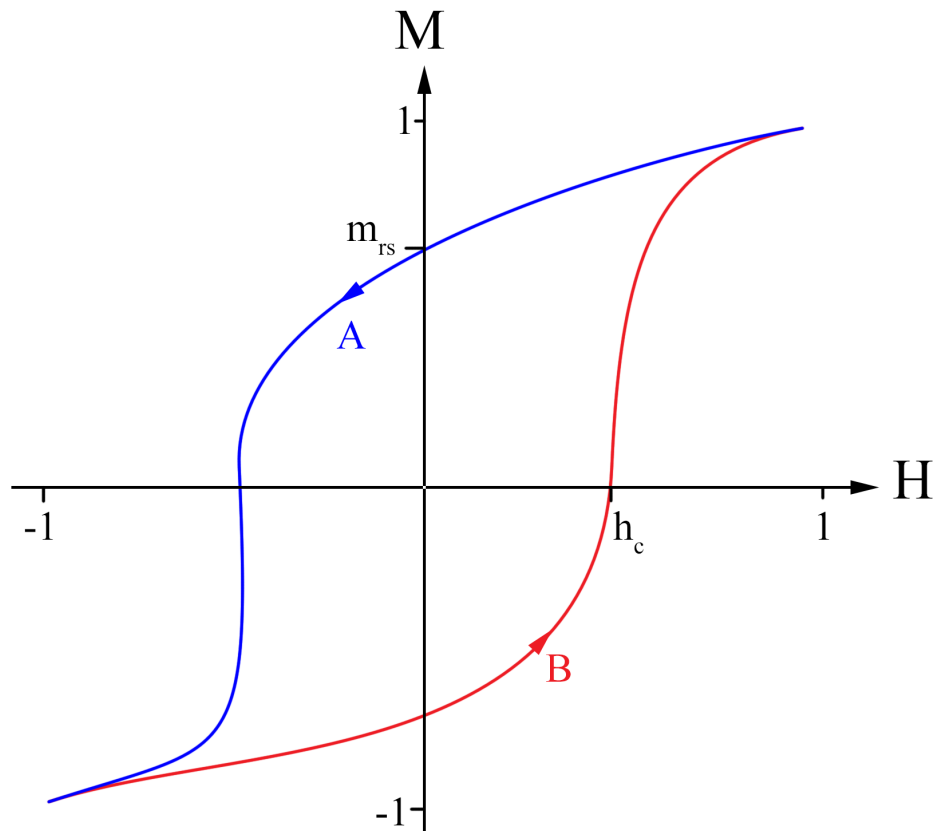


Figure 5.14: For one-dimension (i.e.  $\mathbf{M} = M$  and  $\mathbf{H} = H$ ), a plot of magnetisation,  $M$ , of a ferromagnet vs external field,  $H$ , displaying hysteresis. The path labelled A is followed for reduction in the  $H$ -field and B is followed for increases.

As the induction coil supplies an  $\mathbf{H}$  field, magnetic domains in the ferrule expand along the direction of  $\mathbf{M}$ . During one cycle of the  $H$ -field, the friction between these domains and adjacent defects generates heat. The domain expansion, hence the heat generated, is proportional to the area within the hysteresis loop. Hysteretic heating, like Joule heating, is dramatically reduced when the ferromagnet reaches the Curie temperature.

### 5.5.4 Cooling

During and after brazing, the capillary is subject to heat losses via conduction, radiation and convection. If the capillary's temperature is  $T$ , and ambient temperatures of the air and alumina holders are  $T_S$ , then the total heat intensity lost is given by:

$$I_h = \frac{k\Delta T}{d} + h_c\Delta T + \epsilon_e\sigma_B(T^4 - T_S^4) \quad (5.15)$$

where  $\Delta T = T - T_S$ . The high thermal conductivity of alumina,  $k = 25 \text{ Wm}^{-1}\text{K}^{-1}$ , allows the first term in this equation, conduction, to dominate at low temperatures [SA00]. The very low value of the convective heat transfer coefficient,  $h_c = 10 \text{ Wm}^{-2}\text{K}^{-1}$ , tends to make the second term, convection, negligible in this set up. While convection can be assisted by local air currents, only natural convection is described above, because the air in the induction-brazing chamber is pumped at a slow enough rate to avoid turbulence<sup>(15)</sup>. The Stefan-Boltzmann constant,  $\sigma_B = 5.67 \times 10^{-8} \text{ Wm}^{-2}\text{K}^{-4}$  and kovar's emissivity  $\epsilon_e \approx 0.8$  characterise the efficiency with which heat is radiated in the final term. Radiation dominates at high temperatures due to its fourth-power dependence<sup>(16)</sup>.

### 5.5.5 Induction Heating Summary

Induction heating rapidly heats ferromagnets using the friction between magnetic domains and Joule heating. Both of these effects are drastically reduced once the ferromagnet reaches its Curie temperature. At low temperatures, thermal conduction of the kovar capillary to the alumina holder inhibits its heating, while

---

<sup>(15)</sup>A Reynold's number greater than 2000 would suggest air flows are turbulent. The Reynold's number is given by  $Re = \frac{v_i L}{\nu}$  where argon's kinematic viscosity  $\nu = 1.3 \times 10^{-5} \text{ m}^2/\text{s}$ . The short length scale of the perspex chamber,  $L = 0.5 \text{ m}$ , combined with the low velocity of the argon gas,  $v_i = 0.004 \text{ m/s}$  mean that  $Re < 200$  and so forced convection can be neglected.

<sup>(16)</sup>This picture of heat gains and losses is made slightly more complicated by the fact that the heat energy required to elevate a material's temperature is dependent on its heat capacity. In general, materials become more difficult to heat up as they get hotter. Kovar's specific heat increases by about 50 %, from 0.44 to 0.65 J/gK, between 20 and 430 °C [Mat13]. Beyond this temperature, specific heat remains almost constant up until the kovar melts. The capillary's induction heating rate will thus be reduced at 430 °C, not just because of the Curie transition, but also due to the increase in heat capacity.

at higher temperatures, radiative heat losses begin to dominate.

Induction heated components usually reach thermal equilibrium at some point beyond the Curie temperature. This places a limit on the maximum temperature the ferrule can realise, protecting the housed FBG from thermal damage. Heat can instead be concentrated to the brazing points at the ferrule ends by using steel heat-susceptors (as outlined in §5.5.2).

## 5.6 Induction: Temperature Characterisation

Temperatures in the induction set up were empirically verified using high-temperature regenerated gratings [BCSC08]. This was done to ensure that bare type-I FBGs would not be thermally damaged during packaging. To use the regenerated gratings as thermometers, shifts in the Bragg peak,  $\lambda_B$ , were characterised with oven temperature,  $\Delta T$ . The relationship is shown in figure 5.15.

Once characterised, the grating was slotted through the capillary, as shown in 5.16. Temperatures were monitored at two different points along the ferrule during induction—at the end and at the centre, both with and without steel heat susceptors present. These four variations, shown in figure 5.17, provided extensive information on the evolution of temperature during brazing. For all the arrangements shown, induction current was varied from 0 to 200 A in 20 A steps for 25 s heating time. Current was then kept constant at 200 A while heating time was varied between 5 and 35 s in 5–10 s steps.

### 5.6.1 Split Gaussian Algorithm

In early attempts to characterise the induction set up, it was found that non-uniform heating of the gratings made Bragg peak detection difficult. This is because the heating of one half of a grating can produce two distinct Bragg peaks as shown in Figure 5.18.

An algorithm was developed to locate the two peaks. Both peaks were roughly located by taking a Gaussian fit of the entire spectrum. This gave an average peak wavelength,  $\lambda_{med}$ , as shown in figure 5.19. The wavelengths above and below

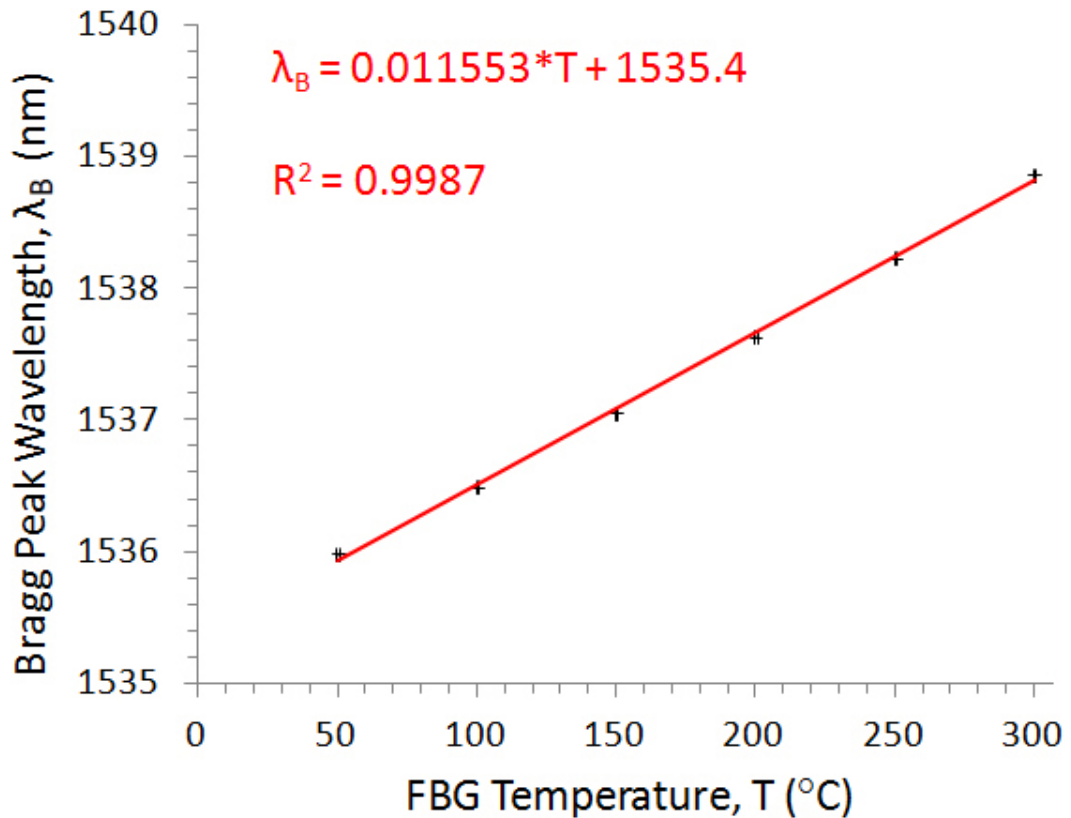


Figure 5.15: Dependence of the Bragg wavelength,  $\lambda_B$ , on FBG temperature,  $T$ , for a regenerated grating written in G1 fibre. At 1535 nm, the thermal sensitivity was 11 pm/°C. The correlation coefficient of the linear fit is 0.9987. The estimated error in the FBG temperature measurement was 1 °C.

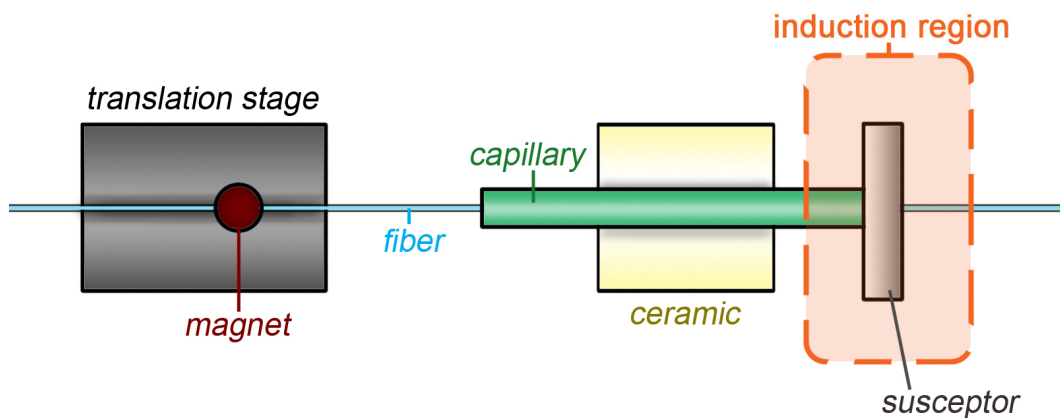


Figure 5.16: Aerial view of the set up used to induction braise the fibre into a kovar ferrule. Ferrules rested on an alumina ceramic base with a steel heat susceptor enveloping one end. The fibre was slotted through the ferrule and held under tension by magnets via a translation stage.



$\lambda_{med}$  were then discarded so that secondary Gaussian fits could locate  $\lambda_{min}$  and  $\lambda_{max}$  respectively. The algorithm was simple, independent of any threshold values and allowed heat differentials to be quantified.

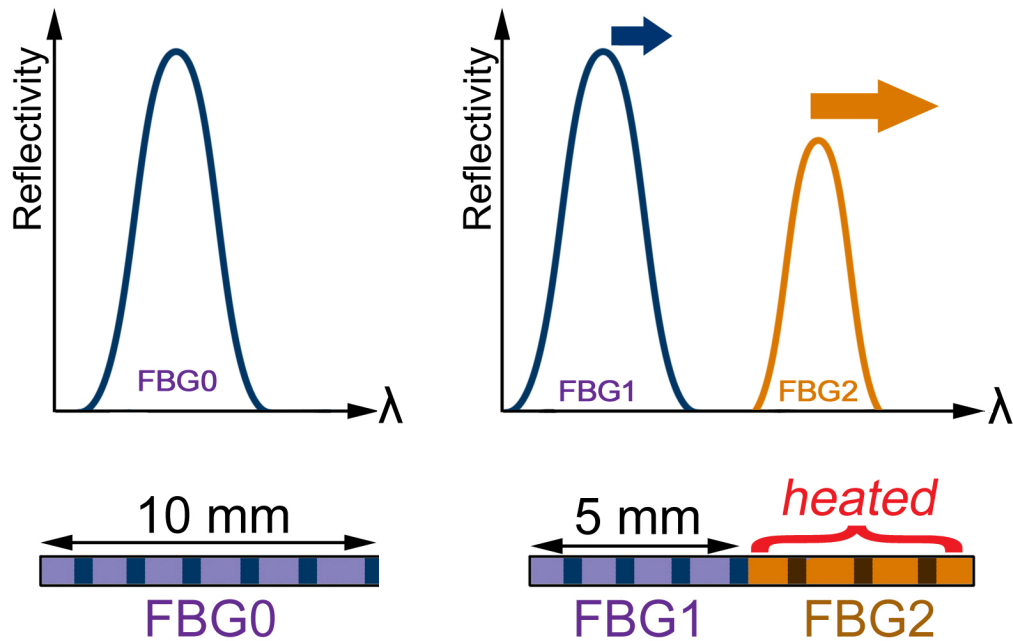


Figure 5.18: The effect of heating only half of a 10mm FBG. The 10mm FBG is equivalent to two 5mm FBGs side-by-side, so heating one FBG more than the other will cause it to red-shift further.

A demonstration of the split Gaussian algorithm, applied to experimental data, is shown in figure 5.20. When half of a regenerated grating is heated using a suscepter, the Bragg peaks split and are fitted to two Gaussians as shown. Broadening of the peaks also occurs as a consequence of thermally induced chirping of the grating.

### 5.6.2 Temperature Characterisation: Results

Figure 5.21 provides an overview of the temperature evolution for three of the heating configurations (these configurations are drawn in figure 5.17 and labeled using the same notation). Induction heating was performed for 35 s at a current of 200 A in all three cases.

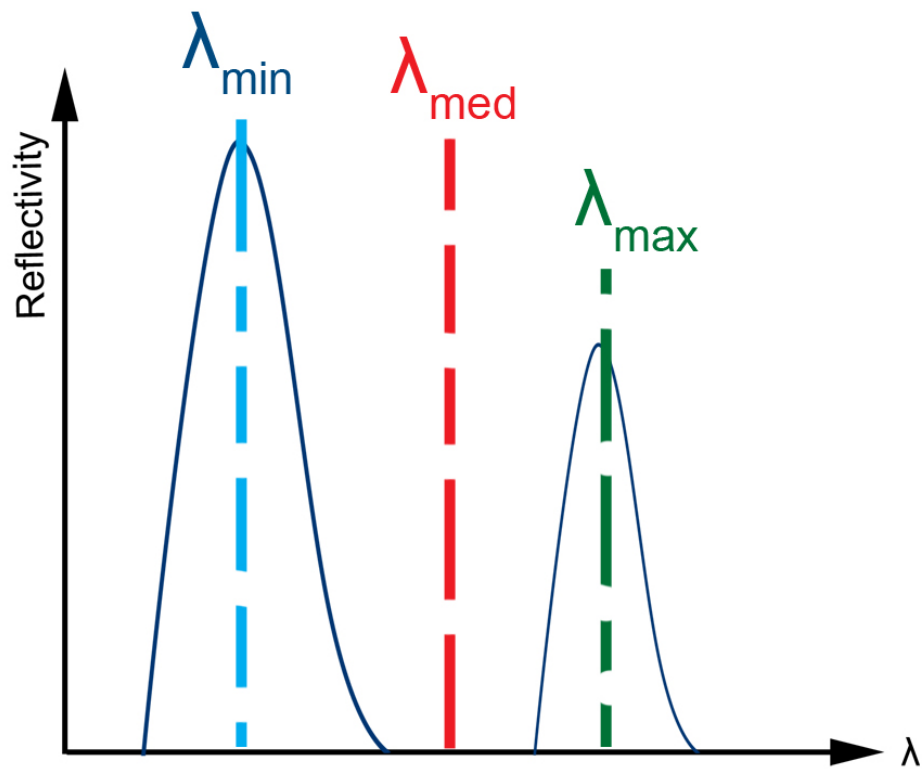


Figure 5.19: Method of detecting the peak values of both Bragg reflections. First an overall average of the spectrum is taken to give  $\lambda_{med}$ . The average intensity below and above this medium value are then used to find  $\lambda_{min}$  and  $\lambda_{max}$ .

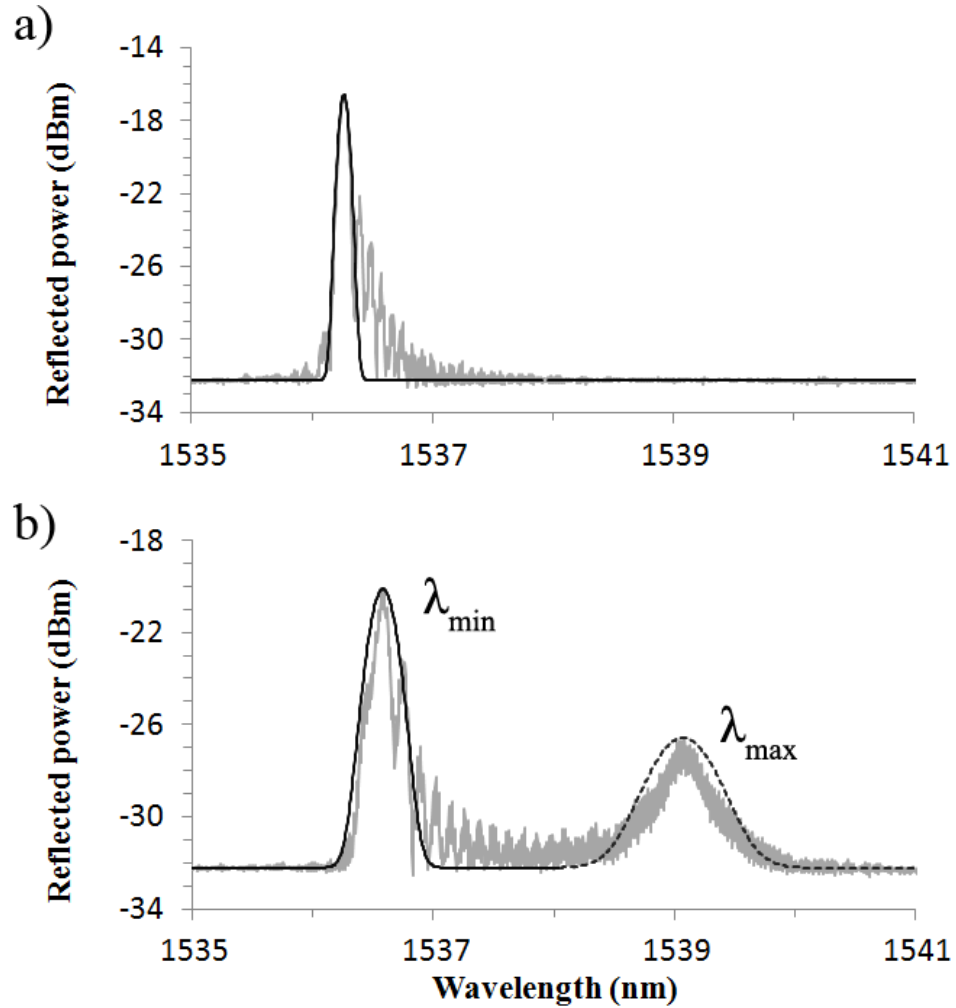


Figure 5.20: Demonstration of the split Gaussian algorithm performed on a heated regenerated grating. Light grey lines show the spectra obtained experimentally, black lines show Gaussian fits. a) the grating is unheated and so  $\lambda_{min}$  and  $\lambda_{max}$  overlap. b) Heating half of the 10 mm grating using a 4 mm wide susceptor causes the peak to split into two. Note that thermally induced grating chirp leads to broadening of the peaks.

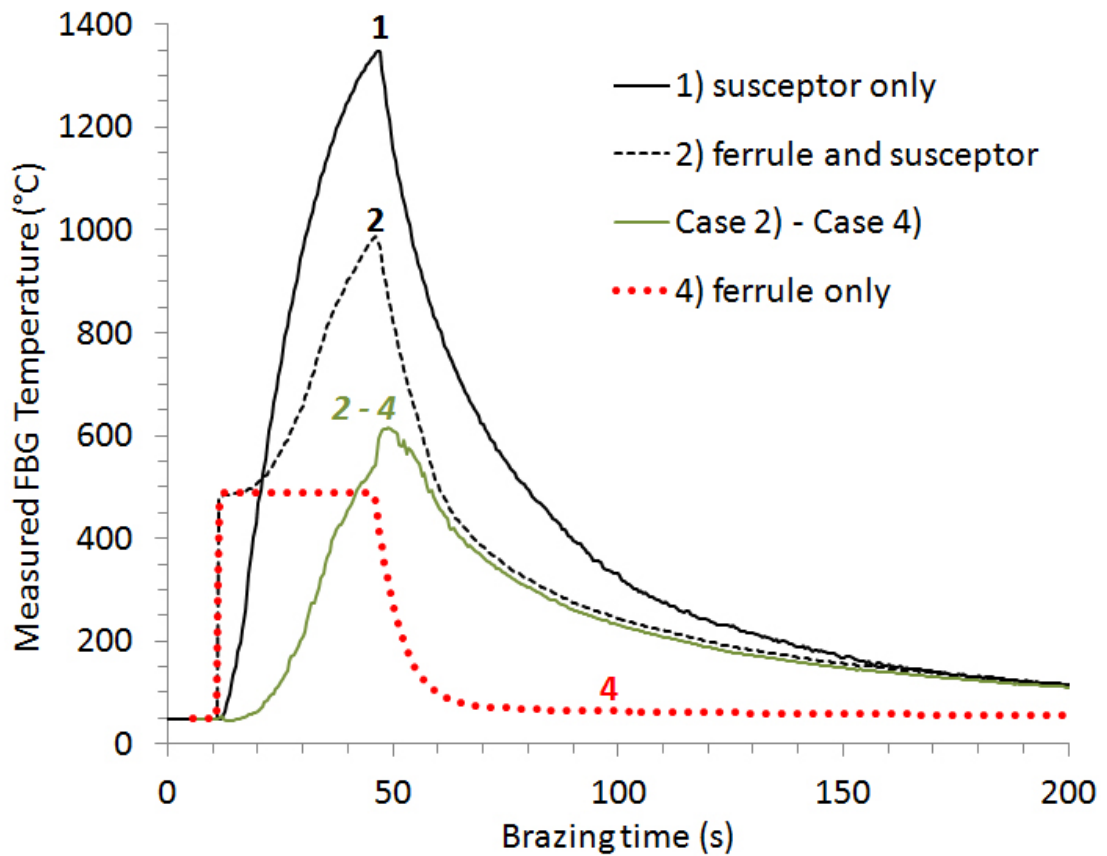


Figure 5.21: Overview of the temperature evolution of three of the heating configurations for 35 s with a 200 A coil current. In case 1, the bare fibre were exposed directly to heat susceptor radiation. In case 4, maximum ferrule temperature was limited in the absence of a heat susceptor. This was because of the Curie transition in the kovar ferrule. Placing the susceptor back in place, however, allowed the temperature limit to be surpassed, as shown in case 2. In this graph, the temperature difference between cases 2 and 4 is also shown — this shows that the ferrule is capable of shielding the fibre from the majority of the susceptor radiation.

### 5.6.2.1 Sole Capillary Heating

As shown in figure 5.17, the temperature in a sole capillary (case 4) rose rapidly to 480 °C, before saturating due to the Curie transition. Figure 5.22 shows that a dramatic reduction in coil current is required to prevent this temperature saturation from occurring.

Finite element models (FEMs) of induction heating were set up and used to verify this result and extend temperature measurements. A full description of the modelling process can be found in appendix A.4. Figure 5.23 shows a comparison between the FEM and experimental results. The model agreed quite well for the first 25 s — induction heating was indeed extremely rapid, followed by a reduced heating rate beyond the Curie transition. This confirmed that the wavelength shifts measured by the regenerated gratings were temperature dependent and not due to anomalous strains <sup>(18)</sup>. There were several notable differences between the modelled and experimental temperature profiles during cooling, simply due to the incomplete modelling of cooling mechanisms such as convection. Addressing these issues and implementing temperature-dependent material properties may further improve agreement.

### 5.6.2.2 Sole Susceptor Heating

While the temperature of the capillary saturated quickly, the result was very different for the heat susceptor, as shown in figure 5.24. Susceptor temperatures did not saturate mainly because of their higher surface-area to volume ratio. Temperatures reached up to 1200 °C for a 200 A current. Under these conditions, the steel susceptor glowed a visible yellow, a rough visual confirmation that temperature was accurately measured.

There were initially concerns that oxidisation of the susceptors may affect their ability to radiate heat. To investigate this, heating schedules were obtained for three heat susceptors of differing geometry and age, shown in figure 5.25. The

---

<sup>(18)</sup>The literature confirms that any magnetostrictive and magnetic-induced-bending of the capillary would only produce enough strain to induce picometer wavelength shifts in the Bragg wavelength [RIBR95, Bre96], much lower than the nanometer shifts measured.

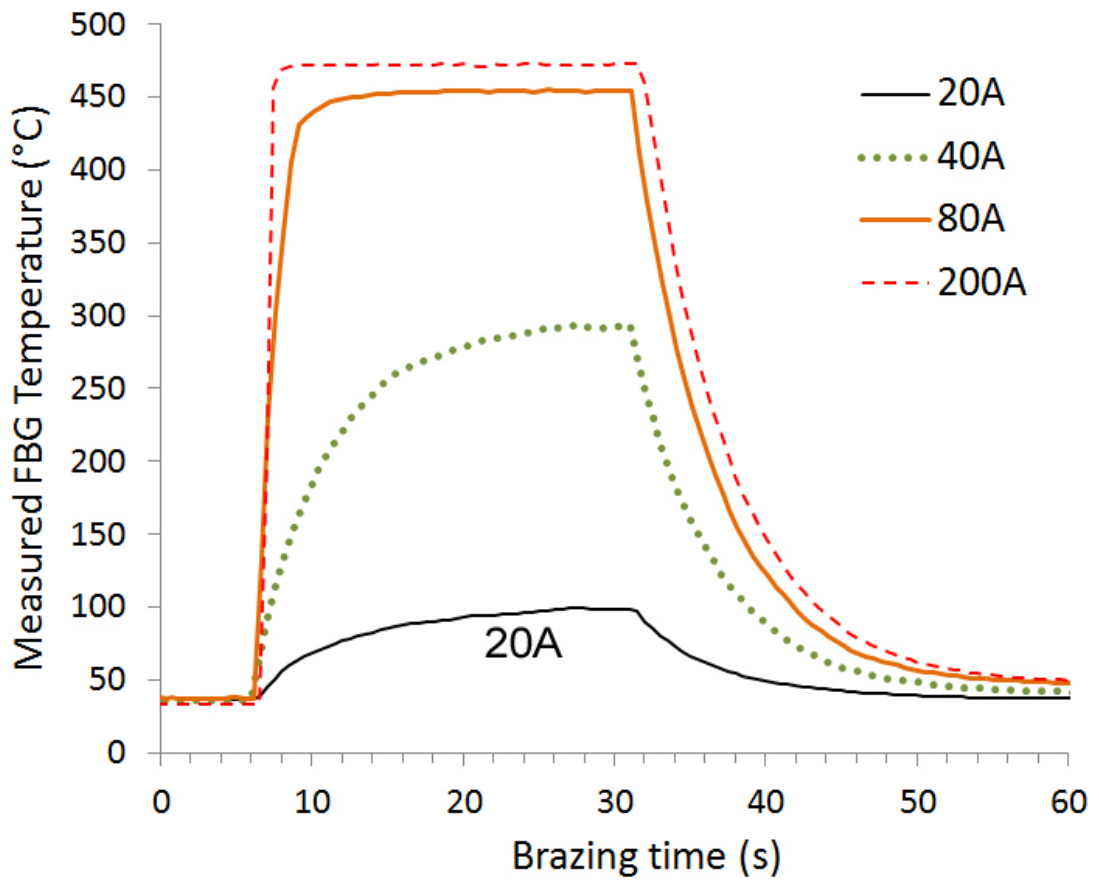


Figure 5.22: Temperature evolution for a sole capillary under induction heating for 25 s at currents between 20 and 200 A. Note the very minor increase in maximum temperature between 80 A and 200 A, due to the Curie transition.

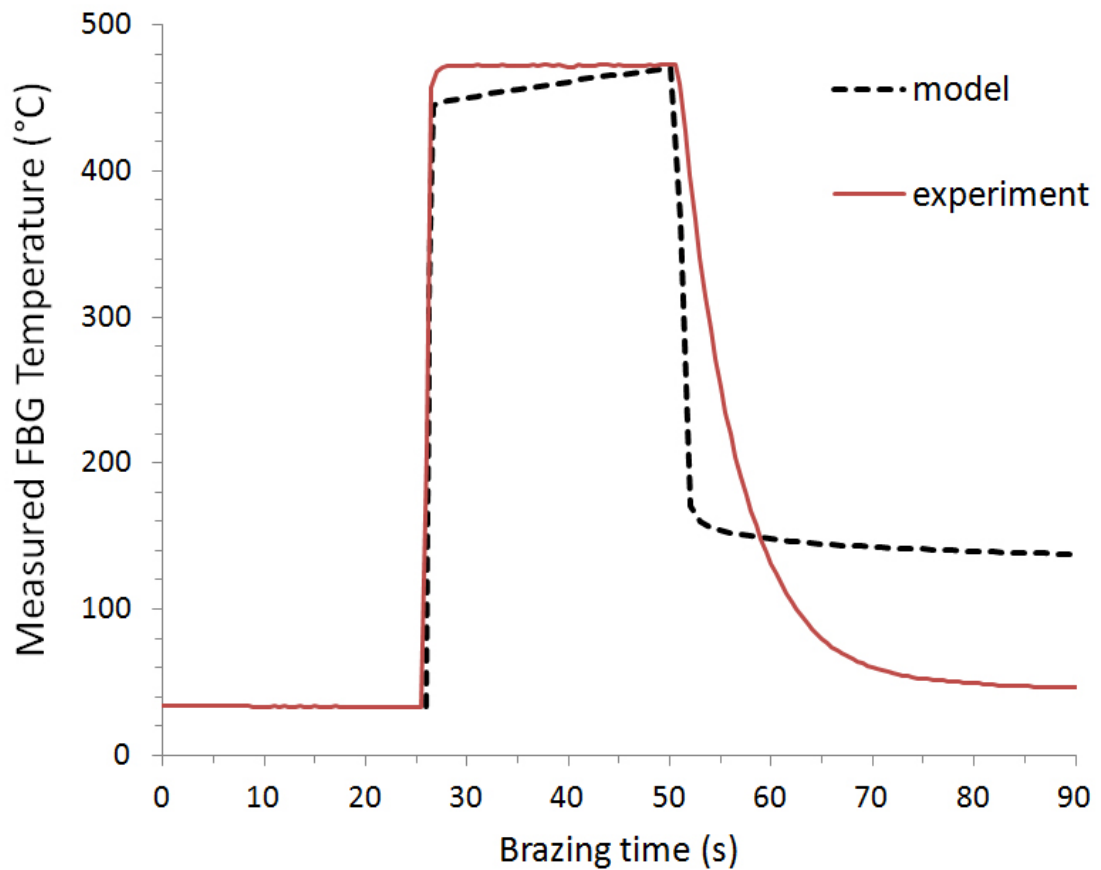


Figure 5.23: Comparison of the temperature evolution of the model and experiment for 25 s heat induction of a sole ferrule at 200 A. Differences between the temperature profiles occurred due to several simplifying assumptions, made by the model, about the active heating and cooling mechanisms.

maximum temperatures realised for various induction heating times and currents are shown in figure 5.26. Both 2 week and 6 month old heat susceptors displayed the same temperature profiles as brand new susceptors. Thicker steel susceptors, on the other hand, displayed significantly higher maximum temperatures as they were able to intersect with more magnetic field lines and retain more heat within their bulk. This demonstrates the importance of keeping susceptor geometry constant and the relative unimportance of the Curie transition in this case.

### 5.6.2.3 Combined Heating

When the ferrule-end temperatures were measured under susceptor radiation, it was found that they were able to surpass their usual Curie-limited temperature, as shown in figure 5.27. The 1000 °C temperatures realised are sufficient to melt

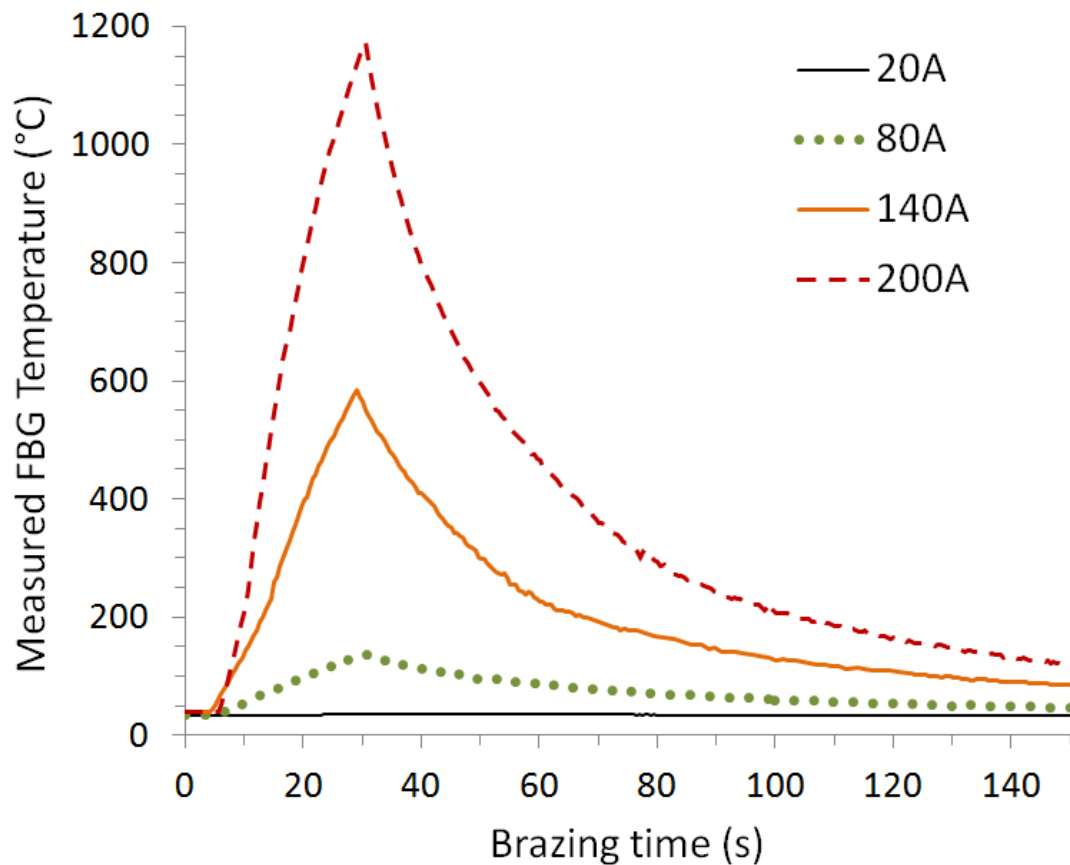


Figure 5.24: Temperature evolution for a sole susceptor heated for 25 s by an induction coil at varying currents between 20 and 200 A. Note the heating rate and maximum temperature increased with current, indicating no saturation.



Figure 5.25: Three examples of heat susceptors tested. A thicker heat susceptor than usual, an old heat susceptor which had been placed under daily induction heating for months and an untarnished, unused brand new heat susceptor fabricated in the workshop.

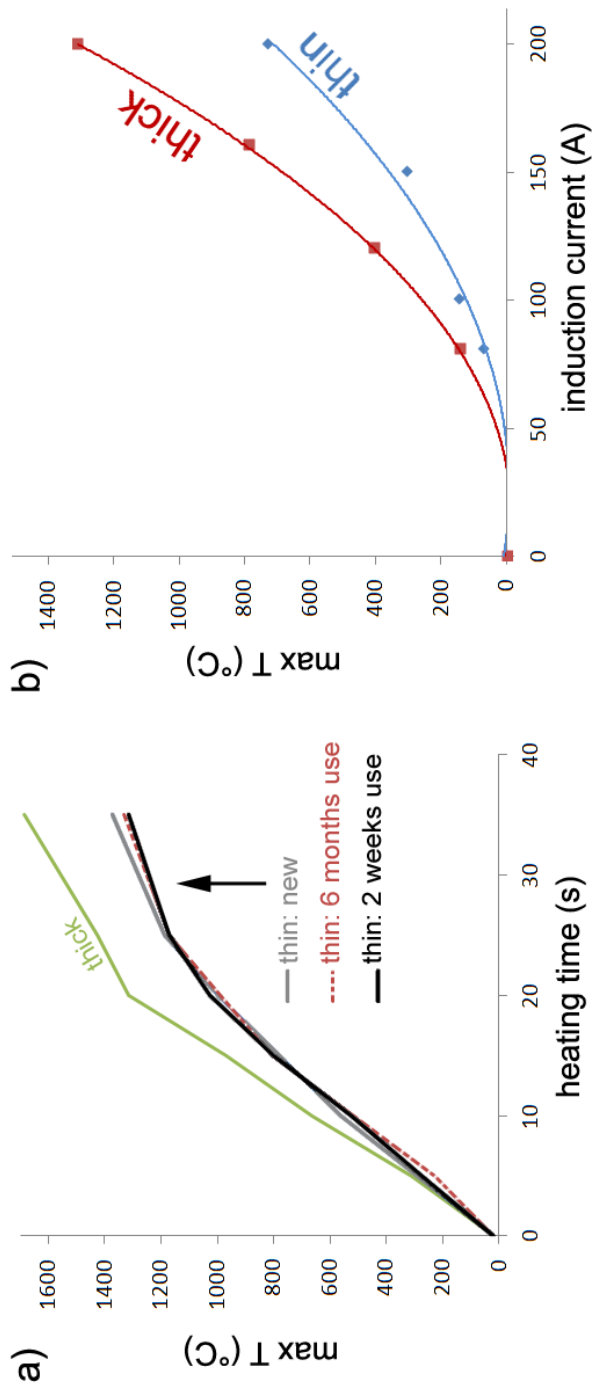


Figure 5.26: a) The maximum temperatures realised by a variety of thin and a thick heat susceptors as a function of induction heating time for a constant (200 A) current. The larger susceptor is able to reach higher temperatures because it intersects with more magnetic field lines and retains heat within its bulk. b) The maximum temperatures realised by both a thin and a thick heat susceptor as a function of induction heating current for a constant (25 s) time. Temperature follows a squared relationship with current, as defined by Ohm's law. The final points are neglected from the fit as they show temperature saturation.

even high-temperature nickel solders. During these heating schedules, it was found that the temperatures in the middle of the ferrule were almost identical to those where the susceptor was absent. This demonstrates that the susceptor was distant enough for its radiation to become negligible and that the alumina holder efficiently conducted heat away from the centre portion of the ferrule. This would reduce the heat exposure of an FBG during sensor packaging.

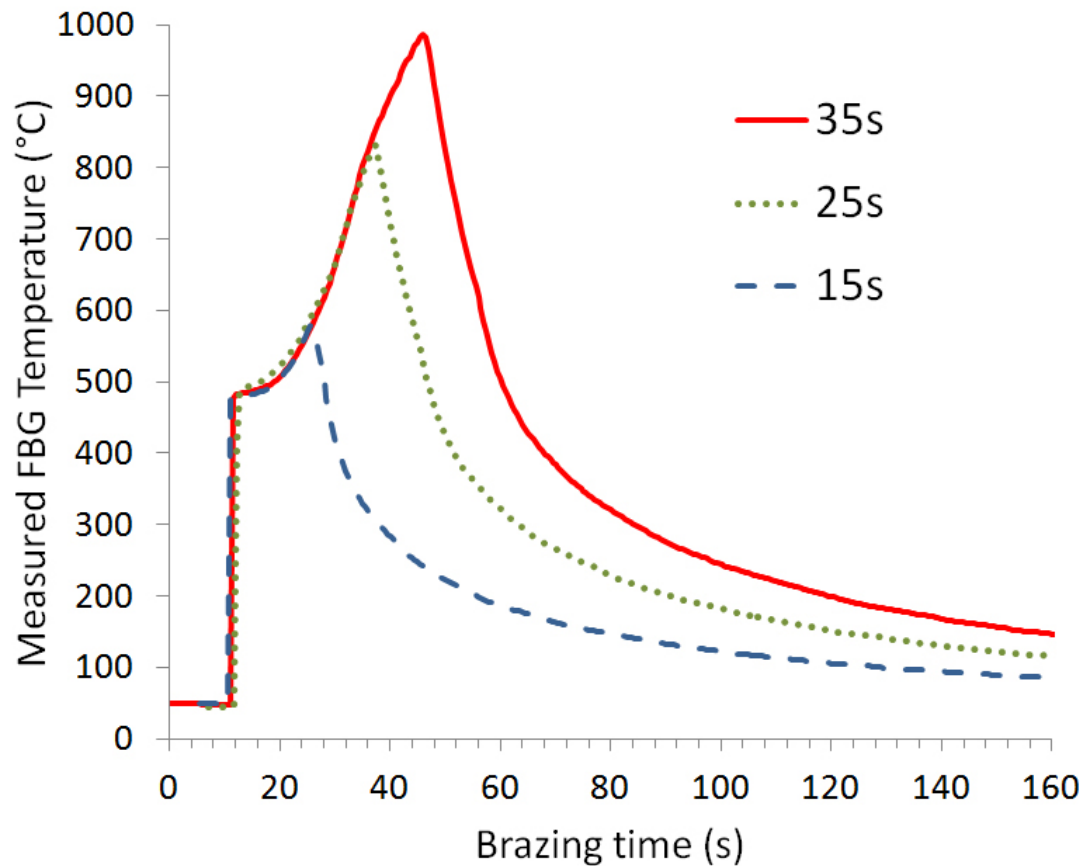


Figure 5.27: Temperature evolution for a capillary end heated directly by a susceptor heated for 200 A induction current at varying times between 15 and 35s. Note the lack of saturation and the similarity between the responses.

#### 5.6.2.4 Maximum Temperature Summary

Figure 5.28a and b summarise the maximum temperatures attained as a function of current and time in all four cases. The susceptor's temperature followed a squared relationship with current (Joule's law) implying that its cooling was minimal. Ferrule-shielded fibre temperatures almost instantly saturated at 480

°C, provided the susceptor was not directly adjacent. When the susceptor was adjacent, temperatures reached 800–1000 °C — enough to melt even high temperature brazing alloys. To reduce thermal stress, flux evaporation and solder beading, induction current could be held at low values for a longer time to allow for a more gradual heating profile [FRV05, Lee02].

### 5.6.3 Application of Results

The in-depth study of induction brazing above allowed commercial, type-I FBGs to be brazed into ferrules. The gratings were stripped of their acrylate coatings and then cleaved to 10 mm lengths. These bare lengths were spliced into the middle of a section of metallised fibre and ferrule ends were then brazed for 25 s at 200 A, one end at a time. The grating reflectivity was measured relative to a reference grating in the same fibre, to account for fluctuations in laser power and fibre attenuation.

The reflectivity of the grating during the first and second brazing cycles,  $R_1$  and  $R_2$ , is displayed along with brazing temperature in figure 5.29. During brazing of the first ferrule end, reflectivity dropped to 10% before recovering to 60%. The overall losses in the second heating cycle,  $R_2$ , were reduced — reflectivity began at 60% and recovered to a final value of 56%. This initially rapid decay in reflectivity followed by stabilisation occurs due to thermal annealing of the index modulation and is very typical of Ge-doped FBGs [BRBG97]. This experiment demonstrated that brazing standard gratings is feasible, provided the 40 % reflectivity losses are acceptable for the application.

## 5.7 Splice Strength After Heating

Because the FBG within the ferrule was spliced in, the long-term reliability of splices after heat exposure needed to be ensured. Electro-arc fusion splices are known to be a point of weakness, with fibre fracture typically occurring in the heat-affected zone [Sen85]. Splice heat treatments such as a 700 °C fire polish are sometimes used to clean the fibre surface and melt surface cracks [Yab05],

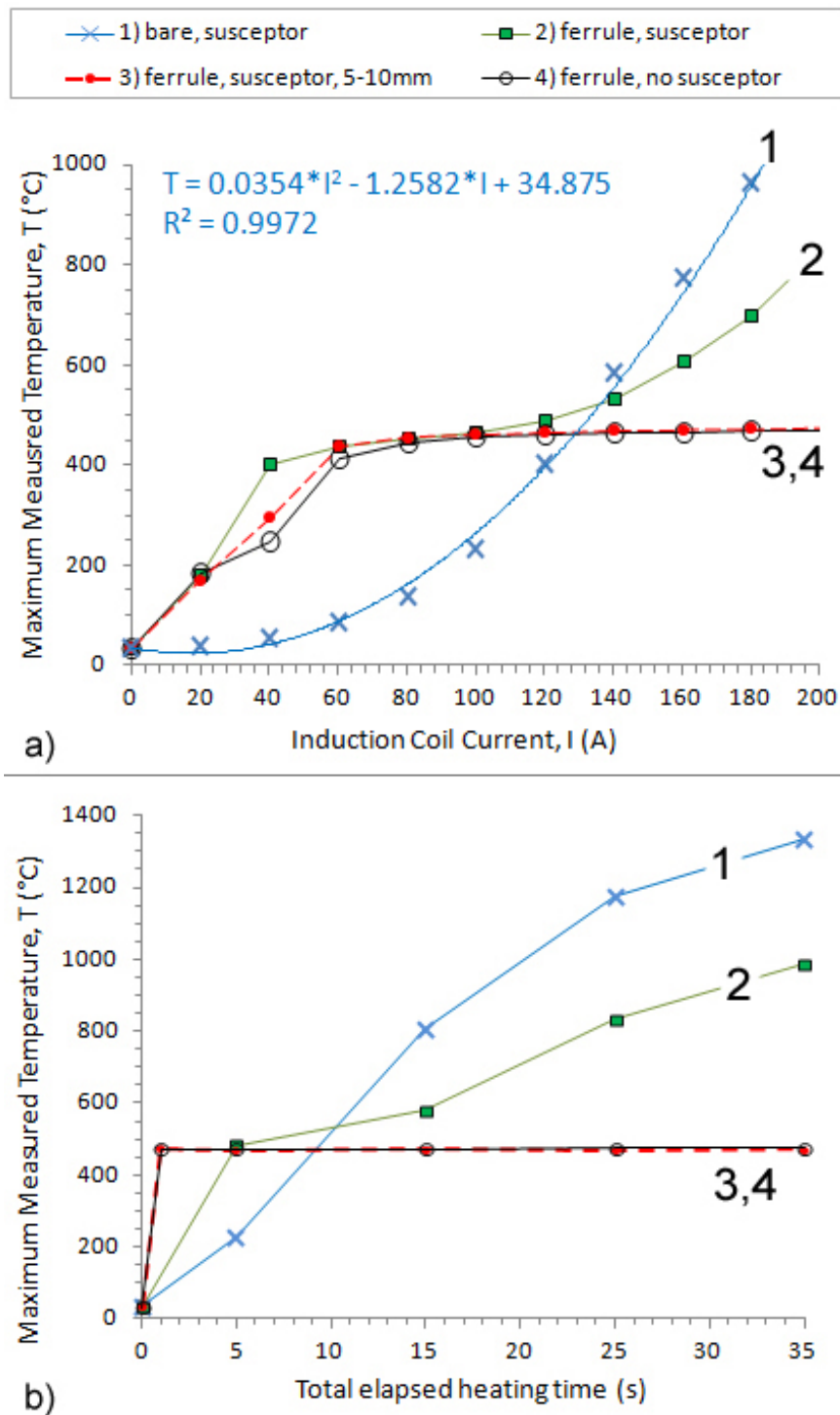


Figure 5.28: Comparison of maximum attainable temperatures in the four cases shown in figure 5.17. (a) Time was kept constant at 25 s and current was varied between 20 and 200 A, (b) Current was kept constant at 200 A and time was varied between 5 and 35 s.

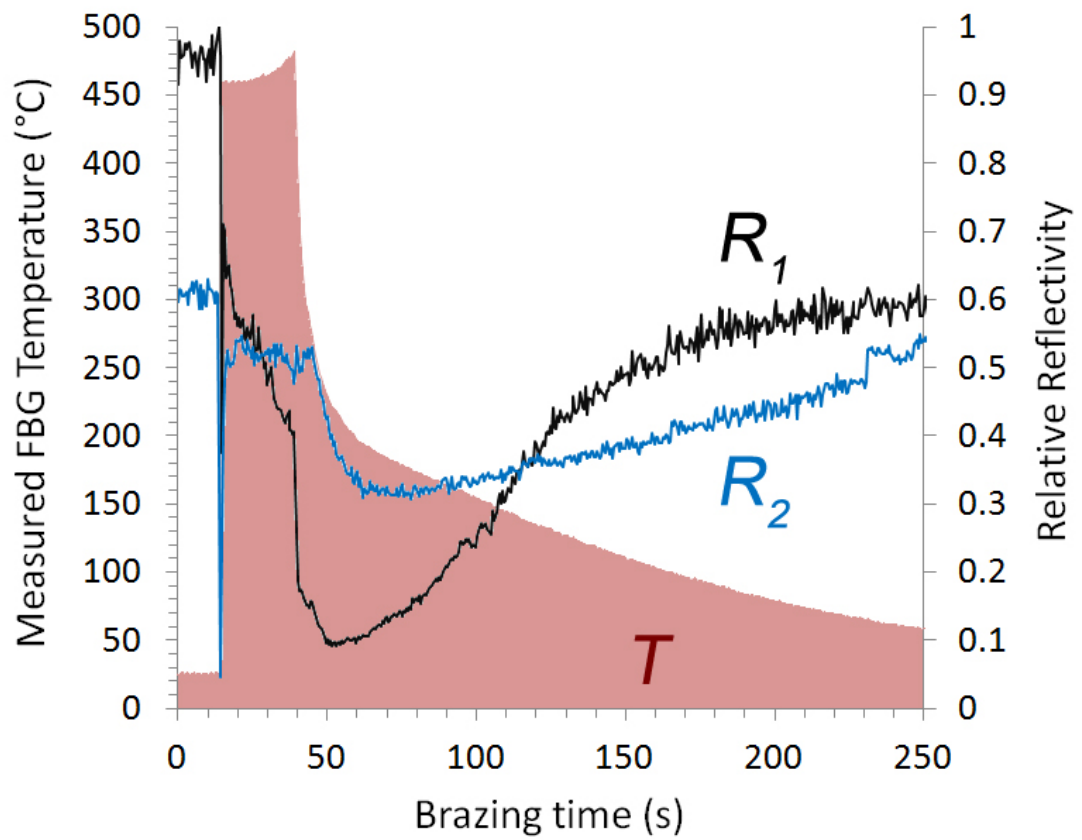


Figure 5.29: Temperature of type-I grating,  $T$ , with reflectivity during two brazing cycles,  $R_1$  and  $R_2$ , over a 25 s brazing period at 200 A. After two brazing cycles, the total decrease in reflectivity was 44%.

but the effects of prolonged heating were less clear. As such, the strength of fibre splices after exposure to temperatures up to 1300 °C was investigated.

### 5.7.1 Splicing Process

Plated fibre specimens were soaked in 63 % nitric-acid for 1 minute to remove their metallic coats. The acrylate coats of SMF-28 fibres were mechanically stripped. Fibres were cleaned with ethanol and had their ends cleaved flat. They were then inserted into a fusion splicer. A pre-fusion cleaning routine of 20 mA current for 0.1 s removed carbon underlayers and contaminants. A hot-push under 15 mA current for 3 s allowed fusion of the two fibre ends. Splice heating and breaking strength tests were then performed immediately.

Fibres were affixed to a translation stage by magnets as shown in figure 5.30. The spliced region was enveloped by a steel heat susceptor, which was in turn heated by an induction coil, operating at 200 A. Heating time was varied from 0 to 35 s, exposing the splices to the maximum temperatures shown in figure 5.31. Splices were then allowed to cool for 3 minutes. The length of fibre was then removed from the heating rig and the points labelled A and B in figure 5.30 were clamped using screws and moved apart by a translation stage. Interrogation of a type-I FBG in the same fibre line was used to infer the strain at which the splices failed at.

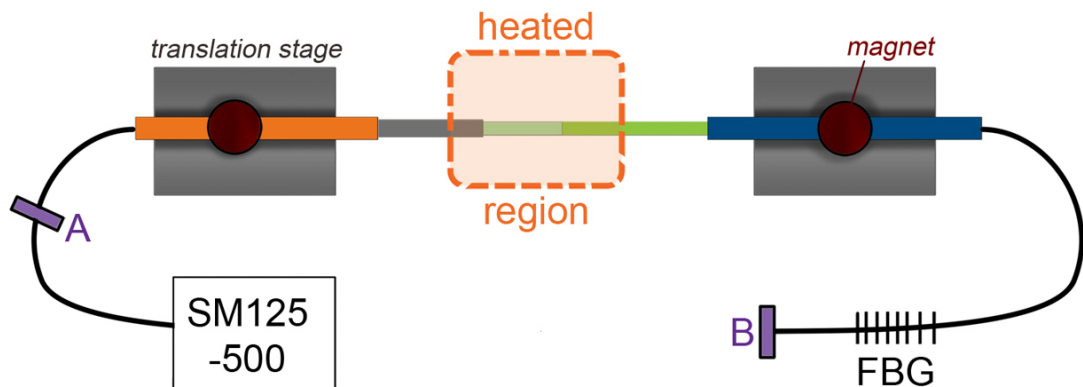


Figure 5.30: Susceptor-induction coil set up used to heat splices. Points A and B were later clamped and moved apart by a translation stage, while the sm125-500 interrogation unit measured strain in the labeled FBG.

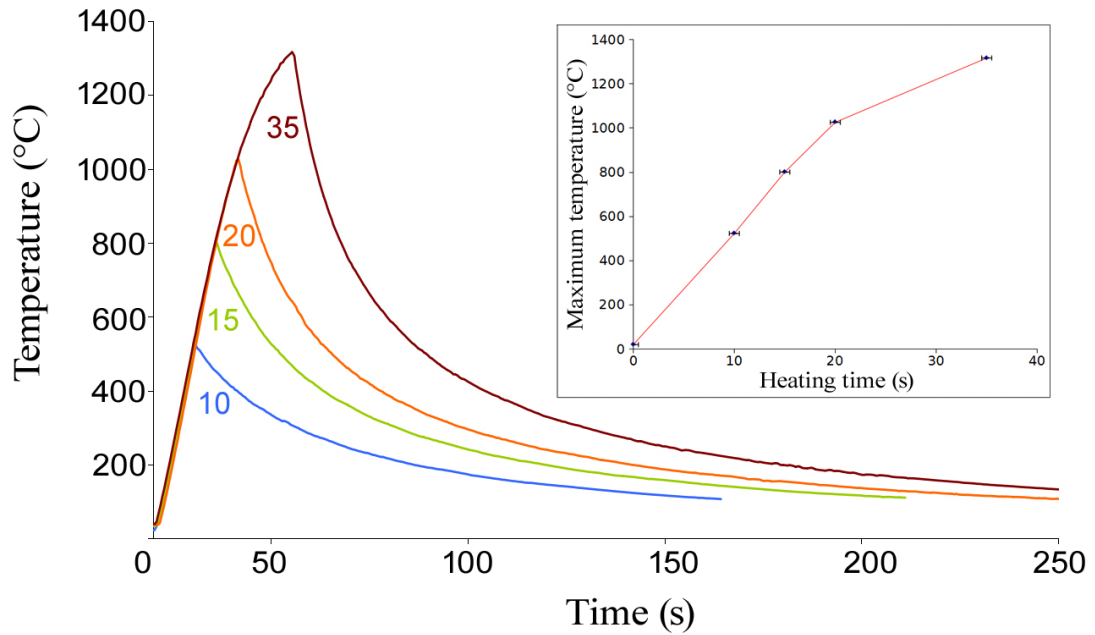


Figure 5.31: Heating profiles for 10, 15, 20 and 35 s induction heating times at 200 A and 370 kHz. Shown inset is the heating time vs maximum temperature relationship, which is linear until saturation due to increased radiative cooling

### 5.7.2 Breaking Test Result

Fibres were strained at  $0.4 \text{ m}\epsilon/\text{s}$  to failure 40 times for each temperature point to ensure statistical significance. Repeated breaking at the splice implied this was always the largest flaw. A selection of breaking strength distributions are shown in figure 5.32, along with a typical strain profile. Splices showed a clear decrease in strength with prolonged heat exposure.

The average splice breaking strength as a function of maximum temperature exposure is shown in figure 5.33. Heating to  $500 \text{ }^\circ\text{C}$  caused almost no decrease in strength, agreeing with previous experiments performed with non-spliced fibres [And39]. Exposure to higher temperatures reduced splice strength, with a logarithmic dependence, with splices heated to  $1300 \text{ }^\circ\text{C}$  displaying an 80 % decrease in strength. This was a major problem for the capillary brazing technique described in the previous section, as splices were located at the ferrule ends beneath the susceptor.

Throughout this experiment, heating led to very little optical attenuation,

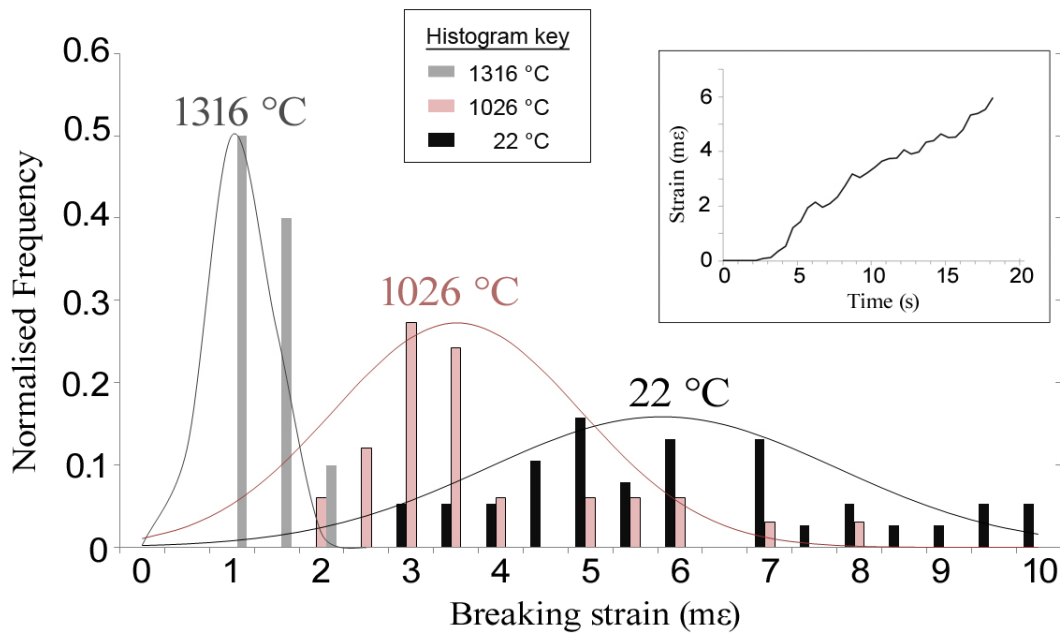


Figure 5.32: Normalised distribution of breaking strains of fibre splices heated to 1316, 1026 and 22 °C. A typical strain profile measured by the FBG during a splice stress test is shown inset.

implying that damage was restricted to the fibre surface. As the rate of hydrolysis of silica is temperature dependent, it is likely that heating lead to accelerated ageing of spliced fibre surfaces [MK88]. While temperatures  $>700$  °C may have caused crack melting, the reduction in strength shows damage mechanisms at the heat-affected zone dominate; a hypothesis further supported by the reduced distribution of strengths at higher temperatures.

Even in the unheated case, splicing reduced the strength of fibres by 90 %. This was consistent with published data, but implied there was weakening via contaminants from the splicer and also the mechanical method of acrylate stripping [KKS96]. Nevertheless, the randomized, unbiased errors demonstrated that repetition of the experiment was consistent. This provides confidence that the reduction in strength with temperature was independent of other factors such as mechanical abrasion [MKHV03].

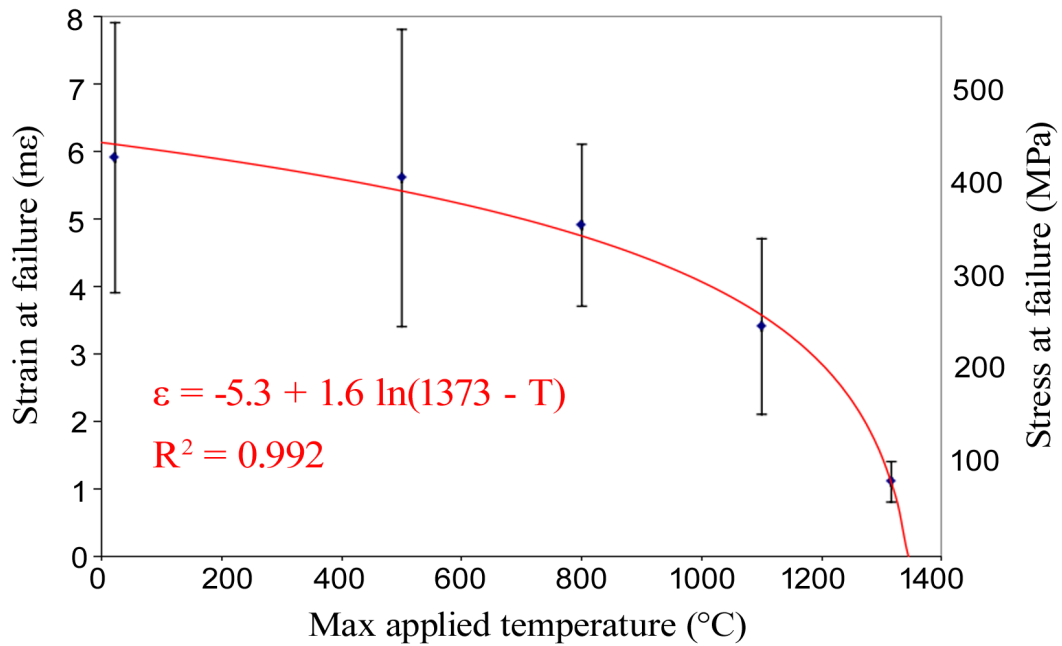


Figure 5.33: Summary of splice strength after exposure to elevated temperature, with logarithmic fit. The splice stress and strain at breakage show a clear decrease with maximum temperature exposure.

### 5.7.3 Alternative Approach

Because splice strength was reduced after heating, the capillary brazing technique had to be modified to become spliceless. In the modified method a 10 mm long section of metal was removed from the centre of a metallised fibre using nitric acid. The carbon underlayer was removed using a flame or electrical discharge (from an arc-fusion splicer) and gratings were then written into the unspliced bare section. These encapsulated FBGs have demonstrated a much higher strength after brazing (see §5.10.1). With a suitably protected FBG strain sensor in hand, the attachment to the prestressing strand could be considered.

## 5.8 Metal Welding

While brazing was suitable for packaging fibre sensors, more care must be taken when exposing prestressing strands to high-temperature processing. This section outlines prestressing steel production in more detail, to demonstrate why localised metal-welding techniques are preferred over brazing when bonding fibres to pre-

stressing strands.

### 5.8.1 Steel phase diagrams

Steel is produced by adding carbon to molten iron. Steel's phase diagram is shown as a function of carbon content in figure 5.34. As steel cools from a melt, crystals made up of iron allotropes become interlaced with various other iron-carbon compounds. Each of these crystal mixtures has a designated name. Austenite, for example, is a solid mixture of gamma-ferrite and pure carbon, while pearlite is a mixture of alpha-ferrite and cementite ( $\text{Fe}_3\text{C}$ ). Prestressing steels have a low (0–2 %) carbon content, and so cool to a pearlite preform.

The type of steel produced is also highly dependent on kinetics, or the cooling rate. An illustration of a continuous cooling transformation (CCT) diagram for low-carbon steel is shown in figure 5.35. When austenite cools slowly, the carbon has time to diffuse into the iron, producing iron compounds layers and hence pearlite, characterised by the layered structure shown in figure 5.36a. There are very few dislocations in the ferrite and so pearlite is a relatively soft form of steel. Cooling the steel faster limits diffusion, leading to bainite or martensite formation. These are characterised by their finer, non-layered crystal microstructure, shown in 5.36b and c. The fast cooling leads to many dislocations, producing harder, less elastic steels. Martensite is not a thermodynamically favourable state for steel to exist in, so can be destroyed by reheating (annealing and tempering) the workpiece to facilitate diffusion.

#### 5.8.1.1 Consequences for Strand Brazing

A combination of cold drawing, annealing and strain tempering in a prestressing wire, described in §3.3.2, is used to promote pearlite growth and ensure that steel crystals align with the prestressing direction. This provides strands with the combination of ductility and strength essential for prestressing. Cycling the a strand's temperature during a brazing process could easily promote residual thermal stress, dislocation and martensitic crystal growth. This may in turn lead to strands which are not only more likely to fracture at a lower stress, but which

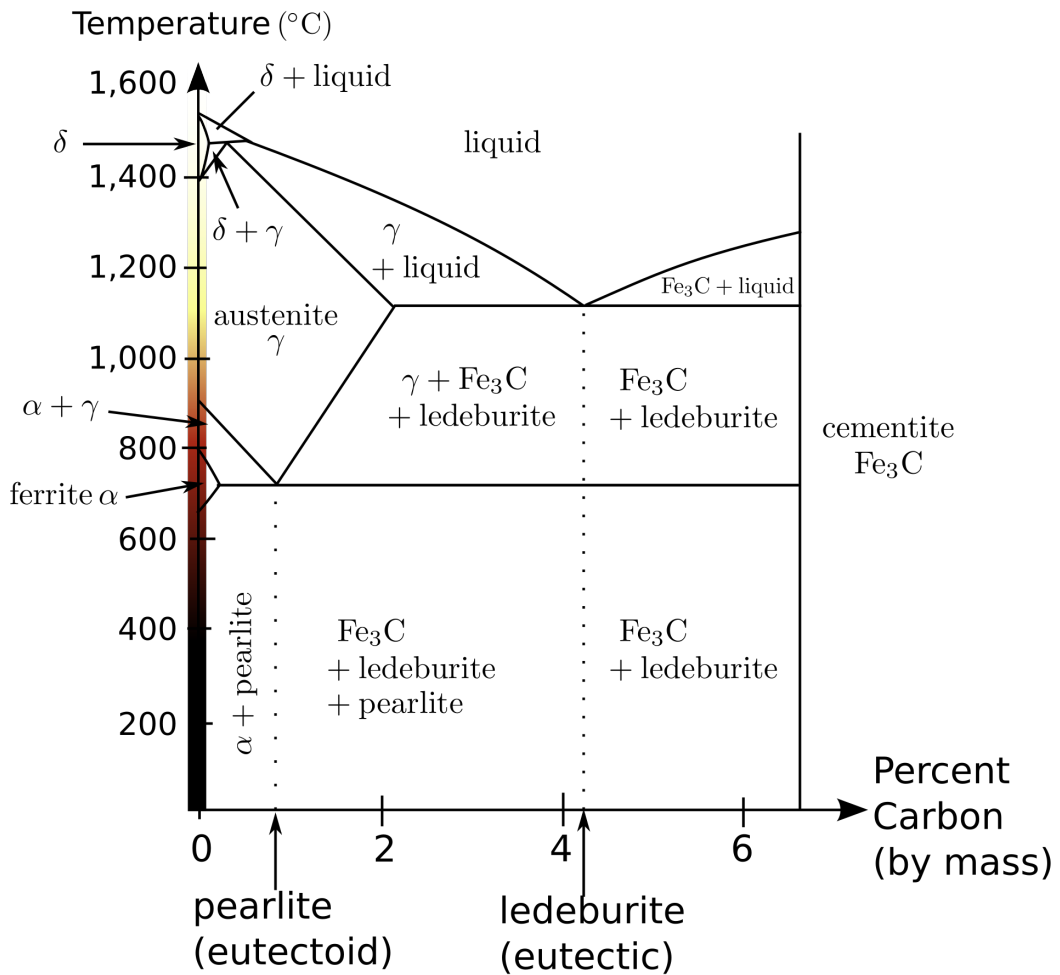


Figure 5.34: The phases of steel at varying temperatures and carbon contents. Iron allotropes tend to coexist with carbon or carbon-iron compounds. These crystal mixtures each have a designation — austenite is a mixture of gamma-ferrite and pure carbon, while pearlite is a mixture of alpha-ferrite and an iron-carbon compound called cementite. Ledeburite is not truly a form of steel as its carbon content is too high (it is a mixture of austenite and cementite).

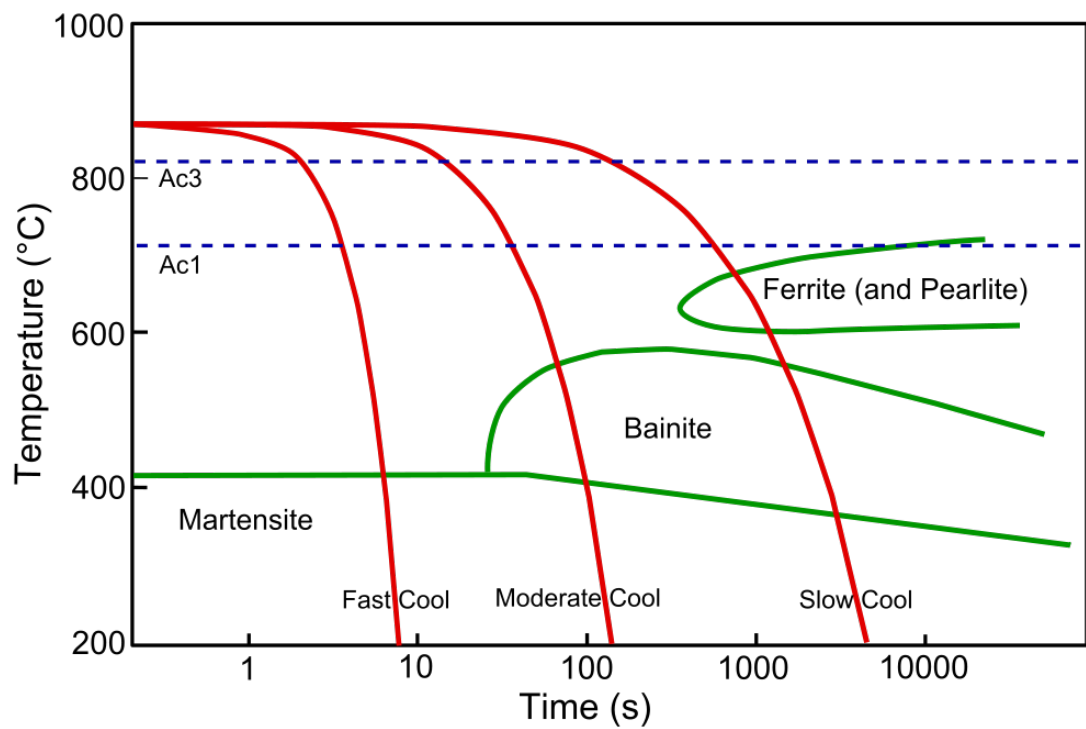


Figure 5.35: Continuous cooling transformation (CCT) diagram for steel. The steel is transformed from austenite into varying quantities of pearlite, bainite and martensite depending on the cooling rate. Cooling more slowly promotes both carbon and iron diffusion and crystal growth, in turn leading to the layers of cementite and gamma-iron seen in pearlite.

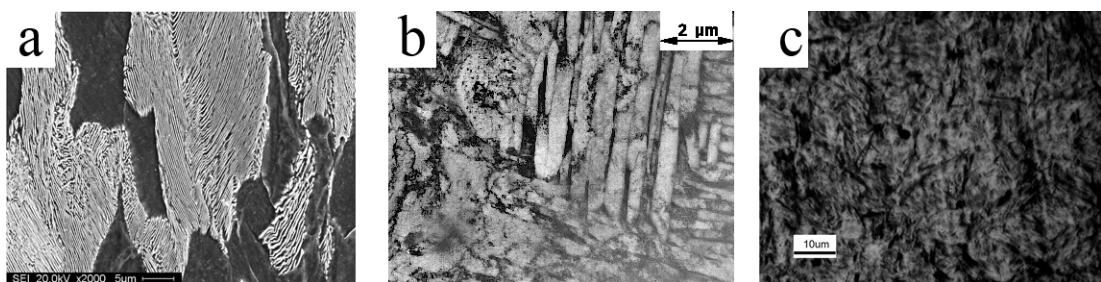


Figure 5.36: Crystal structures of a) pearlite, b) bainite and c) martensite. The cooling rate of the steel from austenite is faster for martensite, slower for pearlite and intermediate for bainite.

may also display different relaxation and bulk mechanical properties. Damage to the steel which penetrates any deeper than 1 mm from the strand surface is more likely to lead to failure. Strands displaying flaws deeper than 1 mm are discarded during inspection.

### 5.8.2 Welding Techniques

Metal welding typically requires lower temperatures and causes smaller damage sites than brazing. The small size of the packaged fibre sensors make them suited only to low-pressure and precise welding techniques, such as:

- Ultrasonic consolidation — In ultrasonic welding, high frequency (50 kHz) ultrasound is applied to a 100  $\mu\text{m}$  thick foil, pressed against a larger metal workpiece [LS09]. The resulting friction breaks up intermediate oxides between the metals and allows them to diffuse into each other, welding any sandwiched fibres into the structure at room temperature [KS05, YJRS09]. The high forces required make it much more suited to soft metals, such as aluminium, rather than steel [ZCZ11].
- Resistance spot welding — In spot welding, 0.05 – 3 mm thick metal sheets are clamped to the base workpiece. Oppositely poled copper electrodes pass current through a highly localised area. The heat generated due to electrical resistance melts the sheet to the base in the vicinity of the electrodes, without causing substantial heating anywhere else [SPKW76, Hor20]. The method is relatively simple and is already used extensively in bonding fibre strain sensors to metal structures [TMJ<sup>+</sup>09, BCF<sup>+</sup>08, She99].
- Laser/electron beam welding — Because the beam focus and heating power can be manipulated with a great degree of precision, beam welding methods are versatile, easily automated and highly suitable for welding fibre sensors to steel [CH05]. Laser welding has already been used extensively in the formation of various fibre packages and attachment processes [VBA95, BCF<sup>+</sup>08, WH11], but the capital costs of the welding system are somewhat prohibitive.

Due to its flexibility, suitability to steel and habitual use in strain sensor welding, the suitability of resistance spot welding was investigated in this project.

### 5.8.3 Spot Welding

It was initially unclear as to what the effects of spot welding on the strength and mechanical properties of the prestressing strand would be. There was also the question of whether spot welded sensors could withstand the strains produced during prestressing. In this section, the theory of spot welding is briefly outlined before the results of practical tests are presented.

#### 5.8.3.1 Method and Theory

A spot welder was used to weld 0.05 mm thick steel shims (rectangular plates of length 2 cm, width 0.5 cm) to the surface of a prestressing strand [Vis13]. The local surfaces of the shim and strand were cleaned using a combination of sandpaper (with a <1 mm grain size), degreasants and ethanol. One electrode of the spot welder was clamped onto the prestressing strand, 5 – 10 cm away from the spot welding location. A second copper needle electrode was used to pass current through a 1 mm diameter area of the surface of the shim, melting the shim-strand interface within a small heat affected zone (HAZ). The weld energy, which was set to between 20 and 30 J, can be roughly characterised by:

$$Q_s = I^2 R t \quad (5.16)$$

where,  $I$  is the current flowing through the metal interfaces of total resistance  $R$  over a time  $t$ . As shown in figure 5.37, the total resistance of the interface is made up of the bulk and contact resistances of and between the workpieces. The low resistivity of the copper electrodes ensure that more heat is generated between the shim and the strand, rather than at the electrode interfaces. Because steel's resistivity increases from 15 to 100  $\mu\Omega\text{cm/K}$  between room temperature and 800 °C, the resulting rapid increases in heating make spot welding highly suited to steels [ZS06].

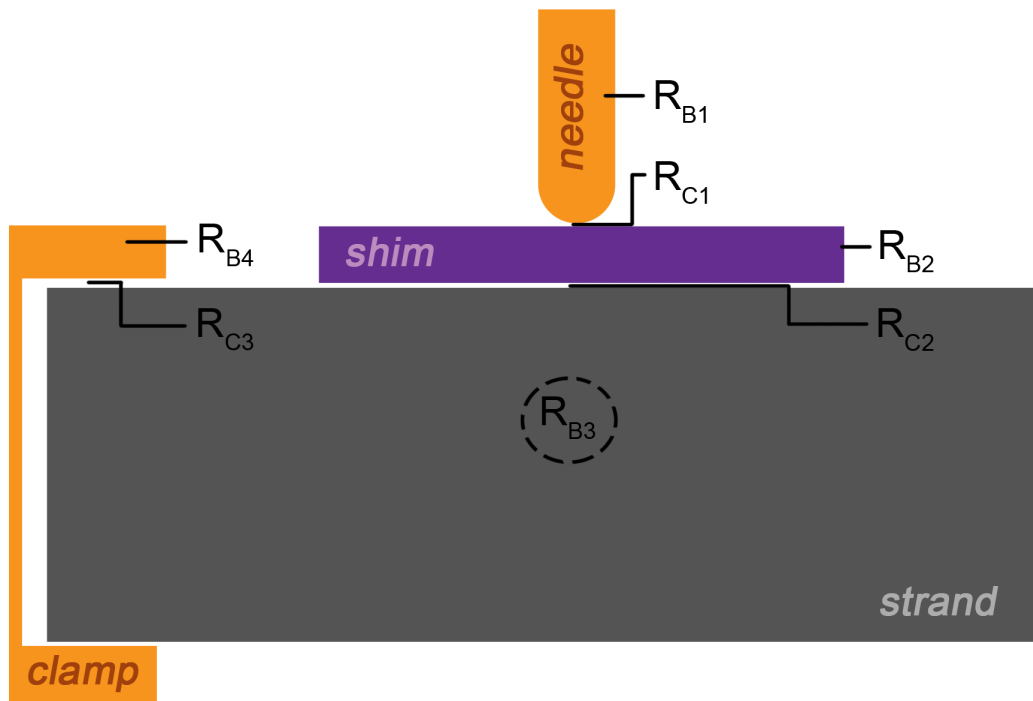


Figure 5.37: Diagram showing an example of the bulk  $R_B$  and contact  $R_C$  resistances in spot welding. Bulk resistances depend on how the current is confined within the workpieces, while contact resistances depend on contact area, pressure and surface cleanliness.

Contact resistance is affected by the contact area between the workpieces (which may change as the interface melts). It is also dependent on the presence of oxides and grease, which form insulating layers. Over all, a high contact resistance can lead to poor welds and workpiece damage through electrical arcing. The strongest welds are achieved when the two welded metals are chemically compatible, or ideally, the same.

As the interface between the workpieces melts and resolidifies during steel welding, carbon migration into the centre of the weld can create eutectics, compounds which solidify at a lower temperature than the surrounding steel. This means the HAZ of welded steels tends to solidify from the outside inwards. Solidification occurs quickly enough to allow local martensite formation, with the steel crystals aligning in the direction in which cooling is most rapid. This may reduce the normal or shear strength of the weld.

### 5.8.3.2 Spot Welding: Effect on Strands

To test the effects of spot welding on the prestressing strands, 0.05 mm thick steel shims were welded to strand surfaces. For the strand designated  $T_1$ , shims were welded across the interstix between two adjacent wires, as shown in figure 5.38. In a second strand, designated  $T_2$ , shims were welded to the surface of a single wire, as shown. Two other strands, labelled  $T_3$  and  $T_4$  were untreated and used as control strands. All four strand samples were sent to an independent contractor for mechanical strength, metallographic and microhardness testing. The full report can be found in appendix A.5, but the findings are summarised as follows:

- *Mechanical Strength* — Tensile tests of the strands until fracture revealed that plastic yield and breaking strengths of both welded and untreated strands were all higher than the values recommended in BS 5896:1980 (as shown in figure 5.39). The elasticity of the strands was also unaffected by spot welding.
- *Metallography* — To conduct a metallographic analysis, the shims were

removed from the strands, as shown in figure 5.40. Cross-sections from the spot welded areas of the strand were cut, polished and etched to reveal the crystal microstructure. Figure 5.41 shows optical microscope images of the welded area under 200 times magnification. The microscope images reveal that a transformation of the steel structure occurred at the weld location, but only down to a 0.1 mm pit depth.

- *Hardness* — The mechanical hardness of both welded and non-welded regions of the strand was tested using indentation under a 300 g force. The 914 HV hardness value found in welded regions was almost double that of the unwelded regions at 481 HV. The high hardness value is very close to the textbook value for martensite (1000 HV) [GT03], proving that martensitic transformations have arisen from rapid cooling.

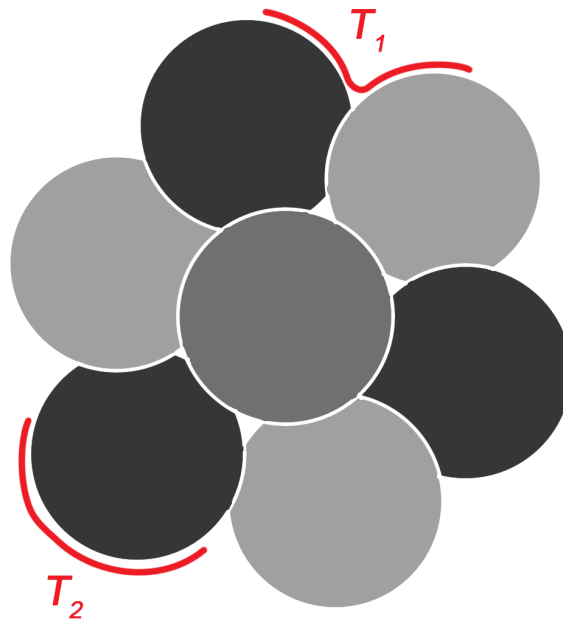


Figure 5.38: Illustration of cross-section of prestressing strand, showing welding across the interstix of two wires,  $T_1$ , and across a single wire,  $T_2$ .

From these tests, we can conclude that while spot welding has indeed lead to a localised martensitic phase transformation, the strand is only affected at its extremities down to a depth of 0.1 mm. Furthermore, spot welding has no effect

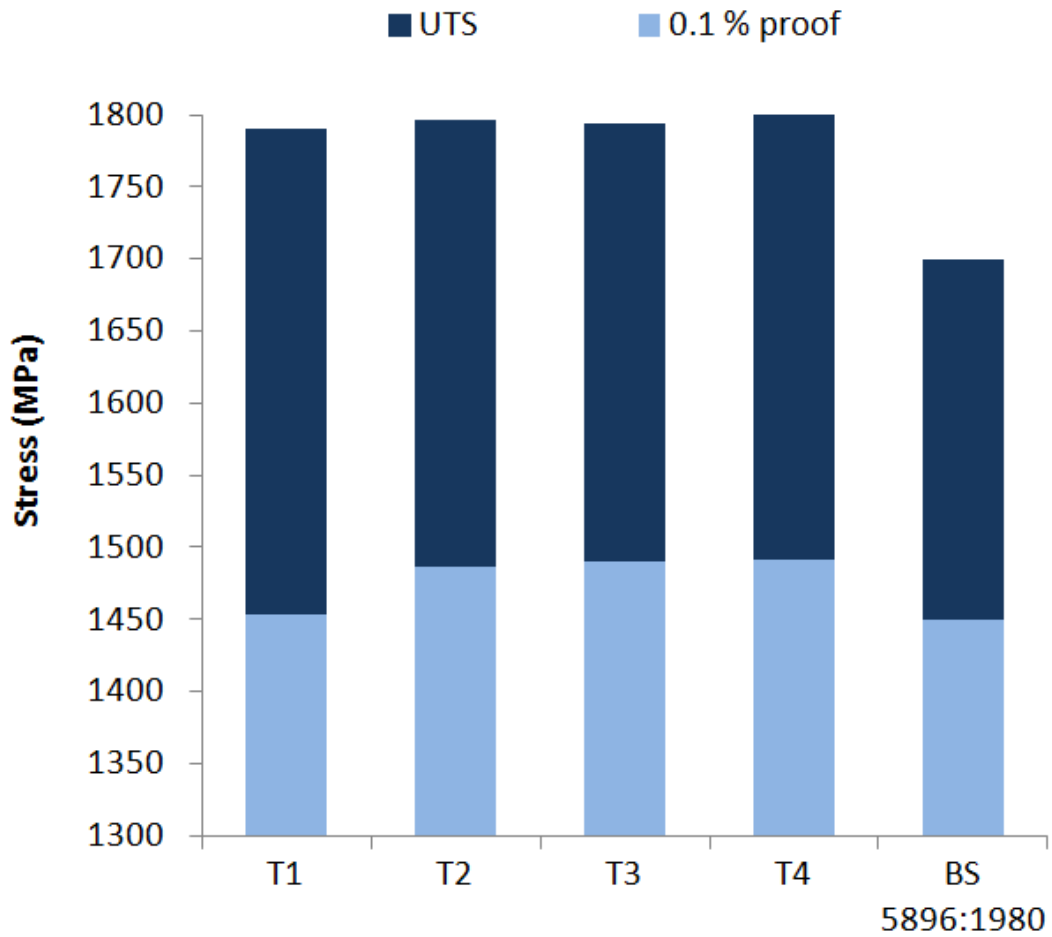


Figure 5.39: Comparison of yield and ultimate tensile strength of the four steel strand specimens. Sections of  $T_1$  and  $T_2$  were cleaned and had steel shims spot welded to them, while  $T_3$  and  $T_4$  were untreated. All four strands display strengths above those recommended in BS 5896:1980.



Figure 5.40: Top surface of the steel strand after the steel shim has been removed.

on the mechanical properties of the strand, allowing it to retain its elasticity and strength.

All of the shims were, unsurprisingly, destroyed during the tests above as the strands were stressed to fracture, so there still remained further work to ensure that the shims could withstand at least regular prestressing forces without failing. In further tests, shims were welded to strand specimens, both to single wires and across the interstix, as shown in figure 5.38. Strands were then stressed to around 250 kN (70 % UTS). The spot welded shims all survived the stressing operation, but differential movement between strand wires caused some creasing of the shims welded across the interstix. These differential movements can make strain measurements more challenging, so it was decided that the strain sensors should only be welded to single wires of the strands.

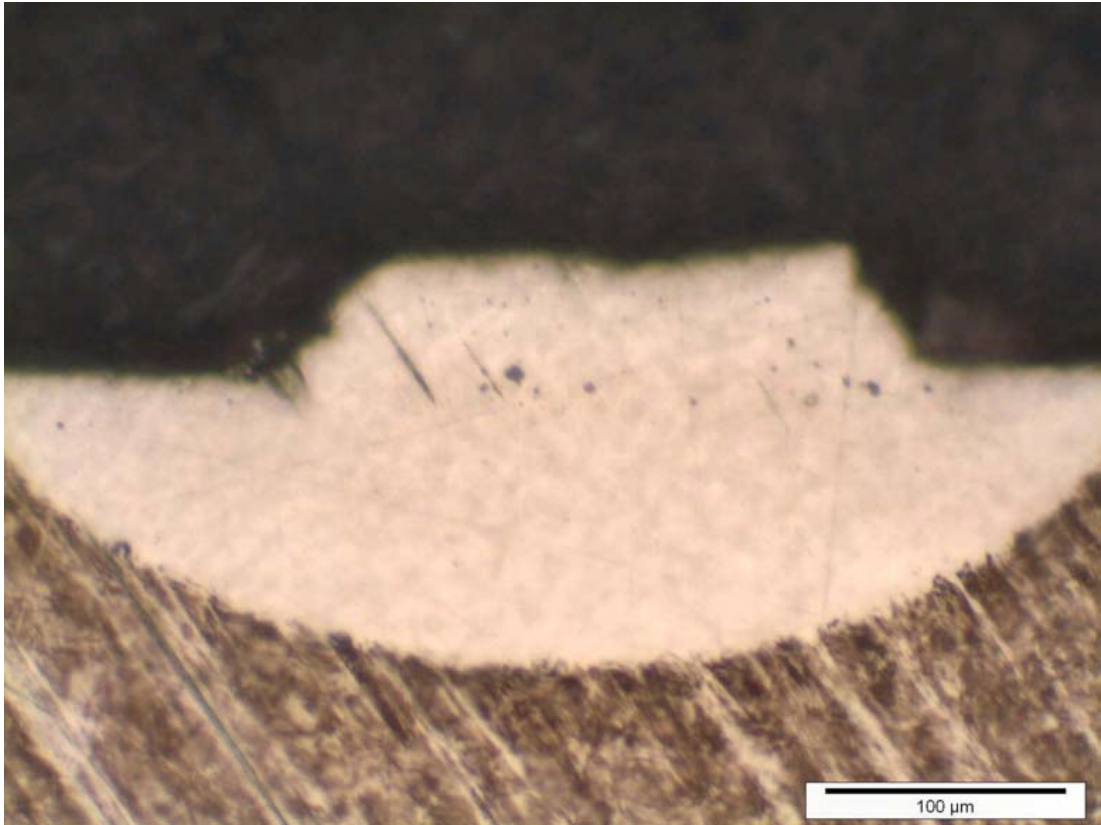


Figure 5.41: Cross section of the steel strand at a spot welded location on strand  $T_2$  under 200 times magnification. This picture shows more clearly that the martensitic region extends to only around 100  $\mu\text{m}$  from the strand surface.

## 5.9 Spot-Weldable FBG Sensor

The results from initial tests were encouraging, so a technique to fabricate spot-weldable FBG strain sensors was developed. The spot-weldable sensor was made up of three components:

1. The metal plated fibre, with a bare, spliceless section for the FBG. Type I, Ge-doped gratings were used for their adequate radiation and thermal resistance.
2. The capillary, used to encapsulate the bare FBG. The capillary offered the FBG the mechanical integrity to resist bending and protection against chemical and mechanical damage.
3. The strain plate. This was a steel shim, designed to be brazed to the capillary and then spot-welded to the prestressing strand. While the strain plate may be heat damaged during induction brazing, it can be treated before spot welding, thereby minimising thermal damage to strands.

### 5.9.1 Shim Stamping

While thicker shims may offer a higher mechanical integrity, they also require higher weld energies, which can in turn increase the penetration depth of martensitic transformations into the strand. Furthermore, the shims had to be shaped and cut to suit the geometry of both the capillary and the helically wound strands, and this is easier with a thinner shim.

Metal forming techniques such as stamping and pressing are highly suited to shaping thin sheet metals, which can be plastically deformed, bent or cut using high forces at room temperature. Precision stamping of the shims was used in this project, and provided some important advantages over other metal forming techniques:

- *Seamless* — there are no interfaces in the part as it is a single shaped body of steel. This improves the part's strength

- *Low temperature* — as the process is performed at room temperature, residual thermal stress in the steel is minimal
- *Automated* — the process can be highly automated, providing many parts with a consistent finish
- *Quick* — cutting and stamping a steel part takes seconds
- *Low cost* — once the stamp and die have been designed, the operational costs are minimised to the cost of the sheet metal.

There are, however, some limitations to the technique. The strain plate design had to be chosen very carefully in the first instance, as even small changes would require refabrication of an entirely new stamp and die. The sizes of the features stamped into the strain plate are also limited by the malleability of the metal. Attempting to bend small diameter curves into a steel shim can cause it to snap rather than bend. Careful design of the stamp's die and punch geometry allowed the shim to undergo plastic flow under force without fracturing. Photographs of the stamping die, punch and stamped part used in this project are shown in figure 5.42.

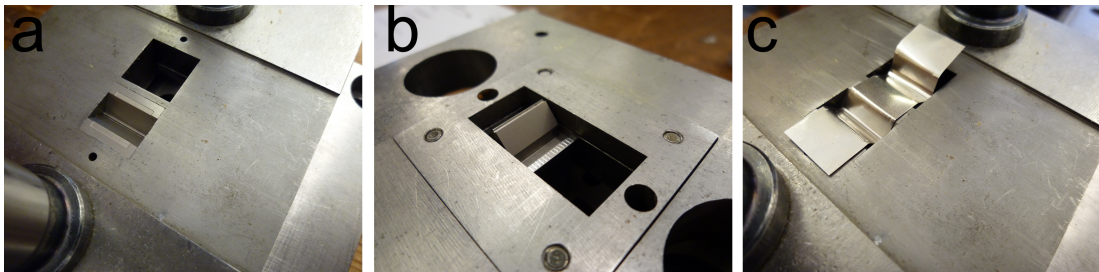


Figure 5.42: Photographs of a) the die used to stamp the part, b) the corresponding punch and c) stamped but uncut steel strain plates.

#### 5.9.1.1 Design evolution

The evolution of the strain plate through some of its original designs is shown in figure 5.43. In all of the designs shown, the capillary was designed to rest within a small semi-circular groove stamped into the shim. The ‘wings’ of the shim were designed to be welded to the prestressing strand.

The finalised strain plate design, however, is shown in figure 5.44. The most obvious changes to the part throughout the design process were a reduction in both material thickness and part complexity. Reducing the shim's thickness reduced the force required for stamping, improved the part's flexibility and allowed it to be spot welded at lower energies. Simplifying the part also substantially reduced the number of steps and hence the cost, time and difficulty of the stamping process.

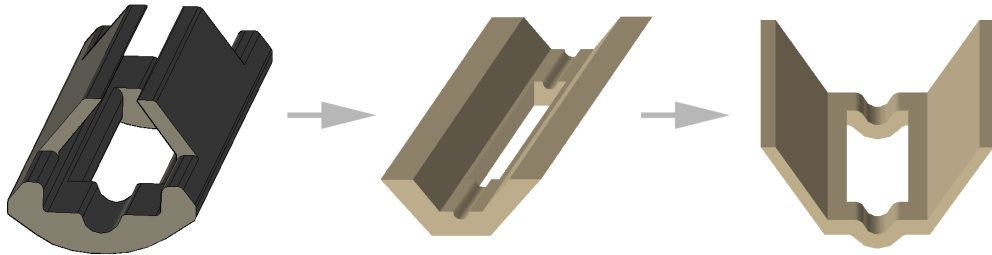


Figure 5.43: Evolution of the strain plate through some old designs. Both the thickness and the complexity of the part were reduced to make it more suitable for stamping and spot welding.

Figure 5.45 illustrates the steps in the assembly and attachment of the weldable strain sensor. In step 1, the 12 mm long strain plate was brazed to the middle-section of the 25 mm capillary, which housed the FBG. After capillary attachment, the strain plate was cleaned and then one wing of the plate was welded to a single wire of the prestressing strand, as shown in step 2. In the final step, the opposite wing of the strain plate was folded and welded over the first wing, to the same strand wire. Welding both wings of the strain plate to the same wire prevented relative movements between the wires from interfering with strand strain measurements.

Photographs showing unattached and attached strain plates are shown in figures 5.46 and 5.47. The excess metal on the strain plates after stamping can be cut prior to or after welding. Figure 5.47 actually shows the entire finalised assembly of the spot-weldable fibre strain sensor — the FBG, housed within a capillary, attached to a strain plate and spot welded to the prestressing strand.

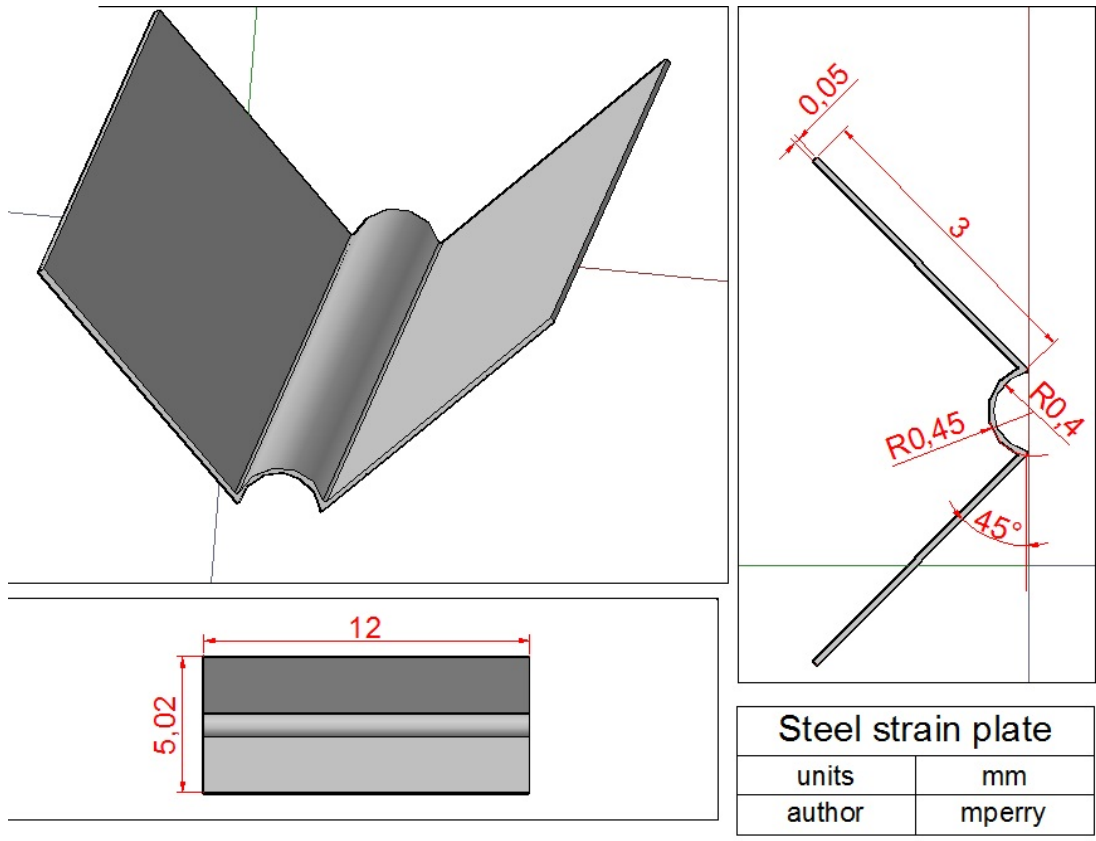


Figure 5.44: The final design of the strain plate, with dimensions shown in millimeters. Again, both the complexity and thickness of the part have been significantly reduced.

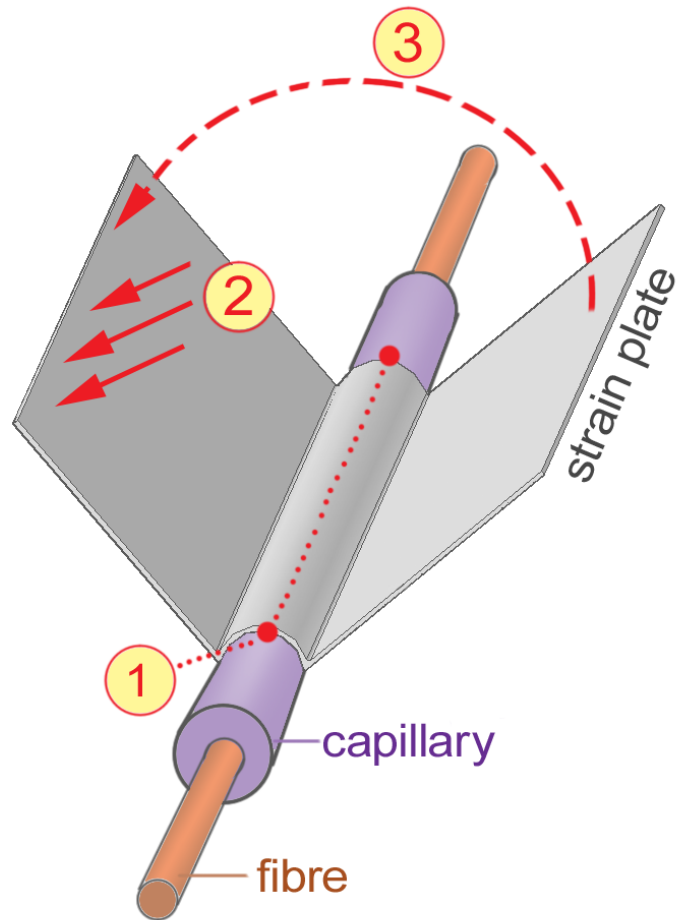


Figure 5.45: Diagram showing the assembly of the FBG packaging and its attachment to the prestressing strand. In step 1, the capillary (which houses the FBG) is brazed to the strain plate. In step 2, the entire length of one wing of the strain plate is spot welded to one wire of the prestressing strand. In step 3, the second wing of the strain plate is folded over and spot welded to the same wire of the strand.

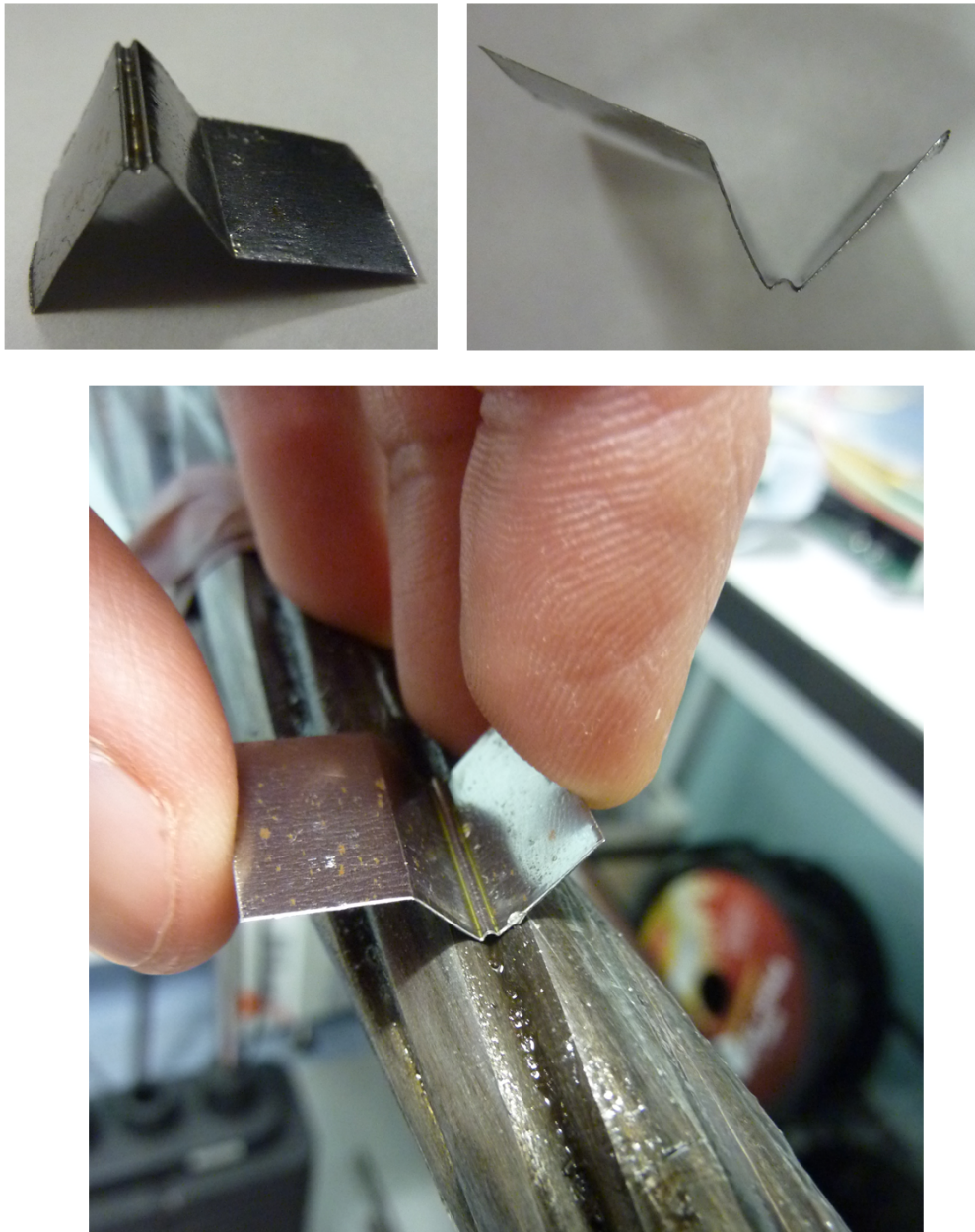


Figure 5.46: Photographs showing a stamped strain plate and its size relative to the grooves between two wires of the prestressing strand. The excess metal on the strain plate can be clipped prior or after welding.



Figure 5.47: Photograph showing the finalised strain sensor assembly, attached to the prestressing strand.

## 5.10 Smart Strand Characterisation

The full process for fabricating and attaching the spot-weldable FBG sensor is summarised as follows:

1. The capillary-housed FBG was fabricated by brazing the FBG into the capillary, as described previously.
2. The capillary was then slotted into the groove of the strain plate, as shown in figure 5.48. Brazing paste was spread along the length of the groove and the capillary was brazed to the strain plate
3. After brazing, the strain plate may be covered in oxides, particularly if the argon atmosphere was not pure or perfectly sealed. To remove the oxides and leave a fresh surface for spot-welding, the assembly was soaked in an acetic acid solution for 2–3 hours and then lightly abraded with sandpaper.
4. The strand was degreased, abraded with fine sandpaper and cleaned with ethanol in a localised region ready for spot welding. The finalised FBG sensor assembly was placed into the groove between two wires of a strand as shown in figure 5.48c.
5. The wings of the strain plate were spot welded to one wire of the prestressing

strand. The finalised and attached strain sensor assembly, shown in figure 5.47, was then coated in grease to prevent strand corrosion.

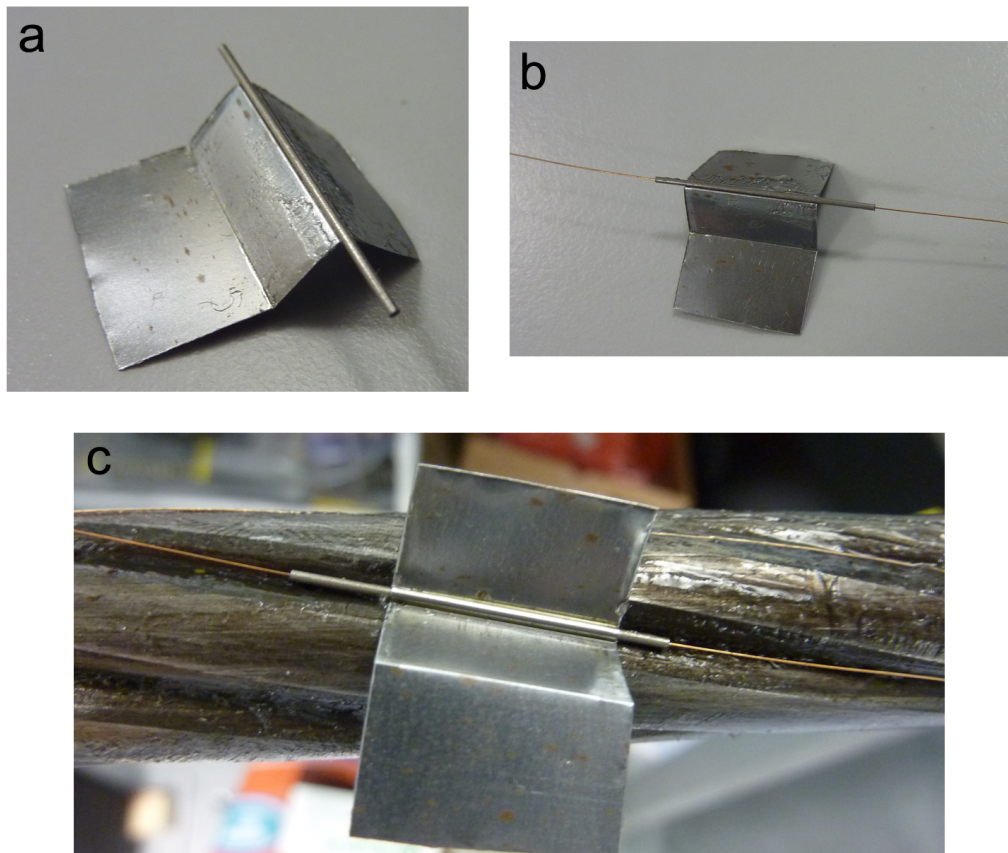


Figure 5.48: Photographs showing a) how the capillary fits to the strain plate, b) how the fibre is then slotted through the capillary, c) how the assembly is protected within the groove between two wires of the prestressing strand prior to spot welding.

### 5.10.1 Strain Characterisation

To characterise strain transfer in attached FBGs, instrumented prestressing strands were inserted into a cantilever stressing rig, as shown in figure 5.49. Spot-welded FBG sensors measured strain along the top surface of the strand, 3–10 cm from the cantilever pivot point, as the free end of the strand was placed under load. To empirically derive the strain transfer of the welded FBG sensors, a second bare FBG was epoxied to the same wire as the spot-welded sensor as a strain

reference. While epoxied FBGs are not suitable for measuring high strains, their strain transfer at low strain can be close to ideal [WYJ<sup>+</sup>01].

The strain measured by both the welded and epoxied FBGs as a function of the force applied to the end of the cantilever is shown in figure 5.50. The strains in the spot-welded FBG were only 12 % of those in the epoxied FBG. Such low strain transfer may be desirable in some sense, as it reduces the stresses in the bare FBG, in turn reducing the likelihood of mechanical failure. However, the reduced strain transfer also places more stringent requirements on the measurement performance of the FBG interrogation system, as smaller strains must be measured.

In this project, finite element models were developed and used to investigate the low strain transfer in the system. A detailed description of the model is given in appendix A.6, but the main findings are summarised briefly here. It was found that strain transfer was reduced in the metal-packaged FBG mainly due to the following effects:

- The extension of the 12 mm long strain plate was transferred to the 25 mm long capillary. This meant the strain (extension per unit length) in the capillary was approximately 50 % of that in the strain plate.
- Strain transfer in this type of system was found to be highly reliant on the contact area between the strain plate and the capillary. As the strain plate was only bonded to a fraction of the circumference of the capillary, strain transfer was significantly reduced.
- The helical winding of the wires in the prestressing strand mean that the welded FBG sensors were placed at a 30 ° angle to the strand's long-axis. This non-axial strain reduces estimated strain transfer by a further 25 %. This effect, however, should also effect the epoxied sensors to some degree.

While the helical winding is inherent to the strand geometry, strain transfer can be improved by enhancing the bonded surface area between the capillary and the strain plate. Indeed, the importance of contact area in strain transfer has been well documented in previous work [LLRS06, LZRL09, LRL12]. The fabrication method for the spot-weldable FBG strain sensors was thus modified to



Figure 5.49: Strand installed into a cantilever stressing rig. One end of the strand is fixed while the other remains free. Force is applied to the free end to induce strain in the top surface of the strand.

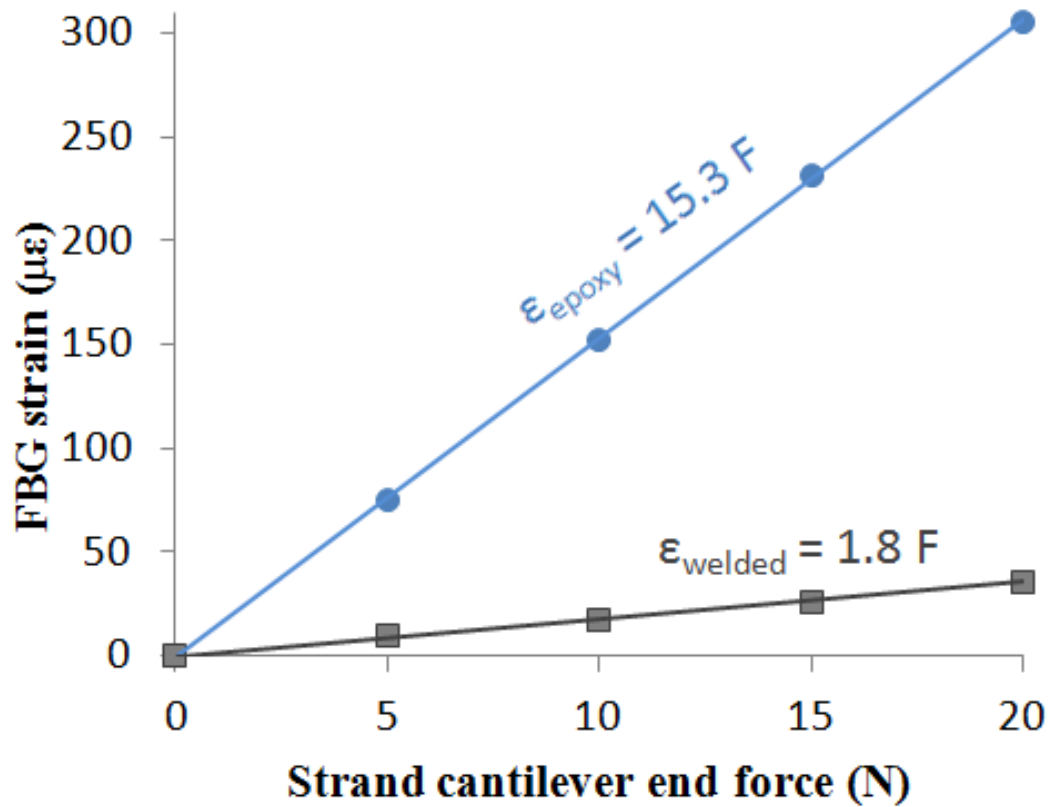


Figure 5.50: The strain vs tip force in a prestressing strand cantilever. The strains were measured using adjacent spot-welded and epoxied FBG sensors. The welded sensor's strain was 12 % that of the epoxied sensor.

improve both the contact length and circumference between the plate and capillary. To improve the bonded circumference, strain plates were used to sandwich the capillary, as shown in figure 5.52. The gap between the strain plates was filled with brazing paste and then brazed to fully encapsulate the capillary.

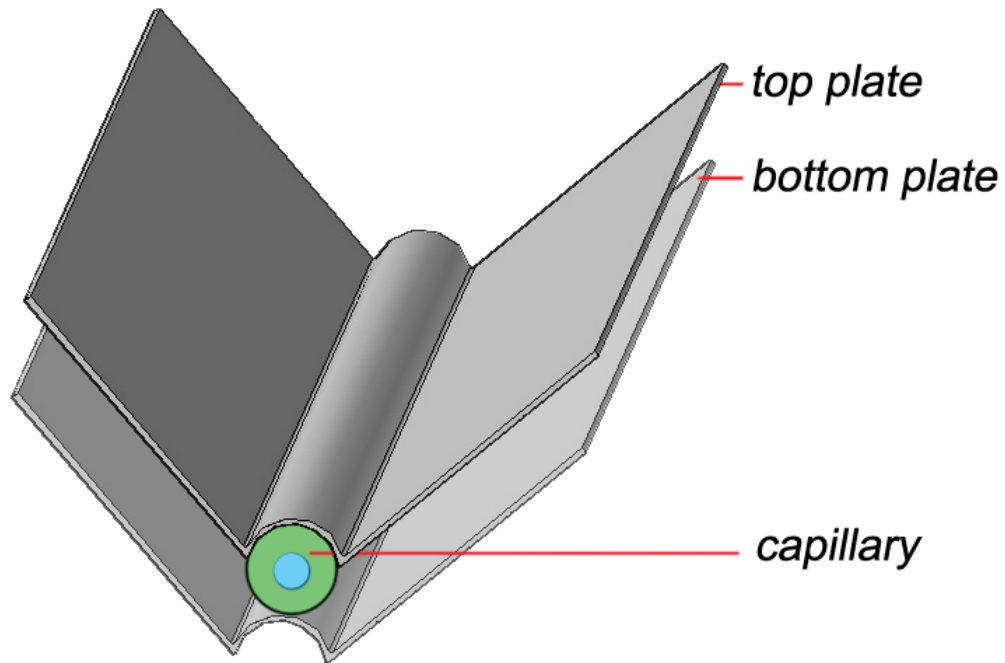


Figure 5.51: Improvement to the bonded circumference between the capillary and strain plate is facilitated by sandwiching the capillary between two strain plates and brazing the assembly. This was an experimental trial — ideally the curvature of the strain plates should match the profile of the capillary over both its top and bottom surfaces.

The bonded length was improved by bonding the strain plates to the capillary at both of its ends, as shown in the aerial view of the arrangement in figure 5.52. Strain plates were allowed to extend beyond the edges of the capillary. This meant that when the strain plates were welded, the strain over a longer length of prestressing strand was transferred to the capillary, facilitating strain amplification.

The rest of the sensor attachment methodology remained the same as discussed previously — the strain plate wings were cleaned and then folded over

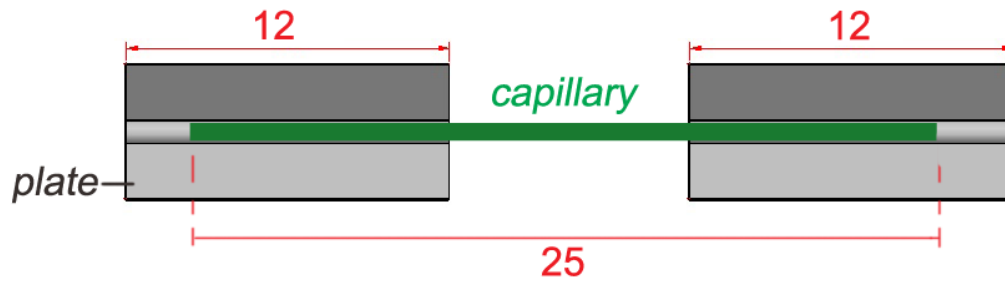


Figure 5.52: Improvements to the grip length are facilitated by bonding the strain plates to the capillary edges. Allowing the strain plates to extend beyond the capillary edges allows for strain amplification. Units shown are in millimetres.

and attached to a single wire of the prestressing strand using a spot-welder. A bare FBG was again epoxied to the same wire as the welded sensor and the sensor was characterised using the cantilever stressing rig.

Figure 5.53 shows the strain measured in adjacent epoxied and improved spot-weldable FBG sensors as a function of the load applied to the strand's free end. Strain transfer in the welded sensors obviously increased compared to figure 5.50. Figure 5.54 shows welded strain values relative to the epoxied sensor for both original and improved packaging designs. The improved packaging increased strain transfer to 87 %.

The manipulation of the packaging design described here demonstrates the flexibility of weldable FBG sensors and how simple finite element models can be used to drive the design process and achieve the desired strain transfer. The ideal strain transfer value for the finalised system will be based on the mechanical strength of the FBG and the strain resolution of the interrogation system. Consistently achieving the desired strain transfer empirically in future will require rigorous definition of the geometry, configuration and materials used to assemble the sensor packaging.

### 5.10.2 Temperature Compensation

As outlined in §4.3.4, achieving reliable measurements from FBG strain sensors requires unbonded FBGs in the vicinity to compensate for the Bragg shifts induced by temperature and radiation. Recall that the temperature dependence of

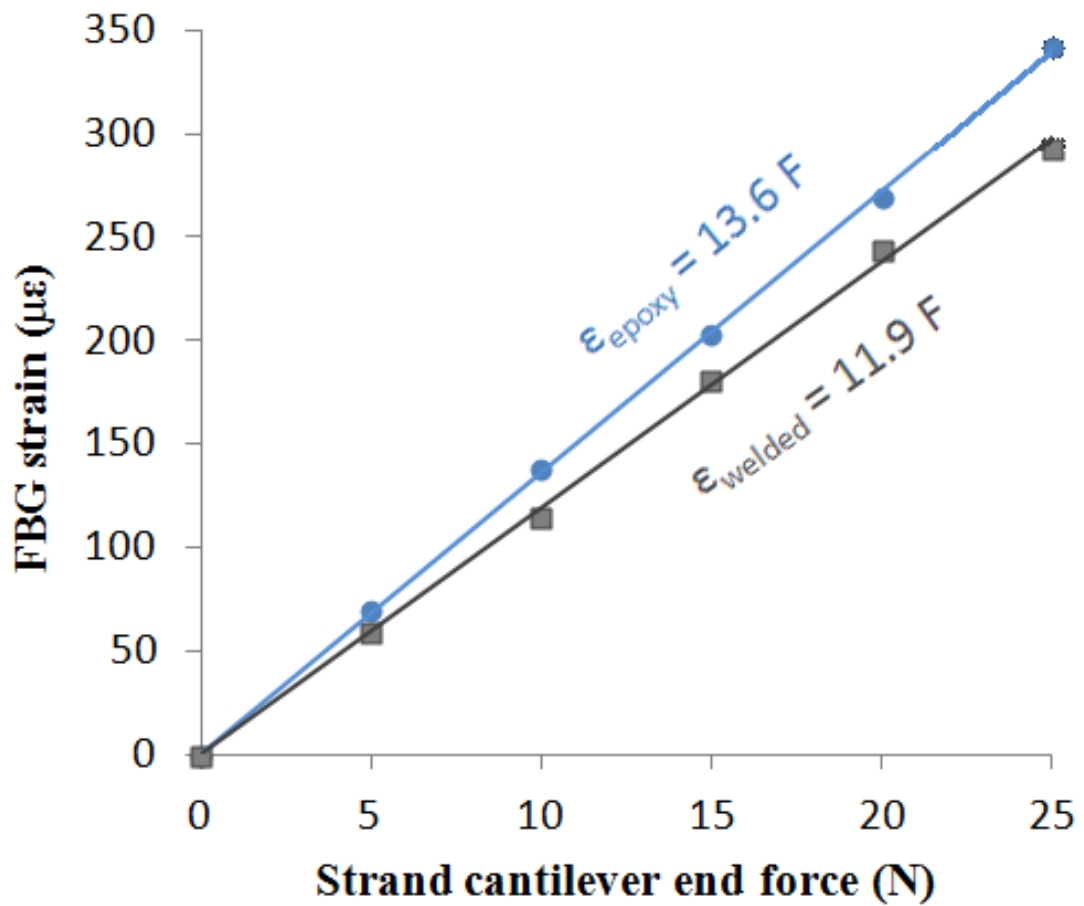


Figure 5.53: The strain vs tip force in a prestressing strand cantilever. The strains were measured using adjacent spot-welded and epoxied FBG sensors. The welded sensor's packaging was improved and strain was 87 % that of the epoxied sensor. Note that the force vs strain values for the epoxied FBG are lower in this figure compared to figure 5.53 as the sensors were welded further from the strand cantilever's pivot point.

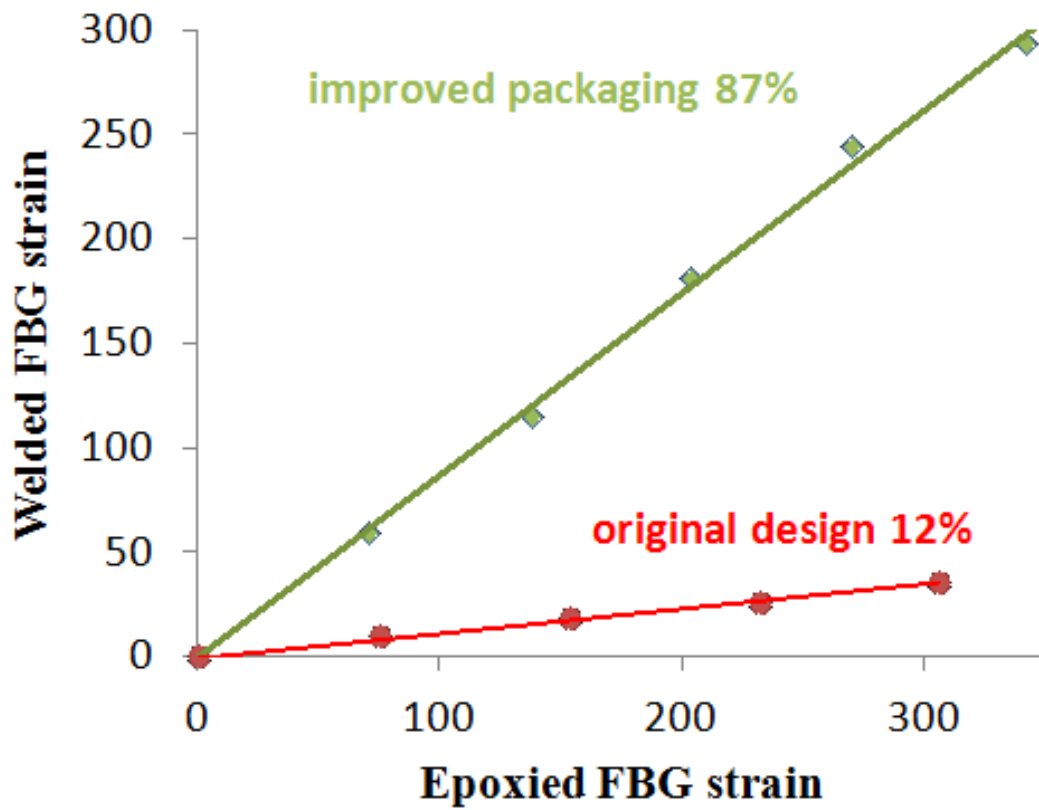


Figure 5.54: Epoxied vs welded FBG strain in both the original and improved packaging arrangements. Original strain transfer was around 12 % of the epoxy values, while improved strain transfer is around 87 %.

the Bragg peak shift is written:

$$\frac{\Delta\lambda_B}{\lambda_B} = (\alpha_\Lambda + \alpha_n)\Delta T \quad (5.17)$$

where  $\alpha_\Lambda$  and  $\alpha_n$  are the thermal-expansion and thermo-optic coefficients for silica. The temperature dependence of bare FBGs is approximately 12pm/°C and is mainly dependent on refractive index changes. The dependence of packaged or attached FBGs, on the other hand, tends to be more dependent on the thermal expansion of the substrates they are bonded to.

The temperature dependence of the peak shift in the weldable FBG sensors was characterised in this work by heating the steel strands up to 35 °C using a heat gun. The results, displayed in figure 5.55, show that the temperature dependence is 19.4 pm/°C. This suggests that the FBG is exposed to an overall thermal expansion coefficient of around 5  $\mu\text{m}/\text{m } ^\circ\text{C}$  — a sensible value mid-way between textbook thermal expansion coefficients for silica, kovar and steel.

Figure 5.56 compares the peak shifts of the welded sensor with an unbonded sensor nearby. The nearby unbonded FBG can thus be used to ascertain the temperature-corrections for the welded FBG. In future work, unbonded FBGs can be fabricated simply by brazing bare FBGs into capillaries for protection. These temperature sensors, much like the rest of the addressing fibre in the system, will be allowed to rest within the gaps between two adjacent wires in the strand. A combination of thick grease and interspaced plastic sheathing may be used to prevent the temperature sensors and addressing fibre from slipping free of the interstix.

## 5.11 Summary

Conventional fibre sensor protection and attachment methods are unsuitable for the high-stress, radioactive environment within PCPVs and PCCs. In this project, efforts were made to protect bare FBGs with nickel coatings, fabricated using evaporative deposition and electroplating, but issues with the repeatability of the methods used lead to low yields.

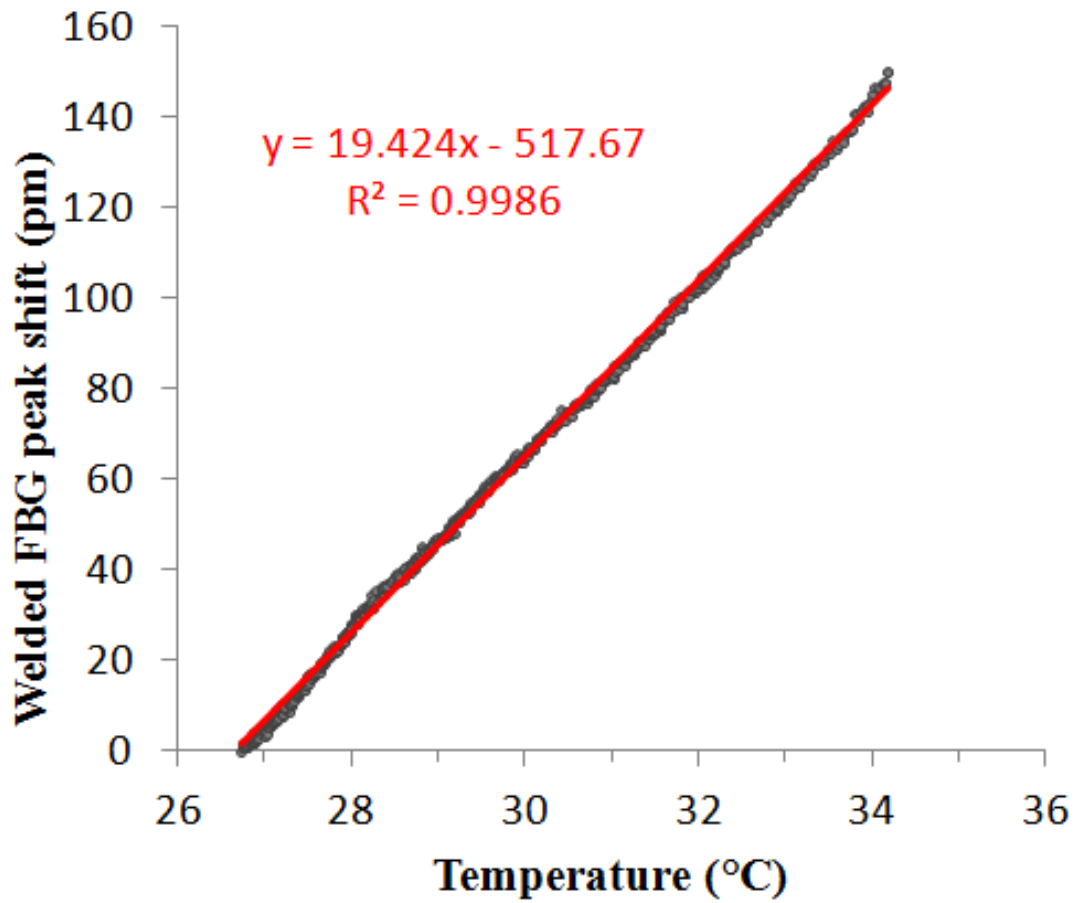


Figure 5.55: The temperature dependence of shifts in the Bragg peak of a welded FBG sensor. The 19.4 pm/°C shift implies the grating is subject to thermal expansion value close to  $5\mu\text{m}/\text{m } ^\circ\text{C}$ .

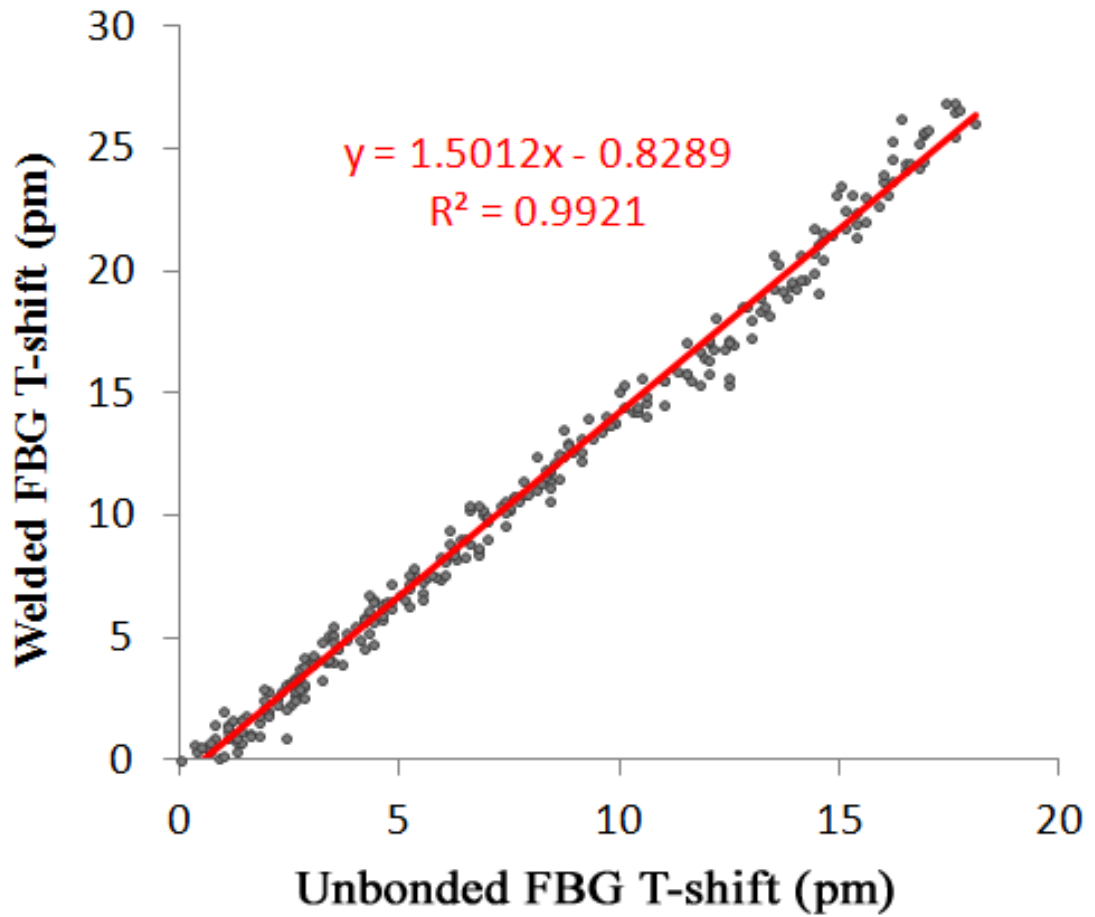


Figure 5.56: The temperature dependence of shifts in the Bragg peak of a welded FBG sensor relative to those of a nearby unbonded FBG sensor. The unbonded FBG sensor displayed shifts of 12.9 pm/°C as expected. The shifts in this nearby unbonded FBG can be used to gauge the shifts in the welded FBG using this graph.

Bare FBGs were instead encapsulated within kovar ferrules using induction brazing. Once brazed to a strain-plate, the packaged sensors could be spot-welded to the surfaces of a prestressing strand, without altering the strand's mechanical properties. Initially, approximately 10 % of the strand strain was transferred to the FBG. Low strain transfer coefficients place harsher requirements on the strain resolution of the FBG interrogation system, but less requirements on the mechanical strength of the FBGs.

Finite element models revealed how further control could be gained over strain transfer values by increasing the contact area between the capillary and the strain plate. In practice, this involved sandwiching the capillary between multiple strain plates to improve strain transfer to 87 %. The work has highlighted that careful characterisation of the strain for different sensor-packaging arrangements may be required in future to ensure that mass-produced sensors all display similar strain transfer characteristics. Nevertheless, a great degree of control over strain transfer is achievable and the strain in the packaged FBG can now be reduced or amplified conveniently.

Achieving perfect strain transfer is unlikely, partly due to the fact that the helical winding of the prestressing strand's wires leads to non-axial strain in the FBG. As such, the resolution and stability requirements of the interrogation system are likely to be even more stringent than first supposed. In the next chapter, an interrogation system capable of monitoring nanoscale static and dynamic strain changes in FBGs will be described. It is hoped that by coupling the smart strands with this interrogator, gradual prestress losses within ageing PCPVs and PCCs will be measurable.

# Chapter 6

## Interrogation Scheme: Passive Interferrometric Interrogator

FBG sensors provide a wavelength-encoded indicator of strain, but measurement resolution and stability are dependent on the method used to demodulate this information. Monitoring long- and short- term prestress losses may demand both nanostrain static resolutions and a dynamic response up to 1 kHz, so a scheme capable of delivering this performance needed to be developed.

### 6.1 Review of Current Technologies

One of the major strengths of FBGs is their ability to form quasi-distributed sensor networks. To take advantage of this, interrogators need to be able to measure and track the reflected peak wavelengths from a multiplexed array. Common methods involve actively scanning wavelength filters or lasers to allow the interrogator to map the spectrum, identify and then track peak locations [ZL04]. Static strain resolutions of  $0.8 \text{ n}\epsilon$  (nanostrain) and quasi-static resolutions of around  $1 \text{ p}\epsilon/\sqrt{\text{Hz}}$  are not uncommon [LTH12, ALT99, CMGL05].

The schemes reported in the cited references, however, all suffer from resolution impairments after multiplexing. For static schemes, distributed sensing increases the already substantial measurement times ( $>10 \text{ s}$ ), while in the dynamic case, the requirement for a range of atomic-absorption lines makes multiplex-

ing inconvenient. Bridging the gap between static and dynamic schemes while retaining full resolution, speed and multiplexing capability was therefore a key objective in this project. While a small selection of schemes had been proposed to solve this problem [WCY06, ALVA12], none of them offered static and dynamic nanostrain-resolution measurements in a single interrogation unit.

Interrogators based on passive interferometry are able to provide extremely high resolutions, so it was of interest to develop these further [Byo03]. In this project, a passive, robust, interferometric wavelength-demodulation technique was combined with fast optical pass-band switching to rapidly interrogate a multiplexed FBG array [ON11]. Static and dynamic strain resolutions as high as 1 n $\epsilon$  and 10 n $\epsilon$ /√Hz were achieved [PONJ12].

Due to the periodic nature of interferometer phase, the scheme was originally only able to measure relative *changes* in the wavelength of each sensor after the system was initialised. However, optical path length tuning was used to extend this system’s measurement capabilities, and use it to retrieve the initial absolute wavelengths of a multiplexed array of FBGs. Application of this robust and high-resolution system to smart tendon monitoring may make fibre optical measurements of prestress loss in PCPVs and PCCs feasible for the first time.

## 6.2 Interrogation System Layout

### 6.2.1 Overview

The interrogation scheme is shown in figure 6.1. Bragg reflections from an FBG sensor array ( $\lambda_1, \dots, \lambda_N$ ) are spectrally filtered and separated by wavelength division multiplexer (WDM) with uniform pass bands. An optical path switch sequentially passes the isolated Bragg peaks to an unbalanced Mach-Zehnder interferometer (MZI). The MZI demodulates each FBG’s wavelength signal.

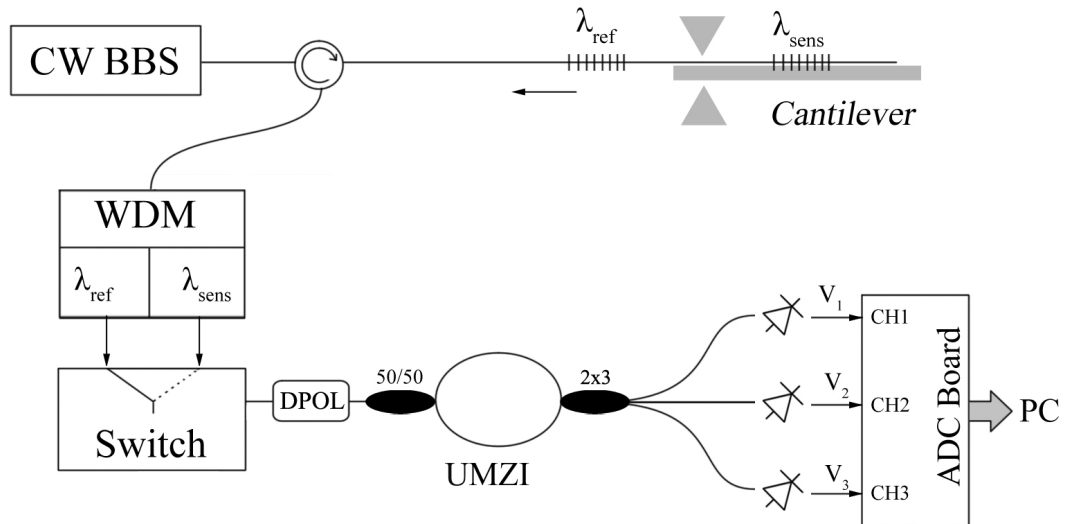


Figure 6.1: Overview of the interferometric interrogation technique. A continuous wave, broadband light source (CW BBS) illuminates an array of multiplexed FBGs. In this diagram, only two are shown; a strain sensor at  $\lambda_{sens}$  and a temperature reference at  $\lambda_{ref}$ , but the scheme can be extended to a larger array. The reflections from the FBGs are passed to and then separated using the wavelength division multiplexing unit (WDM). The windows of the WDM allow the reflected light from one FBG to be selected at a time using a switch. This light is depolarised (DPOL) and then passed to an unbalanced Mach-Zehnder interferometer (UMZI), which acts to convert the FBG wavelength into a measurable voltage signal.

## 6.2.2 Mach-Zehnder Interferometer

A Bragg peak of optical intensity  $I_0 = E_0^2$ , at a wavelength  $\lambda_B$  and angular frequency  $\omega = 2\pi/\lambda_B$ , travels to the input of the MZI:

$$E_{in}(x, t) = E_0 \exp[i(kx - \omega t)] \quad (6.1)$$

where  $k$  ( $= 2\pi/\lambda_B$ ) and  $E_0$  are the wavenumber and amplitude of the wave respectively. Within the MZI, the wave is split and travels along two fibre arms of differing length. This imparts a phase difference between the light in the two arms, given by:

$$\phi = \frac{2\pi nD}{\lambda_B} \quad (6.2)$$

where the optical path difference (OPD),  $nD$ , comprises silica's refractive index,  $n(\lambda) = 1.5$ , and the physical length difference between the arms,  $D$ . The phase offset results in two new waves:

$$\begin{aligned} E_A(x, t) &= \frac{E_0}{\sqrt{2}} \exp[i(kx - \omega t + \phi_A)] \\ E_B(x, t) &= \frac{E_0}{\sqrt{2}} \exp[i(kx - \omega t + \phi_B)] \end{aligned} \quad (6.3)$$

where  $\phi = \phi_A - \phi_B$ . When these waves are recombined at the MZI output, they interfere, producing an output intensity which depends on the phase difference<sup>(1)</sup> [Fra66]:

$$I = |E_A + E_B|^2 = \frac{I_0}{2} (1 + \cos(\phi)) \quad (6.4)$$

Because the phase difference is wavelength dependent, shifts in the Bragg wavelength  $\Delta\lambda_B$  result in phase changes and hence intensity changes at the output:

---

<sup>(1)</sup>This is proven explicitly in appendix A.7

$$|\Delta\phi| = \left( \frac{2\pi nD}{\lambda_B^2} \right) \Delta\lambda_B \quad (6.5)$$

The FBG's strain sensitivity from equation (4.14) can be substituted into equation (6.5) to yield a relationship between FBG strain and MZI phase:

$$\Delta\varepsilon = \frac{\lambda_B}{2\pi nD(1 - 0.22)} \Delta\phi = \zeta \lambda_B \Delta\phi \quad (6.6)$$

If the OPD and input intensity are constant, then the output intensity varies periodically with shifts in the Bragg wavelength, as shown in figure 6.2. The free spectral range (FSR) at any given wavelength,  $\lambda_0$ , is given by:

$$\Delta\lambda_{FSR} = \frac{\lambda_0^2}{nD} \quad (6.7)$$

The OPD of the interferometer used in this work was 3 mm, leading to an FSR of 0.8 nm (nanometres) at  $\lambda_0 = 1550$  nm.

### 6.2.3 Multiple MZI Outputs

In real interrogation systems, the input light intensity can vary, so an interferometer with multiple outputs is usually required to provide phase independently of input intensity. Traditionally, an interferometer with two outputs is chosen so that a ratiometric approach can be used to provide phase demodulation which is independent of intensity fluctuations. However, such approaches are not immune to the imperfections of real interferometers, which are subject to the following effects [TSB02]:

- Asymmetric coupling — this causes imperfect and non-constant phase differences between the MZI outputs
- Asymmetric losses — this means that fringe visibility is, in general, neither perfect nor constant.

Furthermore, losses and asymmetry are highly sensitive to changes in environmental variables. The resulting three unknowns — the dc offset, ac offset and

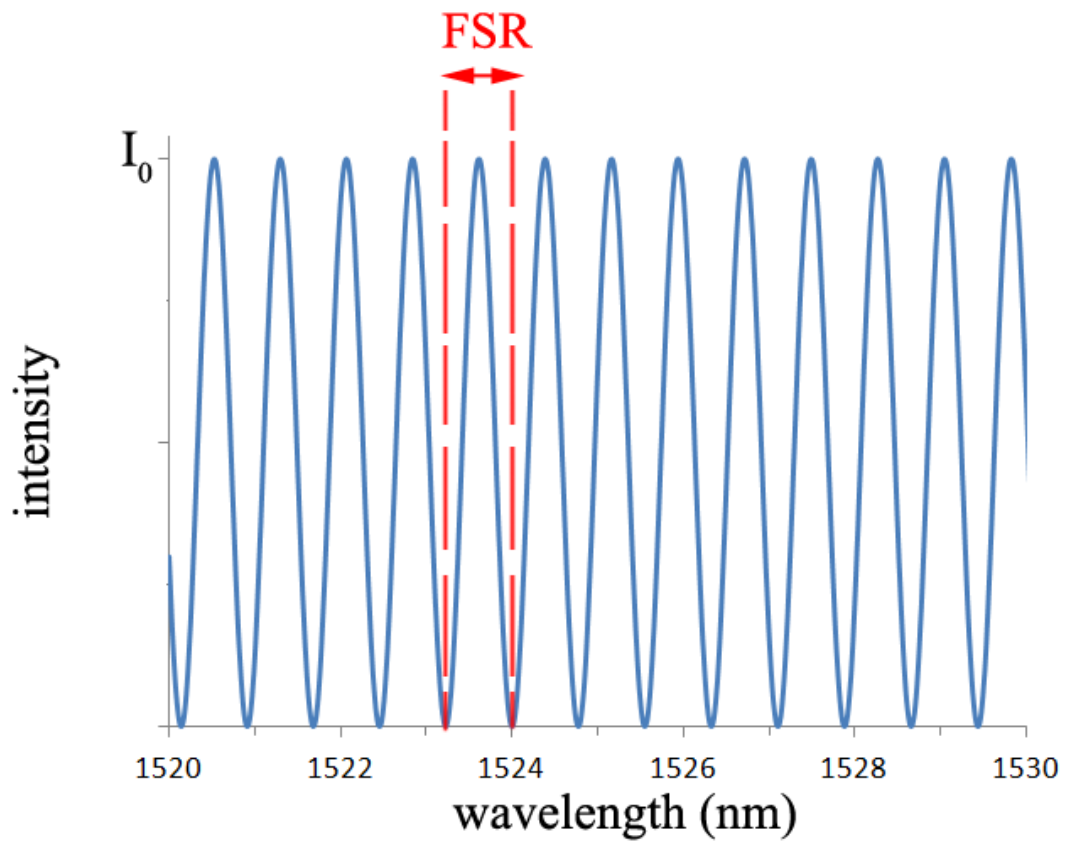


Figure 6.2: The variation of output intensity as a function of input wavelength for a perfect MZI with a constant OPD (of 3mm) and input intensity (of  $I_0$ ). The free spectral range (FSR) is the wavelength separation of the fringes at a given wavelength.

phase of the MZI outputs — mean that three equations are needed for a solution<sup>(2)</sup>.

For an MZI with three outputs, the intensities, once integrated by photodetectors, yield the following voltages ( $m = 1, 2, 3$ ):

$$\bar{V}_m = \frac{V_m}{C_1} = \frac{C_m}{C_1} + \frac{D_m}{C_1} \cos(\phi + \theta_m) \quad (6.8)$$

Here  $\theta_m = 2\pi(m - 1)/3$ , while  $C_m$  and  $D_m$  are parameters which quantify the mean and alternating components of the fringes for each channel. This relationship is shown diagrammatically in figure 6.3a. A Bragg peak entering the MZI is modulated by the three cosine waves to produce the spectra shown in figure 6.3b. The intensity can now be integrated using photodetectors, to produce three unique voltages corresponding to  $\lambda_B$ <sup>(3)</sup>.

The simultaneous equations for voltage in equation (6.8) allow changes in phase to be expressed independently of confounding variables, such as fluctuations in optical source power and attenuation [TJC99]:

$$\tan(\phi) = \frac{(\mu_2 - \mu_3)\bar{V}_1 + (\mu_3 - \mu_1)\bar{V}_2 + (\mu_1 - \mu_2)\bar{V}_3}{(\gamma_2 - \gamma_3)\bar{V}_1 + (\gamma_3 - \gamma_1)\bar{V}_2 + (\gamma_1 - \gamma_2)\bar{V}_3} \quad (6.9)$$

The normalisation parameters,  $\mu_m = \frac{D_m}{C_m} \cos(\theta_m)$  and  $\gamma_m = \frac{D_m}{C_m} \sin(\theta_m)$ , depend on the fringe depth and mean output intensity of the MZI, and the spectral shape of each FBG<sup>(4)</sup>. These parameters also capture the fact that the values of  $\theta_m$  may not be perfectly separated by  $120^\circ$  in a real system. The parameters are calculated by thermally or mechanically tuning a reference Bragg peak across the interferometer's fringes. During this calibration procedure, the amplitudes and dc offsets of the voltage responses are used to evaluate  $\mu_m$  and  $\gamma_m$  [SH92]. The calculated parameters for one FBG are then applied to all others in the array.

---

<sup>(2)</sup>An explicit proof that an interferometer with two outputs is unable to provide phase demodulation independent of extraneous effects is provided in appendix A.8

<sup>(3)</sup>Note that interference between light waves is also dependent on their relative polarisation. To prevent this extra variable from affecting long term stability of the MZI, the light entering the interferometer is depolarised.

<sup>(4)</sup>A proof of this equation can be found in appendix A.9

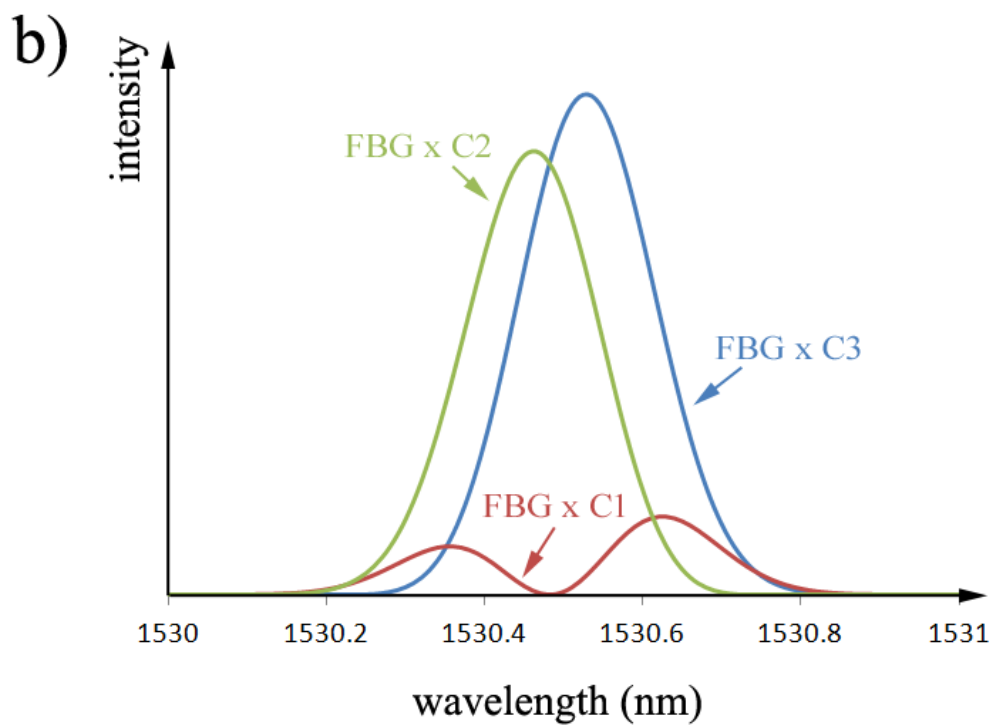
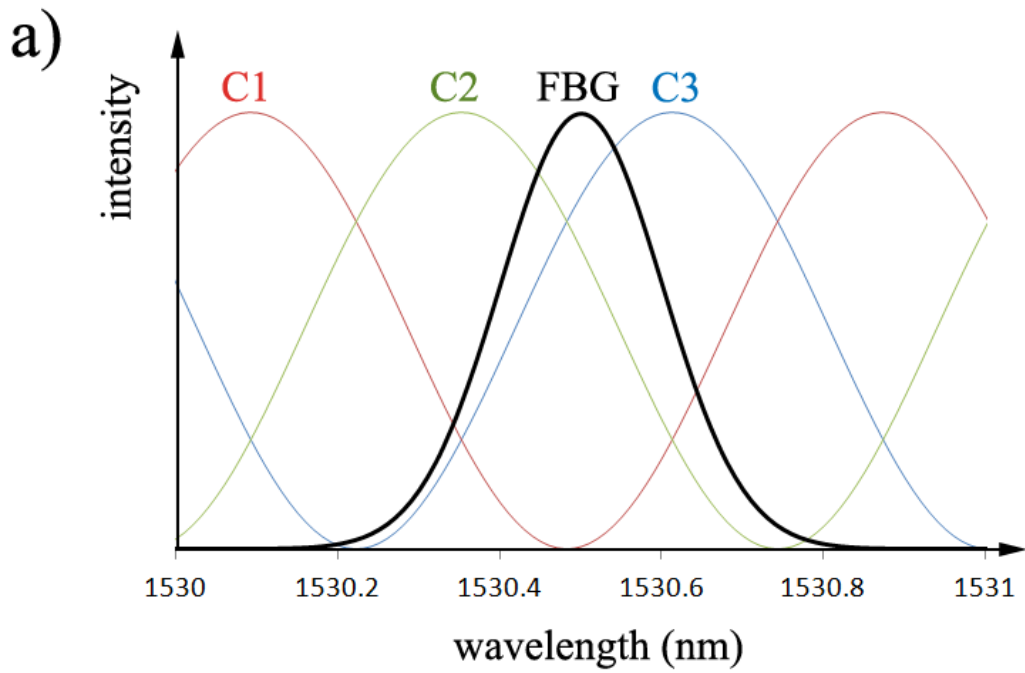


Figure 6.3: a) The three output channels of the MZI are  $2\pi/3$  out of phase from each other. These channels modulate the input Bragg peak, also shown, to produce the three spectra shown in part b). Integrating the intensity of each of these products, using a photodetector, produces three unique voltages which can be used to calculate the central value of the Bragg peak  $\lambda_B$ .

### 6.2.3.1 Advantages and Limitations

It is clear from equation (6.8) that channel voltages periodically repeat as the Bragg peak shifts over the free spectral range of the interferometer. Multiples of  $2\pi$  phase shifts are tracked and unwrapped for each FBG during system operation, but the number of fringes initially separating two FBGs is not generally known. As such, interferometric schemes like this have been historically limited to tracking only the relative wavelength shifts between sensor and reference FBGs after the system is initialised. This limitation is dealt with later in §6.6, but it is only a minor drawback in the current application. This is because if the system monitors the smart strands during the initial prestressing operation, then the strain history will be fully recorded relative to a zero strain measurement. Secondly, even if the system is switched on after initial prestressing, monitoring prestress *losses* does not require an absolute measurement.

Equations (6.5) and (6.7) also suggest that strain sensitivity of the system can be improved by increasing the OPD, as reduction in the FSR improves the fringe modulation density. There are, however, limitations—if the OPD is too large then small shifts in  $\lambda_B$  result in extremely large phase shifts over countless many fringes, making it impossible to track and unwrap phase shifts reliably<sup>(5)</sup>. Furthermore, light in the MZI can only interfere at the output provided its coherence length is larger than the OPD, i.e.  $L_c > \Delta D$ , where:

$$L_c = \frac{2\ln(2)}{\pi n_f} \frac{\lambda_B^2}{B_\lambda} \quad (6.10)$$

An FBG's narrow bandwidth, or FWHM of ( $B_\lambda \approx 0.1$  nm) typically gives rise to relatively short coherence lengths of order 10 mm. The OPD must be at least shorter than this value to ensure interference.

The major advantage of interferometers over tunable filters or lasers is that they are passive components. This means they can demodulate FBG wavelengths near instantaneously without active tuning. This also makes interferometers less

---

<sup>(5)</sup>Increasing the OPD, reduces the FSR, accentuating the modulation the three channels. If the FSR is made shorter than the FWHM of the Bragg peak, then there will be barely any changes in the photodetector voltages as the peak shifts and they become indistinguishable.

prone to faults, damage and noise.

As the system is made up of passive components, the photodetectors are the main sources of measurement noise. Photodetector voltage noise sources are summarised in figure 6.4:

- *Shot noise* — Discrete errors in voltage arise because electrons and photons are quantised. This only becomes noticeable at high photodetector sampling frequencies and when voltages and intensities are small.
- *Flicker noise* — Also called pink or 1/f noise. This arises from slow fluctuations in the metal or semiconductor components which make up the photodetector. Each octave (doubling of frequency) contains the same noise power.
- *Thermal noise* — Thermal generation of electrons in the photodiode and electrical components create dark shot noise and Johnson-Nyquist noise. Both are dependent on temperature, and are only obvious in high frequency regions where flicker noise is inappreciable.

For commercial photodetectors, the combination of the noise sources above is quoted as a power spectral density measurement called the noise effective power (NEP). The NEP for the InGaAs photodetectors used in this work was  $15 \text{ fW}/\sqrt{\text{Hz}}$ <sup>(6)</sup>.

#### 6.2.4 Signal Acquisition of Multiplexed Sensors

The MZI can only interrogate one FBG at a time, so an optical path switch and coarse wavelength division multiplexer (CWDM) are used to separate and time sequence the multiple Bragg reflections [ON11]. Again, a tunable filter could be used for demultiplexing instead of the switch-CWDM combination, but this method allows the system to be completely made up of passive components.

---

<sup>(6)</sup>Note that these values are quoted for frequencies not affected by mains hum. Current drawn from mains sockets alternates at approximately 50 Hz. This can introduce noise at this frequency and multiples or harmonics thereof. Analogue-to-digital conversion of the photodetector voltages also leads to quantisation and discretisation noise in voltage and time, but these errors are, in this case, negligible for the modern ADC boards used.

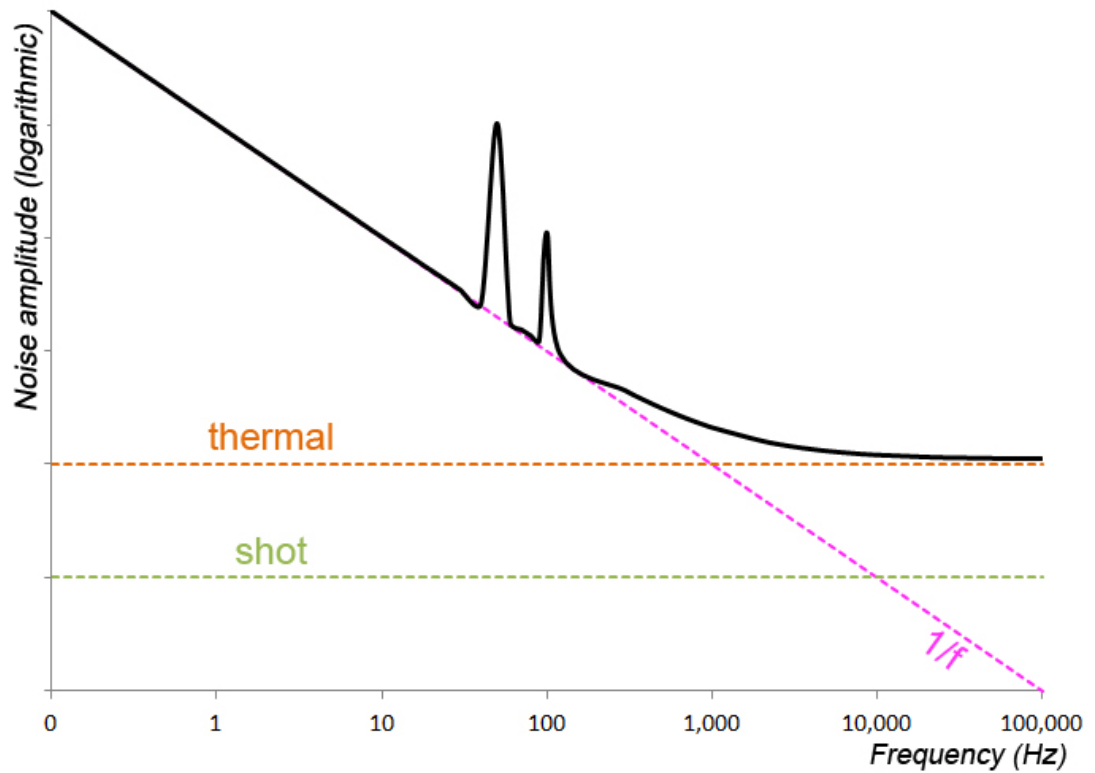


Figure 6.4: Amplitude noise sources in the photodetector system. The addition of thermal, shot, flicker ( $1/f$ ) noise and mains hum leads to the total noise, shown as a solid black line.

If two FBGs are in thermal equilibrium, then switching between them at a rate of  $f_s = 1/\Delta t_s$ , leads to interferometer output intensities which vary as illustrated in Figure 6.5. The height of the resulting square-wave is proportional to the relative static strain between the two FBGs:

$$\Delta\varepsilon = \zeta(\lambda_1\Delta\phi_1 - \lambda_2\Delta\phi_2) \quad (6.11)$$

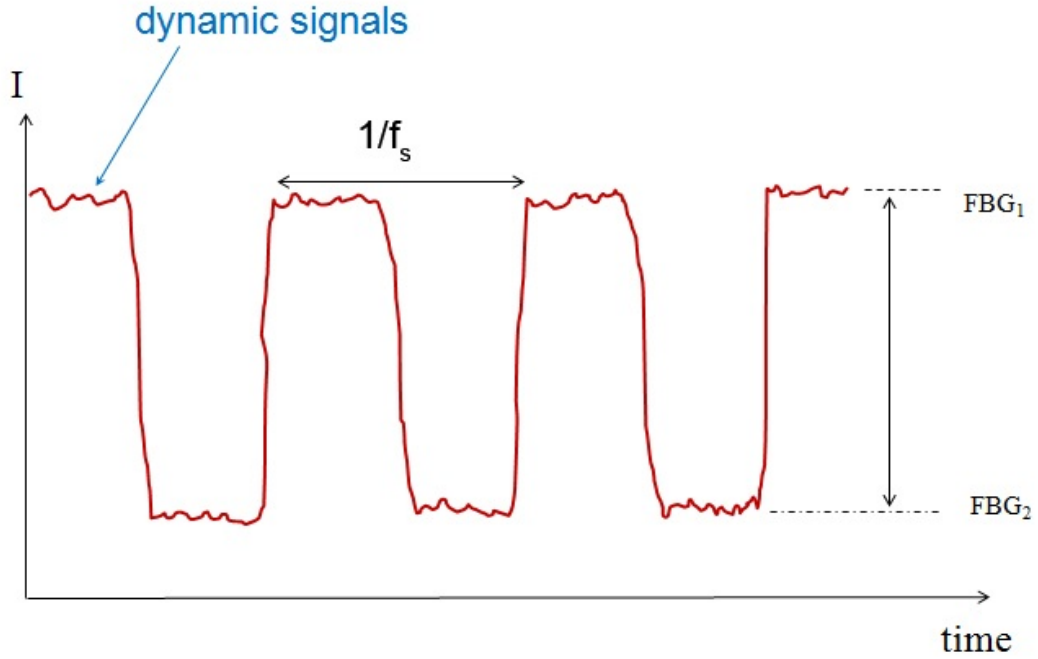


Figure 6.5: Intensity output of an interferometer port after switching between two FBGs which are at different wavelengths. By focusing on the square wave of frequency  $f_s$  the relative wavelengths of the FBGs can be measured. Dynamic information on the system can be obtained from the changes in intensity over one half of a switch cycle.

Photodetectors sample the MZI outputs at a rate  $f_{sp}$ , and so each FBG is sampled  $N = f_{sp}/f_s$  times between each flip of the switch. Any dynamic behaviour in either FBG over  $N$  samples will show up as intensity ‘noise’ in the square wave as shown in figure 6.5. Separating and extracting the dynamic and static strain signals from the square wave requires signal extraction algorithms. Two extraction methods are described in the following sections, Fourier transforms and lock-in amplification, as each provides advantages for either dynamic or static strain monitoring.

## 6.3 Signal Extraction: Fourier Transform

Fourier transforms,  $\mathcal{F}$ , allow the time-varying square waves picked up by the photodetectors to be described in frequency-space [Boa05]. They achieve this by assuming that the temporal signals can be described by an infinite series of sine waves [Bri88]. In a discrete Fourier transform (DFT), the sequence of time-discrete measured values,  $x[n]$ , are converted to the frequency-discrete sequence,  $X[u]$  via:

$$\mathcal{F}(x[n]) = X[u] = \sum_{n=0}^{N-1} x[n].\exp\left(\frac{-2\pi i u n}{N}\right) \quad (6.12)$$

where  $u$  is a counter running from  $u=0$  to  $N$ , and  $i = \sqrt{-1}$ . The inverse DFT is used to convert back to  $x[n]$ :

$$\mathcal{F}^{-1}(X[u]) = x[n] = \frac{1}{N} \sum_{u=0}^N X[u].\exp\left(\frac{2\pi i u n}{N}\right) \quad (6.13)$$

Note that  $x[n]$  and  $X[u]$  are complex numbers and so contain both the amplitude and phase information of the waveforms they describe. DFTs are able to highlight the relative amplitude of underlying frequencies in complicated waveforms. By utilising a DFT algorithm called a fast Fourier transform (FFT), the frequencies which comprise a seemingly useless, noisy signal are highlighted as peaks, as shown in figure 6.6.

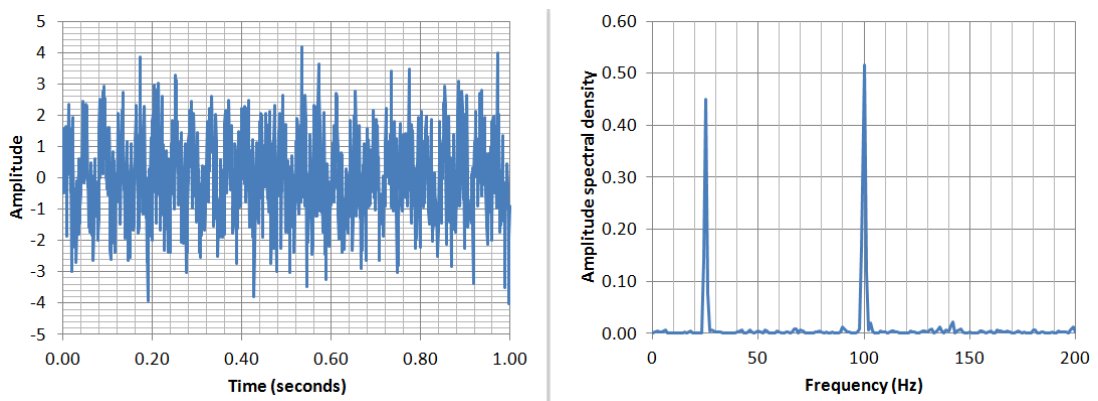


Figure 6.6: Taking the FFT of a seemingly noisy signal (left) reveals the ‘hidden’ 25 and 100 Hz frequency components (right).

In Fourier space, the signal square wave of amplitude  $A$  and angular frequency  $\omega_s = 2\pi f_s$  is described by the series:

$$f(t) = \frac{4A}{\pi} \sum_{k=1}^{\infty} \frac{\sin[(2k-1)\omega_s t]}{2k-1} \quad (6.14)$$

$$= \frac{4A}{\pi} \left( \sin(\omega_s t) + \frac{1}{3}\sin(3\omega_s t) + \frac{1}{5}\sin(5\omega_s t) + \dots \right)$$

as illustrated in figure 6.7. The height of the square wave (or the strain signal, in this case) can thus be found from the amplitude of the peak at  $\omega_s$ . Higher terms, or harmonics, at  $3\omega_s$ ,  $5\omega_s$ , etc. carry proportionally less weight.

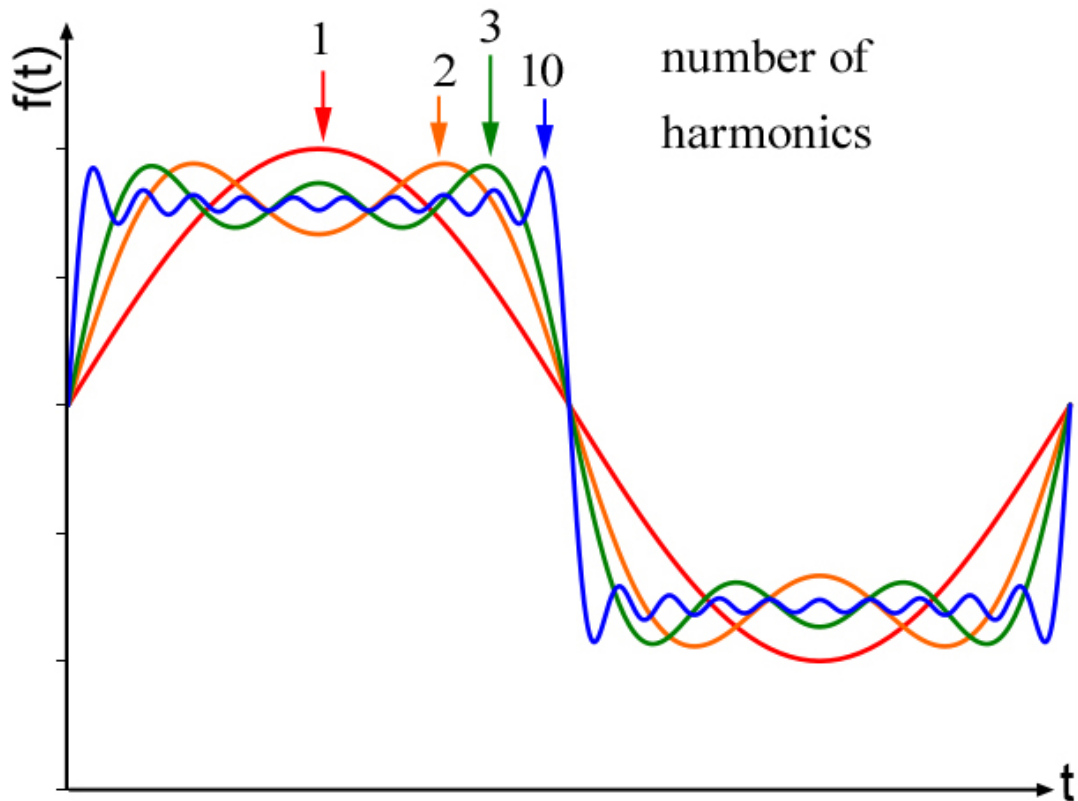


Figure 6.7: As the higher harmonics are added, the function begins to resemble a square wave more closely.

### 6.3.1 Sampling and Aliasing

The limitations of an FFT are mainly governed by how its input sequence is sampled. The sampling frequency,  $f_{sp}$  is the number of samples,  $N$ , the photodetector acquires in a given sampling time  $t_{sp}$ :

$$f_{sp} = \frac{N}{t_{sp}} \quad (6.15)$$

As shown in figure 6.8, sampling a continuous waveform,  $x(t)$ , at 1 Hz produces a time-discrete waveform,  $x[n] = x(n \cdot t_{sp})$  <sup>(7)</sup>.

Higher sampling frequencies improve the ‘discrete description’ of the continuous waveform, allowing it to be reconstructed more accurately through interpolation. The Nyquist-Shannon sampling theorem states that perfect reconstruction of a continuous signal is possible, provided that sampling is performed at above twice the rate of any changes in the waveform:

$$f_{sp} > 2f_w \quad (6.16)$$

Frequencies beyond the Nyquist limit,  $0.5f_{sp}$ , are not described by the FFT. They may, however, still interfere due to a phenomenon known as aliasing. Figure 6.9 shows that when a  $f_w = 10$  Hz waveform is sampled at a rate  $f_{sp} = 12$  Hz, then the sampled points actually describe a 2 Hz ‘alias waveform’ after interpolation. In general, when the sampling rate lies in the region  $f_w > f_{sp} > 2f_w$  an alias appears at the frequency  $f' = f_{sp} - f_w$ .

Aliasing allows frequencies above the Nyquist limit to produce peaks in the observed FFT spectrum. As shown in figure 6.10, sampled frequencies are reflected multiple times about the Nyquist until they fall within the observed FFT. This can lead to inaccuracies, especially when the harmonics from square waves are aliased. Filtering high frequencies or extending the Nyquist-limit through oversampling can reduce aliasing <sup>(8)</sup>. The photodetectors used in this work have

---

<sup>(7)</sup>The amplitudes of each sample in  $x[n]$  can still take any analogue value. Further digitisation of the amplitude would be required to achieve a truly digital signal.

<sup>(8)</sup>Note that aliasing is a result of sampling, not the result of performing an FFT. It will thus also affect a lock-in amplifier, see §6.4.

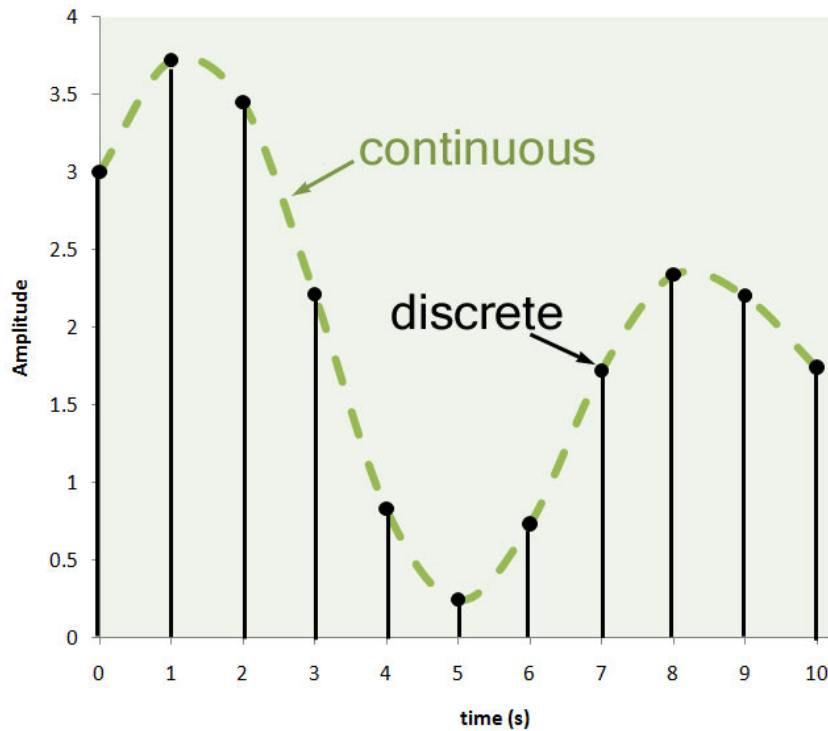


Figure 6.8: Diagram showing the sampling of a continuous signal at a rate of 1 Hz. The discrete description can be interpolated to attempt to recover the original continuous signal.

a limited response time, so they naturally filter any frequencies beyond 1 MHz.

### 6.3.2 Frequency, Time and Amplitude Resolution

The frequency bin size of an FFT is given by:

$$\Delta f = \frac{f_{sp}}{N} \quad (6.17)$$

where  $N$  is the number of samples, acquired at a sampling rate  $f_{sp}$ . Because the time required to acquire these samples scales via  $N/f_{sp}$ , there is a natural trade-off between temporal response and frequency resolution in an FFT.

Amplitude noise or resolution in an FFT is described by amplitude spectral density, in units of  $[V/\sqrt{\text{Hz}}]$ . Because larger bin sizes can group noise together, the amplitude spectral density is used to define the noise floor of an FFT independently of its bin size.

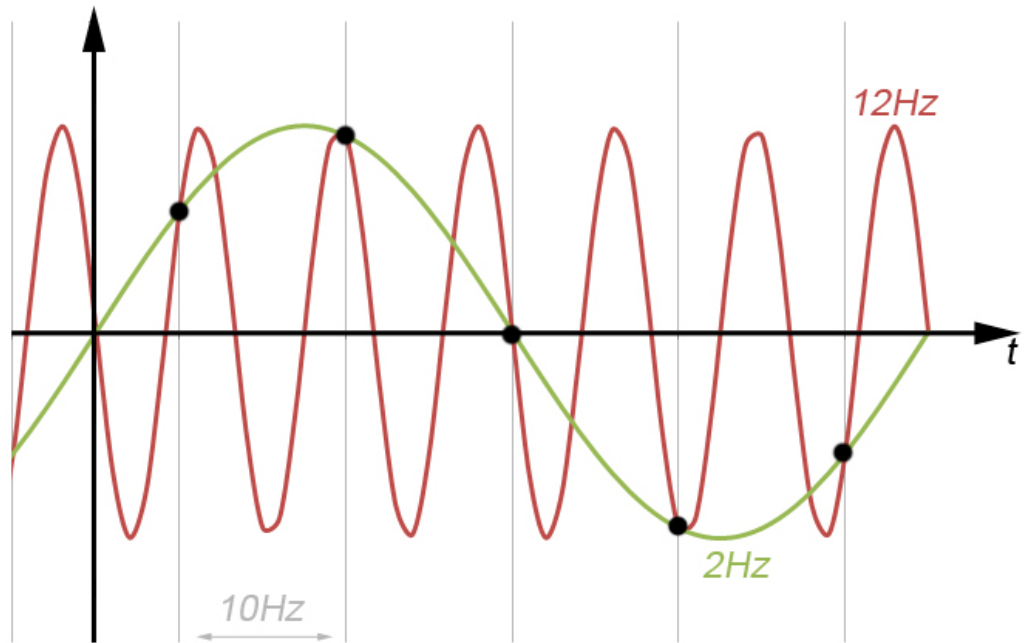


Figure 6.9: A waveform at 10 Hz is depicted by the vertical grey lines, spaced 0.1 s apart. This waveform is sampled at 12 Hz (shown by the red line) and then discretised. The interpolation of the discrete points will be a continuous signal at 2 Hz. This is because the same set of points describe both the 10 Hz and 2 Hz signals, when sampling at 12 Hz.

### 6.3.3 FFT Summary

FFTs are very well suited to frequency domain analysis of complicated signals. Once the frequencies of interest are selected, the Nyquist-Shannon sampling theorem provides the minimum sampling rate. By low-pass filtering before sampling, aliasing down of higher frequencies about the Nyquist limit is avoided. This is particularly important for square waves, which have gradually decaying harmonics at higher frequencies of the base oscillation.

Reducing frequency bin size of the FFT spectrum prevents signal aggregation and allows for accurate amplitude measurements. However, the large sampling rates or sample sizes required to do this can limit a system's cost effectiveness or temporal responsiveness.

The thorough frequency analysis provided by an FFT is its main strength. However, when attempting to extract the amplitude of one signal with one *known* frequency, most of the calculations and results of an FFT are irrelevant and may

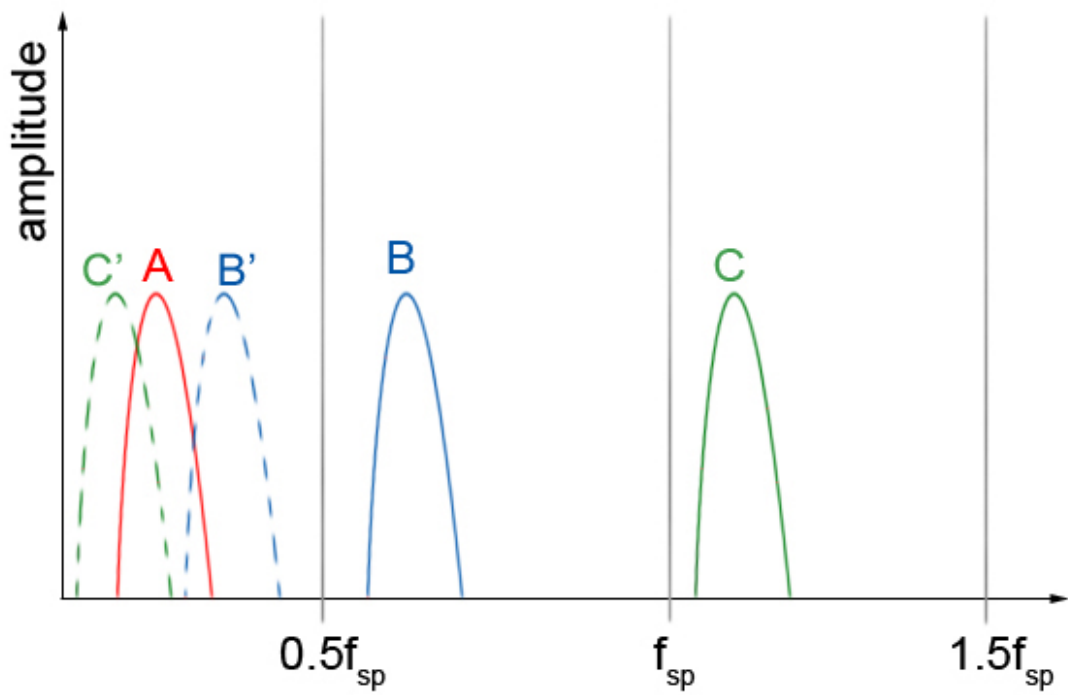


Figure 6.10: Reflection about the Nyquist. While only frequencies  $< 0.5f_{sp}$  should be observable, reflections at multiples of the Nyquist limit ( $0.5, 1, 1.5, \dots f_{sp}$ ), mean higher frequencies are brought into the observable FFT spectrum.

even be damaging to the final strain resolution. For this particular task, lock-in amplification may be superior.

## 6.4 Signal Extraction: Lock-in Amplifier

Lock-in amplifiers are commonly used to extract small signals of a known frequency from a sea of noise [Sco94, Bur05, PJ94]. In this section, the measurement of simple sine waves will first be considered, before adding the complications of real-life systems, such as noise and square waveforms.

### 6.4.1 Basic Theory

The interrogation system is driven by a signal which flips the optical path switch attached to the CWDM. This **input** can be described using the amplitude  $B$ , frequency  $\omega_r$  and phase offset  $\phi_r$  of the square wave:

$$h(t) = B \operatorname{sgn}[\sin(\omega_r t + \phi_r)] \quad (6.18)$$

The interrogation system reacts to this square wave input by producing a **strain signal** output with an amplitude, angular frequency and phase offset given by  $A$ ,  $\omega_s$  and  $\phi_s$  respectively:

$$f(t) = A \sin(\omega_s t + \phi_s) \quad (6.19)$$

To extract the amplitude  $A$  of the strain signal, it is mixed with a **reference** waveform derived from the original input function,  $h(t)$ :

$$g(t) = B \sin(\omega_r t + \phi_r) \quad (6.20)$$

This reference is phase-locked to the input waveform using a feedback loop. Multiplication of the reference with the signal then yields:

$$\begin{aligned} f(t).g(t) &= AB \sin(\omega_s t + \phi_s) \sin(\omega_r t + \phi_r) \\ &= \frac{1}{2} AB \cos([\omega_s - \omega_r]t + [\phi_s - \phi_r]) \\ &\quad - \frac{1}{2} AB \cos([\omega_s + \omega_r]t + [\phi_s + \phi_r]) \end{aligned} \quad (6.21)$$

The two cosine terms are at sum  $(\omega_r + \omega_s)$  and difference  $(\omega_r - \omega_s)$  frequencies of the reference and signal. Feeding the product through a low pass filter, with transfer function  $\mathbb{G}$ , will allow rejection of frequency components  $\omega > \omega_F$  leaving only the difference term:

$$V(t) = V_0(t) = \mathbb{G}[f(t).g(t)] = \frac{1}{2}AB \cos([\omega_s - \omega_r]t + [\phi_s - \phi_r]) \quad (6.22)$$

Furthermore, because the strain signal oscillates at the same frequency as the reference ( $\omega_s = \omega_r$ ), the result above will not vary in time:

$$V_0 = \frac{1}{2}AB \cos(\phi_s - \phi_r) \quad (6.23)$$

The reference amplitude,  $B = 1$ , is a known quantity, so the strain signal amplitude  $A$ , can be obtained from this relationship, provided the phase difference of the two waveforms is known or can be reduced to zero ( $\phi_s = \phi_r$ ). Frequency mixing and low-pass filtering form the basis of lock-in amplification. The choice of the low pass filter in particular defines the lock-in amplifier's response time and resolution.

### 6.4.2 Low Pass Filters

Low pass filters are characterised mainly by their bandwidth/cut-off frequency,  $\omega_F$  and roll off,  $R$ . Oscillations which fall within the pass band of a perfect filter ( $\omega < \omega_F$ ) are allowed to pass through unattenuated. Those above the bandwidth, in the stop band  $\omega > \omega_F$ , experience attenuation (negative gain) with a magnitude characterised by the roll off [HH89]. Filters attenuate stop-band frequencies exponentially, so roll off is defined by how many decibels a signal is attenuated with each decade change in frequency.

The gain-vs-frequency relationship depends on the filter type. A frequency response plot for Butterworth and Chebyshev filters, shown in figure 6.11, highlights their relative advantages. Chebyshev filters typically exhibit a steeper roll off, but the rippling around the cut-off frequency can cause non-uniform attenuation of

pass band frequencies. Butterworth filters allow a much smoother transition over the cut-off frequency, but roll off more gently, allowing some stop band frequencies to pass with mild attenuation. In this work, the cut off frequency could be chosen to lie in a region where there were no important signals. As such, a high-order Chebyshev filter was utilised for lock-in, as it heavily attenuates higher frequencies.

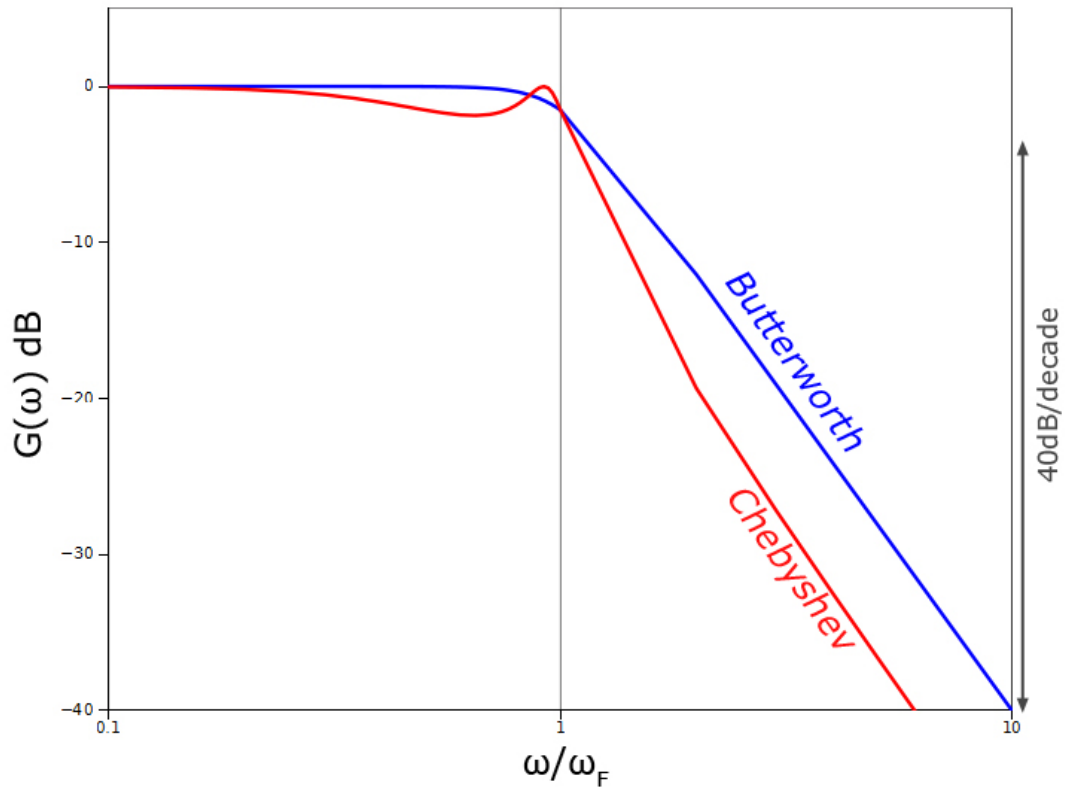


Figure 6.11: Frequency response (Bode plot) of fourth order ( $n=4$ ) Butterworth and type-I Chebyshev filters ( $\epsilon = 1$ ). Chebyshev filters attenuate stop band frequencies more than Butterworth filters, at the expense of rippling gain around the cut-off frequency. Shown also is the roll off,  $R = 40\text{dB/decade}$ , of the Butterworth filter.

#### 6.4.2.1 Noise Rejection

To further appreciate the importance of filtering, noise terms must be introduced to the simple examples given in §6.4.1. Noise terms are introduced to signal and reference waveforms:

$$f(t) = A \sin(\omega_s t) + C_1 \sin(\omega_1 t) \quad (6.24)$$

$$g(t) = B \sin(\omega_r t) + C_2 \sin(\omega_2 t)$$

where  $C_i$  and  $\omega_i$  describe the amplitude and frequency of the noise <sup>(9)</sup>. After mixing and low pass filtering, the resulting terms are:

$$\begin{aligned} V(t) = \mathbb{G}[f(t).g(t)] &= \frac{1}{2}[AB \cos([\omega_s - \omega_r]t) \\ &+ AC_2 \cos([\omega_s - \omega_2]t) \\ &+ BC_1 \cos([\omega_r - \omega_1]t) \\ &+ C_1C_2 \cos([\omega_1 - \omega_2]t)] \\ &= V_0(t) + V_{noise}(t) \end{aligned} \quad (6.25)$$

If any of the above difference frequencies fall below the filter's cut-off, then they will contribute slowly oscillating errors to the final result. As there may be infinite noise components (albeit of varying magnitude), choosing harsh rejection parameters is extremely important to generate a stable result.

#### 6.4.2.2 Settling Time

At this point, it may seem apt to choose a cut-off frequency which is as low as possible. After all, if the result from signal-reference mixing truly is dc, allowing  $\omega_F \rightarrow 0$  Hz will perfectly eliminate all noise sources. A further argument for a 'zero' cut-off frequency stems from the fact that in reality  $\omega_r \neq \omega_s$ . Small fluctuations in the frequencies of either the reference or signal introduce a slowly varying error in the result, which again could be ignored if a 0 Hz cut-off frequency filter is used.

While allowing  $\omega_F \rightarrow 0$  Hz will result in a very stable system, it will also

---

<sup>(9)</sup>In reality there may be numerous noise contributions and phase offsets to each waveform, but only two noise sources are considered here for illustrative purposes.

result in an unresponsive one. The time constant of a filter is a measure of how long it takes to react to a change in the strain signal:

$$\tau_F = \frac{1}{\omega_F} \quad (6.26)$$

The settling time (how long the filter output takes to fall within 10% of the input value) is usually taken as  $4\tau_F$ . Figure 6.12, shows that a filters with a low cut-off frequency will take a long time to respond to sudden changes in the strain signal (10).

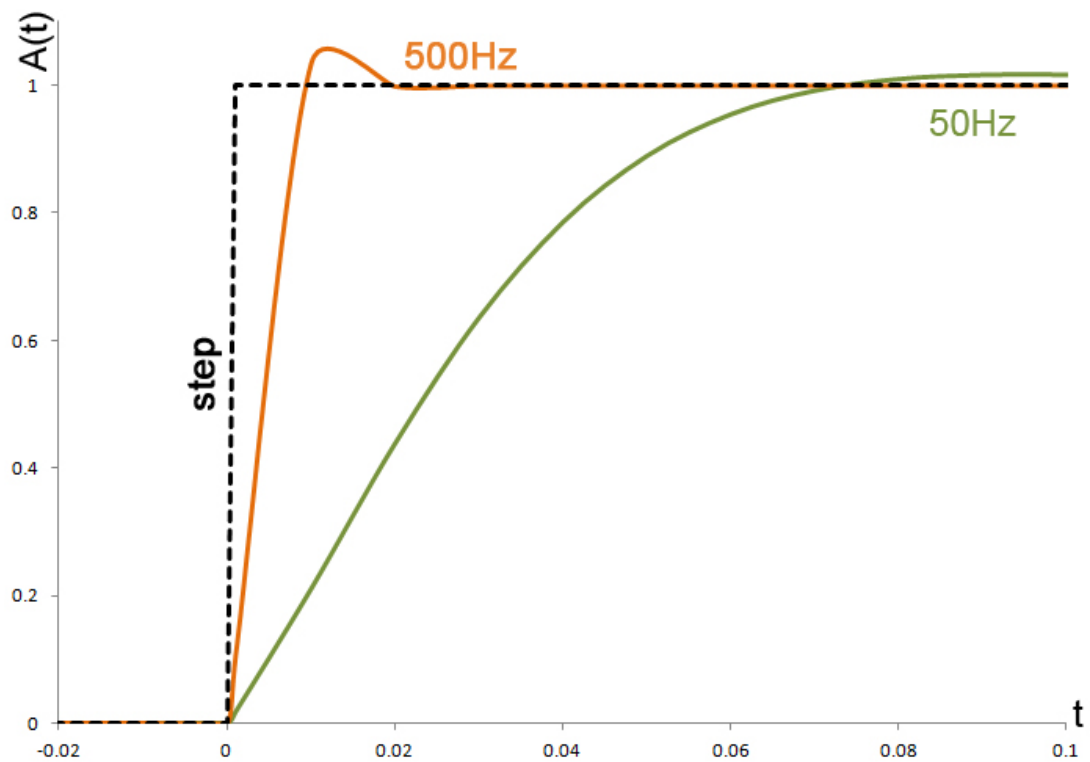


Figure 6.12: The settling time of two filters after a step rise in  $A$ . Settling times for 50 and 500 Hz filters are shown to be 0.08 and 0.008 s respectively.

### 6.4.2.3 FIR vs IIR

Low-pass filters can also have either finite or infinite impulse responses (FIR and IIR). An  $N^{\text{th}}$  order FIR filter compares the current value of  $A$  with the  $N$  before

<sup>(10)</sup>The trade-off between cut-off frequency and settling time can also be understood by considering the step change as a Fourier series. The step change in figure 6.12 is, in fact, composed of an infinite series of sine waves. Limiting  $\omega_F$  discards essential high-frequency components, resulting in a smooth and slow response.

it and uses this to adjust its output. IIR filters react to previous values of  $A$  but also take into consideration the previous adjustments that were made.

IIR filtering is used in this work as it allows the lock-in amplifier to react more quickly to strain changes. Any errors in the input may be compounded in further iterations, however. This can make runaway instabilities more common, if there are, for example, voltage spikes in the photodetectors which are not ignored.

### 6.4.3 Lock-in Summary

Lock-in amplification involves three steps:

1. Phase-locking a sinusoidal reference waveform to the input driving a system
2. Multiplying the reference and system output signal waveforms
3. Low pass filtering the result to retrieve the DC component

High-order IIR Chebyshev filters are used in this work as they allow unwanted noise frequencies to be strongly attenuated. As filter settling time is inversely proportional to the cut-off frequency, there is a trade off between achieving system responsivity and precision.

Ideally, lock-in amplifiers only supply extremely high-resolution, accurate information about a single frequency. This makes them less suited to the measurement of frequencies which are not driven by the system input (such as dynamic, oscillating strain signals). These signals are, however, still picked up as a variation in the dc component of the lock-in. Reliably finding the amplitude and frequency of dynamic strain signals is still better performed using a Fourier transform.

## 6.5 System tests

A simple cantilever set up was used to test the relative merits of the FFT and lock-in amplifier algorithms along with interrogation system's measurement performance. An FBG at a wavelength ( $\lambda_2 = 1554.66$  nm) was attached to a cantilever using epoxy. To eliminate the thermal response, the FBG's wavelength

Parameter	Symbol	Value	Units
Sampling Rate	$f_{sp}$	50	kHz
Switch Rate	$f_S$	500	Hz
Sample size	$N$	100	samples
Result size	$\Gamma$	1000	results
cut-off Freq	$f_F$	500	Hz
Filter roll off	$R$	200	dB/dec
Harmonic Order	$m$	1	

Table 6.1: Default parameters of the interrogation system. Harmonic order states which harmonic of the square wave is used by the lock-in or FFT. The Lock-in amplifier uses an IIR Chebyshev filter with a roll off of  $R$ .

was compared to a temperature reference ( $\lambda_1 = 1536.02$  nm), as shown in figure 6.1.

### 6.5.1 Signal Extraction Software

The default values of the parameters relevant to sampling and signal extraction are given in table 6.1. The block diagram shown in figure 6.13 highlights steps which were taken to evaluate relative algorithm performance. Over a given measurement period, a number,  $\Gamma$ , of strain measurements, were extracted using the primary FFT and lock-in amplifier algorithms. A ‘max-min’ algorithm was also used to find the peak-to-peak amplitude of the square-wave by calculating the difference between its highest and lowest values. This resulted in a minimal response time, at the expense of higher noise and inaccuracy.

The standard deviation of  $\Gamma = 1000$  static strain measurements was used to gauge strain resolutions. Temporal response was measured by striking the cantilever to generate a strain impulse. The temporal evolution of the lock-in and primary FFT were compared with the max-min method. A secondary FFT of  $\Gamma = 400$  strain measurements could also be used to reveal dynamic strain components in the signal.

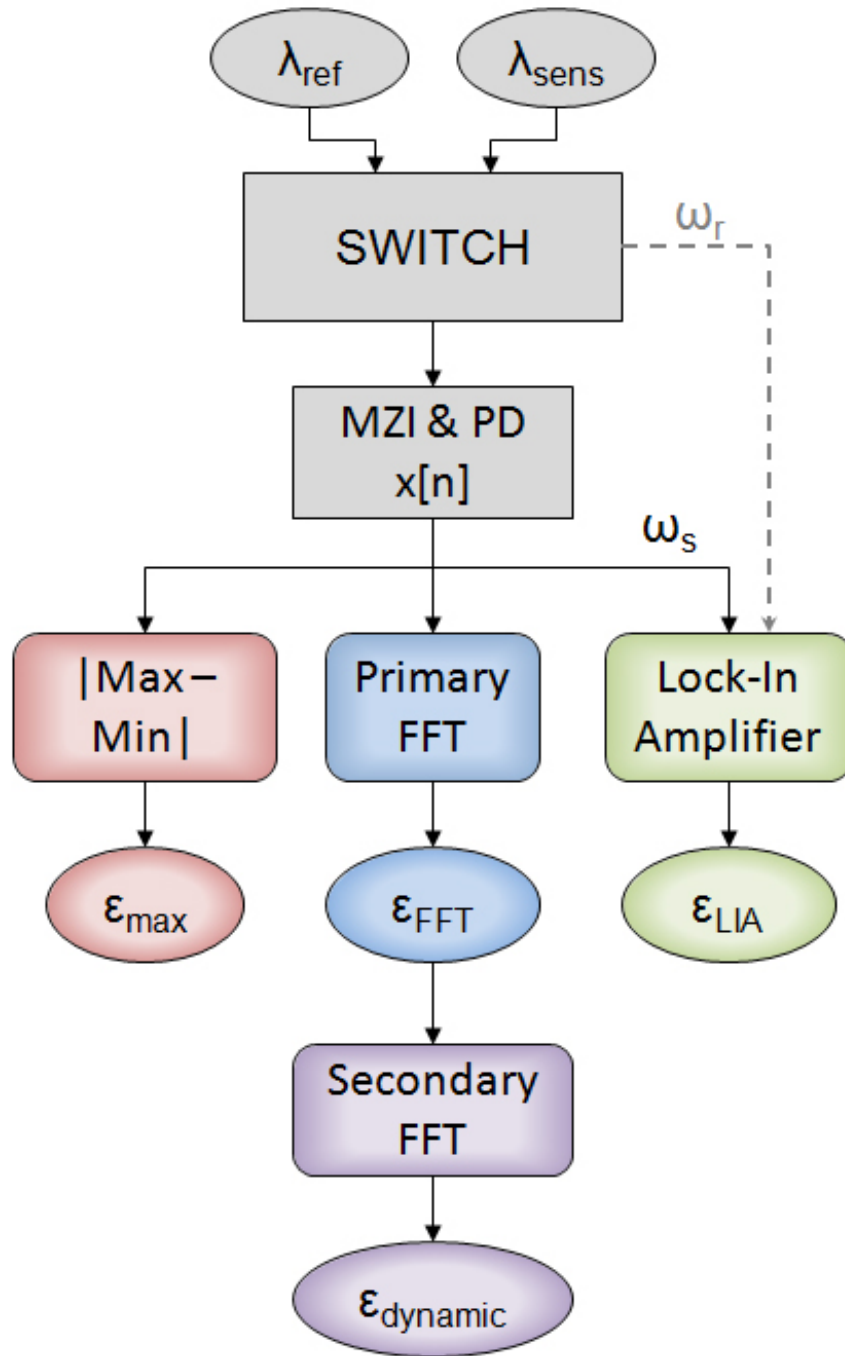


Figure 6.13: Block diagram outlining the steps used to assess relative algorithm performance. The voltages output from the interrogation scheme from the MZI and PDs (photodetectors) are converted to a signal square-wave,  $x[n]$ , with an amplitude proportional to the strain differential  $\Delta\epsilon$ . Algorithms ranging from highly-responsive (max-min) to low-noise (lock-in amplifier) are each used to extract a strain measurement from the amplitude of  $x[n]$ . A number  $\Gamma$  of strain measurements acquired by the primary FFT may be passed to a secondary FFT for a frequency analysis.

## 6.5.2 Cut-off Frequency

The lock-in amplifier's static strain noise as a function of filter cut-off frequency is shown in figure 6.14a. Noise components were gradually attenuated as the cut-off frequency was decreased from 10 kHz. Cut-off frequencies below 3 kHz are shown in figure 6.14b. Strain noise eventually reached a minimum of  $\pm 1 \text{ n}\epsilon$  and was no longer Gaussian. This baseline noise arises due to imperfect temperature compensation between the FBGs and thermal drifts in the MZI. There was, of course, also trade-off between resolution and system response time. Reducing the strain noise from 20 to 2  $\text{n}\epsilon$  increased response times from 1 ms to 0.1 s.

## 6.5.3 Sample Size

Increasing the number of samples,  $N$ , passed to the FFT also improved strain resolution at the expense of response time. As shown in figure 6.15, a minimum strain resolution of 5  $\text{n}\epsilon$  was obtained for a 40 ms sampling time. Increasing  $N$  makes resolving rapid, sequential impulses in the system challenging. This problem equally affects the lock-in amplifier, which does not benefit from the increased sample sizes.

## 6.5.4 Switching Frequency

As shown in figure 6.16, increasing the optical path switch's frequency had little effect on amplitude noise in the FFT, as it mainly depends on the rate and volume of sample acquisition. The strain resolution of the lock-in amplifier, however, was dramatically improved, without reducing system response times. This is because the strain signal is a square wave (of frequency  $\omega_s$ ). When it is mixed with the reference sine wave (of frequency  $\omega_r$ ), harmonic difference frequencies are produced ( $l\omega_s - \omega_r$ ). If  $\omega_s$  is small, then these harmonic frequencies are more likely to pass through the low-pass filter. Switching at a faster rate creates a larger difference between the reference and the harmonics, reducing the likelihood of these components (and their aliases) from passing through the filter.

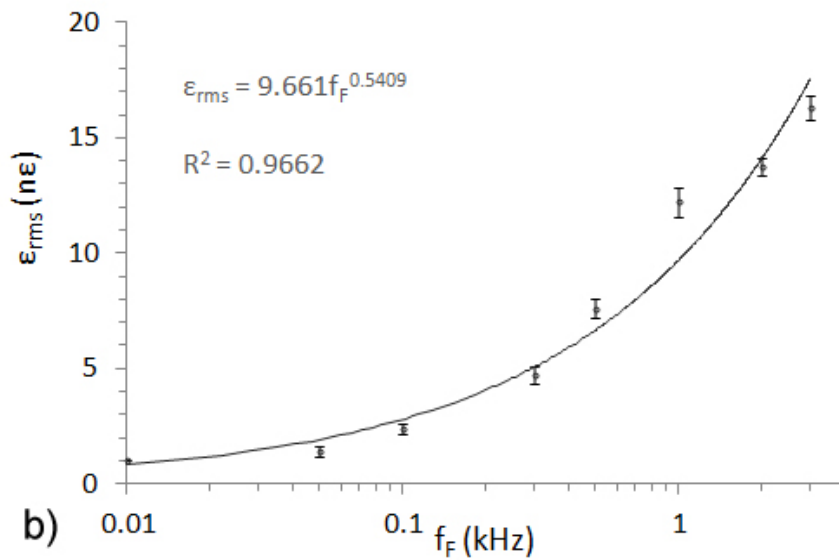
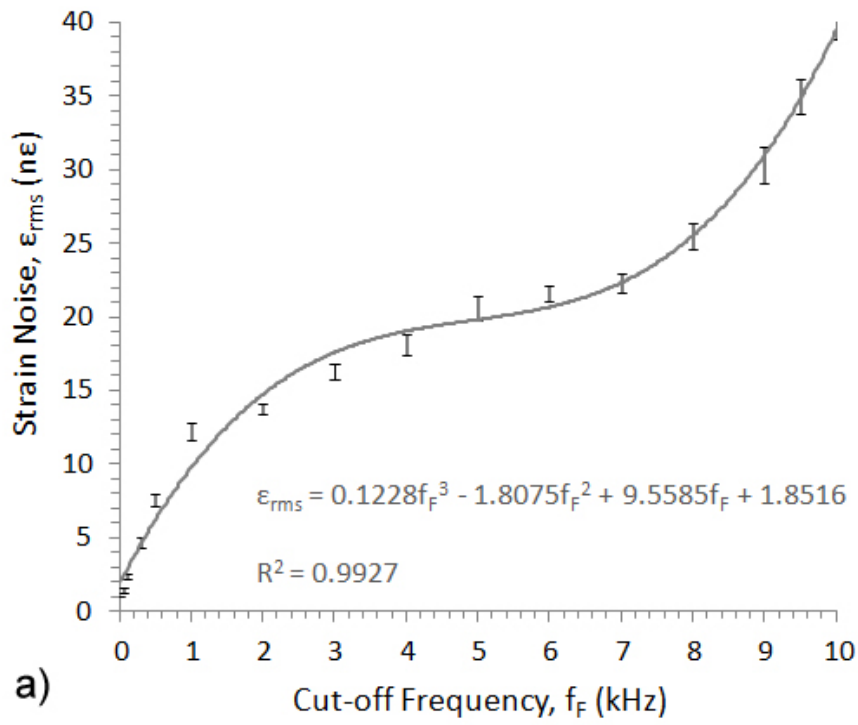


Figure 6.14: Strain noise,  $\epsilon_{rms}$  as a function of lock-in filter cut-off frequency,  $f_F$  between a) 10 Hz and 10kHz and b) 10 Hz and 3000 Hz. The turning point at around 5 kHz is due to the gradual rejection of the sum and difference frequencies arising from signal-reference multiplication. The current system is limited to a minimum noise of  $\pm 1$  n $\epsilon$  due to imperfect temperature compensation.  $R^2$  values show the correlation coefficients of the fits.

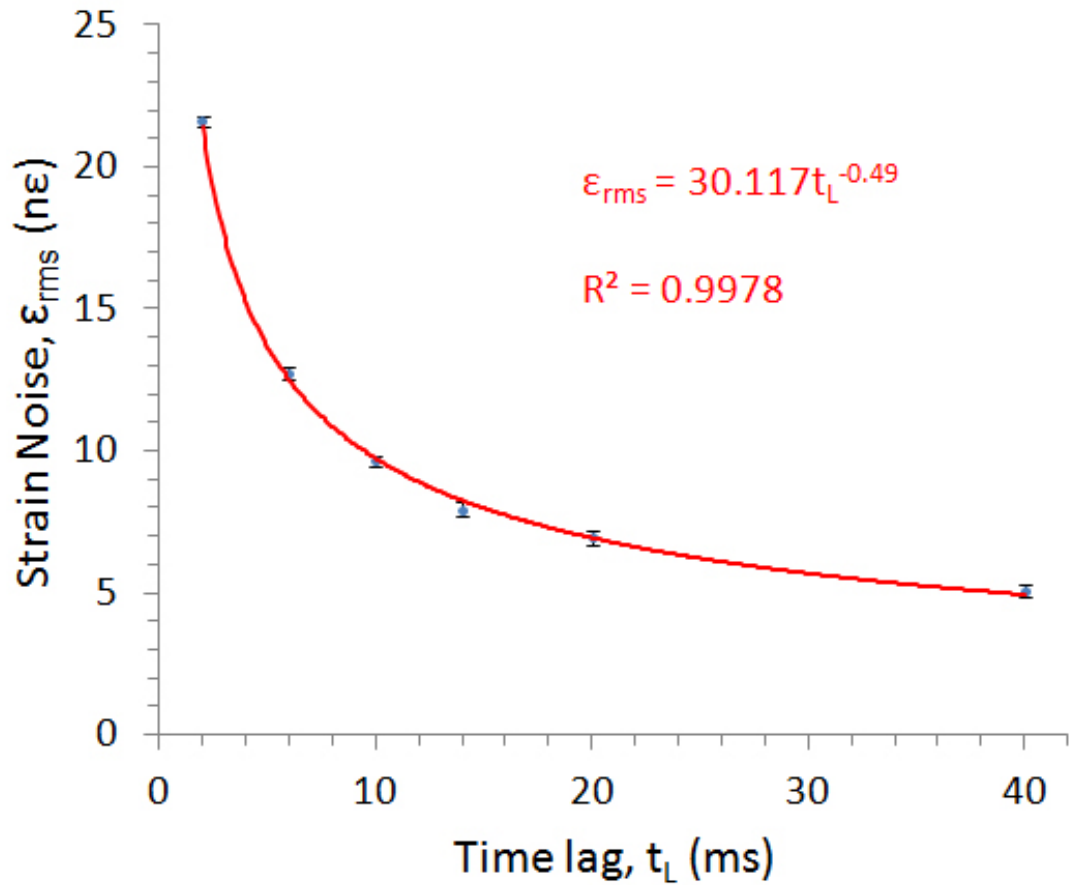


Figure 6.15: Noise,  $\epsilon_{rms}$ , in the strain measured by the FFT as a function of time lag,  $t_L$ . These results were obtained by varying sample sizes in the range  $N=[100,1000]$ . The inverse square root dependence stems from the strain scaling with the square root of FFT power, and fits with a correlation factor of 0.9978.

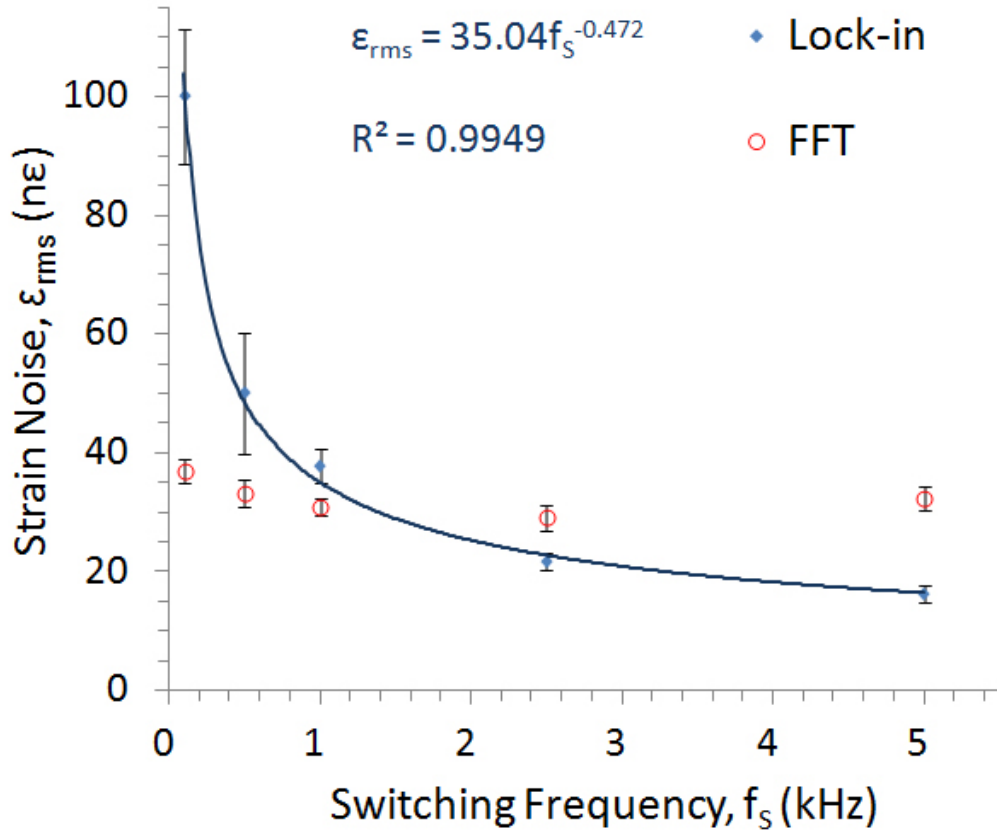


Figure 6.16: The dependence of FFT and lock-in strain noise,  $\epsilon_{rms}$ , on the switching frequency,  $f_s$ , for a cut-off frequency of 1 kHz. There is no correlation between switching frequency and amplitude noise in the FFT. In the lock-in amplifier, the linear introduction of harmonic power noise for reduced switching frequencies leads to an inverse square-root dependence between amplitude noise and switching rate (correlation coefficient 0.9949).

### 6.5.5 High Frequency Measurements

To assess the dynamic performance of the interrogation scheme at mid-range frequencies, a loudspeaker was used to drive the cantilever at frequencies below 2 kHz. A primary FFT of  $N=10$  samples (sampled at a rate  $f_{sp} = 40$  kHz) provided FBG strain measurements. A secondary FFT of  $\Gamma = 400$  of these measurements was then used to analyse dynamic strain oscillations. A collection of secondary FFT spectra for various cantilever driving frequencies are shown in figure 6.17. As shown, the system is fully capable of measuring sub-microstrain signals up to 2 kHz, with a noise floor of  $7 \text{ n}\epsilon/\sqrt{\text{Hz}}$  above 5 Hz.

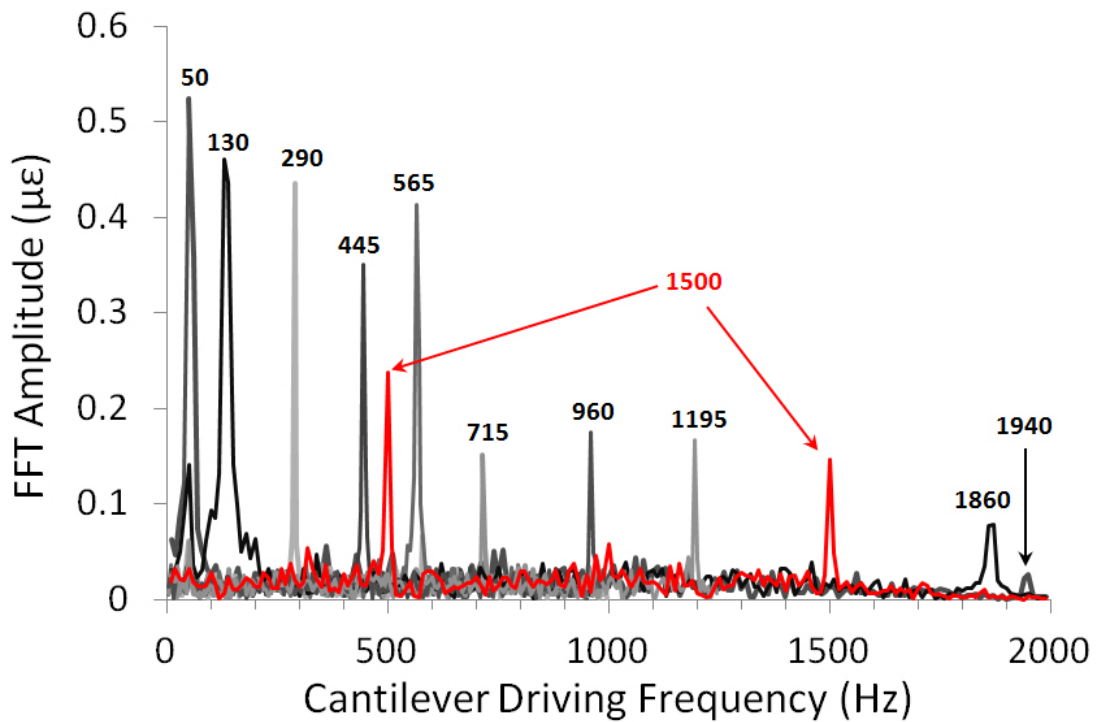


Figure 6.17: Collection of secondary FFTs of FBG strain, as measured for a cantilever driven by a loudspeaker, operating at driving frequencies between 0.05 and 2 kHz. Variations in amplitude and secondary harmonics arise from resonant frequencies within the experimental set. Above 5 Hz, the noise floor is  $7 \text{ n}\epsilon/\sqrt{\text{Hz}}$ .

Due to the two-step process, the second FFT's bandwidth was inversely proportional to the resolution of the primary FFT. As the primary FFT must be able to resolve the signal square-wave accurately, system bandwidth was limited by the 40 kHz sampling rate.

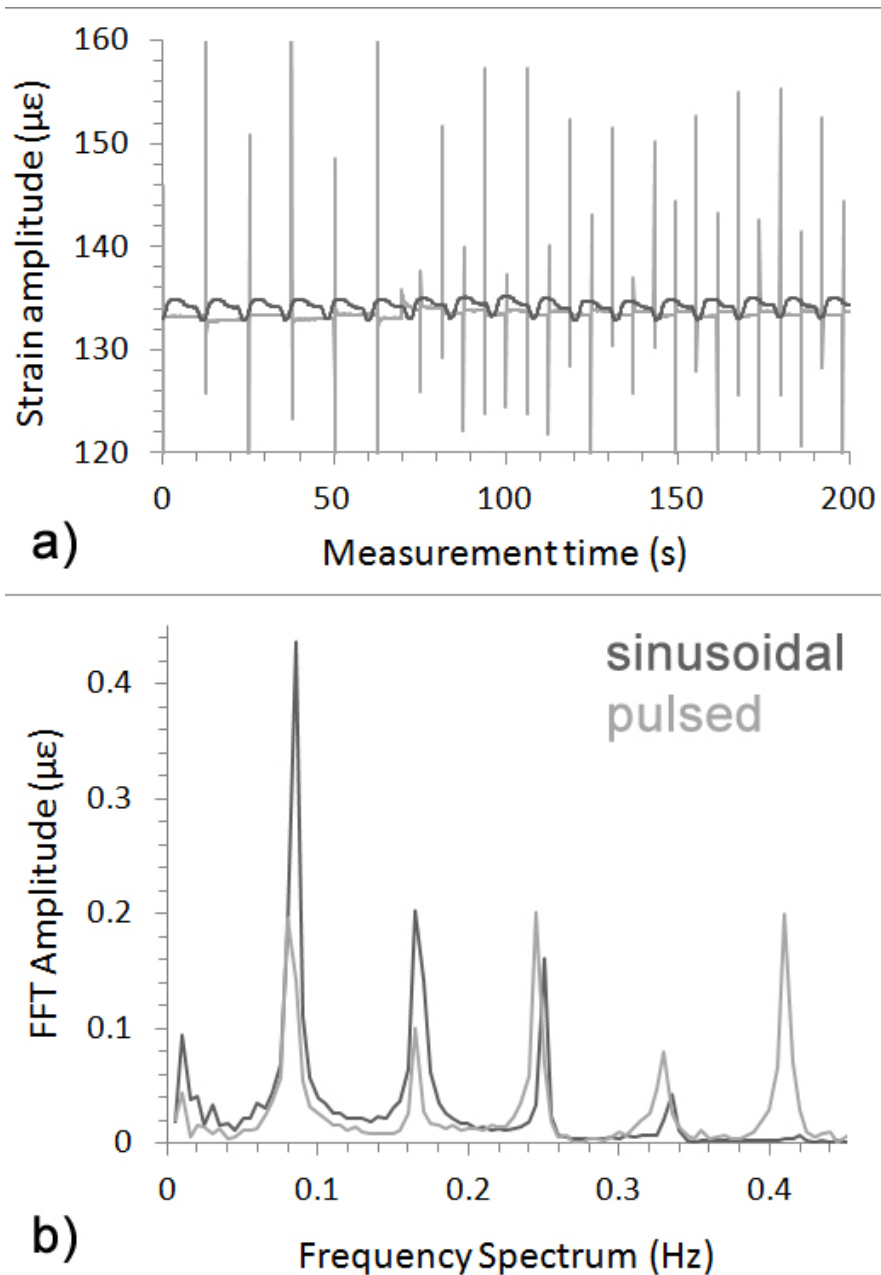


Figure 6.18: Two low-frequency strain profiles and their resulting FFT spectra. a) shows the measured 0.08 Hz strain profiles applied to the cantilever over time for pulsed and sinusoidal actuation of the transducer. Performing primary and secondary FFTs over 4000 and 2000 samples respectively yield b). The FFT bandwidth extends to 1 Hz, but has been terminated earlier for clarity. The low bandwidth reduces the temporal response of the system to 200 s, but also provides a minimum measurable frequency 5 mHz. The noise floor above 50 mHz is  $17 \text{ n}\epsilon/\sqrt{\text{Hz}}$ .

### 6.5.6 Low Frequency Measurements

The scheme's ability to measure seismic frequencies was demonstrated by increasing primary and secondary FFT sample sizes. This yielded high resolution measurements of low (1 Hz) bandwidth strain oscillations. Driving the loudspeaker at 80 mHz in both pulsed and sinusoidal modes resulted in the strain profiles and secondary FFTs shown in figure 6.18. After a 200 s sampling time, the first few harmonics of both low-frequency signals were detected with a resolution of 5 mHz. Crucially, nanostrain resolutions have were retained, as the noise floor was  $17 \text{ n}\varepsilon/\sqrt{\text{Hz}}$  above 50 mHz.

### 6.5.7 Application to Static-Dynamic Strain Measurement

Both the strain and natural frequency of a cantilever vary as a function of the force applied to the cantilever end. The system was used to monitor the natural frequencies and strains in the cantilever while varying masses were added to the cantilever tip. Modelled values were then used to verify those obtained experimentally.

The Euler-Bernoulli equation and the equation of motion for a fixed-free cantilever of thickness  $h$ , length  $L$  and mass  $M_b$  can be solved to find the longitudinal strain along the cantilever's length,  $\varepsilon(z)$  and the natural angular frequency,  $\omega_C$ , for a given tip force,  $F$ :

$$\varepsilon(z) = \frac{(L-z)Fh}{2IE} \quad , \quad \omega_C^2 = \frac{3EI}{L^3(0.2357M_b + \frac{F}{g})} \quad (6.27)$$

where  $E$  is the elastic modulus,  $I$  is the second moment of area and  $g$  is gravitational acceleration. Significant improvements to accuracy, however, can be made through finite element modelling. The geometry, mesh and an example longitudinal strain for a realistic steel cantilever are shown in figure 6.19. Structural mechanics and shell models were solved in stationary and eigenfrequency domains to find the static strain and natural frequencies of the cantilever, as a function of tip force.

As shown in figure 6.20 experimental values showed an excellent agreement

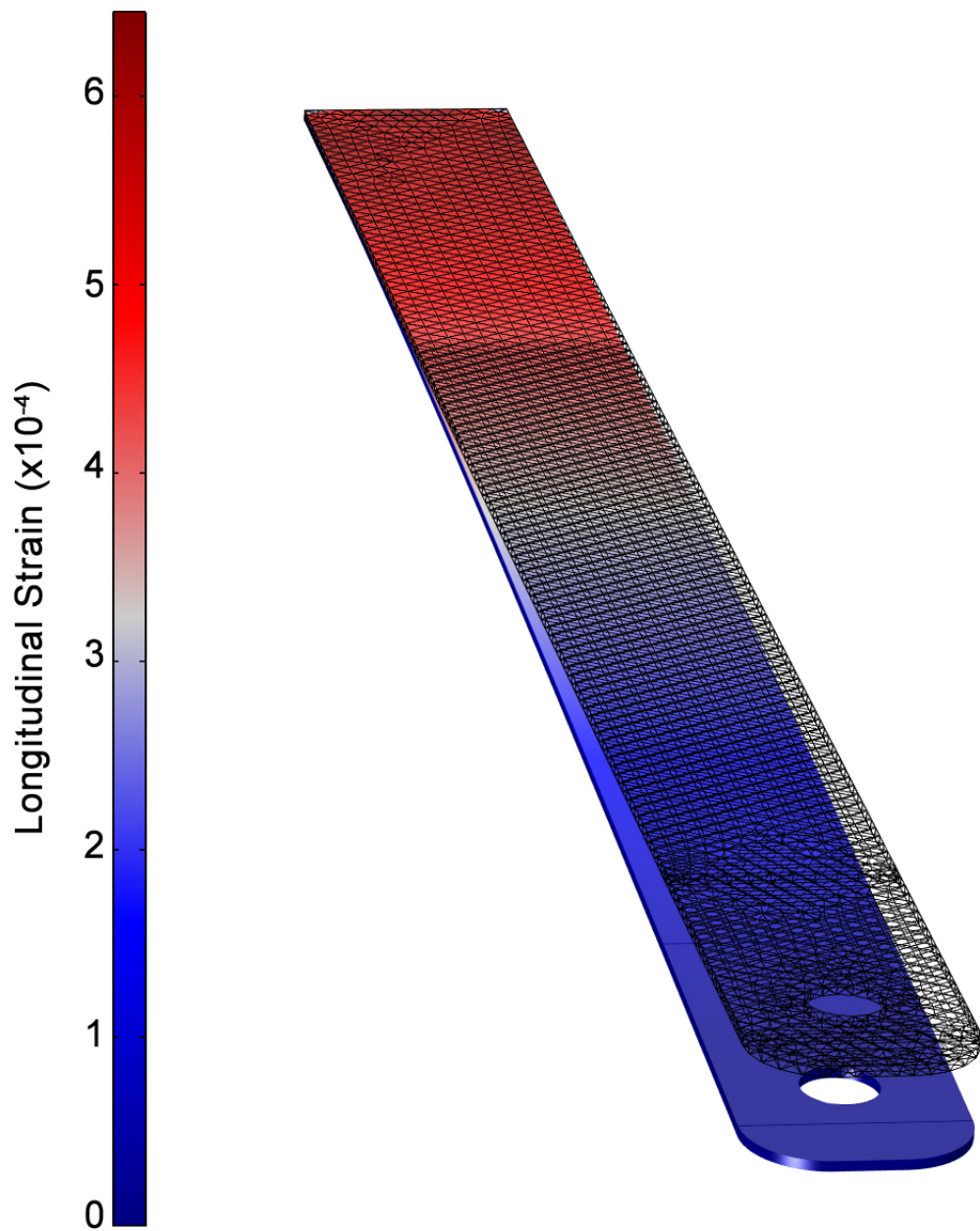


Figure 6.19: Original mesh and deformation of the cantilever beam under a tip force of 3.94N. The longitudinal strain is shown along the top surface of the cantilever.

with both models. This demonstrates the system’s ability to combine both dynamic and static measurements of strain. Furthermore, combining the modelled and measured strain values allows for the stresses in *any* part of the cantilever to be estimated from a single strain measurement. This ‘inverse method’ is something which could in future be applied to the prestressing strand.

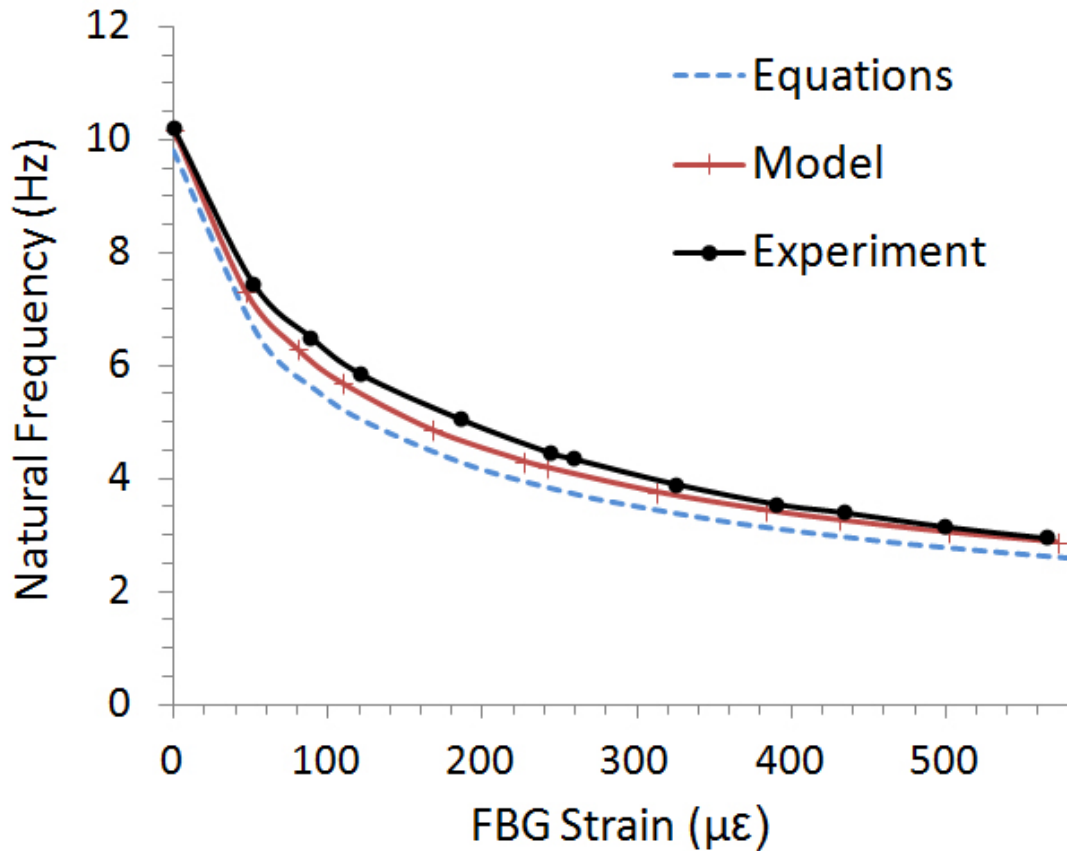


Figure 6.20: The natural frequency of the cantilever as a function of the strain measured by an FBG. Shown are the theoretical, finite element model (FEM) and measured values. Using a Young’s modulus of  $E=200$  GPa allows excellent agreement between the modeled and measured values.

### 6.5.8 Long-term Stability

To test the system’s long-term stability, the wavelengths of two unstrained, co-located FBGs (written at the same point in a fibre) were interrogated over 36 hours. Colocation of the FBGs minimised the relative temperature shifts between them. As shown in figure 6.21, a  $3$  °C shift in ambient lab temperature lead to an apparent  $4$   $\mu\epsilon$  shift in relative FBG strain. Long-term stability of the system

was thus limited by fluctuations in ambient temperature and the reasons for this were investigated.

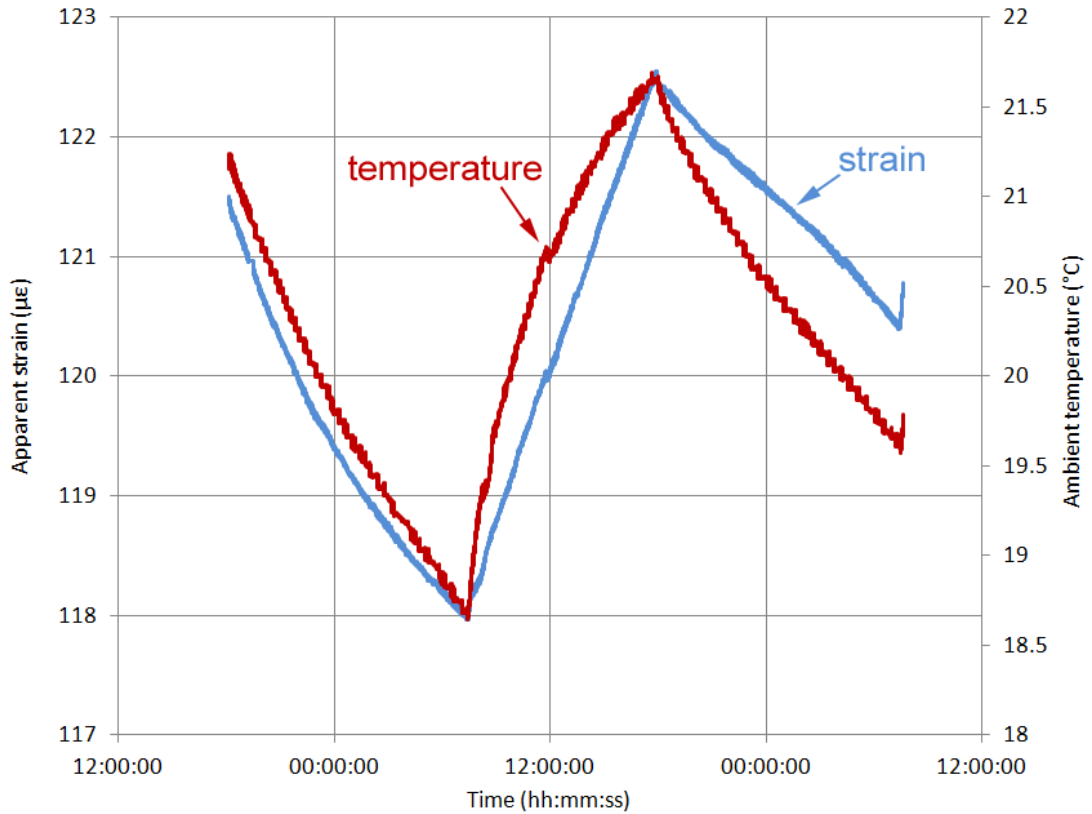


Figure 6.21: Strain measurements of colocated FBGs written at 1535 and 1555 nm. These should remain nearly constant with ambient temperature, but do in fact fluctuate with the temperature. This has an impact on the system’s long term stability.

### 6.5.8.1 FBG Wavelength Dependence

While the two FBGs were exposed to exactly the same temperatures, they may have had a different temperature dependence. Recall that an FBG’s temperature dependence is defined by:

$$\frac{\Delta\lambda_B}{\lambda_B} = (\alpha_\Lambda + \alpha_n)\Delta T = k_T\Delta T \quad (6.28)$$

where  $\alpha_\Lambda$  and  $\alpha_n$  are the thermal-expansion and thermo-optic coefficients for silica. These coefficients are not always constant with wavelength, however [Rao97]. To study this effect, the wavelength difference was measured using a commercial

Fabry-perot interrogator (wavelength resolution 5 pm, measurement rate 2 Hz) as the colocated FBGs were heated in an oven. The result, shown in figure 6.22, demonstrates that the FBGs shift apart by an equivalent of  $0.2 \mu\epsilon$  per  $^{\circ}\text{C}$ . This shift is not quite large enough to account for the drifts seen in figure 6.21.

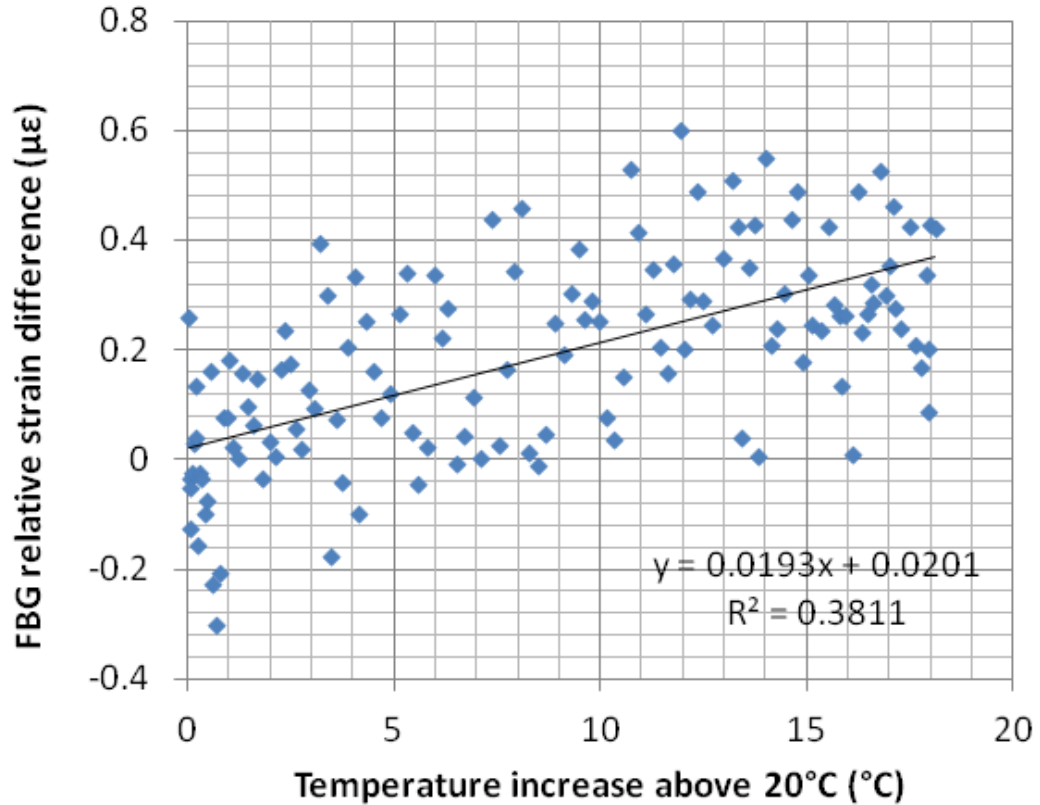


Figure 6.22: The differing temperature sensitivities,  $k_T$ , of colocated FBGs means their wavelengths drift apart during heating, leading to an apparent strain shift.

### 6.5.8.2 Relative Photodetector Drift

The three photodetectors in the system may have reacted differently to changes in temperature. These resulting voltage changes could be erroneously interpreted as strain shifts. To characterise the magnitude of relative photodetector drifts, the system was set up in the simplified arrangement shown in figure 6.23. The variation in the photodetector voltages with measured ambient temperature is shown in figure 6.24. The three photodetectors appear to respond in a similar fashion.

To validate this result, the MZI was simulated in software using the equations

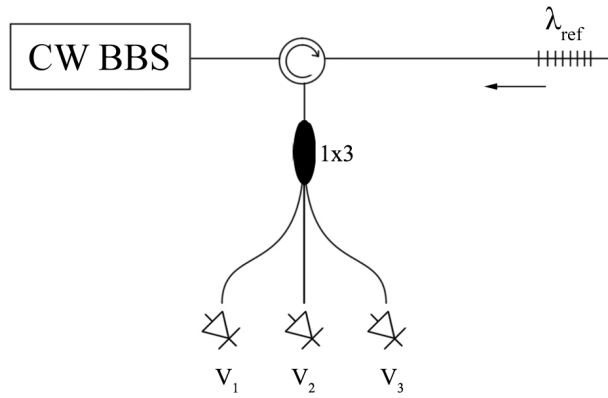


Figure 6.23: Simplified scheme used to test relative gain between three photodetectors.

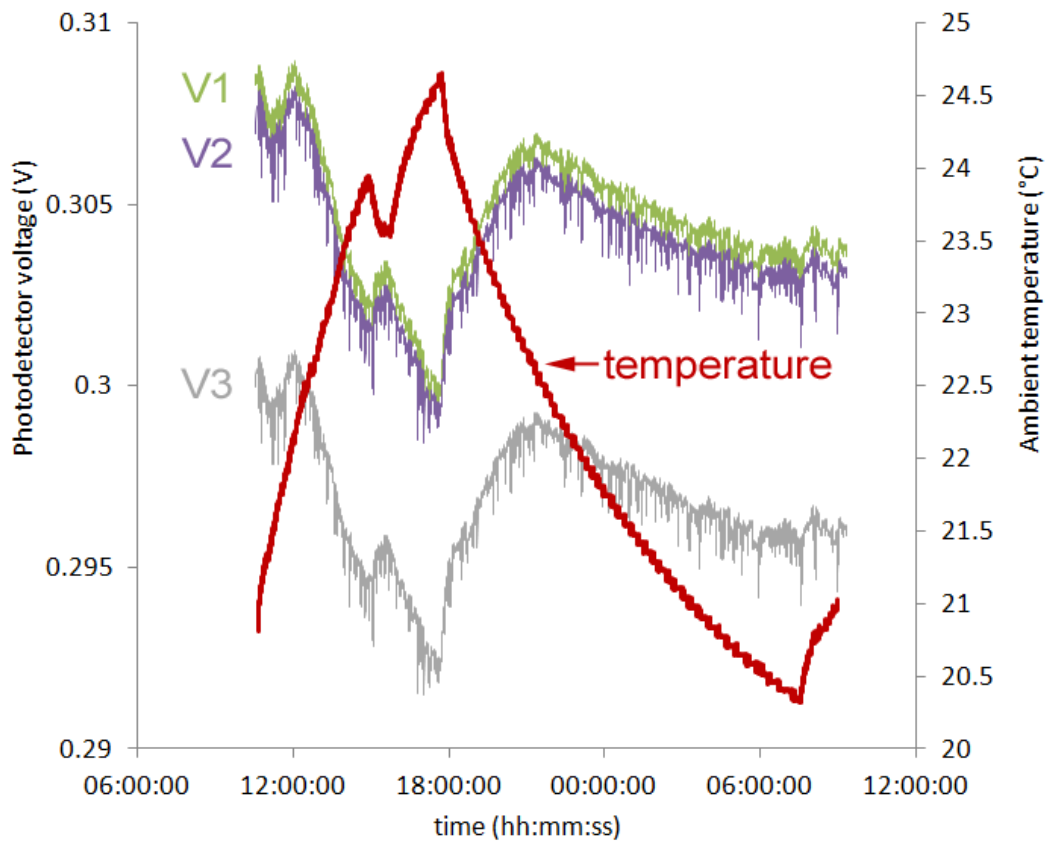


Figure 6.24: The drifts in the three photodetectors along with the changes in ambient temperature.

set out in §6.2. The voltages from figure 6.24 were fed into the model to produce simulated strains, shown in 6.25. It was found that relative photodetector drifts could only account for, at most,  $0.2 \mu\epsilon$  strain changes.

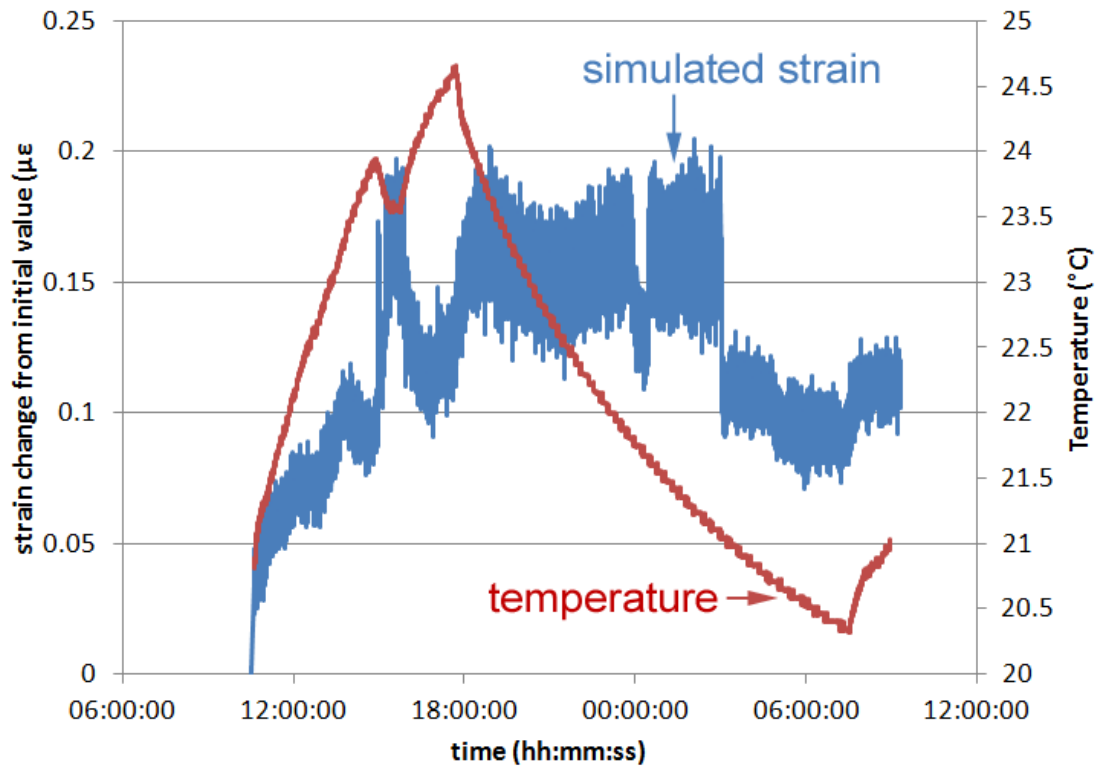


Figure 6.25: The simulated drifts in the strain measurement arising from the data obtained for the relative drift in the three photodetectors. As shown, a  $3^\circ\text{C}$  temperature change leads to a  $0.2 \mu\epsilon$  change in strain.

### 6.5.8.3 Source Power Drift

While fluctuations in input intensity do not affect the measurement of strain, source power fluctuations can change the shape of the light source spectrum as shown in figure 6.26. After the source light is reflected from an FBG, the reflection is described by the FBG's spectrum, multiplied by the source spectrum. The central wavelengths of any FBGs located on the changing slopes of the spectrum, at 1535 nm for example, may thus appear to shift with light source power.

To quantify this effect, FBG spectra were obtained using an optical spectrum analyser for the output powers shown in figure 6.26. These FBG spectra were then

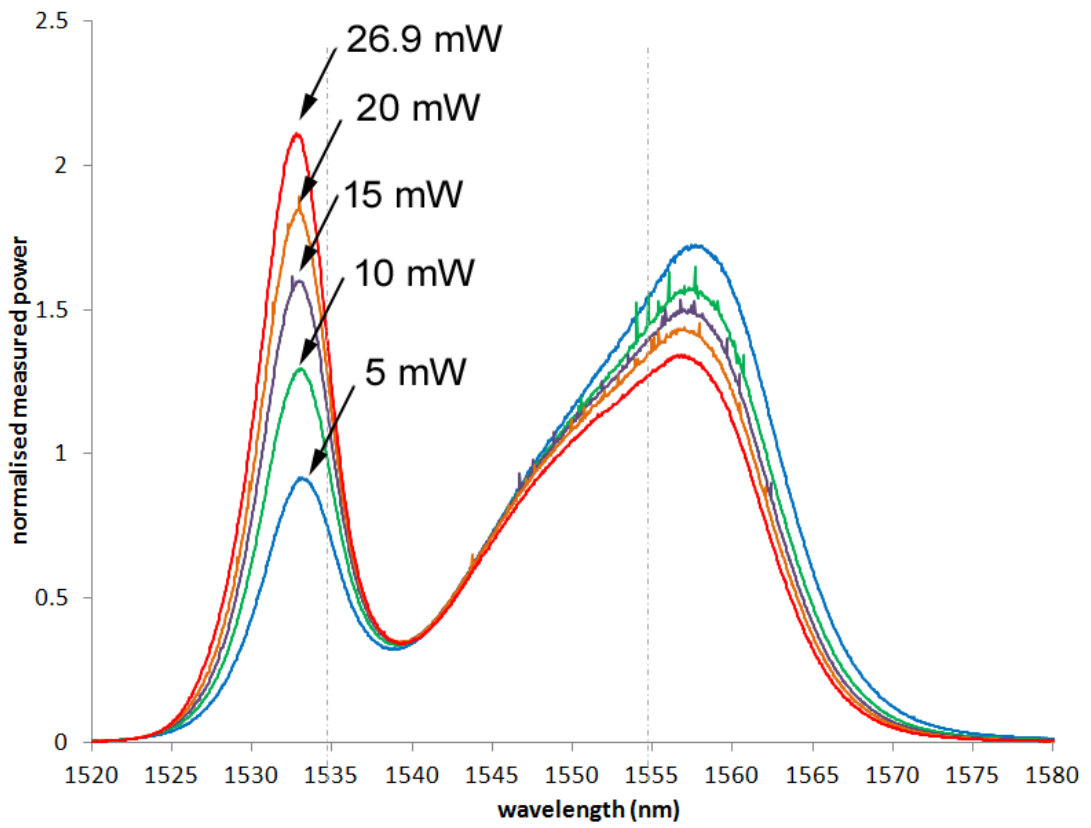


Figure 6.26: Changes in the spectral shape of the light source as the output power is varied between 5 and 26.9 mW.

fed into the MZI simulator to find the resulting changes in the strain measurement. Decreasing the source power from 26.9 mW lead to a  $3 \mu\epsilon$  apparent strain shift after an 80 % decrease, as shown in figure 6.27. The source power variation in the real system is nowhere near this large, however. The maximum changes observed have been around 2 %, so it is unlikely that this effect could yield strain changes any larger than  $0.1 \mu\epsilon$ .

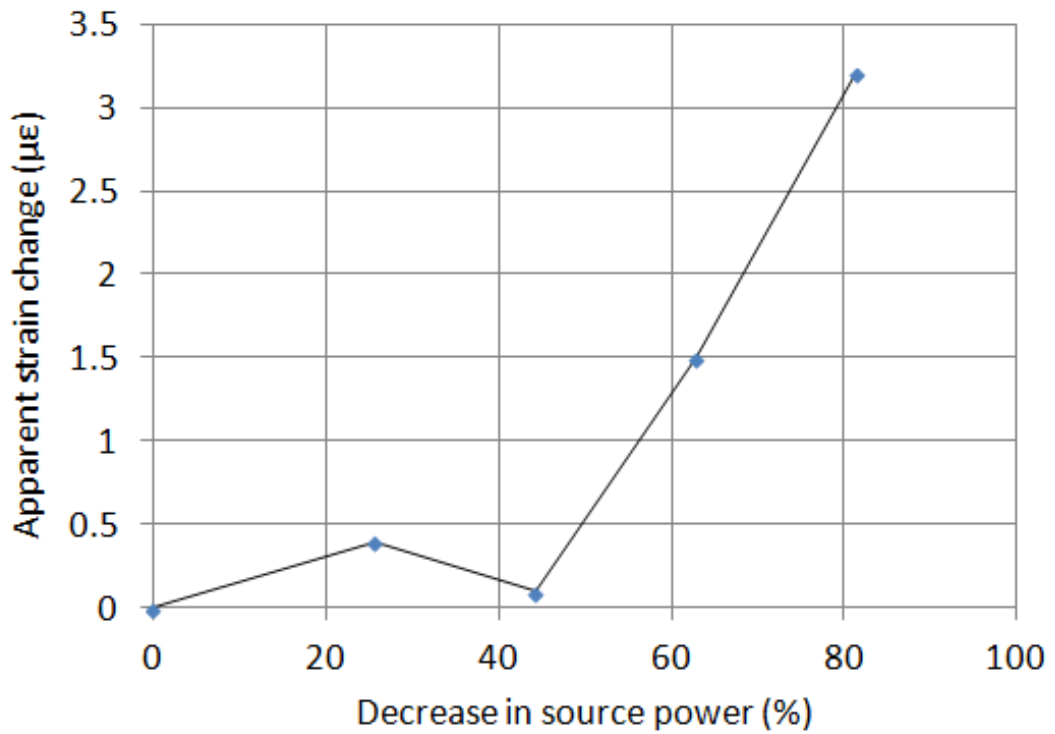


Figure 6.27: Decreasing the source power from 26.9 mW to 5 mW (approximately an 80 % decrease) caused the strain in the simulated interrogation system to change by  $3 \mu\epsilon$ .

#### 6.5.8.4 Remnant Polarisation

A depolariser was used in the set up to ensure that interference in the MZI was independent of polarisation. The depolariser may not have been perfect, however, leaving some remnant polarisation in the light. To quantify how much remnant polarisation remained in the system, the orthogonal fast and slow axes in the fibre were measured after the depolariser using two photodetectors, over a 60 hour period.

If light is fully depolarised then the relative intensity between the fast and slow axes is constant. As shown in figure 6.28, the polarisation was found to change, but its dependence on temperature and the effect that this would have on the MZI interference is still unclear and difficult to quantify. For the time being, it is worth noting that a greater degree of depolarisation or polarisation control may be required in the system.

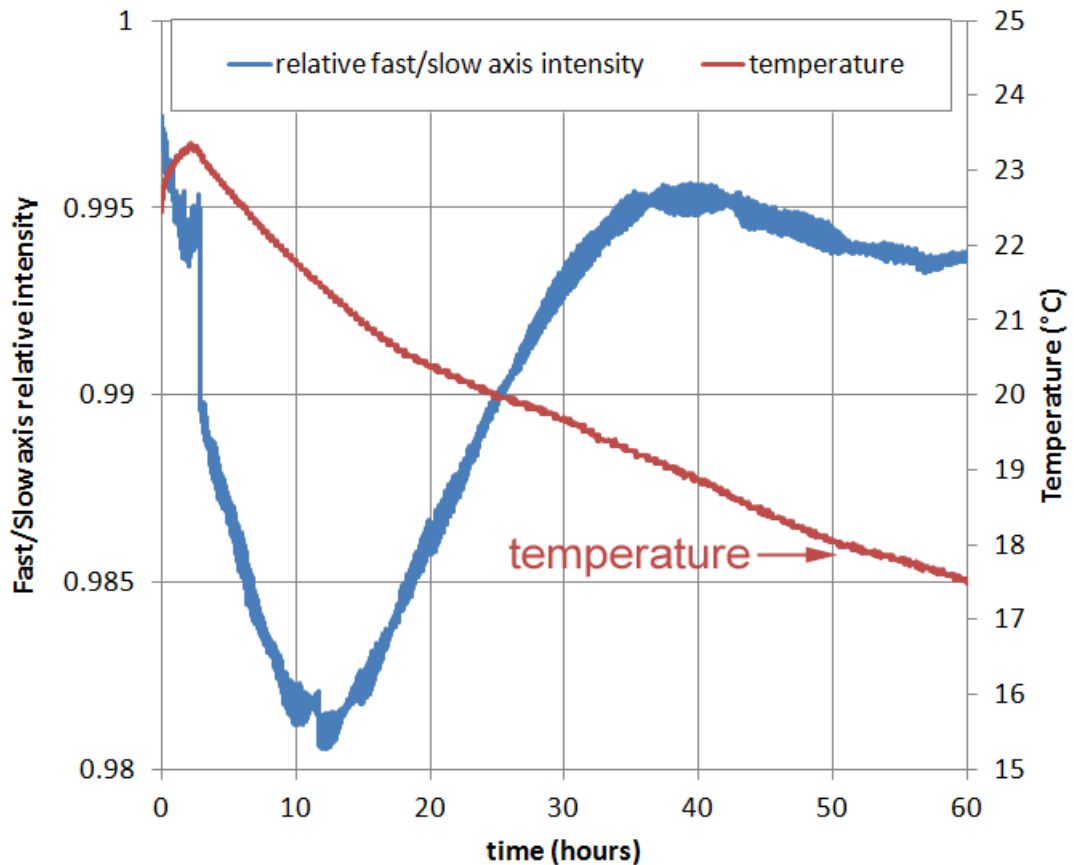


Figure 6.28: The relative intensity between the fast and slow axis of the fibre after depolarisation, as a function of time, along with the changes in ambient temperature. There appears to be very little correlation.

#### 6.5.8.5 Optical Path Difference

Although every effort was made to package the MZI within a box of dielectric gel of low thermal conductivity, the MZI may have still been sensitive to thermal fluctuations. These can alter the OPD through thermal expansion and thermo-optic effects.

To test this, the apparent strain change in the system was measured while MZI was heated in an oven. The results, in figure 6.29, show that even a relatively short thermal impulse is enough to induce a resultant  $1.5 \mu\epsilon$  strain change in the interrogation system. This is likely the main cause of the long-term drifts observed in this system.

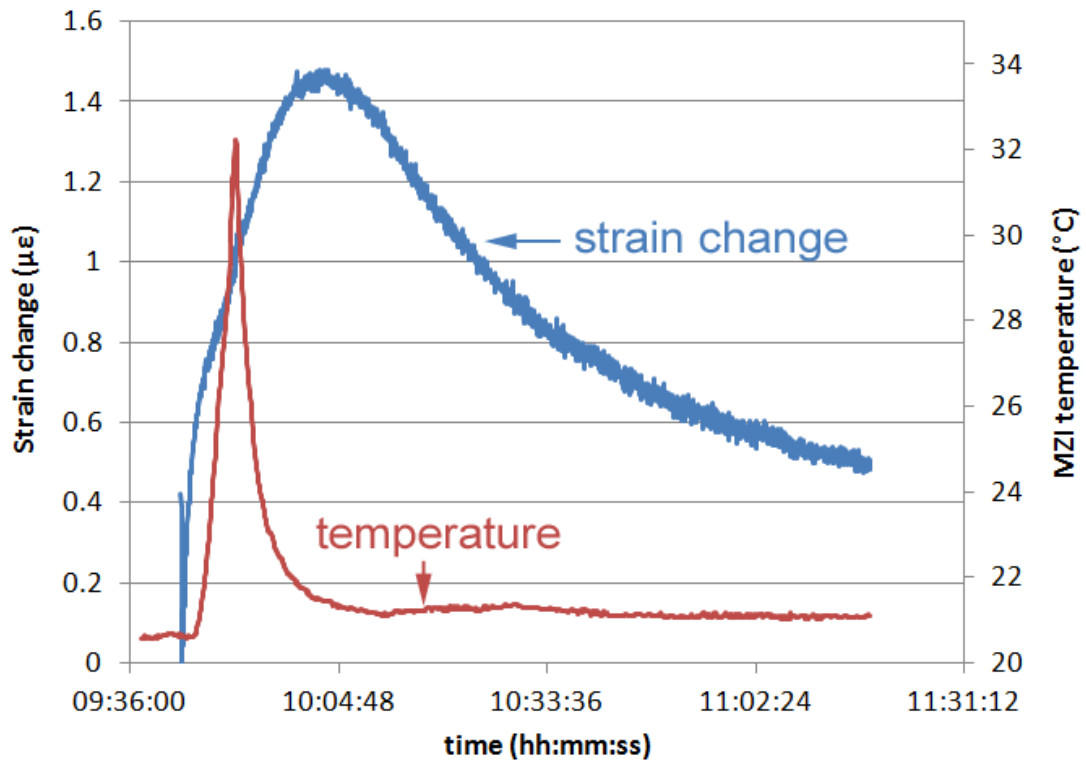


Figure 6.29: The strain measured by the interrogation system as the MZI was heated in an oven for 10 minutes. Apparent strain changes were around  $1.5 \mu\epsilon$  for this short thermal impulse.

As shown in figure 6.30, finite element models of the MZI have demonstrated that while the dielectric gel delays and dampens the effect of a temperature fluctuation, it does not completely negate it. This is particularly true when the thermal fluctuations outside of the box are slow, as daily ambient temperature changes often are. Preventing this effect in future may require the MZI to be temperature-controlled through feedback systems and peltiers.

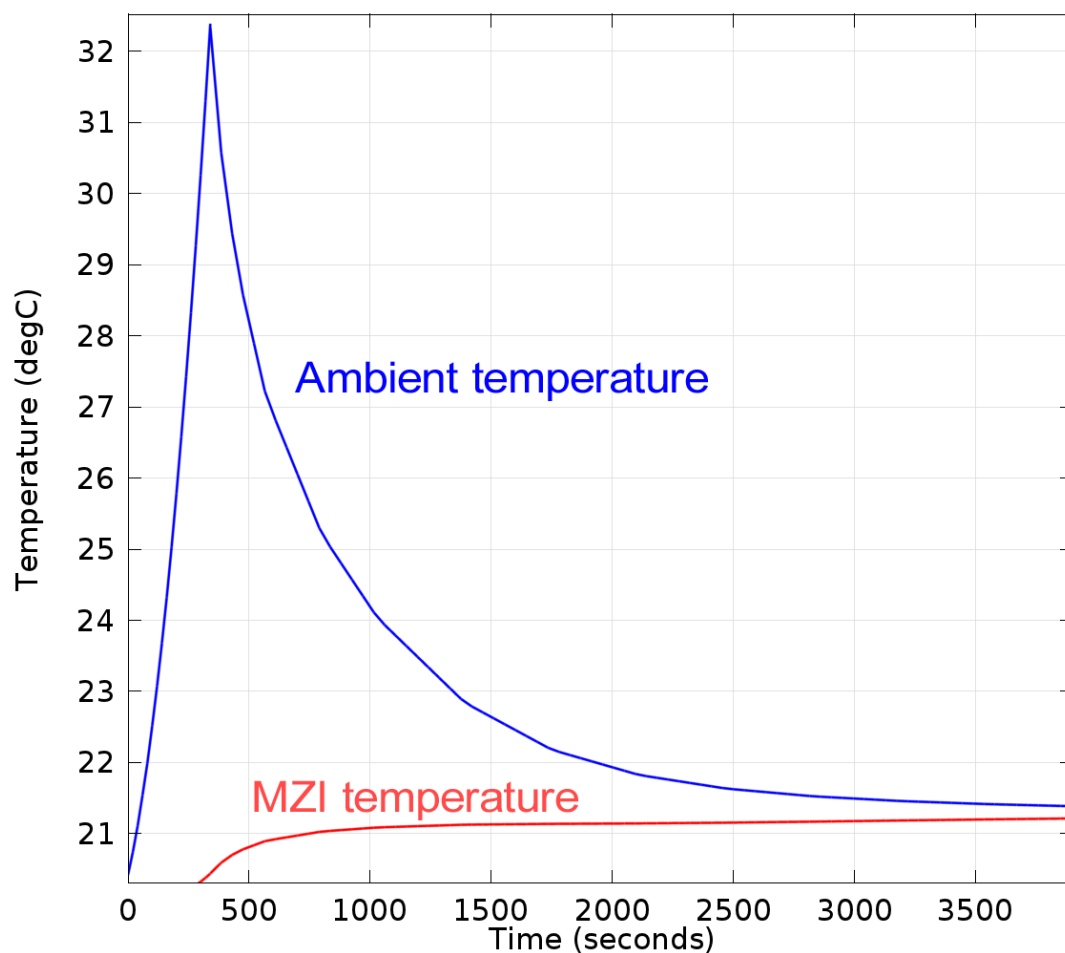


Figure 6.30: A model of the temperature profile outside of the MZI packaging and how these thermal fluctuations affect the temperatures within the box. The dielectric gel delays and reduces the effect of the 12 °C temperature change outside of the box, but there is still a temperature increase.

## 6.6 Absolute Wavelength Interrogation

Due to the periodic dependence of the MZI output, the scheme described above was only able to measure relative changes in the wavelength of each sensor after the system was initialised. In this project, the system's measurement capabilities were further extended, so that it could retrieve the absolute wavelengths of a multiplexed array FBGs upon initialisation.

### 6.6.1 Phase calibration

Recall that the three voltages of the MZI outputs allow phase to be expressed independently of confounding variables, such as fluctuations in optical source power and attenuation [TJC99]:

$$\tan(\phi) = \frac{(\mu_2 - \mu_3)\bar{V}_1 + (\mu_3 - \mu_1)\bar{V}_2 + (\mu_1 - \mu_2)\bar{V}_3}{(\gamma_2 - \gamma_3)\bar{V}_1 + (\gamma_3 - \gamma_1)\bar{V}_2 + (\gamma_1 - \gamma_2)\bar{V}_3} \quad (6.29)$$

For the system to measure the absolute wavelength of the FBGs, detailed knowledge of the MZI's calibration parameters are required. In the system described above, normalisation parameters,  $\mu_m$  and  $\gamma_m$ , were calculated by thermally or mechanically tuning a reference Bragg peak across the interferometer's fringes (see §6.2.3).

However, the method can also be reversed, as the fringes can be scanned over all Bragg peaks simultaneously by tuning the interferometer's path difference. This not only facilitates the absolute wavelength calibration discussed later, but also provides normalisation parameters which are unique to each FBG. Thermally tuning the path imbalance by heating a length section,  $L$ , of one arm of the interferometer results in a linear phase shift with temperature,  $T$ :

$$\frac{d\phi}{dT} = \frac{2\pi}{\lambda} \left( D \frac{dn}{dT} + nL\alpha \right) \quad (6.30)$$

where  $\frac{dn}{dT}$  and  $\alpha$  are thermo-optic and thermal expansion coefficients respectively.

As thermal tuning alters the fiber's refractive index (and hence absorption losses in the MZI),  $\gamma_m$  and  $\mu_m$  are also temperature dependent. As shown in fig-

ure 6.31, this dependence is characterised at discrete temperatures by detecting the peaks and troughs in the voltage responses during thermal tuning. The amplitudes and offsets of the three interferograms can then be estimated continuously by interpolation, providing  $\gamma_m(T)$  and  $\mu_m(T)$ .

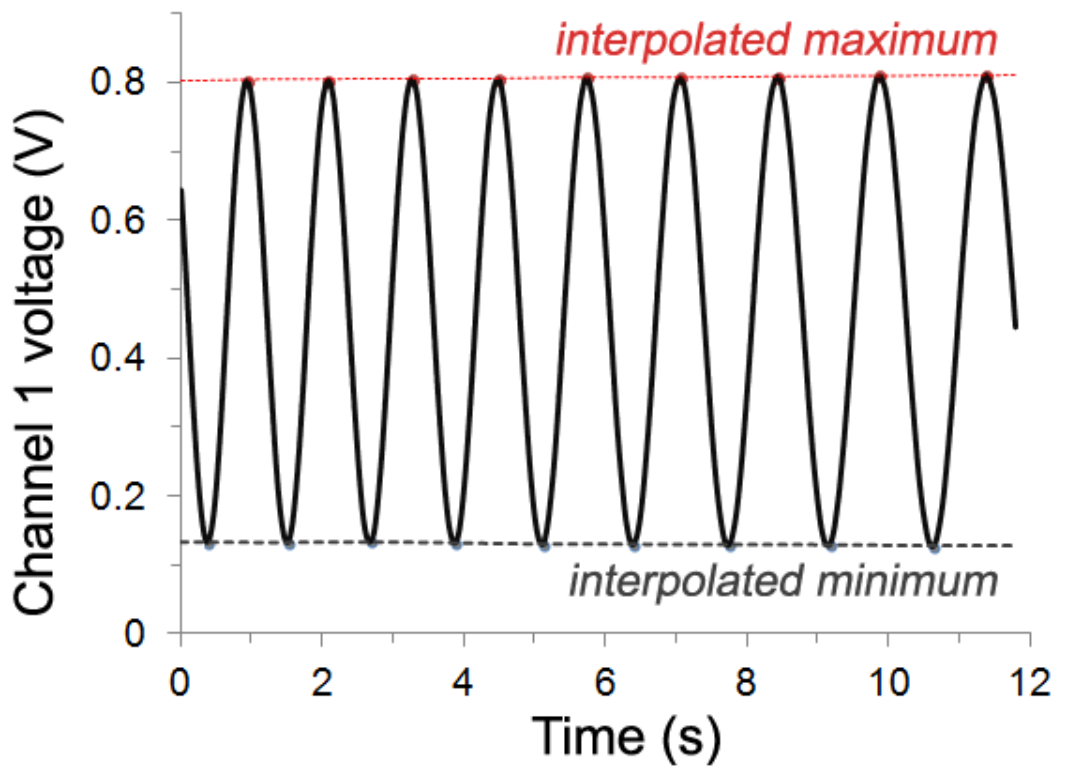


Figure 6.31: The photodetector voltage obtained for one MZI channel during thermal tuning. Interpolation between peak-detected maximum and minimum values allows the ac and dc components of the waveform to be estimated continuously as a function of time. This allows normalisation parameters to be constructed as functions of temperature.

The temperature-dependent normalisation parameters are finally applied, using equation (6.29), to the same voltage history from which they were generated. This determines the phase shift for each FBG during thermal tuning. Using the same data for both calibration and phase interpretation improves measurement accuracy and also reduces the number of steps in the method.

## 6.6.2 Absolute wavelength

It is clear from equation (6.8) that channel voltages periodically repeat as the Bragg peak shifts over the free spectral range of the interferometer. Multiples of  $2\pi$  phase shifts are tracked and unwrapped for each FBG during system operation, but the number of fringes initially separating two FBGs is not generally known. As such, interferometric schemes like this have been historically limited to tracking only the relative wavelength shifts between sensor and reference FBGs.

However, in the latest developments reported here, the *absolute* wavelength of each sensor can be measured when the system is initialised [NO13]. This is possible because the thermal tuning procedure, described above, produces large and accurately monitored phase measurements for each FBG. The wavelength of an unknown sensor at  $\lambda_1$  can therefore be calculated from a known reference, situated at  $\lambda_r$ , using the ratio of the phase shifts:

$$\frac{d\phi_r}{dT} \cdot \frac{dT}{d\phi_1} = \frac{d\phi_r}{d\phi_1} = \frac{\lambda_1}{\lambda_r} \left[ \frac{D \frac{dn(\lambda_r)}{dT} + n(\lambda_r)L\alpha}{D \frac{dn(\lambda_1)}{dT} + n(\lambda_1)L\alpha} \right] \quad (6.31)$$

In cases where,  $D \frac{dn}{dT} \ll nL\alpha$ , this relationship can be simplified to:

$$\phi_r = \left( \frac{\lambda_1}{\lambda_r} \cdot \frac{n(\lambda_r)}{n(\lambda_1)} \right) \phi_1 \quad (6.32)$$

The relative refractive indices are calculated using the Sellmeier equation for fused silica:

$$n^2(\lambda) \approx 1 + \frac{0.7\lambda^2}{\lambda^2 - 4680} + \frac{0.4\lambda^2}{\lambda^2 - 13500} + \frac{0.9\lambda^2}{\lambda^2 - 10^7} \quad (6.33)$$

and so the slope,  $S$ , of  $\phi_r$  against  $\phi_1$  can be corrected to find  $\lambda_1$  without any knowledge of temperature. To re-iterate, the phase calibration and absolute wavelength procedures are both performed from the same voltage history during one thermal tuning operation, providing both the wavelength and phase response of each FBG sensor in a single step.

### 6.6.3 Simulation

A simulation of the system was used to demonstrate the theoretical limit of precision of the absolute wavelength calculation. Phase demodulation of both simulated sensor ( $\lambda_1 = 1540$  nm) and reference ( $\lambda_r = 1560$  nm) Bragg peaks was performed using Todd's passive algorithm [TJC99]. A phase noise floor of  $250 \mu\text{rad}/\sqrt{\text{Hz}}$  was introduced, as this corresponds with the noise floor of the laboratory scheme. To simulate thermal tuning, the initial OPD of 4.6 mm was detuned by 1 % at a rate of  $1 \mu\text{m}/\text{s}$  and phases were sampled at a rate of 500 Hz.

A histogram of the calculated sensor wavelength over 10,000 iterations is shown in figure 6.32. The typical fractional error in the slope of  $\phi_1$  against  $\phi_r$  was  $\Delta S = 1.2 \times 10^{-6}$ . This lead to a standard error in the wavelength of 1.8 pm, equivalent to  $0.14^\circ\text{C}$  or  $1.5 \mu\epsilon$ .

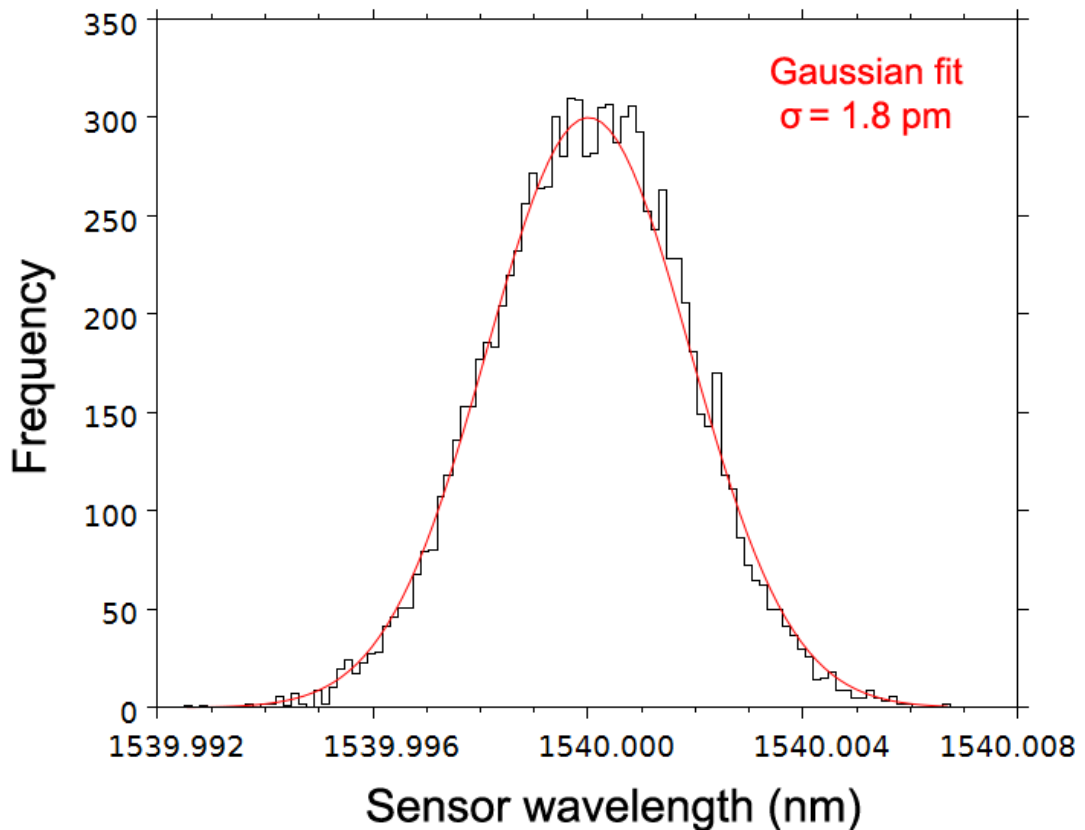


Figure 6.32: Histogram of the calculated absolute wavelength of an FBG at 1540 nm after 10,000 simulated iterations. The standard deviation of the Gaussian fit is 1.8 pm. Bragg peak spectral widths were 0.1 nm. FBG reflectivity and MZI fringe depth were both set to 80 %.

### 6.6.4 Laboratory Demonstration

To better characterise the performance of the technique, a modified proof-of-concept system, based on figure 6.33, was constructed with a limited number of FBGs. An athermal grating (temperature sensitivity  $<0.5$  pm/°C) at  $\lambda_r = 1560$  nm was used as a stable reference. Its phase response was initially compared to another athermal grating at  $\lambda_1 = 1540$  nm, as this allowed the absolute wavelength calibration to be verified without the extraneous influence of Bragg wavelength uncertainty.

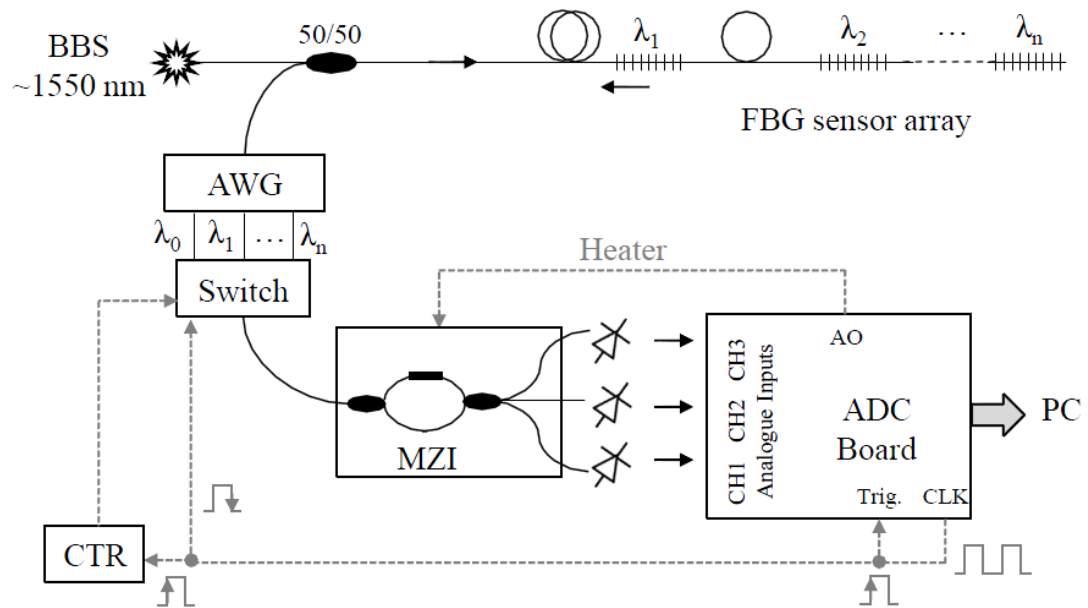


Figure 6.33: Multiplexed FBG interrogator, with optical and electrical connections shown in black and gray respectively. The FBG sensor array is illuminated by a broadband source (BBS). Bragg reflections are sequentially passed to the Mach-Zehnder interferometer (MZI) by using an arrayed waveguide grating (AWG) and optical path switch. The AWG provides denser wavelength division multiplexing than a CWDM. The ADC board supplies the signals required for optical switching and thermal tuning of the MZI.

The interferometer (OPD 4.6 mm) was an all-fiber construction, fabricated by splicing the pigtails of 1x2 and 3x3 couplers. To isolate the MZI from vibration and to hinder heat transfer between the arms during thermal tuning, the device was bonded to a glass slab by epoxy. Tuning was achieved by resistive heating an  $L = 4$  cm section of one fiber arm. Heat conduction was facilitated by thermal

grease. The ADC unit sampled at 4 kHz, and each set of four data points were averaged. After switching between the two FBGs, this provided a measurement rate of 500 Hz per sensor.

### 6.6.5 Initial calibration

The procedures for calibration and absolute wavelength determination are summarised in figure 6.34. Normalisation parameters and phase shifts for both FBGs were calculated continuously over 20–30 seconds of thermal tuning. The empirical relationship between the phase shift of the reference FBG and the resistive heater’s temperature is shown in figure 6.35. The slope of this fit describes equation (6.30), and substituting  $\frac{dn}{dT} = 8.5 \times 10^{-6}$  for silica glass suggests that thermal expansion in the arm was around  $\alpha = 9 \times 10^{-6}$ . This is a sensible value, mid-way between the thermal expansion of silica and epoxy, and so provides verification that phase shifts were measured accurately.

### 6.6.6 Absolute wavelength resolution

The phase relationship between the reference and unknown FBGs during thermal tuning is shown in figure 6.36(a). The uncorrected slope of the linear fit is  $S = 1.01316 \pm 10^{-5}$ . As shown in Figure 6.36(b), the refractive index correction factor is found numerically to yield, in this case,  $\lambda_1 = 1539.989 \pm 0.003$  nm.

The quoted 3 pm wavelength error is derived from phase noise and is thus comparable to the precision found in the simulation. To experimentally verify this wavelength uncertainty, tuning and calibration was repeated 30 times. The resulting histogram, shown in figure 6.37, reveals that the calculated sensor wavelength was accurate to within 20 pm, with a standard error of 15 pm (equivalent to 1.2 °C or 12.5  $\mu\epsilon$ ). Precision and accuracy are lower than expected, due to the influence of uncertainty in the calibration parameters. Initially, these parameters were assumed to be perfectly known, but realistically, uncertainty in  $\mu_m$  and  $\gamma_m$  can have a profound impact on the phase calculation.

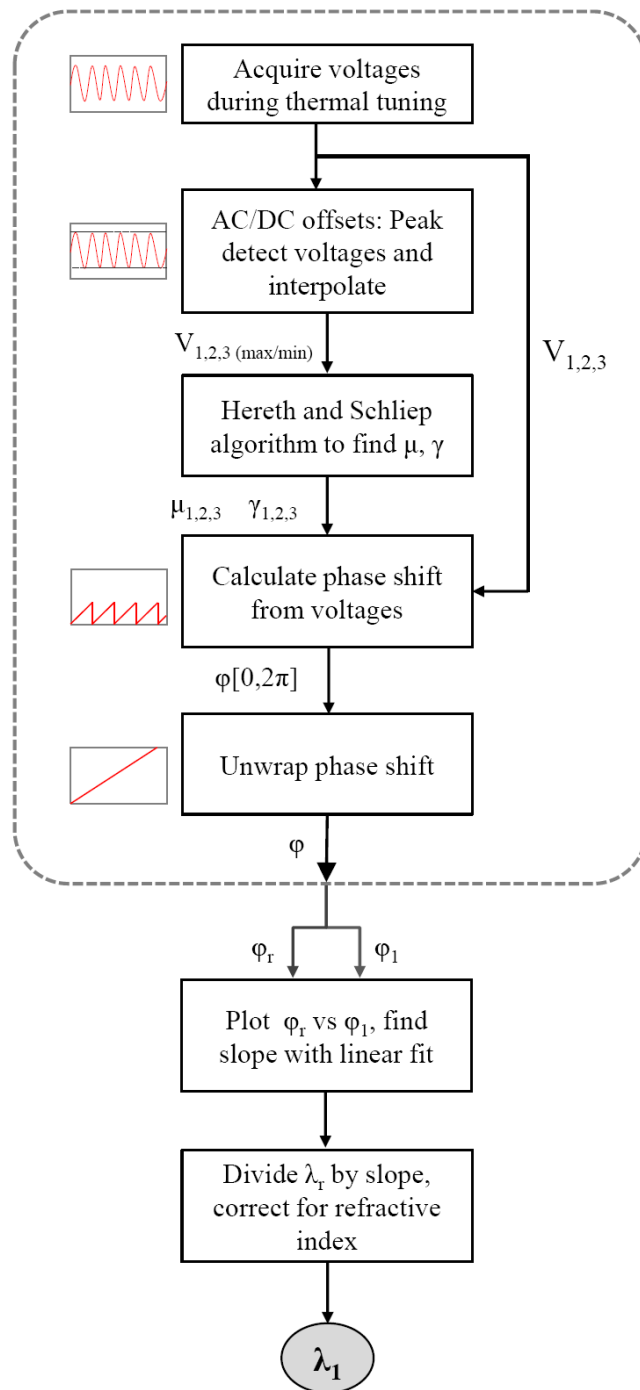


Figure 6.34: Channel voltages were translated into phase shifts for the reference and unknown FBGs during thermal tuning. The relative phase shifts were then used to calculate the wavelength of the unknown FBG.

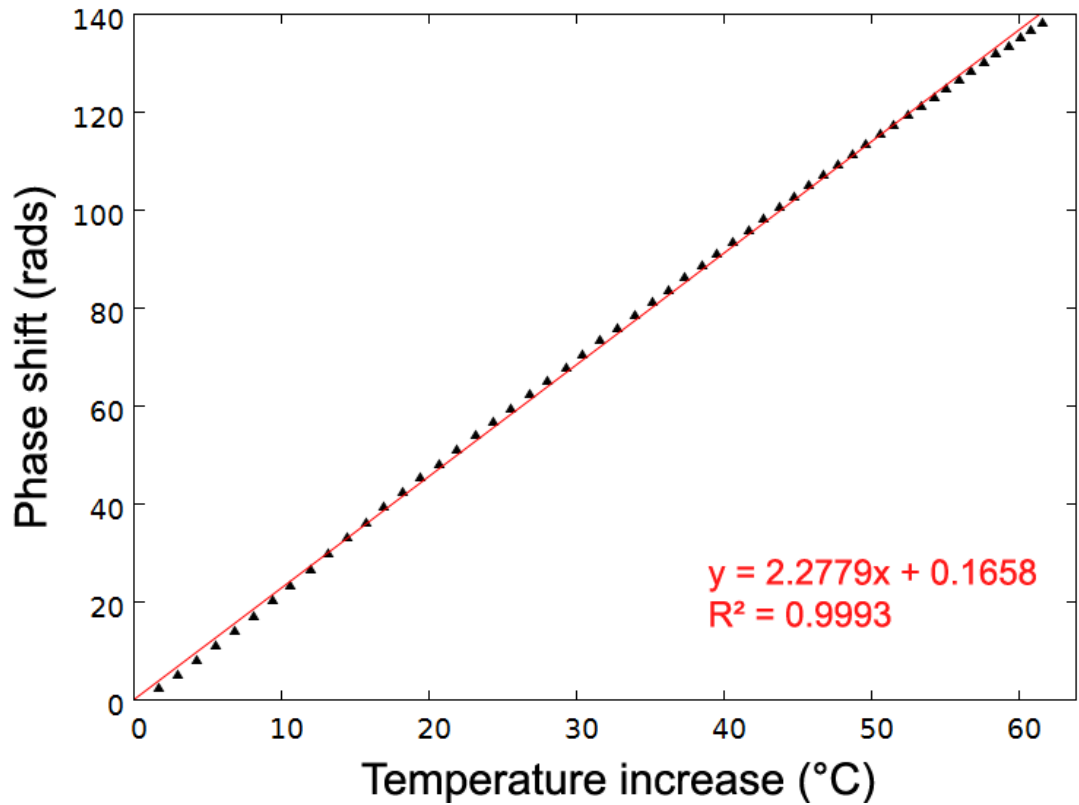


Figure 6.35: Resistive heater temperatures were measured using an FBG thermometer. As the temperature of one arm of the MZI was increased, phase was found to shift linearly, confirming the validity of equation (6.30). The very slight non-linearity may have arisen from thermal cross-talk between the interferometer arms. The R-squared value for the linear fit is 0.9993.

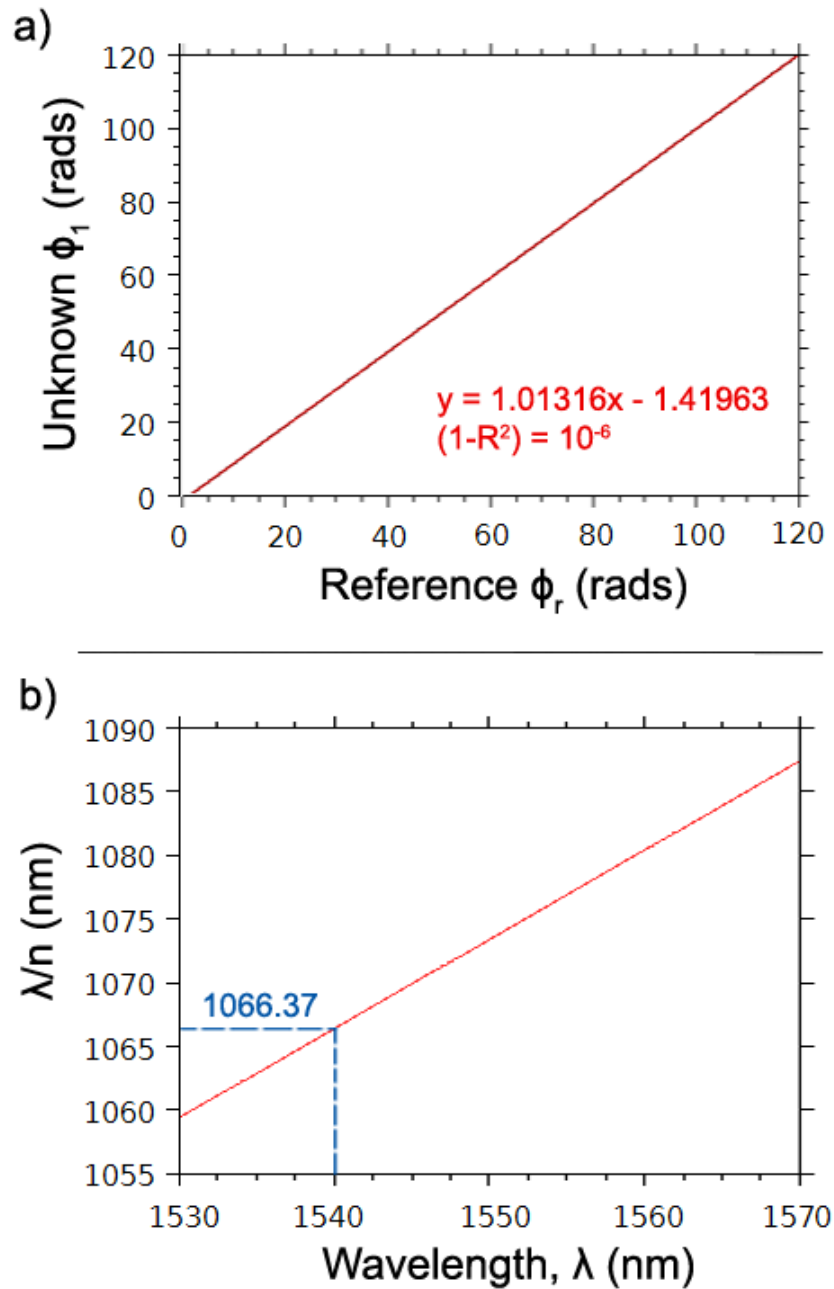


Figure 6.36: (a) Experimental data of the phase relationship between the reference and unknown FBGs during thermal tuning. The slope of the linear fit is  $S = 1.01316 \pm (7 \times 10^{-6})$ . The R-squared value of the linear fit is approximately 1. (b) The correction factor for the slope is found by solving equation (6.32) numerically. A plot of  $\lambda$  against  $\lambda/n(\lambda)$  is used. When  $\lambda/n = 1560/[S \times n(1560)]$  the corrected absolute wavelength is found to be  $\lambda_1 = 1539.989$  nm.

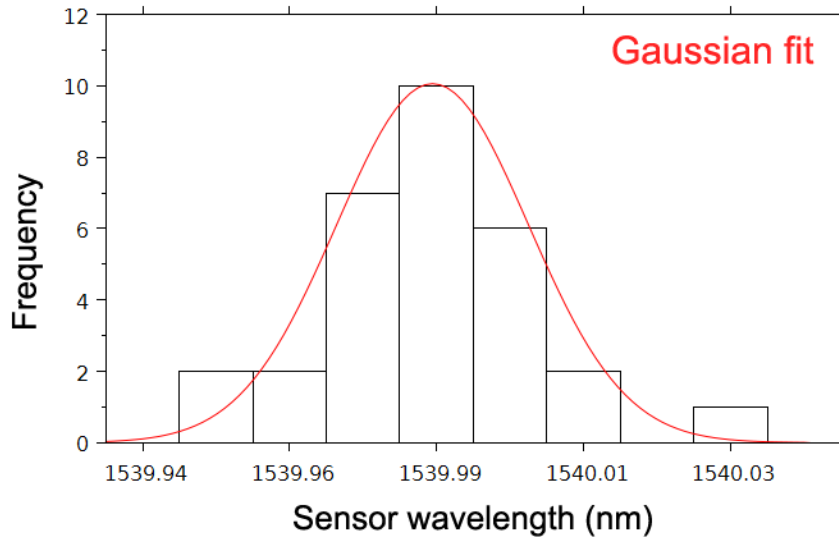


Figure 6.37: Histogram and Gaussian fit of the experimental absolute wavelength calculation for an athermal FBG at 1540 nm after 30 iterations. The mean and standard deviation of the data was 1539.98 and 15 pm. A t-test suggests 99 % confidence that the true sample mean lies within  $\pm 10$  pm of the calculated value.

### 6.6.7 Dynamic strain measurements

A key feature of the proposed scheme is its ability to provide both absolute and dynamic measurements of FBG wavelengths. To analyse the system's dynamic measurement performance, a strain sensing FBG at  $\lambda_2 = 1550$  nm was mounted on a cantilever using epoxy. Because thermal tuning is time-consuming, it is not suitable for real-time monitoring of absolute wavelengths during dynamic loading of an FBG. However, once the absolute wavelength is initially calculated once, subsequent high-speed measurements of relative phase shifts can be used to infer the new wavelength state.

To demonstrate this concept, the cantilever tip was deflected to induce an initial wavelength offset in the FBG. The interrogation system was switched on and the thermal tuning procedure was used to locate the sensor's wavelength. Once the MZI's temperature had restabilised, the cantilever was released. As shown in Figure 6.38, by combining absolute and relative strain measurements, the system was able to identify both the initial  $0.8$  m $\epsilon$  offset and the subsequent decaying oscillations about zero. A Fourier transform of these oscillations reveals

a noise floor of around  $10 \text{ n}\varepsilon/\sqrt{\text{Hz}}$ .

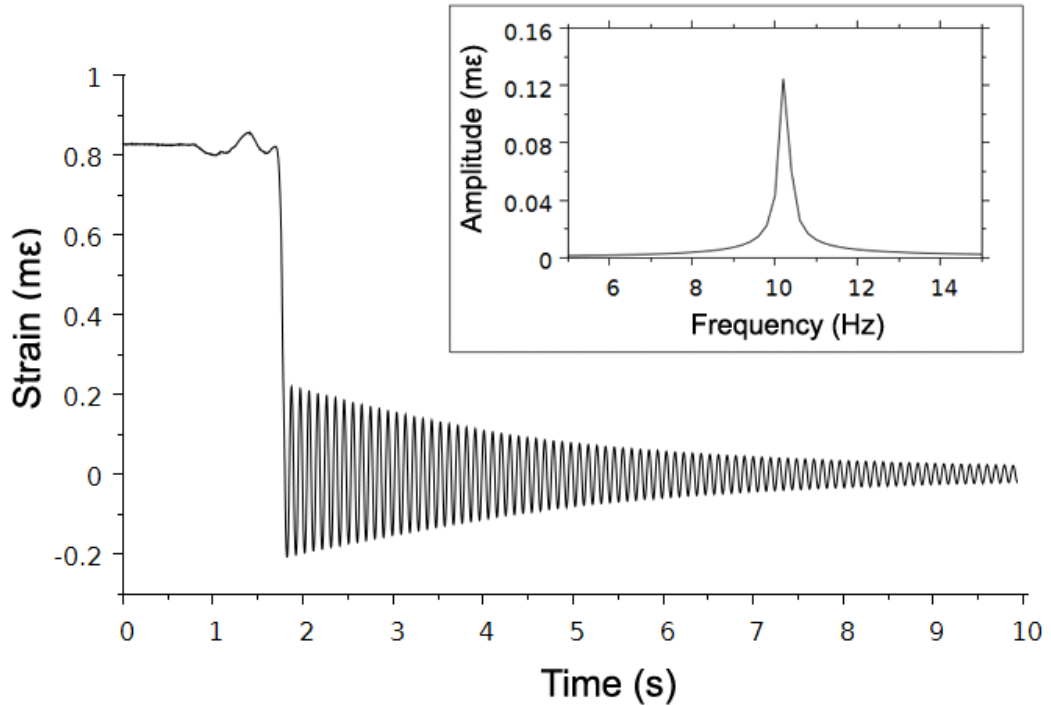


Figure 6.38: Strain measurements from a cantilever-mounted FBG. Before interrogation began, the cantilever was initially held to induce a strain of approximately  $0.8 \text{ m}\varepsilon$  in the FBG. The system was able to interrogate the initial absolute strain and then monitor the subsequent relative changes when the cantilever was released. Shown inset, the Fourier transform of the data between 5 and 10 s, reveals that the cantilever oscillates at its natural frequency of 10.2 Hz. The noise floor was  $10 \text{ n}\varepsilon/\sqrt{\text{Hz}}$ .

### 6.6.8 Static strain measurements

The system's ability to monitor static strain was also evaluated. The cantilever was deflected and then held stationary in five stages, placing the attached FBG under strains ranging from  $0.6$  to  $2.6 \text{ m}\varepsilon$ . The wavelength of the FBG could be determined either by repeatedly calibrating to find the absolute wavelength after each step in cantilever deflection, or the shifts measured *during* deflection could be used to infer the new wavelength from a single initial value. The wavelengths obtained using both of these methods were compared to 'actual values', verified using a commercial Fabry-perot filter interrogation unit.

Figure 6.39 shows that both absolute and relative modes were able to accurately find the ‘true’ wavelength of the FBG as it changed. The stability of relative wavelength measurements is currently limited compared to previously reported systems because this prototype MZI is not yet fully thermally isolated or stabilised. Note that obtaining absolute values of strain by repeated thermal tuning is an active, slow method of demodulation, only used here to demonstrate the accuracy of the absolute wavelength technique. In a real application, absolute wavelength calibration would only be performed once initially. Relative wavelength shifts from this initial value would then be measured, as the interrogation rate and accuracy of the relative mode is far superior.

### 6.6.9 Absolute Wavelength Discussion

There are several contributions to error which may have prevented the prototype system from achieving the simulated measurement performance. For example, uncertainty or inaccuracy in the reference wavelength has an impact both on the phase and refractive index calculations. The athermal reference FBGs were highly stable, but superior accuracy may be achieved with the use of gas cell absorption lines, provided these can be guided by the same optical components [ESAW11, RSG04].

Matching the spectral width of the FBGs to the free spectral range of the MZI is also crucial. In this work, the measurement resolution of athermal FBGs was better not only because of their temperature stability, but also because their spectral width (0.1 nm) was lower than that of the cantilever-bound FBG (0.3 nm). Spectrally narrow reflections allow for a more pronounced modulation of channel voltages, improving the signal to noise ratio. Using, for example, the line emissions from fiber laser sensors would improve system performance in both absolute and relative modes.

In this prototype system, the lack of adequate thermal damping between the MZI and the environment made static measurements challenging. In previous systems, a dielectric gel was used to thermally insulate the interferometer [PONJ12] and in practical implementations, standard telecommunication component pack-

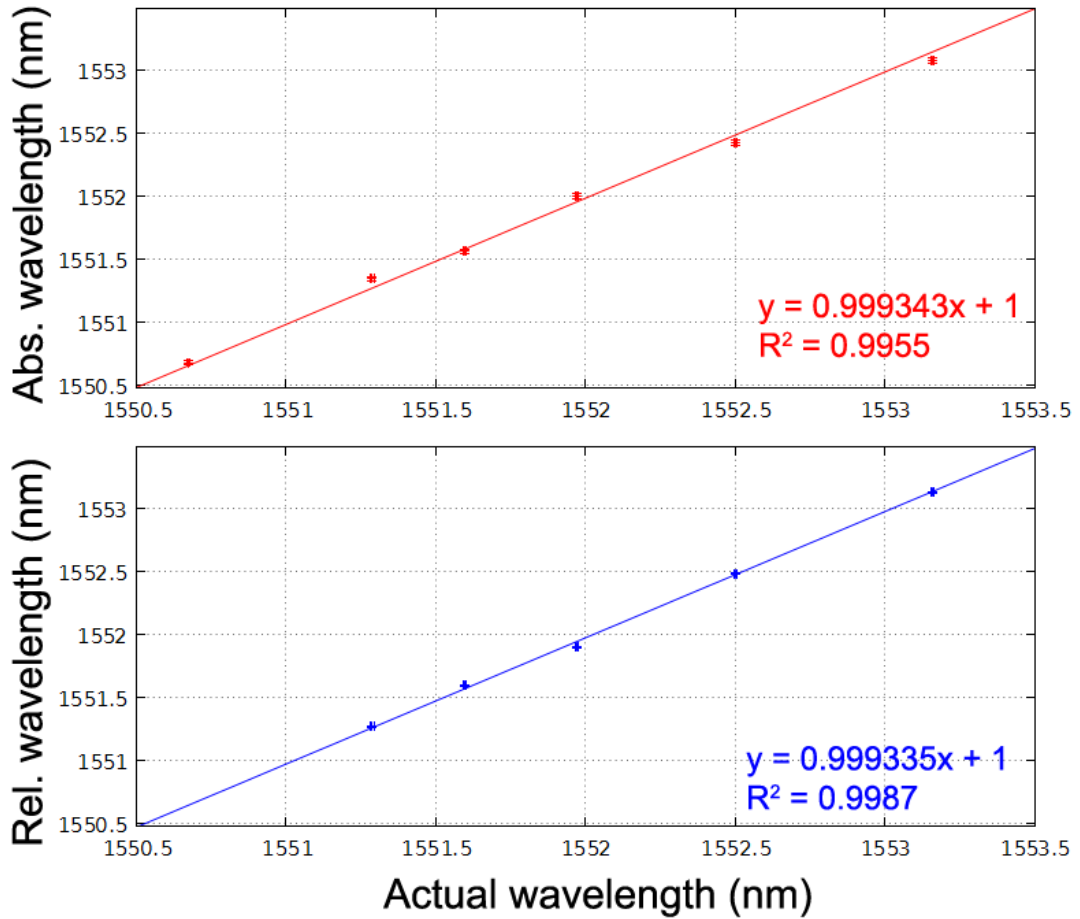


Figure 6.39: The ‘actual’ wavelength of a cantilever-mounted FBG, measured using a commercial interrogator (resolution 5 pm), compared to the wavelengths measured by the interferometric system. Absolute wavelengths were monitored by repeatedly using the thermal tuning technique while the cantilever was stationary. Relative wavelengths were inferred by summing the phase shifts while the cantilever was undergoing deflection and then adding these to the initial value. The gradients of both lines should ideally equal unity, and this is the case to at least 3 significant figures, showing that both modes are able to record wavelength accurately.

aging including active temperature control can enhance thermal stability. For dynamic measurements, thermal drift is less of a concern as unwanted low-frequency components can be filtered out.

The success of the relatively simple prototype interrogator encourages further study. More substantial control over the MZI may be achievable by depositing miniaturised silica waveguides onto a silicon chip. Incorporating the MZI onto a silicon photonics platform [JF06] could improve stabilisation and reduce the time taken to thermally tune the path difference to within tens of milliseconds [HKG<sup>+</sup>09].

Such a platform introduces new challenges, however. In the current system, the high thermal expansion of the epoxy and the low thermo-optic coefficient of silica glass allow refractive index correction factors to be calculated with the simplified equation (6.32). Arguably, this simplification may have been partly responsible for some loss of accuracy. Improvements could be made by using the more complicated correction factor in equation (6.31), but this requires detailed knowledge of parameters such as the heated length of waveguide and the wavelength-dependence of the thermo-optic coefficient. These parameters are not only difficult to measure, but may also themselves harbour some temperature dependence. It may therefore be desirable to design the MZI such that simplifications can be made.

When dealing with miniaturised silicon photonics, the high thermo-optic coefficient leads to a situation which is the reverse of the present one, where  $D\frac{dn}{dT} \gg nL\alpha$ . It may eventually be found that simplifications cannot be made at all, but the parameters can at least be more accurately known and controlled through careful design.

The ratio of the thermal tuning and sampling speed of the system defines parameters such as uncertainty in the slope,  $\Delta S$ . The higher thermal tuning rate of a miniaturised platform thus requires similar improvements to the sampling frequency. In the prototype system, the relatively low 500 Hz sampling rate only produced slope errors corresponding to a 3 pm wavelength uncertainty. A much larger error arose from imperfect knowledge of the calibration parameters, but

this was also the result of phase noise. Thermal tuning speeds may therefore have to be deliberately limited to allow for accurate and precise deduction of  $\mu_m(T)$  and  $\gamma_m(T)$ . Faster tuning may allow several absolute wavelength calibrations to be rapidly made in series, especially if a secondary calibration could be performed during cooling. This would, from a statistical viewpoint, produce a result with a higher confidence. However, because absolute wavelength calibration requires only a single tuning event, there may also be some benefit to modelling  $\mu_m$  and  $\gamma_m$  to gain a better understanding of how these parameters evolve with temperature.

## 6.7 Interrogation System Summary

The characteristics of an FBG interrogation scheme based on a three-output interferometer and a wavelength division multiplexing switching system were investigated. The scheme provided simultaneous interrogation of static and dynamic fiber Bragg grating nanostrain sensors. A software lock-in amplifier was used to extract static strain signals with a  $1 \text{ n}\epsilon$  resolution. Fast Fourier transform algorithms were applied to retrieve dynamic strain measurements in both seismic and audible frequency regimes. Frequency resolutions of 5 mHz and 5 Hz were obtained for bandwidths of 1 Hz and 2 kHz. In both cases, a high strain-resolution was retained as noise floors were  $7$  and  $17 \text{ n}\epsilon/\sqrt{\text{Hz}}$  respectively.

Assessments of fixed and oscillating strains were employed to provide evaluations of the elasticity of a cantilever beam based on its natural frequency. These agreed with modeled and theoretical values. Further application of the model allowed for a full mechanical description of the cantilever, based on an inverse analysis. The scheme's ability to scale conveniently to allow quasi-distributed strain measurements without resolution or response losses make it ideally suited to strain-based structural health monitoring applications, which will benefit from the dual-regime and distributed measurement attributes.

Slow drifts in the measured strain were thought to arise mainly from drifts in the OPD of the MZI. Accurate long-term strain measurements in structural health monitoring will depend on tackling this issue by using temperature controllers and

further characterisation of drifts.

The interrogation scheme was also extended to provide measurements of absolute sensor wavelengths, in addition to its previous ability to measure relative wavelength shifts. By thermally tuning the interferometer once, the phase responses of each sensor in the array were simultaneously characterised and compared. Because phase shifts are wavelength dependent, the phase shifts of unknown sensors were compared to those of a known reference to provide an absolute measure of the wavelength of each sensor.

A prototype system revealed that the absolute wavelengths calculated were both accurate and repeatable to within 20 pm (equivalent to 1.6 °C or 17  $\mu\epsilon$ ). Both accuracy and precision were limited by errors in the characterisation of the interferometer's output response and its dependence on temperature during thermal tuning. The system was able to accurately resolve static and dynamic Bragg grating strains in both absolute and relative wavelength measurement modes.

The passive, solid-state nature of the interrogator lends itself to potential fabrication in planar optics formats, such as silicon photonics. This could in future lead to physically small, cost-effective and mass producible interrogation systems for measuring prestress in PCPVs and PCCs. The scheme described here may help break the long-standing trade-off between multiplexing capability and wavelength measurement quality.

# Chapter 7

## Industrial Application

A packaged, spot-weldable fibre strain sensor and a high-resolution interrogation scheme for monitoring distributed prestress losses in irradiated prestressing strands has been described. In this chapter, methods for extending these technologies to a 1 – 2 % population of the 30 – 40 m long tendons in a PCPV or PCC are considered. This will highlight the advantages and future work for the technologies developed in this project.

### 7.1 Smart Strand Installation Procedure

The procedure for mass-fabrication of smart strands is proposed as follows:

1. Packaged, spot-weldable FBG sensors are prefabricated intermittently along metallised addressing fibre and wound on a spool
2. Lengths of new prestressing strand arrive at a workshop loosely coiled
3. The strand is uncoiled and slowly rotated — the addressing fibre is wound into the grooves of the rotating strand and then coated over with a thick grease, plastic grips or a quick-drying filler material to keep it in place
4. When a sensor is reached, the local area of the strand is cleaned and the sensor is spot-welded, before being coated over in grease to prevent corrosion

5. The other end of the strand is recoiled for storage, transportation and installation into a PCPV or PCC

Typical strand replacement procedures can then be followed. The old strand within the structure is destressed and one end of it is welded to the end of the new instrumented strand. As the old strand is pulled out of the duct, the smart strand is uncoiled and fed into its place. The strand is coated with lubricating oil as it enters the duct to prevent its corrosion in service. Several strands of a single tendon can be replaced in this manner. As not all of the strand ducts in a PCPV are always utilised, it may not be necessary to immediately begin replacing functioning strands with smart strands. For instance, in Torness, there are some 96 ducts which are left free of tendons, so it may be possible to use these ducts for initial tests.

### **7.1.1 Anchorage Load Measurements**

Stress relaxation is the only prestress loss mechanism which does not cause changes in strand strain (§3.4). As it is a relatively large effect in new strands, it can be measured with commercially available load cells at the anchorages. The proposal is to either install small load cells at the barrels of each strand, or larger load cells at the bearing plate to measure the total force changes in the tendon. The force measured by the load cells would be equivalent to the average prestress, the dashed line shown in figure 7.1. Distributed strains measured by the FBG sensors could be combined with force measurements from load cells or lift-off inspections to provide cross-verification and reduce the probability of common mode failures. A comparison of anchorage force and strand strain profiles may also provide some clues as to the effective stiffness of strands. This can be used as an indicator of a strand's friction and corrosion state.

### **7.1.2 Fibre Ingress**

The addressing fibre in the system is coated in a copper alloy, but the fibre at the ingress points (entering the duct) are a weak point and so require more pro-

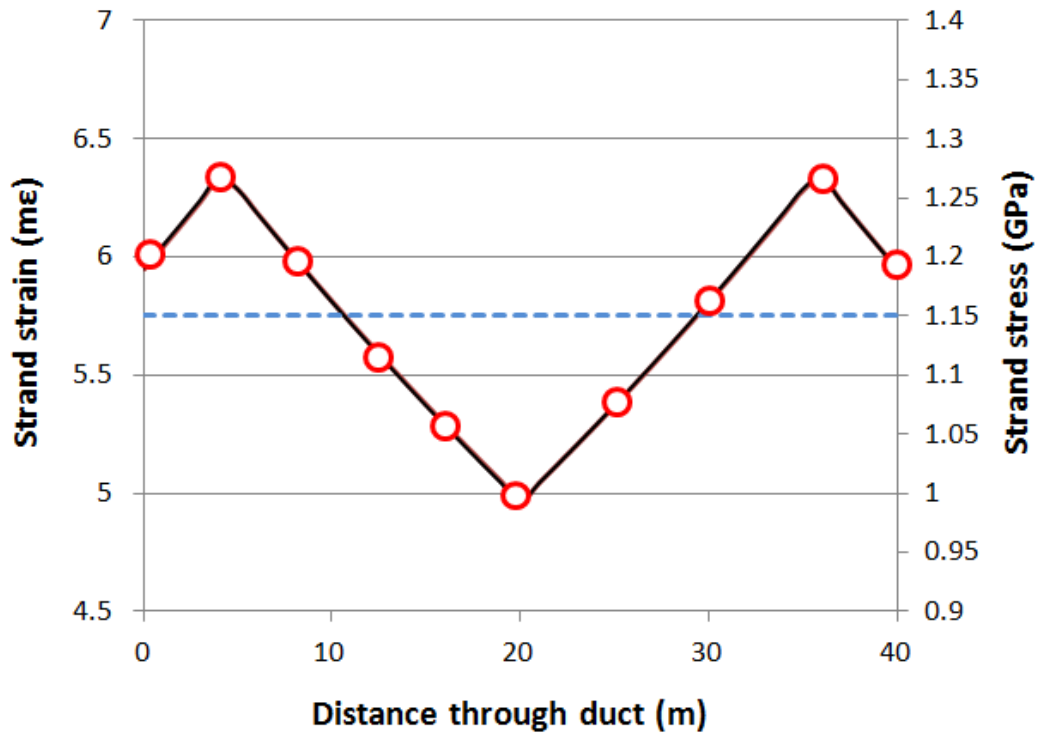


Figure 7.1: The theoretical strain profile arising due to short-term prestress losses in a 40 metre strand. 10 strain measurement points, shown as red circles, would be enough to reconstruct this profile after interpolation. The blue dashed line shows the effective average strain which would be measured by a force cell at the anchorage. If the strands are later found to have strain profiles which are symmetric about the critical point, as they should do in theory, then higher spatial resolution may be achieved from only monitoring strands over one half of their length, up until the critical point.

tection. Commercially available armoured fibre—surrounded with several layers of gel filling, steel wire armouring, rip cord and sheathing—may provide better protection against bending and mechanical impulses at these locations [Kai13].

Fibre ingress through the anchorages must also be made via a route which does not cause obstruction of the prestressing jack. Clearance for the prestressing jack is provided by the stressing stool, so the fibres could exit the duct and strand via a modified anchor barrel or grip wedge, in the location shown in figure 7.2. A proposal for the design of a modified barrel is shown in figure 7.3. The fibre within the barrel fibre would be spliced to the strand fibre on site. Another, option is to allow the fibres to emerge from the strand through modified detensioning spacers—small disks which are sometimes placed between the barrel and the anchorage plate after reshimming, as shown in figure 7.4 [ZSB]. Future work should aim to investigate and expand upon these proposals further.

### **7.1.3 Smart Strand Location**

As radiation effects on normal fibres were found to be minimal beyond one metre from the liner, smart strands with SMF-28 or similar addressing fibre can be installed beyond this distance. If monitoring of prestress closer to the liner is required, then specialist radiation-resistant fibres which exhibit less darkening may be used.

The top caps of PCPVs present further uses for smart strand technology. During current routine plant inspections, the deflection of the top cap is also measured during deliberate pressurisation of the PCPV while the reactor is on- and off- line. This is currently done using laser levels, but a top cap with instrumented strands may be able to monitor deflection using FBGs. This would supplement the available data, improving confidence in both measurements.

## **7.2 Interrogation Scheme Extension**

Prototype strands, fabricated in the lab, were typically 1-metre long and contained a limited number of strain sensors. This section will discuss how the

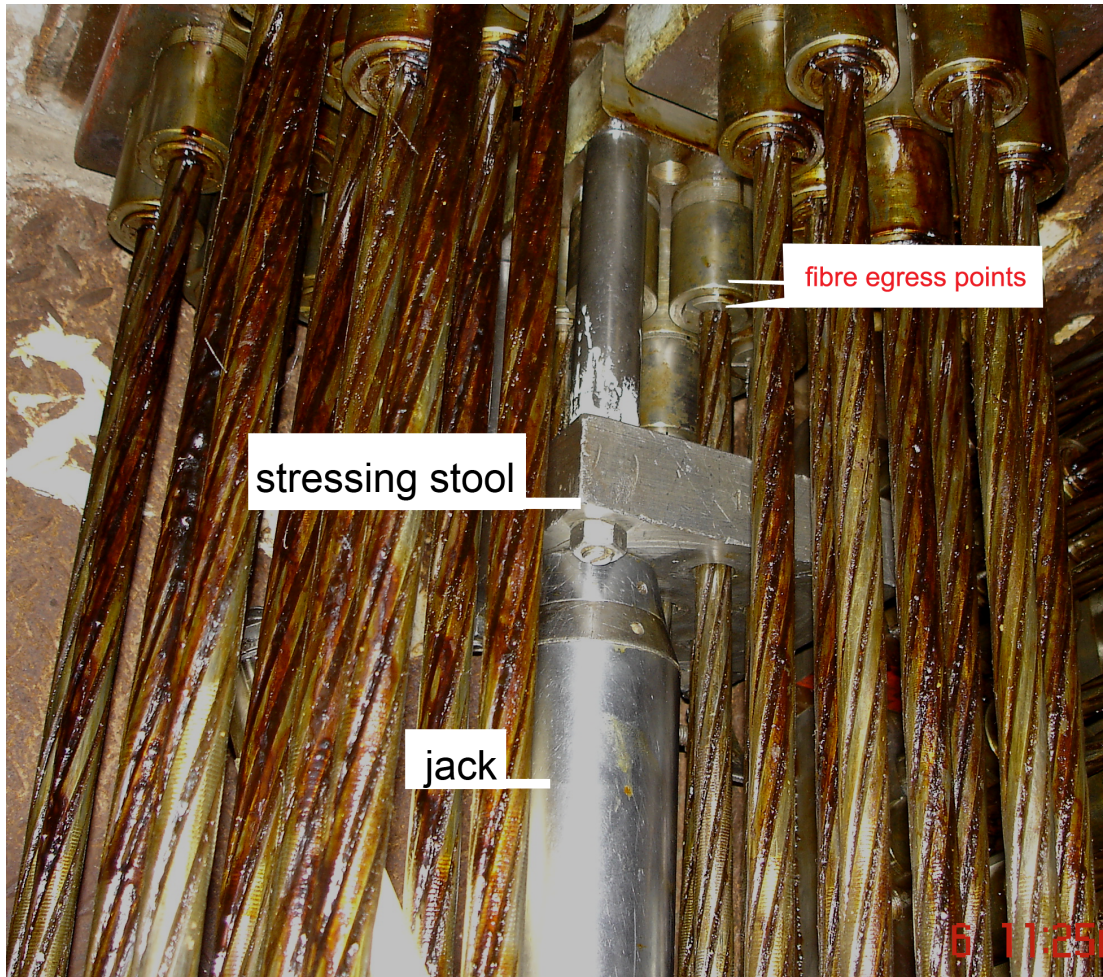


Figure 7.2: The proposed egress (exit) point for the optical fibre, attached to the prestressing strand. A modified anchorage barrel for example, could guide light from the strand, through the addressing fibre in the barrel and to an output port on the side of the barrel, as shown in figure

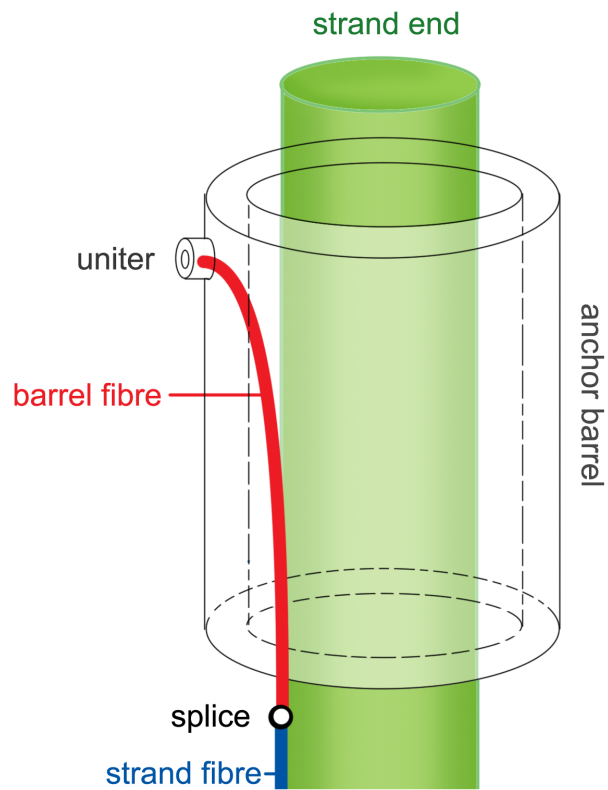


Figure 7.3: A proposed modified anchor barrel, containing an armoured fibre, to be spliced to the fibre on the rest of the strand. A uniter allows optical connection of optical fibre lines to the anchor barrel.

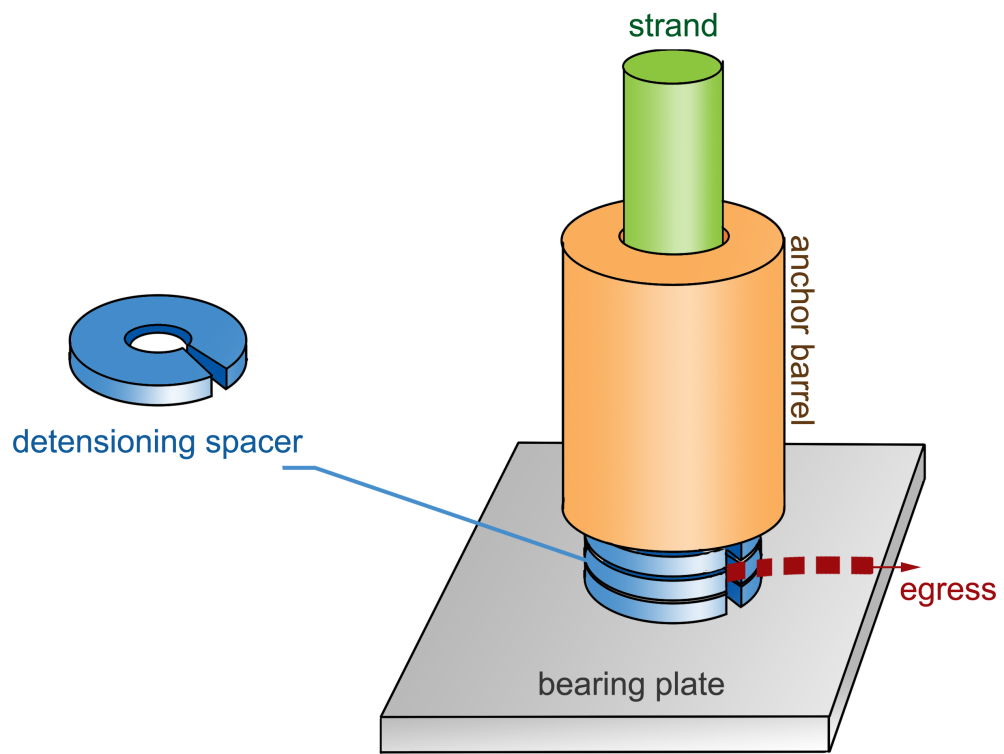


Figure 7.4: A second proposed egress point for the addressing fibre is through the detensioning spacers which sit between the bearing plate and anchor barrel.

interrogation method in this project can be extended to measure prestress losses in a greater number of longer strands.

### **7.2.1 Number of Measurement Points**

As spot-welding was found to cause no changes to the strand's properties, the main limitation to the number of sensors per strand stems from the interrogation system. FBG sensors must fall within the same passband windows of the CWDM or AWG throughout the measurement period. Strain measurements may become difficult to track if the Bragg peaks shift to fall within different passband windows.

The largest sensor wavelength shifts will occur during the strand's initial  $7 \text{ m}\epsilon$  prestressing. Initially, if a strain transfer coefficient of 10 % is assumed, this means an 0.8 nm shift in Bragg wavelength is to be expected. Meanwhile, temperature and radiation red shifts could sum to to 0.25 nm for a  $20 \text{ }^\circ\text{C}$  temperature change and 10 years of neutron-gamma irradiation (§4.3.5). Conservative estimates would thus require that the windows of the CWDM be at least 2 nm wide.

Temperature compensated strain measurements may require double this, a 4 nm bandwidth in total. A broadband optical source of 60 nm bandwidth would thus allow for 15 temperature-compensated strain points per fibre line. Figure 7.1 shows that even with only 10 measurement points, the spatial resolution of 4 m would be enough, through interpolation, to reconstruct the M-shaped strain profile of a 40 m prestressing strand under friction.

Of course, improved strain transfer values may improve measurement resolution, but they also require a larger bandwidth, reducing the number of possible sensors per fibre line. This limitation can be overcome by instrumenting strands with multiple fibre lines, as shown in figure 7.5. This reduces the interrogation rate, but also increases redundancy and limits the consequences of fibre failure in any single line.

#### **7.2.1.1 Multiple Tendon Monitoring**

Extending this idea further, cascades of switches, placed in series, could allow many strands to be monitored around the structure with a single interrogator.

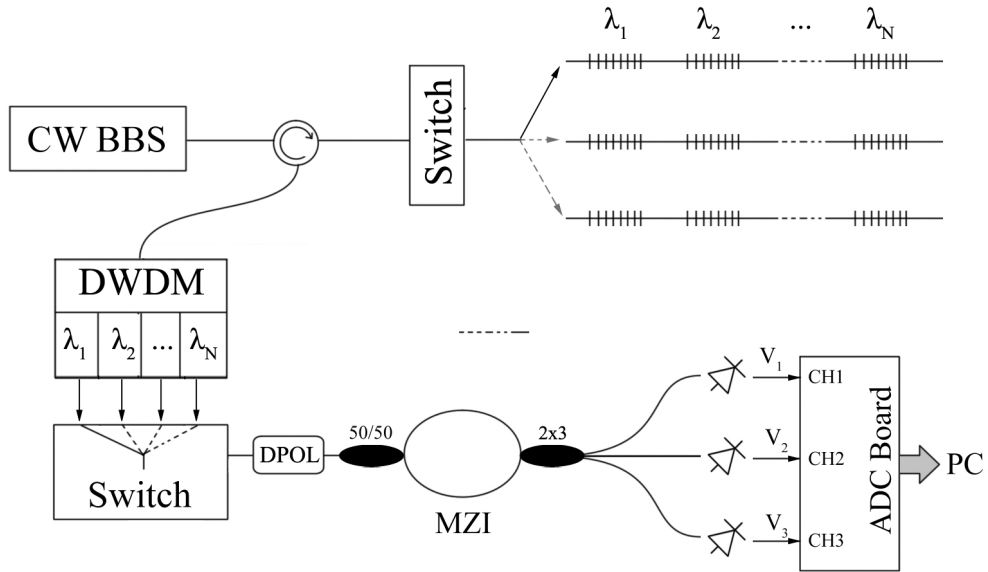


Figure 7.5: The interrogation system, extended to provide measurements of numerous FBGs by using dense wavelength division multiplexing and switched parallel fibre lines. These parallel lines can be used to improve redundancy of the strain measurements in one strand, or used to interrogate different strands.

The limiting factor is the optical power received at the photodetectors. An optical budget calculation for this system, shown in appendix A.10, estimates that the optical power at the photodetectors is still adequate when two switches are cascaded in series. This would provide 1024 parallel fibres lines, enough to interrogate 2–5% of the strands in a PCPV, when using switches with 32 outputs. Switch speeds are typically around 2 kHz, so the interrogation rate of such a large system would be limited to around 1 Hz. This is still fast enough to measure long term prestress losses. Currently, the cost of instrumenting a strand is driven by the price of the interrogator, which is estimated to be below £5k. Using multiple interrogators may be more economical, however, especially if the proposed miniturisation of the MZI using a silicon photonics platforms is successful.

### 7.3 Summary

Due to the modular nature of the interrogator and attachment methods, scaling the proposed smart strand technology up to PCPV and PCC prestress monitoring is reasonably simple and cost-effective. Sensors can be attached during or before strand replacement activities, from a reel of prepared fibre sensors. Safe fibre ingress into the structure can be achieved through the design of modified anchor barrels or detensioning spacers and the use of armoured fibre.

A combination of wavelength and space division multiplexing may allow a single interrogator to monitor 2–5 % of the strands in a PCPV or PCC with a high level of redundancy. The limiting factors are the optical budget and interrogation rate of the system. Once combined with anchorage load measurements, the smart strand can measure strain-inducing prestress losses such as friction, anchorage slip, concrete creep, shrinkage and elastic shortening and also non strain-inducing losses such as strand relaxation. Over all, the technology can facilitate more detailed measurements of prestress evolution in both existing and future PCPVs and PCCs.

# Chapter 8

## Conclusions and Further Work

### 8.1 Conclusions

The manufacture and interrogation of a novel fibre Bragg grating instrumented prestressing strand was demonstrated in this project. The technology was designed to augment the current methods of monitoring the health of prestressed concrete barriers surrounding fission nuclear reactors, improving confidence and safety as the structures age. The sensors have the spatial and strain resolution required to monitor both short- and long- term prestress losses in concrete structures and the robustness to survive prolonged doses of radioactivity and mechanical stress.

Optical attenuation in silica fibres due to mixed neutron-gamma radiation is lowest for pure silica fibres with a fluorine doped cladding. However, due to the effectiveness of concrete as a biological shield, radiation levels are low enough beyond one metre from a fission reactor's liner to cause negligible radiation induced attenuation in non-specialist, germanium-doped fibres such as SMF-28, provided they are metal plated. Type-I fibre Bragg gratings used in this work were written into sections of germanium doped fibre, as these demonstrate reduced radiation-induced shifts in the Bragg peak.

As metal-plated FBGs are not commercially available, fibre metallisation based on evaporative deposition and electroplating was demonstrated in this project. The coating quality of successfully fabricated specimens was high, but

yields were low due in part to the overhandling of fibres and their exposure to moisture and alkaline environments during plating. To better protect the FBGs from mechanical damage, they were brazed into kovar capillaries by induction heating in an argon atmosphere. The Curie transition of kovar at 430 °C prevented the bare FBGs from being exposed to temperatures any higher than 480 °C. Steel heat susceptors at the capillary ends provided localised heating up to 1300 °C to bond the fibre and capillary using a brazing alloy.

High temperatures were found to decrease the mechanical strength of fibre splices, so a spliceless method of FBG capillary encapsulation was developed. A small section was stripped from the mid-section of a metallised fibre to allow type-I FBGs to be written. These were successfully brazed into capillaries with minimal losses to mechanical strength and a 40 % loss in reflectivity.

To attach the packaged FBGs to the strand, a spot-weldable strain plate was designed. The strain plate was stamped from 0.5 mm thick steel sheeting, brazed to the capillary and then resistance-spot-welded to the strand. While spot-welding lead to 0.1  $\mu\text{m}$  deep martensitic regions on the strand surface, this did not affect the bulk mechanical properties or strength of the strand. Because of their all-metal and glass fabrication, these sensors are designed to withstand long-term irradiation, mechanical shear forces, chemical attack and most importantly the 7 m $\epsilon$  strain induced during prestressing. The sensors successfully measured strand strain with up to 87 % strain-transfer efficiency.

A high-resolution, passive interferometric interrogator for the instrumented strand was developed. Static and dynamic strain measurements of multiplexed FBG sensor arrays with 1 n $\epsilon$  and 10 n $\epsilon$ / $\sqrt{Hz}$  resolutions were achieved respectively. The system was further extended to provide measurements of absolute sensor wavelengths, by thermally tuning the interferometer and measuring the relative phase responses of each sensor in the array. A prototype system allowed absolute wavelengths to be calculated to within 20 pm (equivalent to 17  $\mu\epsilon$ ). Both accuracy and precision were limited by errors in the characterisation of the interferometer's response to thermal tuning. Long-term stability of the interrogator was also affected by the thermal stability of the interferometer during

measurement. Temperature controlled environments may therefore be necessary to ensure long-term stability while measuring long-term prestress losses in PCPVs and PCCs.

Both the sensor attachment method and the interrogation system were highly modular. This will allow the technology to be scaled up and integrated more conveniently with current practices. The scheme's spatial resolution is high enough to interpolate the M-shaped profile of the strand arising from the combined effects of friction and anchorage slip. Because strand-relaxation does not induce a strain change, it is proposed that the smart strands are combined with anchorage load measurements via electro-mechanical transducers. This will also provide cross-verification for measurements and reduce the likelihood of common-mode failures.

## **8.2 Future Work**

### **8.2.1 Sensor Fabrication and Attachment**

Future work could aim to address the low yields when metal replating FBGs. The addition of a carbon underlayer and metal sputtered seed coatings may improve coating hermeticity and quality. Metal-coated FBGs would still be useful in this application as they would form an additional layer of protection against thermal, mechanical and water damage. The use of the capillary would still be recommended, however, as it provides mechanical protection, guidance under compression and an intermittent thermal expansion and stiffness between glass and steel. This results in gradients of expansion under stress and temperature rather than sudden transitions, and hence reduces the likelihood of failure.

It would also be beneficial to make sensor fabrication and attachment methods more consistent, as this will allow the strain and temperature sensitivity to be predicted and characterised more reliably. Currently, exact strain and temperature characterisation is somewhat unpredictable and this can physically limit the system's measurement performance.

Some initial longitudinal stress tests have been conducted on instrumented

strand using a commercial stressing jack in this project. The spot-welded sensors were found to survive up to the maximum applied force equivalent to 30% UTS of the strand. Unfortunately, it was found that the flat-faced jaws of the stressing jack caused relative wire movement within the strand as it was clamped. This caused non-uniform loading of the wires in the strand, meaning strain measurements were difficult to analyse. In future work, relative wire movement can be reduced during longitudinal stress tests by potting each end of the instrumented strand a steel cylinder of industrial strength epoxy [Mac08].

Measuring the overall strand strain independently of bend and wire slippage during prestressing, may require that multiple strain sensors are attached to several wires of one strand at the same distance from the bearing plate. The relative strains between the wires would then be able to highlight bend and slippage.

### **8.2.2 Creep and Stress Corrosion**

One aspect not addressed in this project was the creep of the finalised strain sensor assembly under prolonged loads. Stress relaxation, creep or stress-corrosion of the strain plate, brazing material, capillary and even the fibre itself may lead to gradually decreasing measured strains or mechanical failure. Creep can be alleviated somewhat by forcing it to occur before the smart strands are utilised, by using cyclic stressing and destressing of the instrumented strand, but the magnitude of creep effects is currently unknown. Creep could be characterised over the course of months using a suitably stable interrogation system, once it has been developed.

### **8.2.3 Interrogation Stability and Resolution**

Creep measurements require the long-term stability issues with the interrogation system to be addressed. Thermal changes to the optical path difference in the interferometer were found to affect fringe positions and densities, and hence the strain measurement. Although the MZI was thermally insulated using dielectric potting gel, thermal control through peltiers and feedback may prove more

successful.

Incorporating the MZI onto a silicon photonics platform was proposed in §6.6.9. This may allow for a greater degree of thermal control using peltiers, improving the interrogation stability and tuning speed during absolute wavelength calibrations. Further work will aim to construct and characterise the response of the miniaturised MZI. It may be found that other components within the system, such as the switch and photodetectors can also be incorporated within a single chip and mass produced. This would significantly reduce costs and barriers to deployment of the current prototype system.

Once thermal drift is addressed, the resolution of the system can be further improved by using spectrally narrower Bragg peaks. In most of the work in this project, the FWHM of Bragg peaks was 0.3 nm. Reducing this to 0.1 nm in later experiments improved the modulation of voltage channels and hence the signal to noise ratio of the strain signal.

Fibre laser sensors may further improve signal-to-noise ratios and allow for interferometers with larger OPDs to be used, improving strain resolution. In fibre laser sensors, pump light is resonated within a phase-shifted FBG in an erbium doped fibre medium, leading to lasing. The reflected wavelength of the laser is again strain and temperature dependent but the spectral width of the sensors is reduced to sub-femtometre levels. Combining the emissions from fibre lasers with an interferometer with denser fringes may improve absolute and relative strain resolutions even further. Note that ensuring that the pump light can reach an array of multiplexed fibre lasers requires that the FBGs that make up the lasers do not overlap spectrally. This means that although fibre lasers are spectrally thin, they do not have reduced sensor bandwidth requirements [CFK08]. It should also be noted that, unfortunately, the erbium doping may lead fibre lasers to be adversely affected by neutron-gamma radiation. The sensors could be used, however, at strands at the periphery of the PCPV or PCC, or within structures which are unirradiated.

This feeds into future non-nuclear applications for the developed smart-strand technology—applications which are arguably less demanding. Prestressing strands

are used to post-tension a variety of concrete structures in civil engineering, and most of these are unirradiated. It follows that this technology, once applicable to PCPVs and PCCs, will be more than adequate to measure prestress losses in any post tensioned concrete structure. Further work on protecting the fibres from alkaline environments may also allow strands to be used in pretensioned or grouted concrete structures, where the cement may come into direct contact with the fibre.

#### **8.2.4 Radiation and Temperature Dependencies**

For the current application, however, it would be ideal to extend the radiation resistance of the sensors to allow them to be used deeper within PCPVs and PCCs, beyond the 1 metre threshold from the steel liner. In high-radiation locations, type-II damage gratings, regenerated gratings or those written in sapphire fibre may present reduced radiation induced Bragg shifting, but due to the novelty of some of these gratings and the time it takes to conduct a radiation experiment, there have not yet been formal studies. Indeed, there is a general lack of understanding on what radiation is doing to these gratings on the molecular level. There should also be a push to characterise the dependence of radiation-induced Bragg shifts on ambient temperature, as the generally non-rigorous definition of environmental variables makes comparison between studies difficult. Failing a general study of radiation, a study specific to fibres within PCPVs or PCCs would be beneficial.

Characterisation of the strain measured by the FBGs at different ambient temperatures may also be required as strain sensitivity can be temperature dependent [OYJT04]. The behaviour of the sensor packaging is also important. While it may be found that the creep in some brazing alloys is low, the same alloys may creep considerably under the combined effects of high stress, radiation and high temperature. Some characterisation of the brazing alloys used in this project under irradiation will be required if smart strands are going to be used closer to the reactor liner. For instance, the silver solder paste used in this project may be unsuitable in highly radioactive areas because neutrons can transmute

silver into volatile cadmium.

The interactions between the capillary, the metal coating on the fibre and solidified brazing alloy both during and after brazing should also be investigated for different brazing materials. The interaction between the sensor materials and the strand could also be studied further — chemical reactions between the strand and sensor metals, for example, could set up galvanic cells, leading to corrosion of the strand over time.

### **8.2.5 Ingress and Load Cells**

Further study of the entry paths for fibres into the prestressing strand is required. While modified anchor barrels or detensioning spacers have been proposed, such technologies still need to be designed and tested, to ensure that fibres do not obstruct the stressing jack. If the anchor barrel or spacers could be further modified to include the load cells required for the stress relaxation measurement, then this would further simplify the smart strand installation procedures. Load cells could be electronic, hydraulic, or even fibre sensor based. Fibre-instrumented load cells work by measuring the transverse strain in an FBG coiled around a load cell ring. The advantages of using an all-optical solution like this are that one interrogation system could be used to monitor the entire set up, reducing costs and the need to synchronise different measurement methods. This increased dependence on the interrogation scheme could, however, increase the chance of common mode failures.

### **8.2.6 Further Scheme Extension**

Once wavelength division multiplexing is saturated, the interrogation scheme can be extended using switched parallel fibre lines (space-division multiplexing). Time division multiplexing may be used to further extend this scheme, but this was not initially suggested as expensive electronics with nanosecond response times are required. Combined multiplexing schemes do, however, remain a possibility and can provide even more sensing capability in a single network. Weighing the

costs and benefits may show that it is more economical to simply have multiple separate sensor networks, however.

In the current interrogation system, light is depolarised to prevent the interferometer from producing a polarisation-dependent interference intensity (as this can be mistaken for a drifting strain). If, however, polarisation is controlled within the MZI and within the rest of the interrogation system, by using polarisation-maintaining fibre, then two orthogonal polarisations could be guided to each FBG. This would provide two separate measurements which depend slightly differently on strain and temperature. With the dependencies characterised, temperature-corrected measurements of strain could be provided by single FBGs, rather than two. While radiation correction would have to be investigated further, a birefringent system like this can be used to extend sensing density.

### **8.2.7 Field Trials**

Scaling these sensors up from a prototype demonstration directly to the field may be challenging. There are, however, mock-up reactor projects running with EDF Energy. At the time of writing, ‘Vercors’, a project running in France, aims to build and monitor a mock up AGR reactor. There is interest in testing the smart strand technology developed in this project on this mock-up reactor, as its potential for present and future PCPV monitoring has been recognised. The habitual use of grouted ducts around the world arguably makes smart strands even more useful, as lift-off inspections are impossible in these situations.

### **8.2.8 Plant Monitoring**

In the mean time, however, the technology developed here could be applied to the monitoring of other assets around a nuclear power plant. The level of optical fibre sensing in nuclear power plants is currently minimal, but packaged FBGs could be used to monitor strain, temperature, radiation and vibration in the various stand pipes, cranes, fuel stores, vessel penetrations, gas cylinders and waste storages around the plant. Sensible extensions of the technology developed here could

reduce the probability of common mode failures and further ensure the continued safe operation of nuclear power plants in this generation and the next.

# Appendix A

## A.1 Bragg Peak Shift with Strain

Partial differential of the Bragg equation (4.10) with respect to length,  $l$ , yields:

$$\frac{\partial \lambda_B}{\partial l} = n_{eff} \frac{\partial \Lambda}{\partial l} + 2 \left( \Lambda \frac{\partial n_{eff}}{\partial l} \right) = \lambda_B \left( \frac{1}{\Lambda} \frac{\partial \Lambda}{\partial l} + \frac{2}{n_{eff}} \frac{\partial n_{eff}}{\partial l} \right) \quad (\text{A.1})$$

which can alternatively be written as:

$$\frac{\partial \lambda_B}{\lambda_B} = \left( \frac{\partial l}{\Lambda} \frac{\partial \Lambda}{\partial l} + \frac{\partial l}{n_{eff}} \frac{\partial n_{eff}}{\partial l} \right) \quad (\text{A.2})$$

The change in periodicity,  $\Lambda$ , is analogous to strain, so the first term in the equation is  $\varepsilon_z$ . The change in effective refractive index due to strain, however, is negative as the material's density is decreased while its polarisability is increased. The Pockel's coefficients  $p_{11}$  and  $p_{12}$  are used to describe this effect in terms of the axial and radial,  $\varepsilon_r$ , strains on the fibre:

$$\frac{\partial l}{n_{eff}} \frac{\partial n_{eff}}{\partial l} = -\frac{n^2}{2} [p_{11}\varepsilon_r + p_{12}(\varepsilon_r + \varepsilon_z)] \quad (\text{A.3})$$

If the strain is only applied to the FBG axially, then the radial strain will arise due to the Poisson effect and  $\varepsilon_r = -\nu\varepsilon_z$  so that:

$$\frac{\partial l}{n_{eff}} \frac{\partial n_{eff}}{\partial l} = -\varepsilon_z \frac{n^2}{2} [p_{12} - \nu(p_{11} + p_{12})] \quad (\text{A.4})$$

The term in square-brackets is just a constant, which is termed the 'effective strain-optic constant',  $p_e$ . This allows the fractional shift due to strain to be

written as:

$$\Delta\lambda_B = \lambda_B(1 - p_e)\varepsilon_z \quad (\text{A.5})$$

For a Bragg peak at  $\lambda_B = 1550\text{nm}$  the following parameters are quite typical [Mal65]:

Symbol	Name	Typical Value Silica
$n_{eff}$	Effective Refractive Index	1.468
$\nu$	Poisson's Ratio	0.16
$p_{11}$	Pockel Coefficient 11	0.113
$p_{12}$	Pockel Coefficient 12	0.252
$p_e$	Pockel Coefficient 12	0.22

## A.2 Bragg Peak Shift with Temperature

Again note that terms such as the refractive index and periodicity in the Bragg (4.10) are temperature dependent. Partial differential with respect to temperature,  $T$ , yields:

$$\frac{\partial\lambda_B}{\partial T} = 2 \left( \Lambda \frac{\partial n_{eff}}{\partial T} + n_{eff} \frac{\partial\Lambda}{\partial T} \right) = \lambda_B \left( \frac{1}{n_{eff}} \frac{\partial n_{eff}}{\partial T} + \frac{1}{\Lambda} \frac{\partial\Lambda}{\partial T} \right) \quad (\text{A.6})$$

Increases in temperature lead to linear increases in refractive index via thermo-optic coefficient,  $\alpha_n$ , while the coefficient of thermal expansion of the glass,  $\alpha_\Lambda$ , defines temperature's linear effect on thermal strain (and hence periodicity):

$$\alpha_n = \frac{1}{n_{eff}} \frac{\partial n_{eff}}{\partial T} \quad , \quad \alpha_\Lambda = \frac{1}{\Lambda} \frac{\partial\Lambda}{\partial T} \quad (\text{A.7})$$

Substitution of  $\alpha_n$  and  $\alpha_\Lambda$  allow equation (A.6) to be simplified to:

$$\Delta\lambda_B = \lambda_B(\alpha_\Lambda + \alpha_n)\Delta T \quad (\text{A.8})$$

as is required.

### A.3 Fibre Survival Probability

If  $F$  is the probability that a fibre of length,  $L$ , fails below a stress level,  $\sigma$ , then the probability of survival is:

$$S(\sigma, L) = 1 - F(\sigma, L) \quad (\text{A.9})$$

In a given fibre, the tensile stress is gradually increased from in infinitesimal steps of  $d\sigma$ . If a fibre fails between a stress  $\sigma$  and  $\sigma + d\sigma$  then this requires that the fibre has managed to survive thus far,  $S(\sigma)$ , and it also requires that there is a flaw big enough to cause failure in the interval  $\sigma$  to  $\sigma + d\sigma$ :

$$dF = S(\sigma) \times (Ln(\sigma)d\sigma) \quad (\text{A.10})$$

where  $n(\sigma)$  is the number of flaws per unit length which fail between  $\sigma$  to  $\sigma + d\sigma$ . If the above two equations are combined, then we can simplify:

$$\frac{dS}{S} = Ln(\sigma)d\sigma \quad (\text{A.11})$$

and integrate:

$$\ln(S) = -L \int_0^\sigma n(\sigma')d\sigma' = -LN(\sigma) \quad (\text{A.12})$$

where  $N(\sigma)$  is used to define the cumulative number of flaws per unit length which fail before a stress  $\sigma$ .

### A.4 Modelled Induction Heating

Note: Due to limitations in computing power and software, hysteretic friction heating, Eddy current enhancement effects and convection were not modelled. Over all, this meant that the model likely underestimated heating rates.

### A.4.1 Phase 1

The brazing rig is simplified to the 2D axisymmetric geometry and mesh shown in figure A.1. Two 5 mm diameter copper coils surround a 0.7 mm diameter kovar capillary in air. To improve accuracy, element size is reduced near physically important or small domains.

For a coil driven at 350 kHz, kovar's relative permeability of  $\mu_r \approx 3000$  and resistivity of  $\rho_r = 5 \times 10^{-7} \Omega\text{m}$ , lead to a  $10 \mu\text{m}$  skin depth. Induction heating can thus only occur within the top  $13 \mu\text{m}$  of the capillary surface, with the rest of the body warming via conduction. This can be modeled using one of two methods:

1. Ensure the finite element mesh size is less than  $13 \mu\text{m}$  in the kovar domain.
2. Assume that the induced currents are restricted/localised to the very top surface of the capillary

The second option reduces computation time and is not a bad assumption as the magnetic field penetrates less than 5% of the capillary body. As such, the capillary domain is excluded from the magnetic fields interface and instead, its boundaries with the air are subject to an impedance boundary condition. The conductivity and permeability values for kovar are entered manually for this boundary.

Next, a 'coil group domain' is specified for the induction coil. This allows specification of the current,  $I_0$ , flowing through the coils in series. Ampere's law is allowed to act within all domains (except the capillary). This equates any current flows with a suitable induced magnetic field, or vice versa. When combined with the impedance boundary condition at the air-capillary interface, the overall effect is that the magnetic field induces currents which are restricted to the capillary boundaries.

For heat transfer purposes the capillary and fibre are defined as solids. The coils are neglected from heat transfer physics as they are water-cooled, thus there is no interest in their temperature.

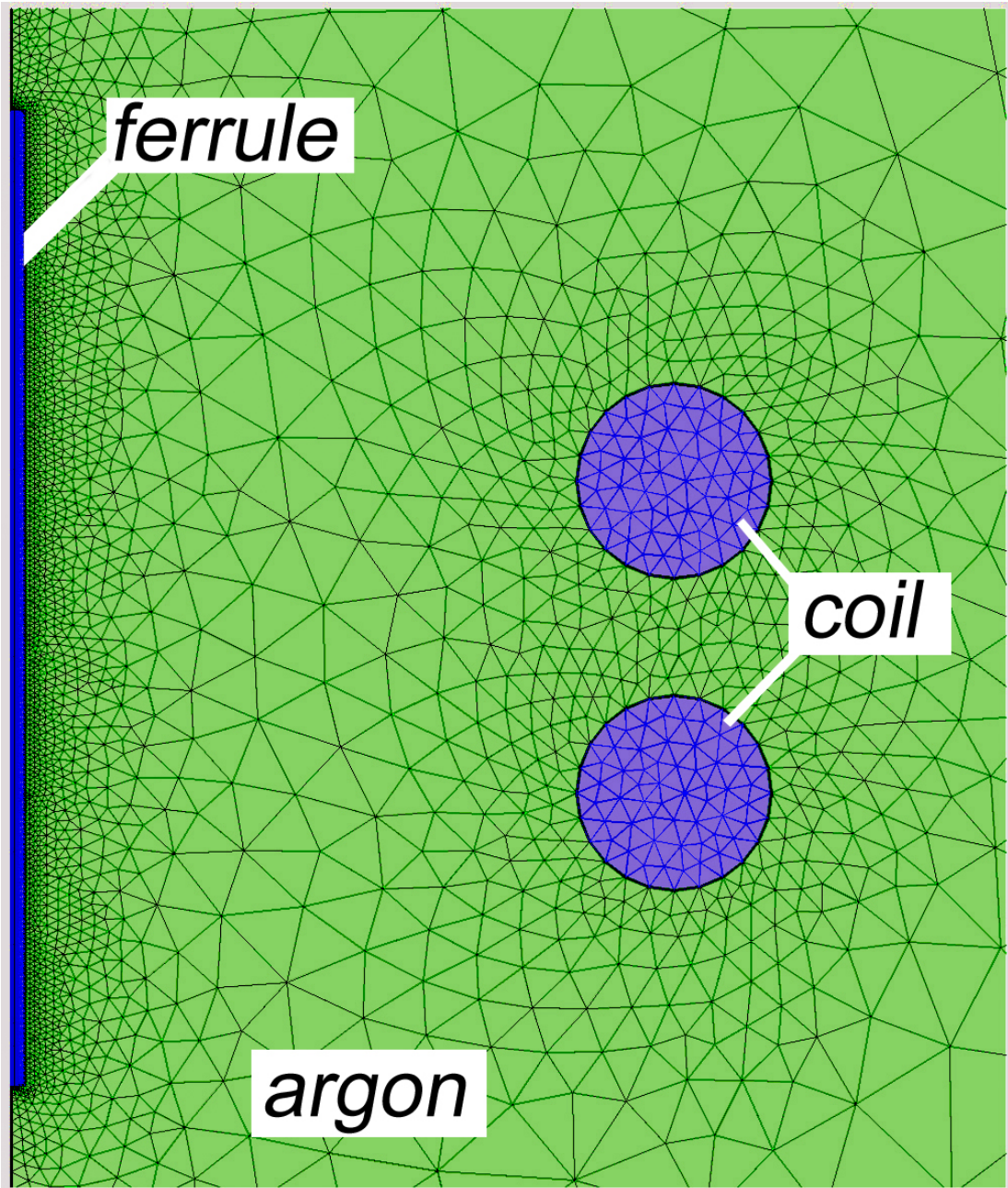


Figure A.1: 2D axisymmetric mesh used to model induction heating. A two-turn induction coil surrounds a cylindrical ferrule in an argon atmosphere.

A boundary heat source is defined for the capillary boundaries; its magnitude is defined as the resistive losses variable ‘mf.Qsh’, calculated by the magnetic fields interface above. Here it is assumed that all electron kinetic energy losses are directly converted to heat.

Magnetic field physics is solved in the frequency domain (for 373 kHz), while the heat transfer interface is solved simultaneously in the time domain. The model is solved between 0 and 1 second in increments of 0.1s. The temperature is monitored to find out when the Curie temperature of kovar (700K) is reached. The permeability of the capillary boundary is then reduced to  $\mu_r = 1$  and solutions are obtained for the remaining 24s.

The magnitude of the heating in the capillary must be collected and passed on to phase 2. The surface power gains at the capillary boundary are shown in figure A.2. As using these results point-by-point would take up computer resources, the sine function shown will be used to represent the heating function. Heating functions vary between the ferromagnetic and paramagnetic stages of the model. Both are collected and passed to phase 2.

#### **A.4.2 Phase 2**

In this geometry, the capillary rests upon an alumina block as shown in figure A.3. The base of the alumina block is thermally insulated and surface to ambient radiation with emissivity 0.8 occurs on all other external boundaries. Heat sources described by the heat intensity from phase 1 act on the ferrule. The model is solved for 25 s of induction heating before heat sources are reduced for a further 35 s of cooling.

During this phase, the capillary is heated using the heating functions found during phase 1. In reality, the base of the alumina block is in contact with a silica holder. As silica is a poor conductor of heat, the base can be thermally insulated in the model. Surface to ambient radiation with emissivity 0.8 occurs on all external boundaries except the base of the alumina block. The thermal

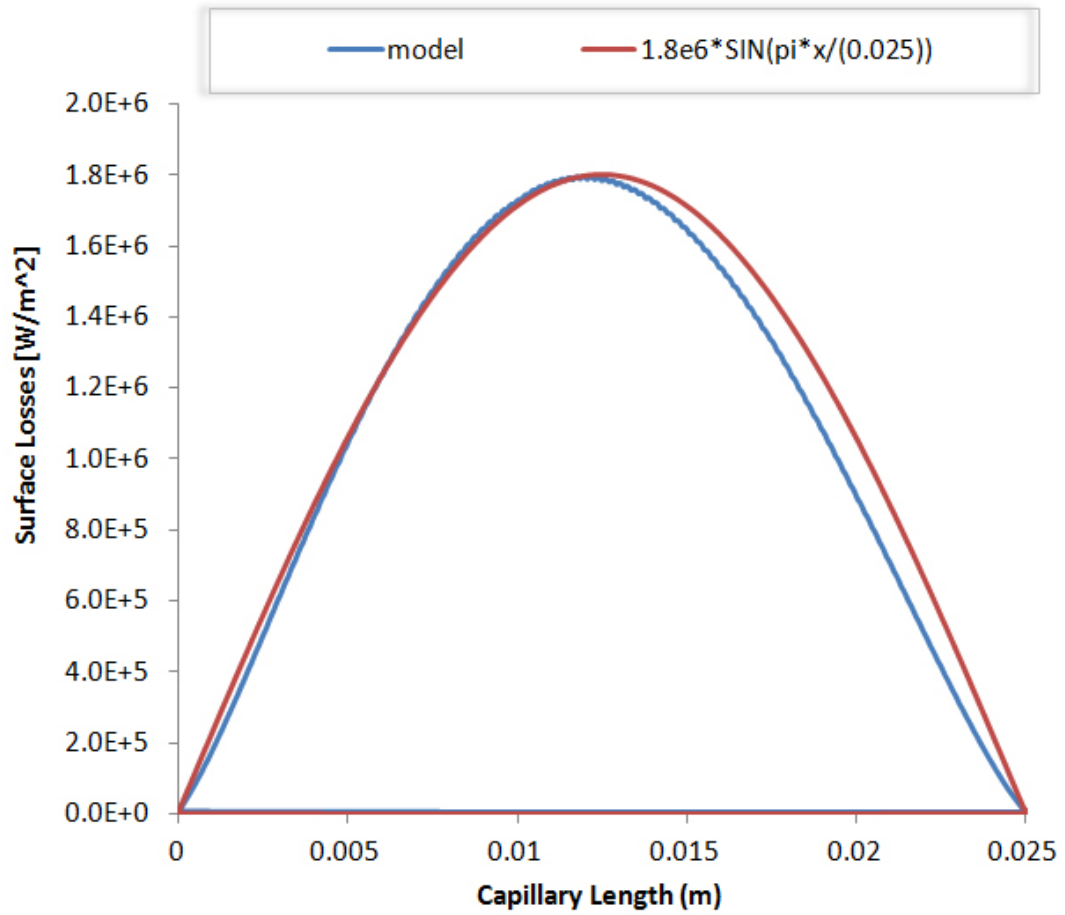


Figure A.2: Magnitude of electromagnetic surface losses along the length of the capillary for the ferromagnetic stage. Shown is the model outputs along with a sin fit.

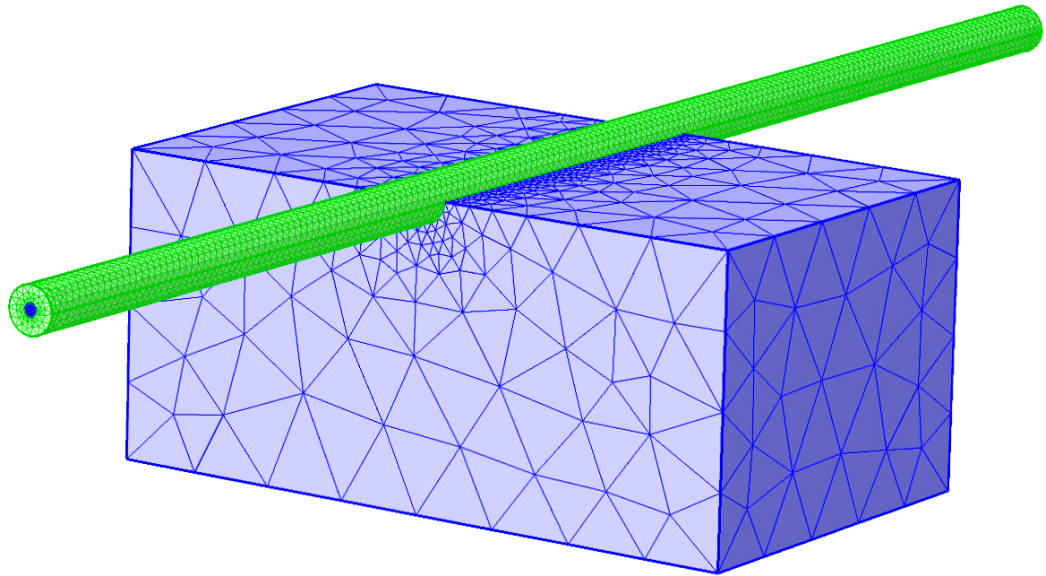


Figure A.3: 3D model used to describe cooling of the capillary in contact with an alumina block.

conductivity of the alumina block is overwritten with a user defined, temperature dependent linear fit. The function is that found for ceramic aluminium oxide in Figure A.4.

A boundary heat source acts on the outer edges of the capillary (that described by the heating function from phase 1). This model is also used to find the cooling rate of the capillary once the induction coil is switched off – the boundary heat source is simply set to 0.

The model is solved over the induction heating time ( $t=0-25s$ ) and then also for cooling ( $t=25-60s$ ). Time increments are 0.1s for heating and 1s for cooling.

## A.5 Contractor Report: R-tech

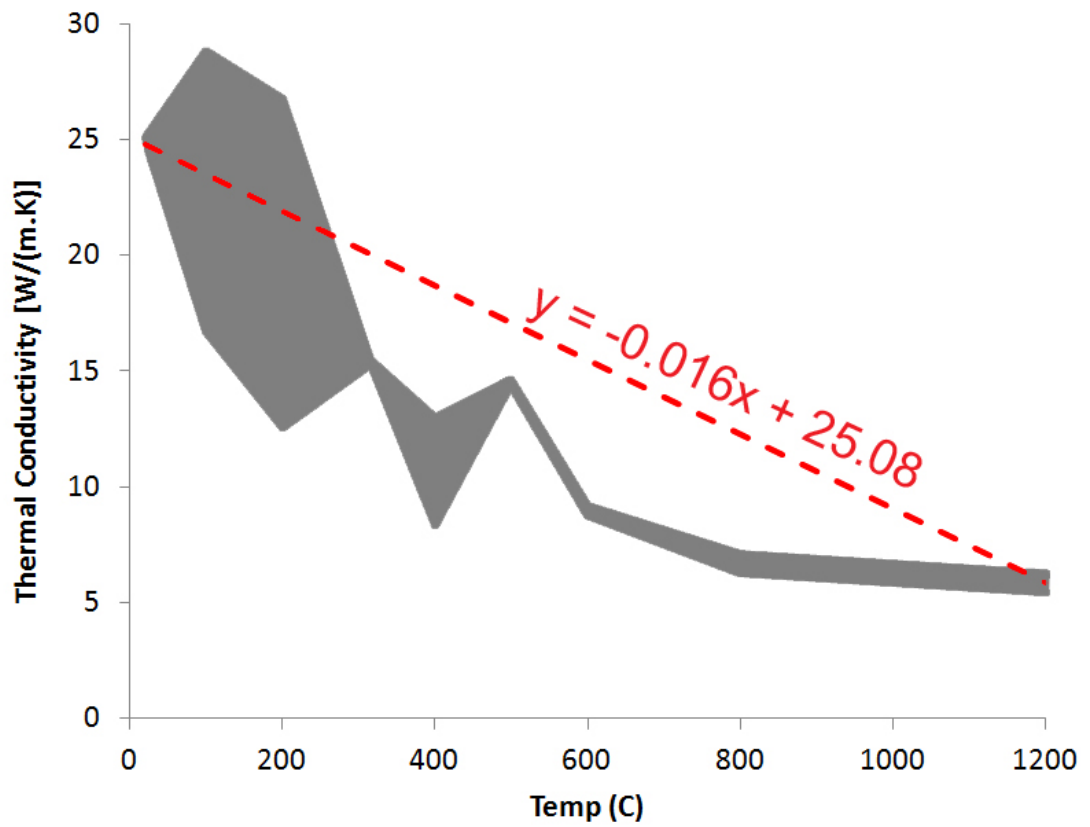


Figure A.4: Thermal conductivity of alumina with respect to temperature. Shown are the range of possible values (depending on composition) in grey, with the linear fit used in the model.

University of Strathclyde  
204 George Street  
Glasgow  
G1 1XW

For the attention of Mr Marcus Perry

22nd September 2011

**Laboratory Test Report No. 11378**

Client's order No. 2882542

Specimen identification

Four (4) 18.0 mm diameter 7 wire drawn strand samples to BS 5896:1980 approximately 1.0 m in length, identified as in the following table:

Sample ID's	Laboratory Ref. Number
T1	11378/1/T1
T2	11378/1/T2
T3	11378/1/T3
T4	11378/1/T4

Strand T1 and T2 had had strain gauges spot welded on to them. On strand T1, the strain gauges had been applied across an interstix between two adjacent wires in the strand. On strand T2, the strain gauges had been applied onto a single wire of the strand. In each case there had been some light abrading of the surface in the area where the strain gauge had been attached.

Date of test 20<sup>th</sup> September 2011

Tests conducted

Tensile properties tested according to BS EN ISO 15630-3:2010, with percentage total elongation at maximum force (Agt) measured using the method described in clause 5.3.1 Note 1 of BS EN ISO 15630-3:2010

After the tensile tests, metallographic sections were taken through two areas on each of strands T1 and T2 where the strain gauges had been applied. These sections were mounted in Bakelite, ground to a 600 grit finish and then polished to a 1µm diamond finish. Samples were etched in 5% nital solution, and then examined under the optical microscope. Microhardness measurements were also made in the area of the spot welds on both samples sectioned.

Note: Optical microscopy, microhardness testing and the interpretation of optical microstructures are outside the scope of our UKAS accreditation.

### Tensile test results

Specimen Identification	Area (mm <sup>2</sup> )	Young's Modulus <sup>‡</sup> (GPa)	0.1% Proof Load F <sub>p0.1</sub> (kN)	Load at 1% Elong. F <sub>t0.1</sub> (kN)	Breaking Load F <sub>m</sub> (kN)	0.1% Proof Stress R <sub>p0.1</sub> (MPa)	Tensile Stress R <sub>m</sub> (MPa)	Elongation A <sub>gt</sub> <sup>†</sup> (%)
11378/1/T1	225.9	184	324.1	337.7	399.3	1453	1790	5.6
11378/1/T2	225.7	184	331.5	342.7	400.7	1487	1797	6.3
11378/1/T3	225.8	187	332.4	343.7	400.1	1490	1794	6.2
11378/1/T4	225.7	184	332.8	343.0	401.3	1492	1800	6.5

All tensile tests carried out in the as delivered condition.

The above tensile stresses have been calculated on nominal area

All samples exhibited ductile failure of the individual strand wires.

Notes:

<sup>†</sup> Percentage elongation at maximum load (A<sub>gt</sub>) was calculated using a combination of extensometer and cross-head separation, as described in BS EN ISO 15630-3:2002 clause 5.3.1 Note 1. Gauge length of the dual averaging extensometer used was 400 mm.

<sup>‡</sup> Young's modulus determined from the slope of the linear portion of the force-extension diagram between 0.2F<sub>m</sub> and 0.7F<sub>m</sub> as described in BS EN ISO 15630-3:2002 clause 5.3.2.

Load-extension curves for these samples are given in Appendix A

### Metallographic results

Figures 1 to 4 show the strand wire surfaces where spot welds had been made on strands T1 and T2. Two positions were selected on each of the two strands. The red markings were made for location purposes prior to sectioning.

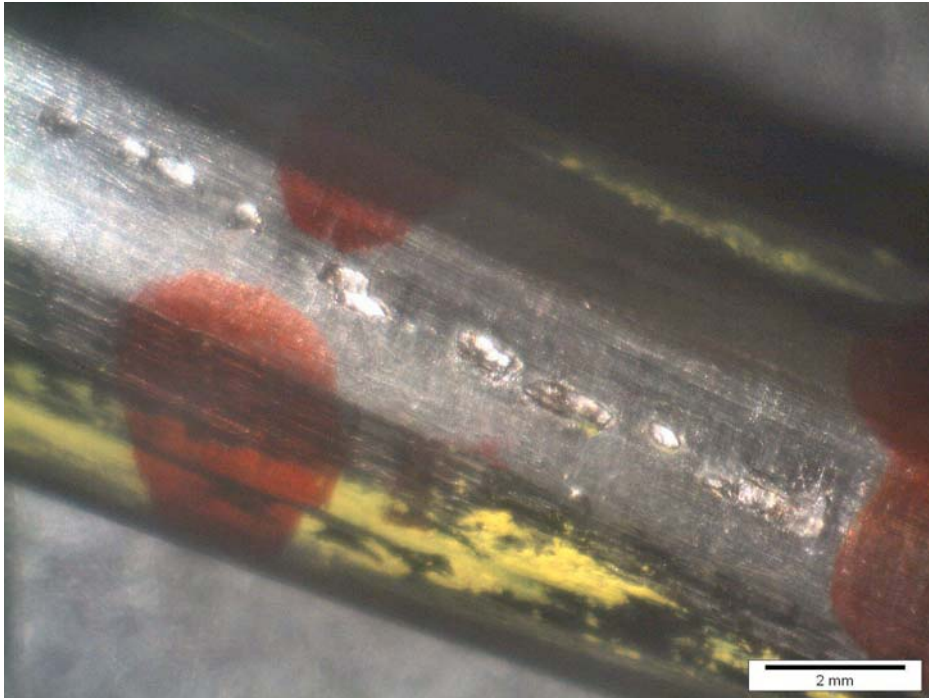


**Figure 1** Strand sample T1-1

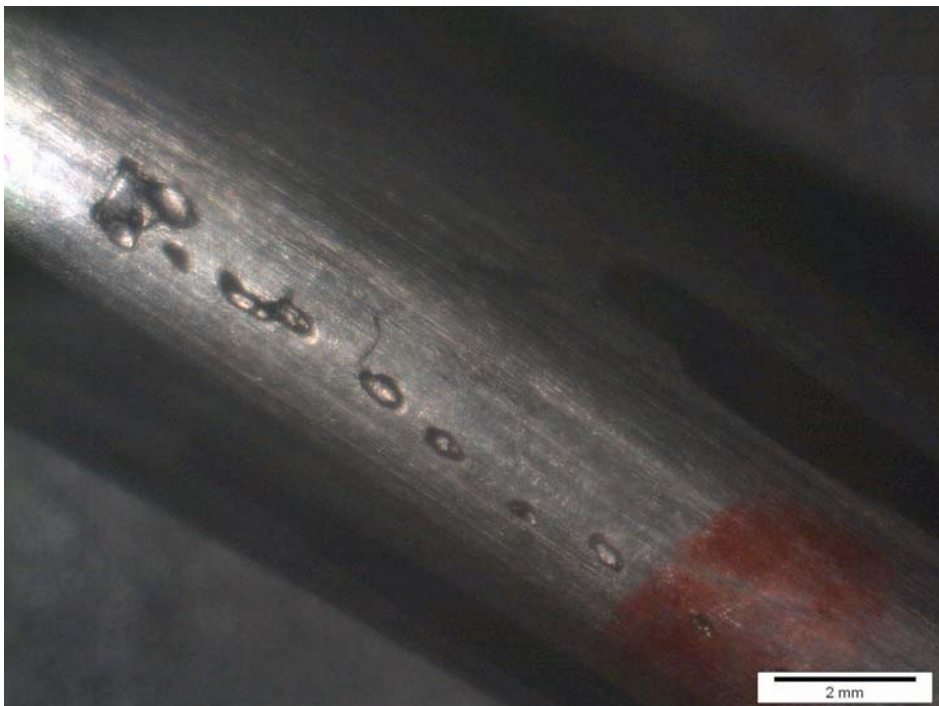


**Figure 2** Strand sample T1-2

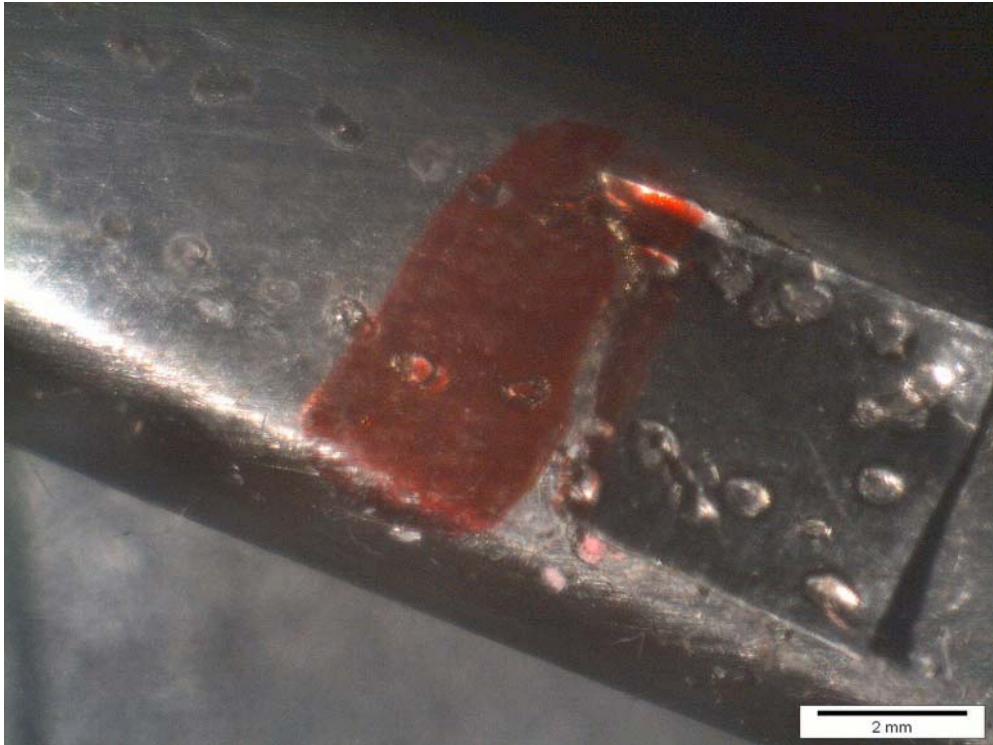


**Figure 3** Strand sample T2-1

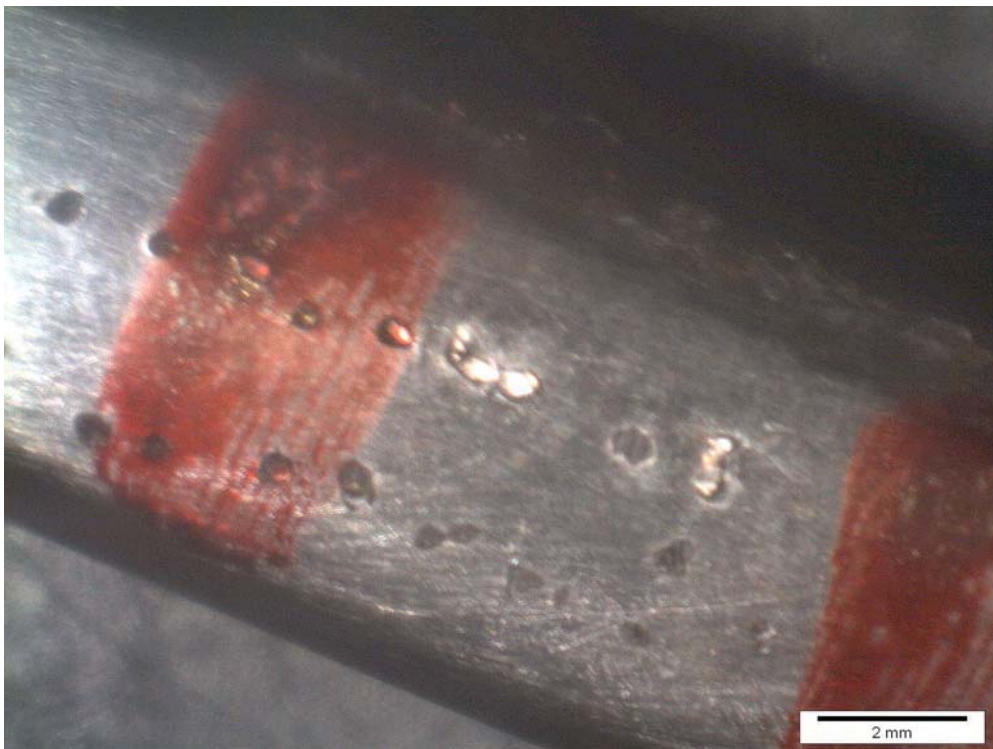


**Figure 4** Strand sample T2-2

Transverse sections were cut from each of the four positions. And subsequently mounted, ground and polished to a 1 $\mu$ m finish. These were then etched with a 0.5% nital solution to reveal the microstructures. Of the four sections, three exhibited evidence of the spot welding. The fourth polished section did not coincide exactly with a weld without grinding further. Figures 5 to 9 show the areas of the microstructure affected by the spot welding.

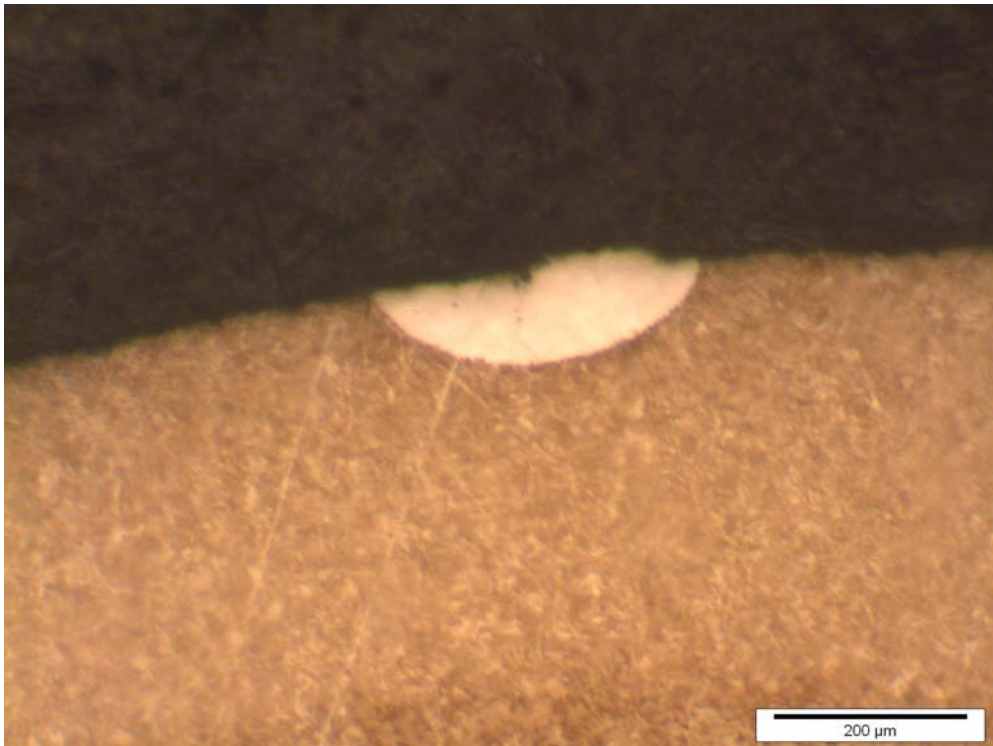


**Figure 5 Strand Sample T1-1 welded area (original magnification x100)**

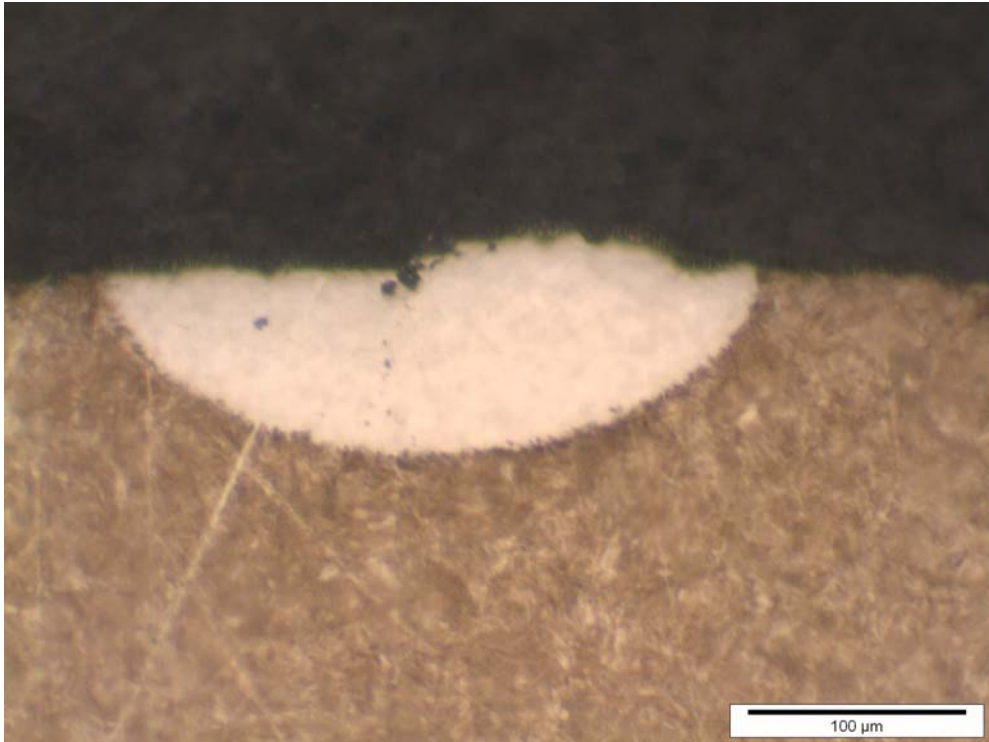


**Figure 6** Strand Sample T1-1 welded area (original magnification x200)

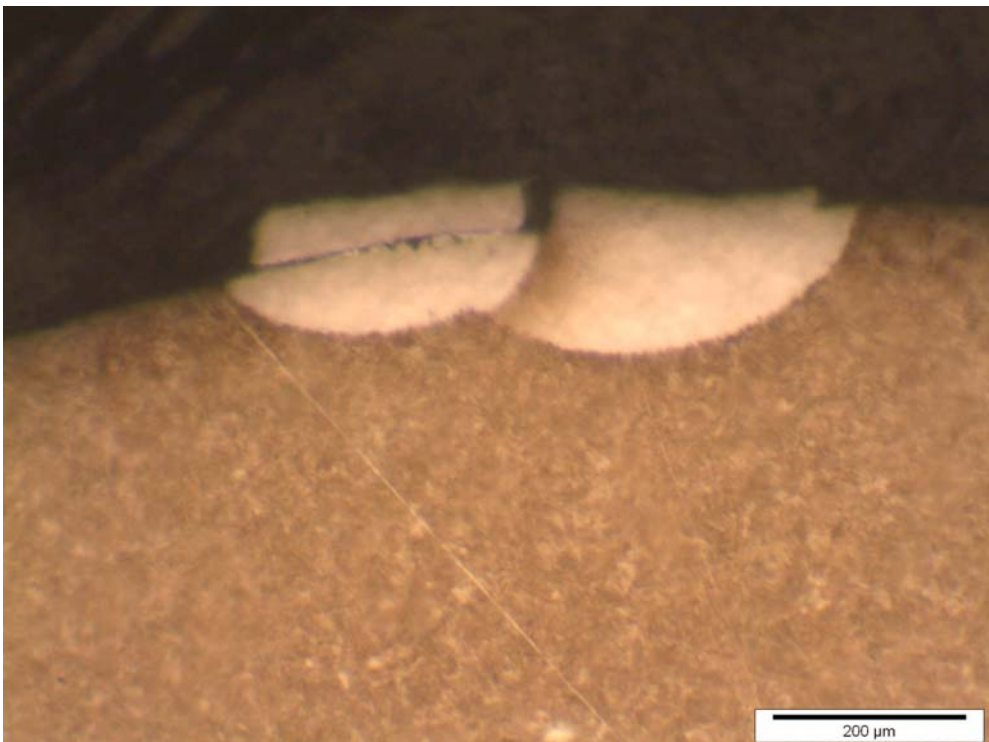


**Figure 7** Strand Sample T1-2 welded area (original magnification x100)

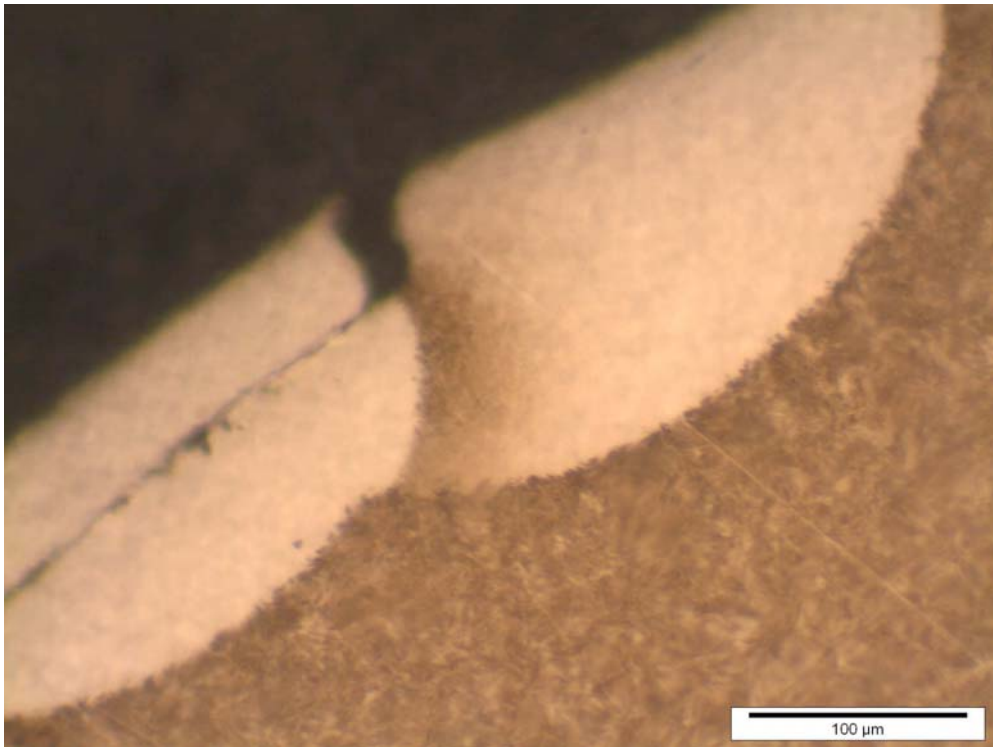


**Figure 8 Strand Sample T1-2 welded area (original magnification x200)**

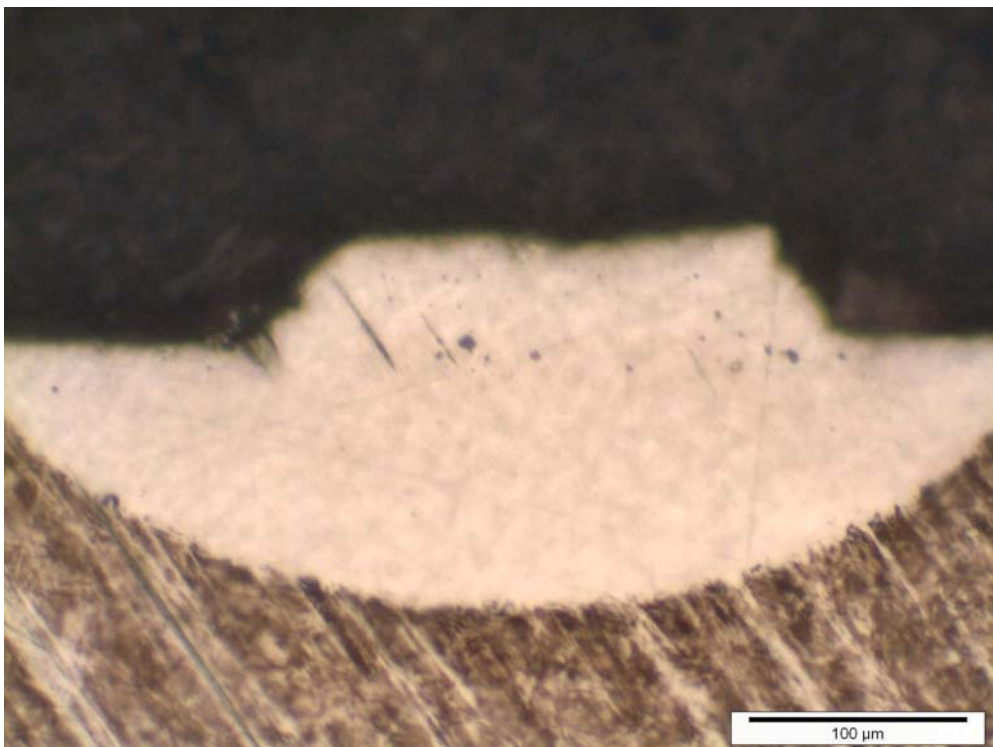


**Figure 9 Strand Sample T2-1 welded area (original magnification x200)**

The surfaces of each of these three positions that had evidence of welding appeared as though the extreme surface layers at the welds had become martensitic. In order to confirm this, Vickers microhardness measurements using a 300g load were made within the areas that had not etched with nital, and also within the core of the wires. The results are given in the table below.

Sample	Surface HV	Average		Core HV	Average
T1-1	862 / 942 / 938	914		463 / 512 / 467	481
T2-1	876			476	
T2-2	911			524	

All three samples were similar in hardness. The unetched surface positions were between 876 and 914HV and the core positions were between 476 and 524HV. The hardnesses within the areas that had not etched are typical of those attained when the microstructure transforms to martensite due to rapid cooling. The hardnesses within the core are typical of those found in normal strand microstructures.

Test report authorised by:



Dr A R Franks  
Director

**End of report**

## A.6 Strain Transfer Model

The model geometry describing the packaged FBG is shown in figure A.5. The fibre is bonded to a 1 mm long section at either end of the 25 mm long capillary. Within the rest of the capillary, the fibre is left bare and unattached. Rather than applying strain to the ends of the capillary, strain is applied to a 12 mm long middle-section shown, as this mimics the action of the strain plate.

Note also that the strain plate does not apply strain to the entire outer surface of the capillary, as it is only bonded to a fraction of the circumference. As shown in figure A.6, the fraction of the circumference which the strain plate is bonded to can be expressed as a ‘grip angle’,  $0 < \theta_g \leq 2\pi$ . In the model, strain is applied along the 12 mm long middle-section of the capillary over various grip angles.

The maximum fibre strain along the capillary resulting from various grip angles is shown in figure A.8. Attaching the strain plate to a larger fraction of the circumference of the capillary provides superior strain transfer. However, because only 12 mm of the 25 mm long capillary is bonded to the strain plate, strain transfer can never exceed 50 %, even when the entire circumference of the capillary is bonded to the strain plate. As shown in the same plot, exceeding 50 % strain transfer requires that a longer bonding length,  $L$ , between the capillary and strain plate. Indeed, strain amplification may be achievable by bonding to a strain plate which is longer than the capillary.

Strain transfer may be further reduced when stress is applied in a non-axial direction along the host material, at an angle  $\theta_z$  as shown in figure A.9. This is the case for the packaged FBGs in this project as they are attached to the surface of a cylindrical, helically wound prestressing strand. Finding the modified strain transfer ratio is not simply a matter of multiplying values by  $\cos(\theta_z)$  due to the influence of the Poisson effect [LZRL07].

The FEM from figure A.5 was modified so that strain could be applied to the 12 mm long middle section of the capillary at angles  $\theta_z = [0, 90]^\circ$ . As shown in figure A.10, increasing the orthogonality of the applied strain reduced the maximum strain transfer by factor,  $\mu$ .

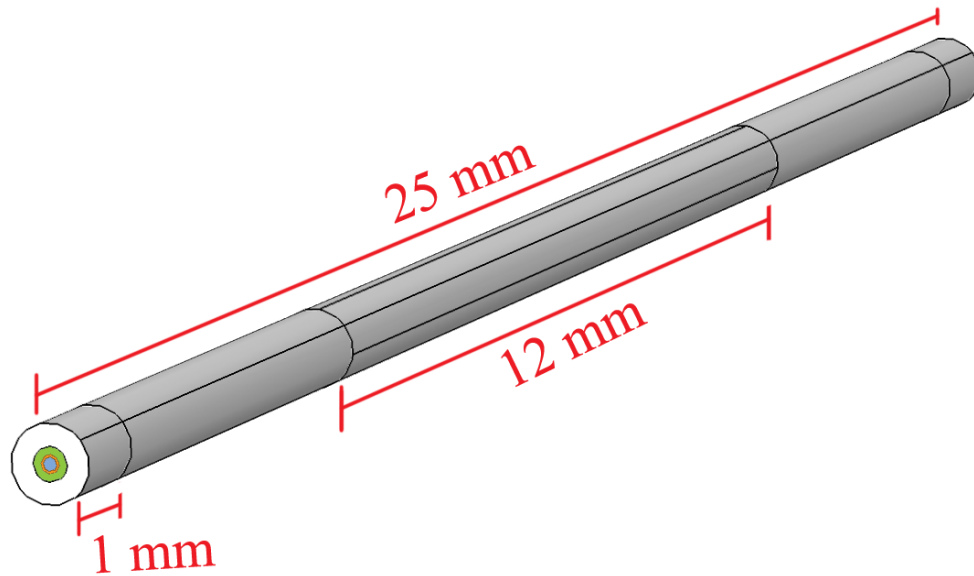


Figure A.5: Geometry used to calculate strain transfer in the real system. The capillary of total length 25 mm holds the optical fibre. The fibre is bonded to the capillary ends over a bonding distance of 1 mm, throughout the rest of the 23 mm of the capillary, the fibre is free. Strain is applied to a 12 mm midsection of the capillary, as shown. This simulates the strain transfer from the 12 mm strain plate to the capillary. Note that the lines shown on the capillary surface are guiding lines for the model and do not represent any discontinuities in the material.

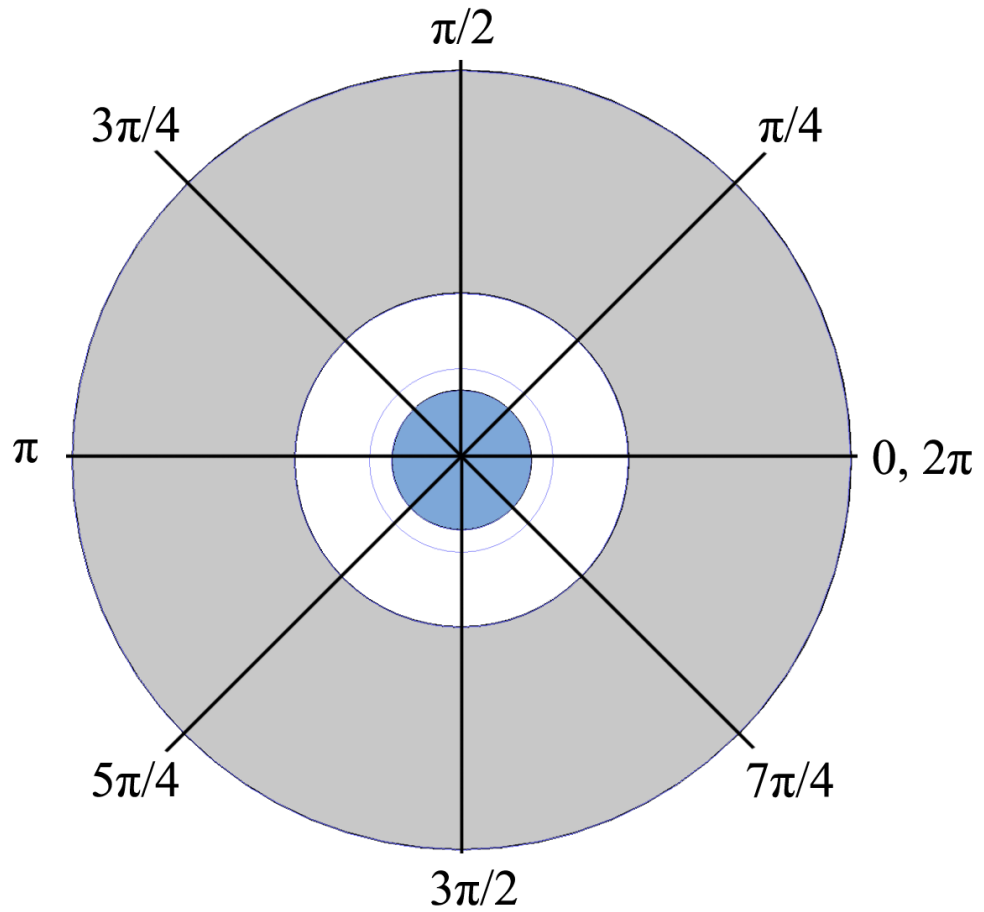


Figure A.6: Cross-section of the capillary within the 12 mm section shown in figure A.5. In this model, varying amounts of the capillary outer circumference are held and placed under strain. For example, if 1/4 of the capillary's outer surface is held, then the grip angle is  $\pi/2$ . If the entire capillary outer surface is held under strain, the grip angle is  $2\pi$ .

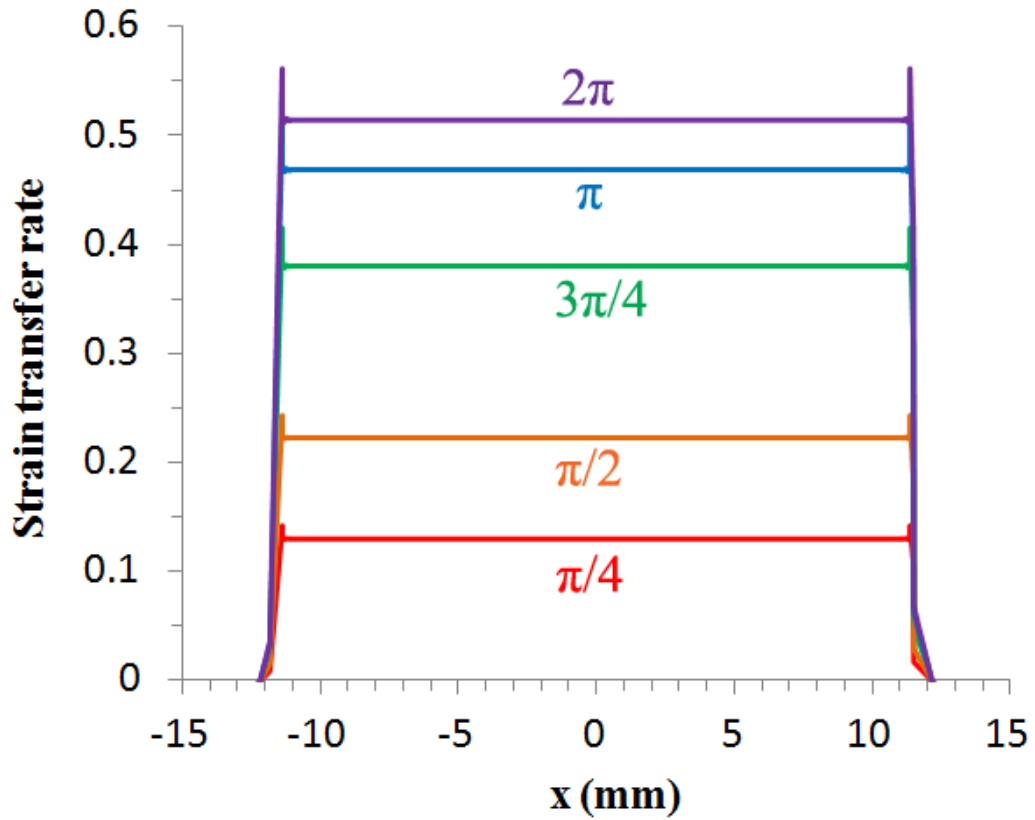


Figure A.7: Strain transfer along the 25 mm long capillary shown in figure A.5 for various grip angles between  $\pi/4$  and  $2\pi$ .

The model can be further expanded to include rotations around the y-axis,  $\theta_y = [0, 90]^\circ$ . The combination of  $\theta_y$  and  $\theta_z$  produce the surface plot shown in figure A.12. This plot can be used to calculate strain transfer between the prestressing strand and the capillary. Because the pitch of the helical winding in the prestressing strand is 270 mm, a 25 mm long capillary makes an angle of  $\theta_y = \theta_z = 360 \times \frac{25}{270} \approx 30^\circ$ . This results in a strain transfer modifier of  $\mu = 0.75$ . Applying this multiplier to the data in figure A.8 provides a corrected description of the strain transfer's dependence on grip angle, as shown in figure A.12.

## A.7 MZI Interference for Single Output

For two light waves of equal amplitude and wavelength, but differing phases:

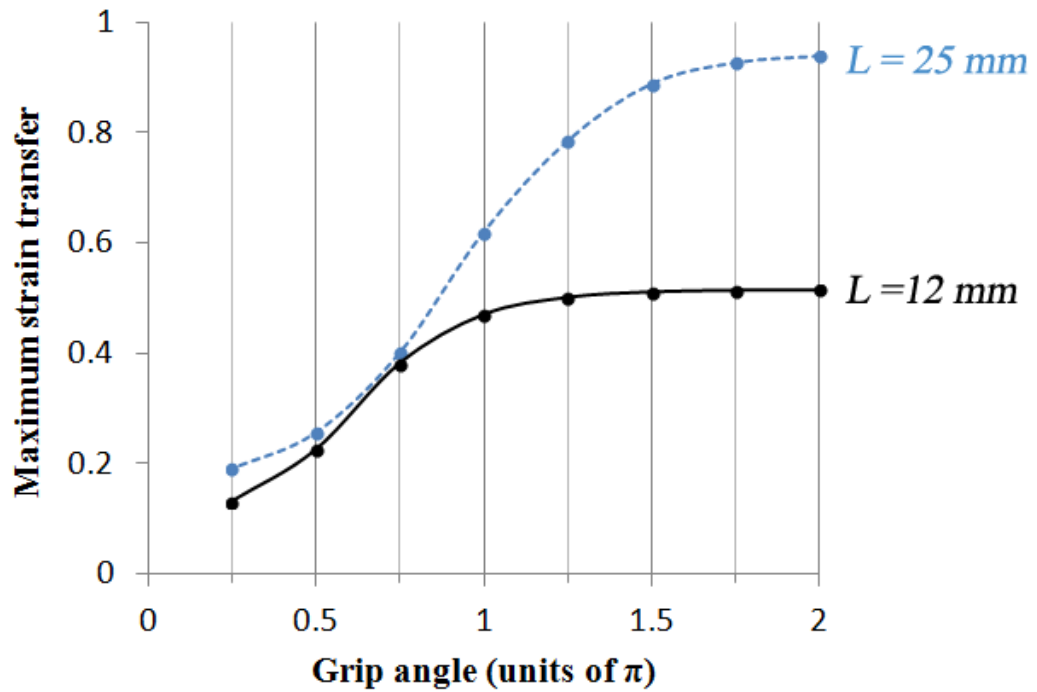


Figure A.8: Strain transfer vs grip angle for a gripped length of 12 mm and 25 mm. When the strain plate is bonded to a 12 mm long section of the capillary, strain transfer cannot exceed 50 %.

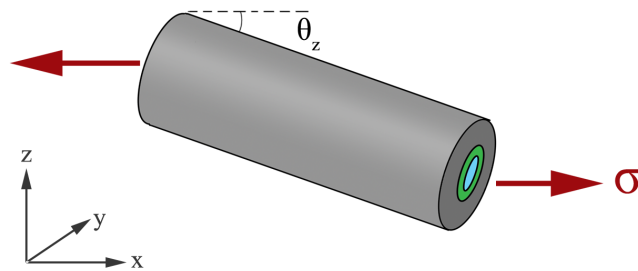


Figure A.9: Diagram showing non-axial stressing of a capillary host. Because the capillary is at an angle  $\theta_z$  to the stressing direction, axial stresses are reduced.

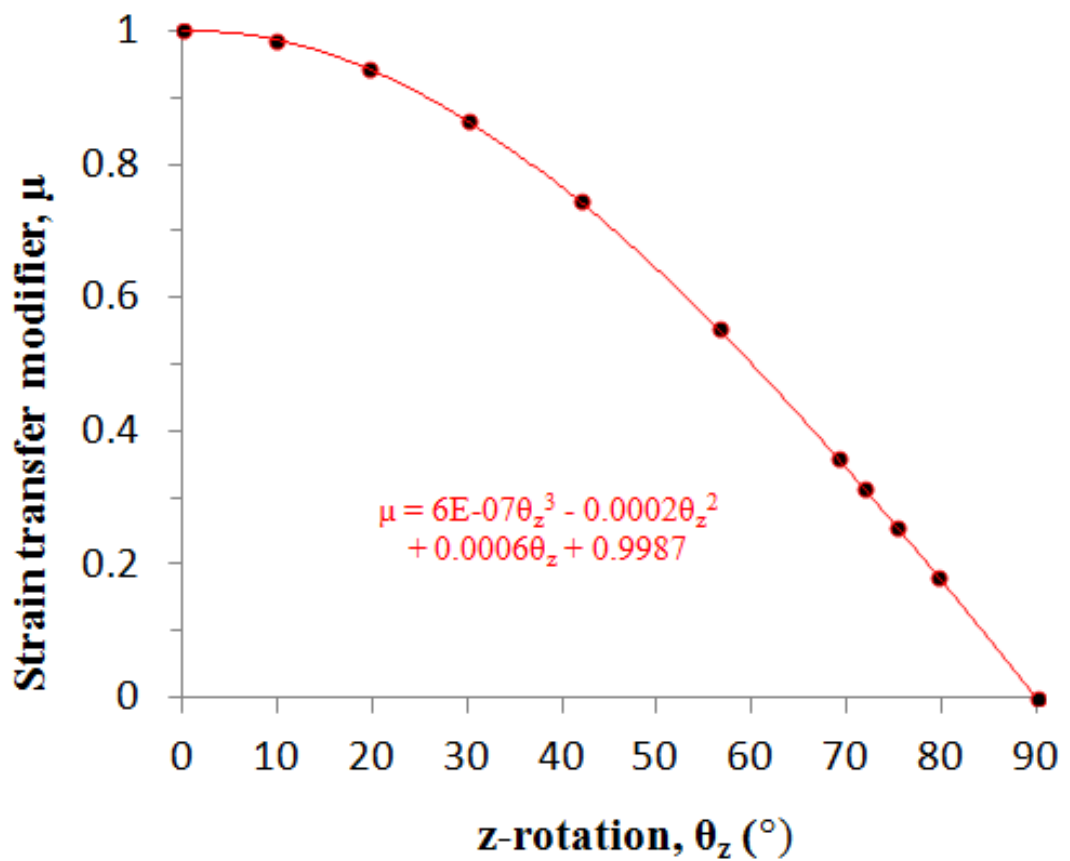


Figure A.10: Strain transfer modifier as a function of the angle of stress application in the capillary. Increasing the orthogonality of the stress application relative to the axial direction reduced strain transfer. The relationship could be interpolated using a third-order polynomial.

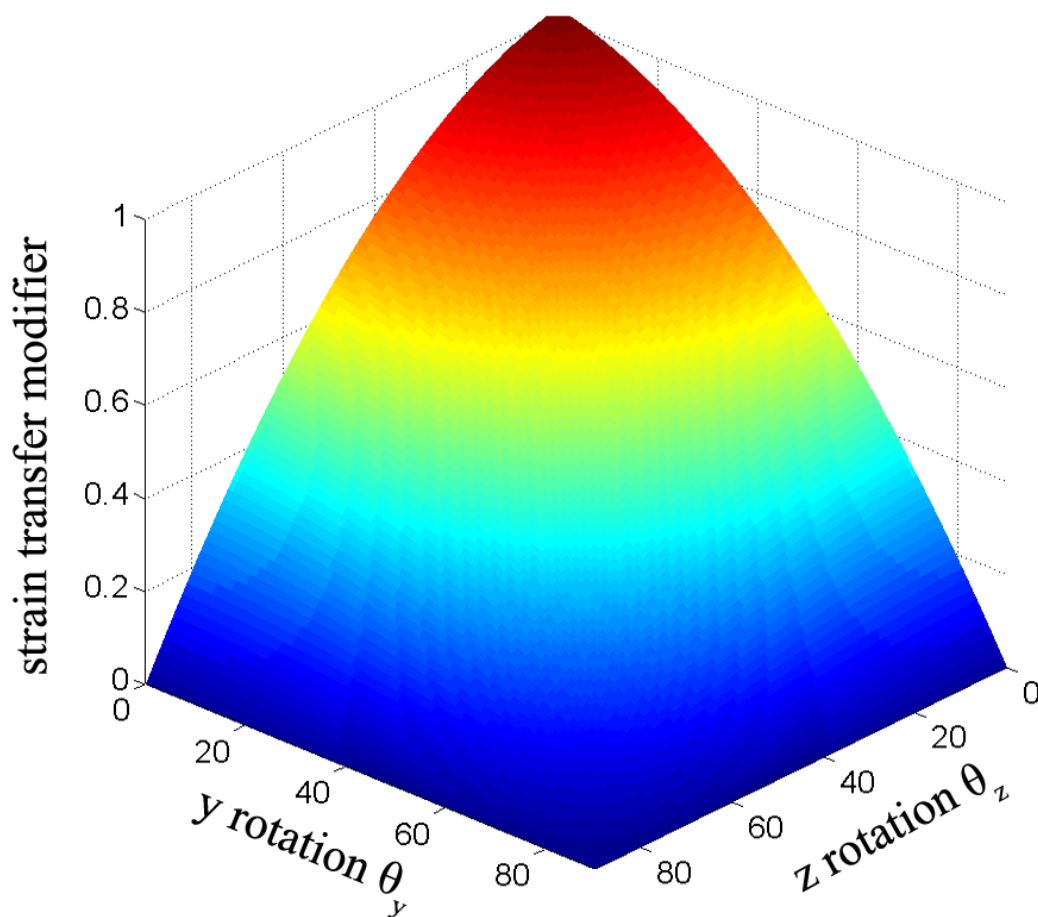


Figure A.11: Strain transfer modifier as a function of the angle of stress application in the capillary. In this case, rotations around the z and y axes produced the surface plot shown.

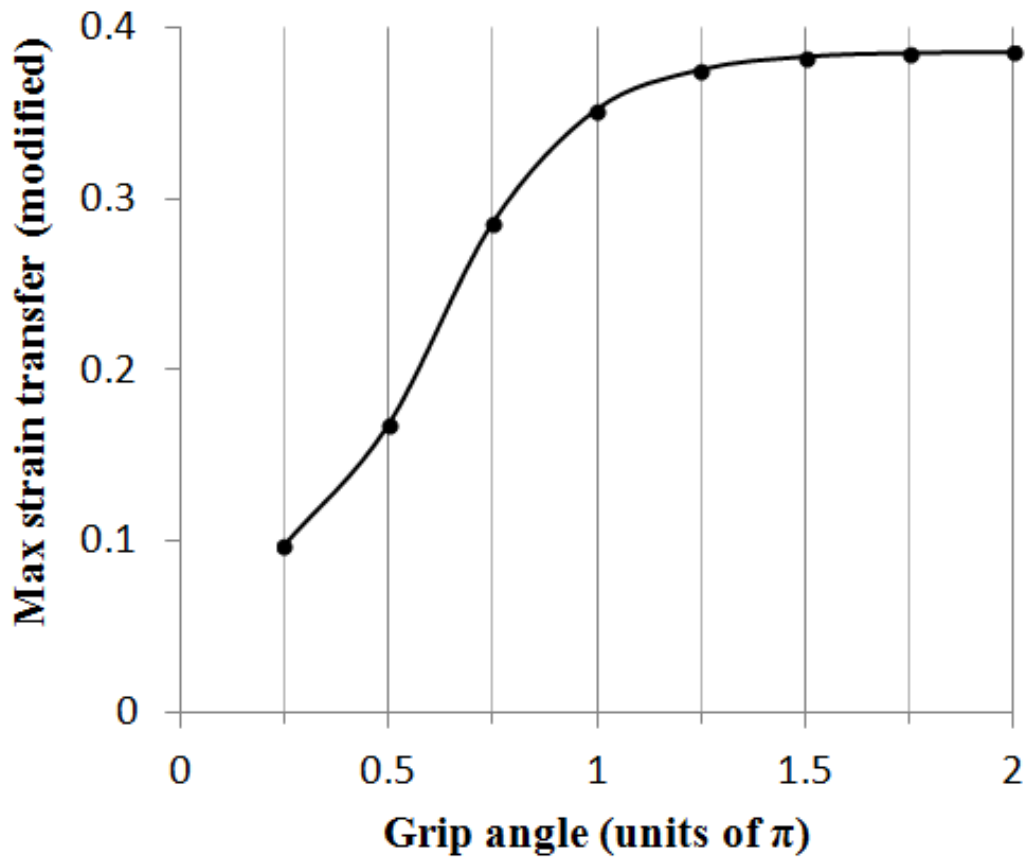


Figure A.12: Modified strain transfer vs grip angle for a gripped length of 12 mm of capillary. Because the capillary is stressed non-axially, strain transfer between the strand and capillary is reduced further.

$$\begin{aligned}
E_A(x, t) &= \frac{E_0}{\sqrt{2}} \exp[i(kx - \omega t + \phi_A)] \\
E_B(x, t) &= \frac{E_0}{\sqrt{2}} \exp[i(kx - \omega t + \phi_B)]
\end{aligned} \tag{A.13}$$

Interference will lead to an intensity given by:

$$\begin{aligned}
I &= |E_A + E_B|^2 = (E_A + E_B)(E_A + E_B)^* \\
&= \frac{E_0^2}{2} (e^{i(kx - \omega t + \phi_A)} + e^{i(kx - \omega t + \phi_B)}) (e^{-i(kx - \omega t + \phi_A)} + e^{-i(kx - \omega t + \phi_B)}) \\
&= \frac{E_0^2}{2} (e^0 + e^0 + e^{\phi_A - \phi_B} + e^{\phi_B - \phi_A})
\end{aligned} \tag{A.14}$$

Using Euler's formula,  $e^{ix} = \cos(x) - i\sin(x)$ , this can be simplified to:

$$I = \frac{E_0^2}{2} (2 + \cos(\phi_A - \phi_B) + \cos(\phi_B - \phi_A) + i[\sin(\phi_A - \phi_B) + \sin(\phi_B - \phi_A)]) \tag{A.15}$$

Noting that  $\cos(x) = \cos(-x)$  and  $-\sin(x) = \sin(-x)$ :

$$I = I_0(1 + \cos(\phi_A - \phi_B)) \tag{A.16}$$

Where  $I_0 = E_0^2$ .

## A.8 MZI Interference for 2 Outputs

For a perfect interferometer with 100 % fringe visibility, there is no dc offset in the phase modulation. In this case, an interferometer with two outputs is sufficient to demodulate phase. The voltages of the two outputs can be expressed:

$$\begin{aligned}
I_1 &= \frac{I_0}{2}(1 + \cos(\phi)) \\
I_2 &= \frac{I_0}{2}(1 - \cos(\phi))
\end{aligned}
\tag{A.17}$$

and so phase can be extracted using a ratiometric approach:

$$\frac{(I_1 - I_2)}{(I_1 + I_2)} = \cos(\phi)
\tag{A.18}$$

However, because the losses in real interferometers are typically asymmetric, the intensities follow the more general form:

$$\begin{aligned}
I_1 &= C_1 + D_1 \cos(\phi) \\
I_2 &= C_2 - D_2 \cos(\phi)
\end{aligned}
\tag{A.19}$$

Here it is assumed that the two outputs are  $\pi$  out of phase. In fact, even this assumption is rarely correct so some calibration is required. Nevertheless, the high number of unknowns in the equations above mean that the ratiometric approach fails to provide phase information independently of variations in source intensity and interferometer losses:

$$\frac{(I_1 - I_2)}{(I_1 + I_2)} = \frac{(C_1 - C_2) + (D_1 + D_2)\cos(\phi)}{(C_1 + C_2) + (D_1 - D_2)\cos(\phi)}
\tag{A.20}$$

Achieving phase information independently of losses thus requires more equations to deal with the higher number of unknowns — as is demonstrated for a three-output interferometer in 6.2.3.

## A.9 MZI Interference for 3 Outputs

For an interferometer with N=3 outputs, the intensities follow:

$$I_n = C_n + D_n \cos[\phi + \theta_n] \quad (\text{A.21})$$

Where the phase difference between the two arms,  $\phi = \phi_A - \phi_B$  and  $\theta_n = [2\pi(n - 1)]/3$ . The real part of Euler's identity:

$$\begin{aligned} \cos(x + y) &= \text{Re}[\cos(x + y) + i\sin(x + y)] \\ &= \text{Re}[e^{i(x+y)}] = \text{Re}[e^{ix} e^{iy}] \end{aligned} \quad (\text{A.22})$$

Can be used to express equation (A.21) as:

$$I_n = \text{Re} [C_n + D_n e^{i\phi} e^{i\theta_n}] \quad (\text{A.23})$$

Dividing both sides by  $C_n$  yields a normalised output:

$$\frac{I_n}{C_n} = \bar{I}_n = \text{Re} \left[ 1 + \frac{D_n}{C_n} e^{i\phi} e^{i\theta_n} \right] \quad (\text{A.24})$$

Expressing the second exponent as a complex number, i.e.:

$$\frac{D_n}{C_n} e^{i\theta_n} = \mu_n + i\gamma_n \quad (\text{A.25})$$

Allow equation (A.24) to be written:

$$\bar{I}_n = \text{Re} [1 + e^{i\phi} (\mu_n + i\gamma_n)] \quad (\text{A.26})$$

These equations can now be combined with the fact that  $\bar{I}_1 + \bar{I}_2 + \bar{I}_3 = 1$  and manipulated to yield results which are independent of the input intensity, for example:

$$\frac{\bar{I}_1 - \bar{I}_2}{\bar{I}_2 - \bar{I}_3} = \frac{\text{Re} [e^{i\phi}[(\mu_1 - \mu_2) + i(\gamma_1 - \gamma_2)]]}{\text{Re} [e^{i\phi}[(\mu_2 - \mu_3) + i(\gamma_2 - \gamma_3)]]} \quad (\text{A.27})$$

$$\begin{aligned} & \quad \quad \quad (\text{A.28}) \\ & = \frac{(\mu_1 - \mu_2)\cos(\phi) + (\gamma_2 - \gamma_1)\sin(\phi)}{(\mu_2 - \mu_3)\cos(\phi) + (\gamma_3 - \gamma_2)\sin(\phi)} \end{aligned}$$

Or alternatively:

$$\tan(\phi) = \frac{(\mu_2 - \mu_3)\bar{I}_1 + (\mu_3 - \mu_1)\bar{I}_2 + (\mu_1 - \mu_2)\bar{I}_3}{(\gamma_2 - \gamma_3)\bar{I}_1 + (\gamma_3 - \gamma_1)\bar{I}_2 + (\gamma_1 - \gamma_2)\bar{I}_3} \quad (\text{A.29})$$

## A.10 Optical budget calculation for interrogator

In the basic interrogation system without switch cascades, the maximum voltage output of each of the three photodetectors is given by the equation:

$$V_{PD} = \frac{1}{3}[0.7S_D B_\lambda R_{FBG}] \times 10^{-0.1\alpha_{att}} \times [R_{PD} G_{PD}] \quad (\text{A.30})$$

The bright broadband source of spectral density  $S_D = 1$  mW/nm reflects from an FBG of bandwidth  $B_\lambda = 0.3$  nm and reflectivity  $R_{FBG} = 60$  %, resulting in a 125  $\mu$ W reflection (the factor of 0.7 accounts for the fact that the Bragg reflection is roughly Gaussian in shape) [Amo13].

Attenuation in the system of  $\alpha_{att} = 14$  dB is calculated by adding the (experimentally verified) attenuation in the basic interrogation system (6 dB) plus radiation induced attenuation (which was found to be negligible beyond 1 metre from the reactor's steel liner in §4.2.5) plus the 8 dB attenuation arising from an estimated 40 splices in the system. The 1.7  $\mu$ W of optical power is scaled by photodetector's responsivity  $R_{PD} = 0.95$  A/W and transimpedance gain,  $G_{PD} = 10^6$  V/A, to yield a maximum possible voltage signal of 1.6 V per photodetector.

In this project, signal processing techniques worked acceptably provided voltage signals were greater than 0.5 V. Each switch in the system adds 1 dB of

optical loss (equivalent to 20 %) so it follows that at least 2 switches could be placed in series [Agi13].

# Bibliography

- [22493] ACI Committee 224. *Cracking of Concrete Members in Direct Tension*. American Concrete Institute, 1993. (cited on page 37)
- [ACC<sup>+</sup>12] M. Aslund, J. Canning, A. Canagasabay, R. Assis de Oliveira, Y. Liu, K. Cook, and G. Peng. Mapping the thermal distribution within a silica preform tube using regenerated fibre bragg gratings. *Int. J. Heat Mass Tran.*, 55(1112):3288 – 3294, 2012. (cited on page 109)
- [ACFT10] M.L. Aslund, J. Canning, H. Fu, and H. Tam. Single-mode optical fibre thermocoupler based on regenerated fibre Bragg gratings evaluated at 1500C. *2nd Workshop on Specialty Optical Fibers and Applications (WSOF), Oaxaca City, Mexico*, 2010. (cited on pages 104, 109)
- [ACSC10] M.L. Aslund, J. Canning, M. Stevenson, and K. Cook. Thermal stabilization of Type I fiber Bragg gratings for operation up to 600 degrees C. *Optics letters*, 35(4):586–8, 2010. (cited on page 109)
- [Agi13] Agiltron. Crystalatch Optical Switch Series Specifications and Product Line, 2013. Available from <http://www.agiltron.com/>. (cited on page 304)
- [ALT99] A. Arie, B. Lissak, and M. Tur. Static Fiber-Bragg Grating Strain Sensing Using Frequency-Locked Lasers. *J. Lighwave Tech.*, 17(10):1849–1855, 1999. (cited on page 195)
- [ALVA12] P. Antunes, H. Lima, H. Varum, and P. André. Optical fiber sensors for static and dynamic health monitoring of civil engineering infrastructures: Abode wall case study. *Measurement*, 45(7):16951705, 2012. (cited on page 196)

- [Amo13] Amonics. C-Band ASE Broadband Light Source, 2013. Available from [http://www.amonics.com/amonics/php/en/products\\_details.php?id=50/](http://www.amonics.com/amonics/php/en/products_details.php?id=50/). (cited on page 303)
- [AN] A Aminian and M R Nematollahi. Determination of shielding parameters for different types of concretes by Monte Carlo methods  $\mu$   $\rho$ . *ICENES 2007 Conference*. (cited on page 25)
- [And39] F.O. Anderegg. Strength of glass fbires. *Industrial & Engineering Chemistry*, 31(3):290–298, 1939. (cited on page 162)
- [Ans97] F. Ansari. State-of-the-art in the applications of fiber-optic sensors to cementitious composites. *Cement and Concrete Composites*, 19(1):3 – 19, 1997. (cited on page 114)
- [APPF97] C.G. Askins, M.A. Putnam, H.J. Patrick, and E.J. Friebele. Fibre strength unaffected by on-line writing of single-pulse bragg gratings. *Electronics Letters*, 33(15):1333–1334, 1997. (cited on pages 121, 121)
- [ARPS] R E Abdi, A D Rukinski, M Poulain, and I Severin. Damage of optical fibers under wet environments. *Exp. Mech.*, 50:1225–1234. (cited on pages 121, 122)
- [ASC07] M.F. Ashby, H. Shercliff, and D. Cebon. *Materials: engineering, science, processing and design*. Butterworth-Heinemann, 2007. (cited on page 110)
- [AT11] H. Alemohammad and E. Toyserkani. Metal embedded optical fiber sensors: Laser-based layered manufacturing procedures. *Journal of manufacturing science and engineering*, 133(3), 2011. (cited on page 134)
- [AY88] C. Amar and M. Yiu-Wing. Failure mechanisms in toughened epoxy resins: A review. *Composites Science and Technology*, 31(3):179 – 223, 1988. (cited on page 116)
- [Baz01] Z.P. Bazant. Prediction of concrete creep and shrinkage: past, present and future. *Nuclear Engineering and Design*, 203(1):27–38, January 2001. (cited on page 60)

- [BBC84] Z.P. Bazant, T.B. Belytschko, and T.P. Chang. Continuum Theory for Strain Softening. *Journal of Engineering Mechanics*, 110(12), 1984. (cited on page 37)
- [BBF<sup>+</sup>01] B. Brichard, P. Borgermans, F. Fernandez, K. Lammens, and a. De-creton. Radiation effect in silica optical fiber exposed to intense mixed neutron-gamma radiation field. *IEEE Trans. Nucl. Sci*, 48(6):2069–2073, 2001. (cited on pages 83, 91, 93)
- [BBF<sup>+</sup>06] F. Berghmans, B. Brichard, A.F. Fernandez, A Gusarov, M. Van Uf-felen, and S. Girard. *Optical Waveguide Sensing and Imaging, "An Introduction to Radiation Effects on Optical Components and Fiber Op-tic Sensors*. Springer Science+Business Media B.V., 2006. (cited on pages 92, 93, 93, 94)
- [BC11] X. Bao and L. Chen. Recent progress in brillouin scattering based fiber sensors. *Sensors*, 11(4):4152–4187, 2011. (cited on page 100)
- [BCF<sup>+</sup>08] C Barbosa, N Costa, L A Ferreira, F M Arajo, H Varum, A Costa, C Fernandes, and H Rodrigues. Weldable fibre bragg grating sen-sors for steel bridge monitoring. *Measurement Science and Technology*, 19(12):125305, 2008. (cited on pages 115, 132, 168, 168)
- [BCSC08] Somnath Bandyopadhyay, John Canning, Michael Stevenson, and Kevin Cook. Ultrahigh-temperature regenerated gratings in boron-codoped germanosilicate optical fiber using 193 nm. *Optics Letters*, 33(16):1917–1919, 2008. (cited on page 145)
- [BDB<sup>+</sup>97] V Bogatyrjov, E Dianov, A Biriukov, A Sysoliatin, V Voronov, A Khi-tun, M Do, and J Kim. Performance of highstrength Cu-coated fibers at high temperatures. *Optical Fiber Communication*, page 182, 1997. (cited on pages 85, 121)
- [Bel13] Belden. Copper Media: Datatwist 6 Data sheet, 2013. Avail-able from [http://www.belden.com/pdfs/techinfo/DS\\_DataTwist\\_6.pdf/](http://www.belden.com/pdfs/techinfo/DS_DataTwist_6.pdf/). (cited on page 81)

- [BFOB07] B. Brichard, A.F. Fernandez, H. Ooms, and F. Benoit. Fibre-optic gamma-flux monitoring in a fission reactor by means of Cerenkov radiation. *Meas. Sci. Technol.*, 18:3257–3262, 2007. (cited on pages 86, 87)
- [BGC04] Z.P. Bazant, Cusatis. G., and L. Cedolin. Temperature effect on concrete creep modeled by microprestress-solidification theory. *Journal of Engineering Mechanics*, 130(6):691 – 699, 2004. (cited on page 59)
- [BGT08] W.J. Bock, I. Gannot, and S. Tanev. *Optical waveguide sensing and imaging*. Springer, 2008. (cited on page 98)
- [BHSU97] Z.P. Bazant, A.B. Hauggaard, Baweja S., and F. Ulm. Microprestress-solidification theory for concrete creep. i: Aging and drying effects. *Journal of Engineering Mechanics*, 123(11):1188–1194, 1997. (cited on page 60)
- [Bje89] L. Bjerkan. Optical fiber splice loss predictions from one-way OTDR measurements based on a probability model. *J. Lightwave Tech.*, 7(3):490–499, March 1989. (cited on page 97)
- [BKBK89] G.M. Bubel, J.T. Krause, B.J. Bickta, and R.T. Ku. Mechanical reliability of metallized optical fiber for hermetic terminations. *J. Lightwave Tech.*, 7(10):1488–1493, 1989. (cited on pages 85, 121)
- [Bla08] J Black. *DeGarmo’s materials and processes in manufacturing*. Wiley, Hoboken NJ, 10th ed. edition, 2008. (cited on page 123)
- [BLBH90] M. Bredol, D. Leers, L. Bosselaar, and M. Hutjens. Improved model for OH absorption in optical fibers. *J. Lightwave Tech.*, 8(10):1536–1540, 1990. (cited on page 85)
- [BMC05] L. Barcelo, M. Moranville, and B. Clavaud. Autogenous shrinkage of concrete: a balance between autogenous swelling and self-desiccation. *Cement and Concrete Research*, 35(1):177 – 183, 2005. (cited on page 58)
- [Boa05] M. Boas. *Mathematical Methods in the Physical Sciences*. Wiley, New Jersey, 3rd edition, 2005. (cited on page 207)

- [BR03] D. Barber and N. Rizvi. Characterization of the effects of different lasers on the tensile strength of fibers during laser writing of fiber bragg gratings. In Thomas J. Glynn, editor, *Opto-Ireland 2002: Optics and Photonics Technologies and Applications*, volume 4876, pages 321–329, Galway, Ireland, March 2003. SPIE. (cited on page 121)
- [Bra12] E. Brainis. *Recent Progress in Optical Fiber Research: Chapter 2*. In-Tech, 2012. (cited on page 82)
- [BRBG97] S.R. Baker, H.N. Rourke, V. Baker, and D. Goodchild. Thermal decay of fiber Bragg gratings written in boron and germanium codoped silica fiber. *J. Lightwave Tech.*, 15(8):1470–1477, 1997. (cited on pages 109, 158)
- [Bre96] R. Brendel. Influence of a Magnetic Field on Quartz Crystal Resonators. *IEEE Trans Ultrasonics, Ferro, Freq Contr*, 43(5):818–831, 1996. (cited on page 152)
- [Bri88] E.O Brigham. *The fast Fourier transform and its application*. Prentice Hall, New Jersey, 1988. (cited on page 207)
- [BRT<sup>+</sup>01] M.W. Beranek, M. Rassaian, C.-H. Tang, C.L. St John, and V.a. Loebis. Characterization of 63Sn37Pb and 80Au20Sn solder sealed optical fiber feedthroughs subjected to repetitive thermal cycling. *IEEE Transactions on Advanced Packaging*, 24(2):576–585, 2001. (cited on page 117)
- [BTB<sup>+</sup>07] B Brichard, A Tomashuk, V Bogatyryov, A Fernandez, S Klyamkin, S Girard, and F Berghmans. Reduction of the radiation-induced absorption in hydrogenated pure silica core fibres irradiated in situ with  $\gamma$ -rays. *J. Non-Cryst. Solids*, 353(5-7):466–472, 2007. (cited on page 85)
- [BTS90] S.E. Baldini, D.J. Tubbs, and W.A. Stange. Embedding fiber optic sensors in titanium matrix composites. In *San Jose-DL tentative*, pages 162–168. International Society for Optics and Photonics, 1990. (cited on page 134)
- [Bur05] R. Burdett. *Amplitude Modulated Signals: The Lock-in Amplifier*. Wiley, New Jersey, 2005. (cited on page 214)

- [BX95] Z.P. Bazant and Y. Xi. Continuous retardation spectrum for solidification theory of concrete creep. *Journal of Engineering Mechanics*, 121(2):281–288, 1995. (cited on page 60)
- [Byo03] L. ByoungHo. Review of the present status of optical fiber sensors. *Optical Fiber Technology*, 9(2):57–79, 2003. (cited on pages 3, 196)
- [BZ02] G.L. Brodt and A.M. Zikic. CE/GNSR/5117. INGENCO: Technical Services Research Project On The measurement of tendon loads in prestressed concrete pressure vessels and containment buildings. Revision 1. Technical report, EDF Energy Nuclear Generation Engineering Advice Note., Sep 2002. (cited on page 117)
- [Can08] J. Canning. Fibre gratings and devices for sensors and lasers. *Laser & Photonics Review*, 2(4):275–289, 2008. (cited on page 104)
- [CB12] I. Costa and J.A.O. Barros. Creep of structural adhesives: an overview. CICE 2012 6th International Conference on FRP Composites in Civil Engineering, 2012. (cited on page 117)
- [CBS<sup>+</sup>09] J. Canning, S. Bandyopadhyay, M. Stevenson, P. Biswas, J. Fenton, and M. Aslund. Regenerated gratings. *J. European Opt. Soc. - Rapid Publications*, 4, 2009. (cited on page 109)
- [CCS12] J. Canning, K. Cook, and L. Y. Shao. Helium and regeneration in optical fibres. *Proc. SPIE 8421, OFS2012 22nd International Conference on Optical Fiber Sensors*, pages 8421CA–8421CA–5, 2012. (cited on page 104)
- [CFK08] G. Cranch, G. Flockhart, and C. Kirkendall. Distributed feedback fiber laser strain sensors. *Sensors Journal, IEEE*, 8(7):1161–1172, 2008. (cited on page 270)
- [CG09] B.D. Cullity and C.D. Graham. *Introduction to magnetic materials*. John Wiley and Sons, 2009. (cited on page 140)
- [CH05] H.B. Cary and S.C. Helzer. *Modern welding technology*. Pearson/Prentice Hall, 2005. (cited on page 168)

- [CHS02] J. Chae, P. Hyoung-Sang, and K. Sang-won. Atomic layer deposition of nickel by the reduction of preformed nickel oxide. *Electrochemical and Solid-State Letters*, 5(6):C64–C66, June 2002. (cited on page 123)
- [CLVB08] G. Cheymol, H. Long, J.F. Villard, and B. Brichard. High Level Gamma and Neutron Irradiation of Silica Optical Fibers in CEA OSIRIS Nuclear Reactor. *IEEE Trans. Nucl. Sci*, 55(4):2252–2258, 2008. (cited on pages 91, 98)
- [CMGL05] J. Chow, D. McClelland, M. Gray, and I. Littler. Demonstration of a passive subpicostrain fiber strain sensor. *Opt. Lett.*, 30(15):1923–1925, Aug 2005. (cited on page 195)
- [CNA97] J.W. Chin, T. Nguyen, and K. Aouadl. Effects of environmental exposure on fiber-reinforced plastic (frp) materials used in construction. *Journal of Composites Technology and Research*, 19:205–213, 1997. (cited on page 116)
- [Cor13] Corning. SMF-28 Optical Fiber Product Information, 2013. Available from <http://www.photonics.byu.edu/FiberOpticConnectors.parts/images/smf28.pdf/>. (cited on page 81)
- [CYT+06] T.H.T. Chan, L. Yu, H.Y. Tam, Y.Q. Ni, S.Y. Liu, W.H. Chung, and L.K. Cheng. Fiber bragg grating sensors for structural health monitoring of tsing ma bridge: Background and experimental observation. *Engineering Structures*, 28(5):648 – 659, 2006. (cited on page 115)
- [Dan94] P.H. Daniel. Thermal spray and adhesive bonding of optical fibres to high-temperature compsie materials. *Advanced Materials for Optics and Electronics*, 4(5):327–335, 1994. (cited on page 124)
- [Daw06] J W Dawson. *E/EAN/BBCB/0095/AGR/06, "The Assessment of Radiation Damage to the Hinkley Point B/Hunterston B Pre-Stressed Concrete Pressure Vessels", Revision 0*. EDF Nuclear Generation, Engineering Advice Note, November 2006. (cited on page 25)
- [dB99] Fédération Internationale du Béton. *Structural Concrete: Textbook on Behaviour, Design and Performance : Updated Knowledge of the*

- CEB/FIP Model Code 1990*. Number v. 1 in Bulletin (Fédération internationale du béton). International Federation for Structural Concrete, 1999. (cited on page 37)
- [Dev92] R.A.B Devine. Radiation Induced Structural Changes in Amorphous SiO<sub>2</sub>: I. Point Defects. *J. App. Physics*, 31(1):4411–4421, 1992. (cited on page 83)
- [DLK01] M Tomozawa D. L Kim. Fictive temperature of silica glass optical fibers re-examination . *J. Non-Cryst. Solids*, 286(1-2):132–138, 2001. (cited on page 80)
- [DPL07] S Dong, G Peng, and Y Luo. Preparation techniques of metal clad fibres for corrosion monitoring of steel materials. *Smart Materials and Structures*, 16:733–738, 2007. (cited on pages 123, 124)
- [Ene13] EDF Energy. List of UK Nuclear Power Stations, 2013. Available from <http://www.edfenergy.com/about-us/energy-generation/nuclear-generation/nuclear-power-stations/>. (cited on page 22)
- [Erd97] T. Erdogan. Fiber grating spectra. *Lightwave Technology, Journal of*, 15(8):1277–1294, 1997. (cited on page 103)
- [ESAW11] W. Ecke, K. Schröder, A. Andreev, and R. Willsch. Thermally stable optical fibre bragg grating wavelength reference. *Optics Communications*, 284(6):1557–1560, 2011. (cited on page 251)
- [Eva88] B D Evans. The role of hydrogen as a radiation protection agent at low temperature in low-OH, pure silica optical fiber. *IEEE Trans. Nucl. Sci*, 35(6):1215–1220, 1988. (cited on pages 85, 93)
- [FAGL84] E J Friebele, C G Askins, M E Gingerich, and K J Long. Optical Fiber Waveguides in Radiation Environments II. *Nucl. Instrum. Methods*, 1984. (cited on pages 80, 86)
- [FB03] G. Fanourakis and Y. Ballim. Predicting creep deformation of concrete: A comparison of results from different investigations. *11th FIG Symposium on Deformation Measurements*, 2003. (cited on page 56)

- [FBB<sup>+</sup>01] A.F. Fernandez, F. Berghmans, B. Brichard, P. Borgermans, A.I. Gusarov, M. Van Uffelen, P. Megret, M. Decreton, M. Blondel, and A. Delchambre. Radiation-Resistant WDM Optical Link for Thermonuclear Fusion Reactor Instrumentation. *IEEE Trans. Nucl. Sci.*, 48(5):1708–1712, 2001. (cited on pages 91, 94, 95, 106)
- [FBB<sup>+</sup>02] F. Fernandez, B. Brichard, P. Borgermans, F. Berghmans, M. Decreton, P. Megret, M. Blondel, and a. Delchambre. Fibre Bragg grating temperature sensors for harsh nuclear environments. *15th Optical Fiber Sensors Conference Technical Digest. OFS 2002*, pages 63–66, 2002. (cited on pages 106, 108)
- [FBB<sup>+</sup>06] A F. Fernandez, B. Brichard, F. Berghmans, H.E. Rabii, M. Fokine, and M. Popov. Chemical composition fiber gratings in a high mixed gamma neutron radiation field. *IEEE Trans. Nucl. Sci.*, 53(3):1607–1613, 2006. (cited on page 109)
- [FBBD02] A F. Fernandez, B. Brichard, F. Berghmans, and M. Decreton. Dose-rate dependencies in gamma-irradiated fiber bragg grating filters. *IEEE Trans. Nucl. Sci.*, 49(6):2874–2878, 2002. (cited on pages 106, 110)
- [FGB<sup>+</sup>02] A.F. Fernandez, A.I. Gusarov, B. Brichard, S. Bodart, K. Lammens, F. Berghmans, M. Decreton, P. Meigret, M. Blondel, and A. Delchambre. Temperature monitoring of nuclear reactor cores with multiplexed fiber Bragg grating sensors. *Opt. Eng.*, 41(6):1246, 2002. (cited on page 108)
- [Fie04] R.S. Fielder. High Neutron Fluence Survivability Testing of Advanced Fiber Bragg Grating Sensors. *AIP Conf.*, pages 650–657, 2004. (cited on page 111)
- [FNB11] G. Fusiek, P. Niewczas, and G. Burt. Preliminary evaluation of a high-pressure, high-temperature downhole optical sensor. In *Sensors, 2011 IEEE*, pages 409–412. IEEE, 2011. (cited on page 134)

- [Fok04] M Fokine. Underlying mechanisms, applications, and limitations of chemical composition gratings in silica based fibers. *J. Non-Cryst. Solids*, 349:98–104, December 2004. (cited on page 109)
- [Fox10] M. Fox. *Optical Properties of Solids*. Oxford Master Series in Condensed Matter Physics Series. OUP Oxford, 2010. (cited on page 77)
- [FR77] W.N. Findley and RM Reed. Effect of cross-linking on hydrostatic creep of epoxy. *Polymer Engineering & Science*, 17(12):837–841, 1977. (cited on page 117)
- [Fra66] M Francon. *Optical Interferometry*. Academic Press, New York, 1966. (cited on page 198)
- [FRK<sup>+</sup>97] R. Feced, M.P. Roe-Edwards, S.E. Kanellopoulos, N.H. Taylor, and V.A. Handerek. Mechanical strength degradation of UV exposed optical fibres. *Electronics Letters*, 33(2):157–159, 1997. (cited on page 121)
- [FRV05] X. Fan, G. Raiser, and V. Vasudevan. Effects of Dwell Time and Ramp Rate on Lead-Free Solder Joints in FCBGA Package. *IEEE Elec comp and Tech Conf*, pages 901–906, 2005. (cited on page 158)
- [FSG80] E J Friebele, P C Schultz, and M E Gingerich. Compositional effects on the radiation response of Ge-doped silica-core optical fiber waveguides. *Applied optics*, 19(17):2910–6, 1980. (cited on page 92)
- [FZL09] Y. Feng, H. Zhang, and Y. Li. Experiment on embedding FBG sensor into intelligent metal structures. *Piezoelectrics & Acousto-optics*, 3:010, 2009. (cited on page 115)
- [GBF<sup>+</sup>00] A.I. Gusarov, F. Berghmans, A Fernandez Fernandez, O. Deparis, Y. Defosse, D. Starodubov, M. Decreton, P. Megret, and M. Blondel. Behavior of fibre Bragg gratings under high total dose gamma radiation. *1999 Fifth European Conference on Radiation and Its Effects on Components and Systems. RADECS 99*, 41(3):461–465, 2000. (cited on pages 106, 107)

- [GBL05] S. Girard, J. Baggio, and J.-L. Leray. Radiation-induced effects in a new class of optical waveguides: the air-guiding photonic crystal fibers. *IEEE Trans. Nucl. Sci.*, 52(6):2683–2688, 2005. (cited on page 98)
- [GCM<sup>+</sup>08] A. Gusarov, C. Chotjetzki, I. Mckenzie, H. Thienpnt, and F. Berghmans. Effect of the Fiber Coating on the Radiation Sensitivity of Type I FBGs. *IEEE Phot. Tech. Lett.*, 20(21), 2008. (cited on page 108)
- [GFV<sup>+</sup>02] A.I. Gusarov, A Fernandez Fernandez, S Vasiliev, O Medvedkov, M Blondel, and F Berghmans. Effect of gamma-neutron nuclear reactor radiation on the properties of Bragg gratings written in photosensitive Ge-doped optical fiber. *Nucl. Instrum. Methods Section B*, 187(1):79–86, 2002. (cited on pages 106, 111)
- [Gil97] K Gill. Gamma and neutron radiation damage studies of optical fibres. *J. Non-Cryst. Solids*, 216:129–134, 1997. (cited on page 93)
- [GLB<sup>+</sup>05] Y.M. Gebremichael, W. Li, W.J.O. Boyle, B.T. Meggitt, K.T.V. Grattan, B. McKinley, G.F. Fernando, G. Kister, D. Winter, L. Canning, and S. Luke. Integration and assessment of fibre bragg grating sensors in an all-fibre reinforced polymer composite road bridge. *Sensors and Actuators A: Physical*, 118(1):78 – 85, 2005. (cited on page 115)
- [GMSD04] D. Grobnic, S. J. Mihailov, C. W. Smelser, and H. Ding. Sapphire Fiber Bragg Grating Sensor Made Using Femtosecond Laser Radiation for Ultrahigh Temperature Applications. *IEEE Photon. Technol. Lett.*, 16:2505–2507, November 2004. (cited on page 109)
- [Gra09] C. Grant. E/REP/BNCB/0241/TOR/09, 2009 Statutory Examination of the R2 Pre-stressed Concrete Pressure Vessel, Revision 000. Technical report, EDF Energy Nuclear Generation Engineering Advice Note., Jul 2009. (cited on page 63)
- [Gro08] K McNally: Health Improvement Group. MSU/2008/17: A statistical Analysis of PCPV Tendon loads at Hinkley Point B Power Station. Technical report, EDF Energy Nuclear Generation Engineering Advice Note., Sep 2008. (cited on page 69)

- [GT85] A. Ghali and J. Trevino. Relaxation of steel in prestressed concrete. *Journal of Prestressed Concrete Institute*, 30(5):82–90, 1985. (cited on page 60)
- [GT98] A. Ghatak and K. Thyagarajan. *An Introduction to Fiber Optics*. Cambridge University Press, 1998. (cited on page 80)
- [GT03] W.F. Gale and T.C. Totemeier. *Smithells Metals Reference Book*. Elsevier Science, 2003. (cited on page 172)
- [Gus10] A Gusarov. Long-Term Exposure of Fiber Bragg Gratings in the BR1 Low-Flux Nuclear Reactor. *IEEE Trans. Nucl. Sci*, 57(4):2044–2048, 2010. (cited on page 108)
- [GVM<sup>+</sup>07] A. Gusarov, S. Vasiliev, O. Medvedkov, I. Mckenzie, and F. Berghmans. Stabilization of fiber Bragg gratings against gamma radiation. *2007 9th European Conference on Radiation and Its Effects on Components and Systems*, pages 1–8, 2007. (cited on page 106)
- [HAM12] N. Hassoun and A. Al-Manaseer. *Structural Concrete: Theory and Design*. Wiley, 2012. (cited on page 59)
- [Hen94] H. Henschel. Radiation hardness of present optical fibres. *Proc. SPIE*, 2425, 1994. (cited on page 122)
- [HFS<sup>+</sup>88] P. L. Higby, E. Friebele, C. Shaw, M. Rajaram, E. Graham, D. Kinser, and E. Wolff. Radiation Effects on the Physical Properties of Low-Expansion-Coefficient Glasses and Ceramics. *J. Am. Ceram. Soc.*, 71(9):796–802, 1988. (cited on page 110)
- [HGH<sup>+</sup>11] H. Henschel, D. Grobnic, S. Hoeffgen, J. Kuhnhenh, S. Mihailov, and U. Weinand. Development of Highly Radiation Resistant Fiber Bragg Gratings. *IEEE Trans Nuc Sci*, 58(4):2103–2110, 2011. (cited on pages 106, 110)
- [HH89] P Horowitz and W Hill. *The Art of Electronics*. Cambridge University Press, Cambridge, 1989. (cited on page 215)

- [HH94] W. R. Habel and D. Hofmann. Strain measurements in reinforced concrete walls during the hydration reaction by means of embedded fibre interferometers. pages 180–183, 1994. (cited on page 115)
- [HKG<sup>+</sup>09] C Holmes, DO Kundys, JC Gates, CBE Gawith, and PGR Smith. 150 ghz of thermo-optic tuning in direct uv written silica-on-silicon planar bragg grating. *Electronics letters*, 45(18):954–956, 2009. (cited on page 253)
- [HKL<sup>+</sup>98] H. Henschel, O. Kohn, W. Lennartz, S. Metzger, H.U. Schmidt, J. Rosenkranz, B. Glessner, and B.R.L. Siebert. Comparison between fast neutron and gamma irradiation of optical fibres. *IEEE Trans. Nucl. Sci*, 45(3):1543–1551, 1998. (cited on pages 91, 92, 94, 122)
- [HKMS99] R. Heinz, E. Klusmann, H. Meyer, and R. Schulz. PECVD of transition metals for the production of high-density circuits. *Surface and Coatings Technology*, 116-119:886–890, September 1999. (cited on page 123)
- [HKW05] H. Henschel, J. Kuhnenn, and U. Weinand. High radiation hardness of a hollow core photonic bandgap fiber. *2005 8th European Conference on Radiation and Its Effects on Components and Systems*, pages LN4–1–LN4–4, 2005. (cited on page 98)
- [HM97] K.O. Hill and G. Meltz. Fiber bragg grating technology fundamentals and overview. *J. Lightwave Tech.*, 15(8):1263–1276, 1997. (cited on page 102)
- [HNO<sup>+</sup>12] A. Hohl, A. Niccolai, C. Oliver, D. Melnychuk, Zibtsev S., J.G. Goldammer, and Gulidov V. The Human Health Effects of Radioactive Smoke from a Catastrophic Wildfire in the Chernobyl Exclusion Zone: A Worst Case Scenario. *Earth Bioresources and Quality of Life*, 1, 2012. (cited on page 29)
- [Hor20] H.A. Hornor. *Spot and arc welding*. J.B. Lippincott company, 1920. (cited on page 168)

- [HP90] M. Hill and B. Poborets. Solder-Glass Attachment, in Cerdip/Cerquad Packages: Thermally Induced Stresses and Mechanical Reliability. *ECTC 1990*, 2:1043–1052, 1990. (cited on page 117)
- [HSE<sup>+</sup>94] H Henschel, H U Schmidt, D Euskirchen, E Bawirzanski, and A Landers. Optical Fibres for High Radiation Dose Environments. *IEEE Trans. Nucl. Sci.*, 41(3):510–516, 1994. (cited on page 122)
- [HTS<sup>+</sup>98] V. Hagemann, M.N. Trutzel, L. Staudigel, M. Rothhardt, H.-R. Muller, and O. Krumpholz. Mechanical resistance of draw-tower-bragg-grating sensors. *Electronics Letters*, 34(2):211 –212, jan 1998. (cited on page 100)
- [Hur98] M.K. Hurst. *Prestressed concrete design*. Taylor & Francis, May 1998. (cited on pages 41, 53)
- [HWZ<sup>+</sup>10] Y. Huang, T. Wei, Z. Zhou, Y. Zhang, G. Chen, and H. Xiao. An extrinsic Fabry-Perot interferometer-based large strain sensor with high resolution. *Measurement Science and Technology*, 21(10):105308, 2010. (cited on page 100)
- [IBCYMY02] K. Il-Bum, K. Chi-Yeop, and C. Man-Yong. Continuous measurement of temperature distributed on a building construction. pages 273–283, 2002. (cited on page 115)
- [Ibr00] M. Ibrahim. Attenuation of fission neutrons by some hydrogeneous shield materials and the exponential dependence of the attenuated total neutron dose rate on the shield thickness. *Applied radiation and isotopes : including data, instrumentation and methods for use in agriculture, industry and medicine*, 52(1):47–53, January 2000. (cited on page 24)
- [ID01] J.M. Illston and P.L.J. Domone. *Construction Materials: Their Nature and Behaviour, Third Edition*. Spon, 2001. (cited on page 40)
- [idb99] Federation internationale du beton. *Structural concrete: textbook on behaviour, design and performance : updated knowledge of the CEB/FIP Model code 1990*. FIB - Fed. Int. du Beton, 1999. (cited on page 56)

- [IfS08] ACI Committee 318, American Concrete Institute, and International Organization for Standardization. *Building Code Requirements for Structural Concrete (ACI 318-08) and Commentary*. American Concrete Institute, 2008. (cited on page 36)
- [Ins68] Prestressed Concrete Institute. *Fundamentals of prestressed concrete design*. Prestressed Concrete Institute., 1968. (cited on page 36)
- [INS96] INSAG. Defence in depth in nuclear safety. *INSAG*, 10, 1996. (cited on page 26)
- [Irv00] J. Irving. PCPV/3166/V03. The measurement of tendon loads in prestressed concrete pressure vessels and containment buildings, appendices to volume 3: The theory and practice of tendon loads based on a case study of measurements and tests on the Hinkley Point B PCPVs. Technical report, EDF Energy Nuclear Generation Engineering Advice Note., Feb 2000. (cited on pages 56, 68)
- [ITE99] ITER Physics Expert Group on Diagnostics and ITER Physics Basis Editors. Chapter 7: Measurement of plasma parameters. *Nuclear Fusion*, 39(12):2541, 1999. (cited on page 109)
- [IVG13] IVG. Speciality Single Mode Optical fibers: Cu1300, 2013. Available from [http://www.ivgfiber.com/datasheet\\_singlemode.pdf/](http://www.ivgfiber.com/datasheet_singlemode.pdf/). (cited on pages 81, 122)
- [JF06] B. Jalali and S. Fathpour. Silicon photonics. *Journal of Lightwave Technology*, 24(12):4600–4615, 2006. (cited on page 253)
- [Jin03] F Jin. Material requirements for optoelectronic packaging –fiber soldering: San Jose State University, 2003. (cited on page 117)
- [JXH<sup>+</sup>09] B. Jiang, L. Xiao, S. Hu, J. Peng, H. Zhang, and M. Wang. Optimization and kinetics of electroless Ni-P-B plating of quartz optical fiber. *Optical Materials*, 31(10):1532–1539, August 2009. (cited on pages 124, 130)

- [Kai13] Kaiphone. Simplex Armored Optical Fiber Patchcord Specification, 2013. Available from [http://www.bbnint.co.uk/documents/pdfs/Kaiphone/SX\\_armoured\\_fibre.pdf/](http://www.bbnint.co.uk/documents/pdfs/Kaiphone/SX_armoured_fibre.pdf/). (cited on page 259)
- [KDP+97] A.D Kersey, M.A Davis, H.J Patrick, M LeBlanc, K.P Koo, C.G Askins, M.A Putnam, and E.J Friebele. Fiber grating sensors. *Lightwave Technology, Journal of*, 15(8):1442–1463, August 1997. (cited on page 3)
- [KGB10] C. Kurkjian, P. Gupta, and R. Brow. The strength of silicate glasses: What do we know, what do we need to know? *International Journal of Applied Glass Science*, 1(1):27–37, 2010. (cited on pages 118, 121)
- [Kha09] S. A. Khan. E/REP/BNCB/0222/HPB/08, Reactor 4 PCPV Statutory Examination Report 2008, Revision 000. Technical report, EDF Energy Nuclear Generation Engineering Advice Note., Jan 2009. (cited on pages 63, 70)
- [KHW06] K. Krebber, H. Henschel, and U. Weinand. Fibre Bragg gratings as high dose radiation sensors? *Meas. Sci Tech*, 17:1095–1102, 2006. (cited on page 106)
- [Kit04] C Kittel. *Introduction to Solid State Physics, Chapter 13*. John Wiley & Sons, 8th edition, 2004. (cited on page 77)
- [KKM89] C.R. Kurkjian, J.T. Krause, and M.J. Matthewson. Strength and fatigue of silica optical fibers. *Lightwave Technology, Journal of*, 7(9):1360–1370, 1989. (cited on page 121)
- [KKS96] JT Krause, SN Kher, and D. Stroumbakis. Arc fusion splices with near pristine strengths and improved optical loss. In *Optical Communication, 1996. ECOC'96. 22nd European Conference on*, volume 2, pages 237–240. IEEE, 1996. (cited on page 163)
- [KP83] C.R. Kurkjian and UC Paek. Single-valued strength of perfectsilica fibers. *Applied Physics Letters*, 42(3):251–253, 1983. (cited on page 119)

- [KS05] C. Y. Kong and R. C. Soar. Method for embedding optical fibers in an aluminum matrix by ultrasonic consolidation. *Applied Optics*, 44(30):6325–6333, 2005. (cited on page 168)
- [KWB<sup>+</sup>07] G. Kister, D. Winter, R.A. Badcock, Y.M. Gebremichael, W.J.O. Boyle, B.T. Meggitt, K.T.V. Grattan, and G.F. Fernando. Structural health monitoring of a composite bridge using bragg grating sensors. part 1: Evaluation of adhesives and protection systems for the optical sensors. *Engineering Structures*, 29(3):440 – 448, 2007. (cited on page 115)
- [LCB<sup>+</sup>09a] E. Lindner, C. Chojetzki, S. Brückner, M. Becker, M. Rothhardt, and H. Bartelt. Thermal regeneration of fiber Bragg gratings in photosensitive fibers. *Optics express*, 17(15):12523–31, 2009. (cited on page 109)
- [LCB<sup>+</sup>09b] E. Lindner, C. Chojetzki, S. Brueckner, M. Becker, M. Rothhardt, J. Vlekken, and H. Bartelt. Arrays of Regenerated Fiber Bragg Gratings in Non-Hydrogen-Loaded Photosensitive Fibers for High-Temperature Sensor Networks. *Sensors*, 9(10):8377–8381, 2009. (cited on page 109)
- [LCC<sup>+</sup>11] E. Lindner, J. Canning, C. Chojetzki, S. Brückner, M. Becker, M. Rothhardt, and H. Bartelt. Thermal regenerated type IIa fiber Bragg gratings for ultra-high temperature operation. *Optics Communications*, 284(1):183–185, 2011. (cited on page 109)
- [LCCW04] Y. Lin, K. Chang, J. Chern, and L. Wang. The health monitoring of a prestressed concrete beam by using fiber bragg grating sensors. *Smart Materials and Structures*, 13(4):712, 2004. (cited on page 115)
- [Lee02] N. Lee. *Reflow soldering processes and troubleshooting: SMT, BGA, CSP, and flip chip Technologies*. Elsevier, 2002. (cited on page 158)
- [LGA<sup>+</sup>91] CE Lee, WN Gibler, RA Atkins, JJ Alcoz, and HF Taylor. Metal-embedded fiber-optic fabryperot sensors. *Optics letters*, 16(24):1990–1992, 1991. (cited on page 133)
- [LHYG09] Y. Li, Z. Hua, F. Yan, and P. Gang. Metal coating of fiber bragg grating and the temperature sensing character after metallization.

- Optical Fiber Technology*, 15(4):391–397, August 2009. (cited on pages 122, 123, 132, 134)
- [Li01] X. Li. Embedding sensors in layered manufacturing. *PhD Thesis, Stanford University*, pages 26–28, 2001. (cited on page 123)
- [LL01] E.R. Lyons and H.P. Lee. An efficient electrically tunable etched cladding fiber bragg grating filter tested under vacuum. *Photonics Technology Letters, IEEE*, 13(5):484–486, 2001. (cited on page 124)
- [LLRS06] D. Li, H. Li, L. Ren, and G. Song. Strain transferring analysis of fiber bragg grating sensors. *Optical Engineering*, 45(2):024402–024402, 2006. (cited on page 184)
- [LLS04] H. Li, D. Li, and G. Song. Recent applications of fiber optic sensors to health monitoring in civil engineering. *Engineering Structures*, 26(11):1647–1657, September 2004. (cited on page 112)
- [LPS01a] X. Li, F. Prinz, and J. Seim. Thermal behavior of a metal embedded fiber bragg grating sensor. *Smart Materials and Structures*, 10(4):575, 2001. (cited on page 115)
- [LPS01b] X.C. Li, F. Prinz, and J. Seim. Thermal behavior of a metal embedded fiber bragg grating sensor. *Smart materials and structures*, 10(4):575, 2001. (cited on page 134)
- [LPS<sup>+</sup>12] M. Lezius, K. Predehl, W. Stower, A. Turler, M. Greiter, C. Hoeschen, P. Thirof, W. Assmann, D. Habs, A. Prokofiev, C. Ekstrom, T.W. Hansch, and R. Holzwarth. Radiation induced absorption in rare earth doped optical fibers. *IEEE Trans. nucl. Sci.*, 59(2):425–433, april 2012. (cited on page 93)
- [LRL12] D. Li, L. Ren, and H. Li. *Fiber Optic Sensors: Chapter 18: Mechanical Property and Strain Transferring Mechanism in Optical Fiber Sensors*. Intech, 2012. (cited on page 184)

- [LS09] D. Li and R.C. Soar. Characterization of process for embedding sic fibers in al 6061 o matrix through ultrasonic consolidation. *Journal of engineering materials and technology*, 131(2), 2009. (cited on page 168)
- [LSJ<sup>+</sup>11] S. Lin, N. Song, J. Jin, X. Wang, and Yang G. Effect of Grating Fabrication on Radiation Sensitivity of Fiber Bragg Gratings in Gamma Radiation Field. *IEEE Trans Nuc Sci*, 58(4):2111–2117, 2011. (cited on page 108)
- [Ltd00] Multi-Design Consultants Ltd. MDF/3166/V01. The measurement of tendon loads in prestressed concrete pressure vessels and containment buildings: Volume 1: The design, installation and in-service monitoring of PCPV and PCC prestressing systems. Technical report, EDF Energy Nuclear Generation Engineering Advice Note., Jan 2000. (cited on page 64)
- [LTH12] W. Liu, T. Tokunaga, and Z. He. Sub-nano resolution fiber-optic static strain sensor using a sideband interrogation technique. *Opt. Lett.*, 37(3):434–436, Feb 2012. (cited on page 195)
- [LZRL07] H. Li, G. Zhou, L. Ren, and D. Li. Strain transfer analysis of embedded fiber bragg grating sensor under nonaxial stress. *Optical Engineering*, 46(5):054402–054402, 2007. (cited on page 292)
- [LZRL09] H. Li, G. Zhou, L. Ren, and D. Li. Strain transfer coefficient analyses for embedded fiber bragg grating sensors in different host materials. *Journal of engineering mechanics*, 135(12):1343–1353, 2009. (cited on page 184)
- [LZW<sup>+</sup>99] K.T. Lau, L.M. Zhou, C.H. Woo, K.C. Chan, and W. Jin. Strengthening and monitoring concrete structures using glass fibre composites and fbg sensor. *Mater Sci Res Int (Jpn)*, 5(3):216–21, 1999. (cited on page 116)
- [Mac08] S. MacLean. Comparison of the Corrosion Resistance of New and Innovative Prestressing Strand Types used in the Post Tensioning of Bridges: University of Texas Thesis. 2008. (cited on page 269)

- [Mal65] I. H. Malitson. Interspecimen comparison of the refractive index of fused silica. *Journal of the Optical Society of America*, 55(10):1205, 1965. (cited on page 276)
- [MAM<sup>+</sup>95] R M Measures, A T Alavie, R Maaskant, M Ohn, S Karr, and S Huang. A structurally integrated bragg grating laser sensing system for a carbon fiber prestressed concrete highway bridge. *Smart Materials and Structures*, 4(1):20, 1995. (cited on page 115)
- [MAM<sup>+</sup>97] R. Maaskant, T. Alavie, R.M. Measures, G. Tadros, S.H. Rizkalla, and A. Guha-Thakurta. Fiber-optic bragg grating sensors for bridge monitoring. *Cement and Concrete Composites*, 19(1):21 – 33, 1997. [;ce:title;Fiber Optic Sensors;/ce:title;](#) (cited on pages 115, 115)
- [Mat13] Matweb. Kovar Alloy Material Properties, 2013. Available from <http://www.matweb.com/>. (cited on page 144)
- [Mau75] R.D. Maurer. Strength of fiber optical waveguides. *Appl. Phys. Lett*, 27(4):220, 1975. (cited on page 118)
- [MBST05] P. Moyo, J.M.W. Brownjohn, R. Suresh, and S.C. Tjin. Development of fiber bragg grating sensors for monitoring civil infrastructure. *Engineering Structures*, 27(12):1828 – 1834, 2005. [;ce:title;SEMC 2004 Structural Health Monitoring, Damage Detection and Long-Term Performance;/ce:title;](#) [;xocs:full-name;Second International Conference on Structural Engineering, Mechanics and Computation;/xocs:full-name;](#). (cited on page 115)
- [MCH94] T. Mayer, E. Chason, and A. Howard. Roughening instability and ion-induced viscous relaxation of SiO<sub>2</sub> surfaces. *J. App. Physics*, 76(3):1633–1643, 1994. (cited on page 122)
- [MCM<sup>+</sup>97] W.C. Michie, B. Culshaw, A. McLean, M. Konstantaki, and Sillas Hadjiloucas. Distributed water ingress and water potential measurements using fibre optics. *Cement and Concrete Composites*, 19(1):35–44, 1997. (cited on page 115)

- [MCT09] P. Meshgin, K. Choi, and M. Taha. Experimental and analytical investigations of creep of epoxy adhesive at the concrete frp interfaces. *International Journal of Adhesion and Adhesives*, 29(1):56 – 66, 2009. (cited on page 117)
- [Mea13] Interface Advanced Force Measurement. 1000 Fatigue Rated High Capacity Load Cell, 2013. Available from <http://www.interfaceforce.com/1000-fatigue-rated-high-capacity-load-cell-us-metric-p-2.html/>. (cited on page 67)
- [Men07] A Mendez. Fiber bragg grating sensors: a market overview. In *Proceedings SPIE*, volume 6619, page 661905. International Society for Optical Engineering; 1999, 2007. (cited on page 3)
- [MF39] L. Meitner and O. R. Frisch. Disintegration of Uranium by Neutrons: a New Type of Nuclear Reaction. *Nature*, 143:239–240, February 1939. (cited on page 10)
- [MGD06] C. Montarou, T. Gaylord, and A. Dachevski. Residual stress profiles in optical fibers determined by the two-waveplate-compensator method. *Optics Communications*, 265(1):29 – 32, 2006. (cited on page 80)
- [MGK<sup>+</sup>08] M. Majumder, T. Gangopadhyay, A. Kumar, K. Dasgupta, and D.K. Bhattacharya. Fibre bragg gratings in structural health monitoring - present status and applications. *Sensors and Actuators A: Physical*, 147(1):150 – 164, 2008. (cited on page 114)
- [MH88] T Maruyama and L W Hobbs. Radiation effects in ceramics. *Am Ceram Soc Bull*, 574(67), 1988. (cited on page 90)
- [Mih12] S.J. Mihailov. Fiber bragg grating sensors for harsh environments. *Sensors*, 12(2):1898–1918, 2012. (cited on page 2)
- [MK88] M.J Matthewson and C.R. Kurkjian. Environmental effects on the static fatigue of silica optical fiber. *J. Am. Ceram. Soc.*, 71(3):177–183, 1988. (cited on pages 121, 163)

- [MKF96] C I Merzbacher, A D Kersey, and E J Friebele. Fiber optic sensors in concrete structures: a review. *Smart Materials and Structures*, 5(2):196, 1996. (cited on page 114)
- [MKH97] M.J Matthewson, C.R Kurkjian, and R Hamblin. Acid stripping of fused silica optical fibers without strength degradation. *Journal of lightwave technology*, 15(3):490–497, 1997. (cited on page 121)
- [MKHV03] M.J. Matthewson, C.R. Kurkjian, C.D. Haines, and N. Venugopal. Temperature dependence of strength and fatigue of fused silica fiber in the range 77 to 473 k. In *Proc. of SPIE Vol*, volume 4940, page 75, 2003. (cited on page 163)
- [MMB05] R. Maier, W. Macpherson, and J. Barton. Fiber Bragg gratings of type I in SMF-28 and B/Ge fibre and type IIA B/Ge fibre under gamma radiation up to 0.54 MGy. *Proc. SPIE*, 511, 2005. (cited on page 109)
- [MME81] R. M. Megahid, A. S. Makarious, and M. A. El-Kolaly. Attenuation of reactor thermal neutrons in a bulk shield of ordinary concrete. *Annals of Nuclear Energy*, 8(2):79–85, 1981. (cited on page 21)
- [MME92] Z Mei, J W Morris, and Mineral Engineering. Superplastic Creep of Low Melting Point Solder Joints. *J Electron. Mat.*, 21(4), 1992. (cited on pages 117,132)
- [MN93] MH Maher and EG Nawy. Evaluation of fiber optic bragg grating strain sensor in high strength concrete beams. In *Applications of Fiber Optic Sensors in Engineering Mechanics*, pages 120–133. ASCE, 1993. (cited on page 115)
- [Moo71] R.V. Moore. *IEEE Monograph Series 6: Nuclear Power*. Cambridge University Press, 1971. (cited on page 12)
- [Mou91] P. Mounfield. *World Nuclear Power: A Geographical Appraisal*. Taylor & Francis, 1991. (cited on page 14)
- [MS01] D.K. Mynbaev and L.L. Scheiner. *Fiber-Optic Communications Technology*. Prentice Hall, 2001. (cited on page 80)

- [MS09] P. Majda and J. Skrodzewicz. A modified creep model of epoxy adhesive at ambient temperature. *International Journal of Adhesion and Adhesives*, 29(4):396–404, 2009. (cited on page 117)
- [MSDP95] C D Marshall, J A Speth, L D Deloach, and S A Payne. Neutron and Gamma Irradiated Optical Property Changes for the Final Optics of the National Ignition Facility. *Annual International Conference on Lasers for Application to Inertial Confinement Fusion*, 1995. (cited on page 86)
- [MSS64] D. Magura, M.A. Sozen, and C.P. Siess. A study of stress relaxation in prestressing reinforcement. *Journal of Prestressed Concrete Institute*, 9(2):13–57, 1964. (cited on page 60)
- [MSZ<sup>+</sup>04] N. Mohammad, W. Szyszkowski, WJ Zhang, EI Haddad, J. Zou, W. Jamroz, and R. Kruzelecky. Analysis and development of a tunable fiber bragg grating filter based on axial tension/compression. *Journal of lightwave technology*, 22(8):2001, 2004. (cited on page 132)
- [Ner79] A.V. Nero. *A Guidebook to Nuclear Reactors*. University of California Press, 1979. (cited on page 14)
- [Neu94] V B Neustrnev. Colour centres in germanosilicate glass and optical fibres. *IOP Science*, 6901, 1994. (cited on pages 83, 85, 106)
- [NF11] P. Niewczas and G. Fusiek. Induction heating assisted optical fiber bonding and sealing technique. In *21st International Conference on Optical Fibre Sensors (OFS21)*, pages 77536H–77536H. International Society for Optics and Photonics, 2011. (cited on page 135)
- [NM11] P. Niewczas and J. McDonald. Fibre Optic Sensor System, US Patent 2011/0264398, Oct 2011. (cited on page 134)
- [NNT90] J. Norris, S.A. Norman, and M.J. Tribble. The mechanical degradation of polymer coated glass optical fibres under gamma irradiation. *Proc. SPIE*, 1314, 1990. (cited on page 122)

- [NO13] P. Niewczas and P. Orr. Optical fibre sensor interrogation system, January 4 2013. WO Patent 2,013,001,268. (cited on page 242)
- [Nuf] Nufern. Nufern Data Sheet: Single-Mode Bend Insensitive &/ or Radiation Hardened Fibers Single-Mode Bend Insensitive &/ or Radiation Hardened Fibers. (cited on pages 94, 95)
- [oA99] Concrete Institute of Australia. *Curing of concrete : recommended practice / Concrete Institute of Australia*. Concrete Institute of Australia, Crows Nest, N.S.W. :, 2nd ed. edition, 1999. (cited on page 33)
- [Ofg12] Ofgem: Energy Market Research and Economics team. Electrical Capacity Assessment. 2012. (cited on page 1)
- [OM76] R. Olshansky and R.D. Maurer. Tensile strength and fatigue of optical fibers. *Journal of Applied Physics*, 47(10):4497–4499, 1976. (cited on page 119)
- [ON11] P. Orr and P. Niewczas. High-speed, solid state, interferometric interrogator and multiplexer for fibre bragg grating sensors. *J. Lightwave Techn*, (99):1 – 1, 2011. (cited on pages 3, 196, 204)
- [Oth99] A. Othonos. *Fiber Bragg gratings : fundamentals and applications in telecommunications and sensing*. Artech House, Boston Mass., 1999. (cited on page 111)
- [OYJT04] M. O’Dwyer, C. Ye, S. James, and R. Tatam. Thermal dependence of the strain response of optical fibre bragg gratings. *Measurement Science and Technology*, 15(8):1607, 2004. (cited on page 271)
- [OzO13] OzOptics. Fiber Optic Distributed Brillouin Sensor Applications, 2013. Available from [http://www.ozoptics.com/ALLNEW\\_PDF/APN0008.pdf/](http://www.ozoptics.com/ALLNEW_PDF/APN0008.pdf/). (cited on page 100)
- [OZZ03] J. Ou, Z. Zhou, and X. Zhao. Encapsulation techniques for fbgs and smart monitoring for bridges with fbg sensors. In *Structural Health Monitoring 2003: From Diagnostics & Prognostics to Structural Health*

- Management: Proceedings of the 4th International Workshop on Structural Health Monitoring, Stanford University, Stanford, CA, September 15-17, 2003*, page 180. DEStech Publications, Inc, 2003. (cited on page 132)
- [PB58] R.H. Pry and C.P. Bean. Calculation of the Energy Loss in Magnetic Sheet Materials Using a Domain Model. *J Appl Physics*, 29(3):532, 1958. (cited on page 140)
- [PCH12] J. Pullen, J. Chang, and S. Hanna. Air/Sea Transport, Dispersion and Fate Modeling in the Vicinity of the Fukushima Nuclear Power Plant: A Special Conference Session Summary. *Bulletin of the American Meteorological Society*, june 2012. (cited on page 29)
- [PE62] W. Primak and E. Edwards. Radiation Induced Dilations in Vitreous Silica. *Phys. Rev.*, 128(6), 1962. (cited on page 90)
- [PHM<sup>+</sup>07] R. Prokopec, K. Humer, RK Maix, H. Fillunger, and HW Weber. Mechanical strength of various cyanate ester/epoxy insulation systems after fast neutron irradiation to the ITER design fluence and beyond. *Fusion Engineering and Design*, 82(5):1508–1512, 2007. (cited on page 117)
- [PHM<sup>+</sup>09] R. Prokopec, K. Humer, R.K. Maix, H. Fillunger, and H.W. Weber. Influence of various catalysts on the radiation resistance and the mechanical properties of cyanate ester/epoxy insulation systems. *Fusion Engineering and Design*, 84(711):1544 – 1547, 2009. (cited on page 117)
- [PI01] D C Psaila and H G Inglis. Packaging of Optical Fibre Bragg Gratings. In *ECTC 2010*, number C, 2001. (cited on page 117)
- [Pic42] G. Pickett. *The Effect of Change in Moisture-content on the Creep of Concrete Under a Sustained Load*. Bulletin (Portland Cement Association. Research and Development Laboratories. Research Dept.). Portland Cement Association, 1942. (cited on page 59)
- [PJ94] P.A. Probst and A. Jaquier. Multiple-channel digital lock-in amplifier with PPM resolution. *Rev. Sci. Inst.*, 65:747–750, March 1994. (cited on page 214)

- [PK69] W. Primak and R. Kampwirth. Ionization Expansion of Pile-Exposed Vitreous Silica. *J. App. Physics*, 40(6):2565–2570, 1969. (cited on page 90)
- [PLP<sup>+</sup>08] R Le Parc, C Levelut, J Pelous, V Martinez, and B Champagnon. Influence of fictive temperature and composition of silica glass on anomalous elastic behaviour. *J. Phys.: Condens. Matter*, 21(7):7507–7527, 2008. (cited on page 110)
- [POH00a] F. Piao, W. Oldham, and E. Haller. Ultraviolet-induced densification of fused silica. *J. App. Physics*, 87(7):3287, 2000. (cited on page 90)
- [POH00b] F. Piao, W.G. Oldham, and E. Haller. The mechanism of radiation-induced compaction in vitreous silica. *J. Non-Cryst. Solids*, 276:61–71, 2000. (cited on page 90)
- [PONJ12] M. Perry, P. Orr, P. Niewczas, and M. Johnston. Nanoscale resolution interrogation scheme for simultaneous static and dynamic fiber bragg grating strain sensing. *Journal of Lightwave Technology*, 30(20):3252–3258, 2012. (cited on pages 3, 196, 251)
- [Pri57] W. Primak. Fast-Neutron-Induced Changes in Quartz and Vitreous Silica. *Phys. Rev.*, 110(6), 1957. (cited on page 90)
- [Pri64] W Primak. Radiation-Induced Stress Relaxation in Quartz and Vitreous Silica. *J. App. Physics*, 35(4):1342–1347, 1964. (cited on pages 122, 122)
- [Pri68] W. Primak. Impurity Effect in the Ionization Dilatation of Vitreous Silica. *J. App. Physics*, 39(13):6010, 1968. (cited on page 90)
- [Pri82] W Primak. Stress relaxation of vitreous silica on irradiation. *J. App. Physics*, 53(11):7331–7342, 1982. (cited on page 110)
- [Raj06] K. Raju. *Prestressed Concrete: Chapter 9*. Tata McGraw-Hill Publishing Company, 2006. (cited on page 38)
- [Rao97] YJ Rao. In-fibre bragg grating sensors. *Measurement Science and Technology*, 8(4):355, 1997. (cited on page 231)

- [RIBR95] Z. Ren, B. Ionescu, M. Besbes, and A. Razeq. Calculation of Mechanical Deformation of Magnetic Materials in Electromagnetic Devices. *IEEE Trans Mag*, 31(3):1873, 1995. (cited on page 152)
- [RM94] V. Rondinella and M. Matthewson. Effect of chemical stripping on the strength and surface morphology of fused silica optical fiber. In Dilip K. Paul and Hakan H. Yuce, editors, *Fiber Optics Reliability and Testing: Benign and Adverse Environments*, volume 2074, pages 52–58, Boston, MA, USA, March 1994. SPIE. (cited on page 121)
- [Ros99] C. Ross. *Mechanics of Solids*. Horwood Series in Engineering Science. Woodhead Publishing, 1999. (cited on page 42)
- [RS75] B. Rita and P.K. Sharma. Impurity dependence of the Curie temperature and microwave absorption in ferroelectric crystals. *Phys. Rev. B*, 12(1), 1975. (cited on page 135)
- [RSG04] M. Rowe, W. Swann, and S. Gilbert. Multiple-wavelength reference based on interleaved, sampled fiber bragg gratings and molecular absorption. *Applied optics*, 43(17):3530–3534, 2004. (cited on page 251)
- [Rus03] P Russell. Photonic Crystal Fibers. *Science*, 299(17), 2003. (cited on page 98)
- [RY91a] R. S. Robinson and Hakan H. Yuce. Scanning tunneling microscopy of optical fiber corrosion: Surface roughness contribution to Zero-Stress aging. *J. Am. Ceram. Soc.*, 74(4):814–818, 1991. (cited on page 122)
- [RY91b] RS Robinson and H.H. Yuce. Scanning tunneling microscopy of optical fiber corrosion: Surface roughness contribution to zero-stress aging. *Journal of the American Ceramic Society*, 74(4):814–818, 1991. (cited on page 121)
- [S88] ACI Committee 309, D.L. Schlegel, and American Concrete Institute. Committee 309. *Guide for Consolidation of Concrete*. American concrete institute. American Concrete Institute, 1988. (cited on page 33)

- [SA00] J.F. Shackelford and W. Alexand. *CRC Materials Science and Engineering Handbook*. CRC Press, 2000. (cited on page 144)
- [SAO<sup>+</sup>98] V. Saouma, D. Anderson, K. Ostrander, B. Lee, and V. Slowik. Application of fiber bragg grating in local and remote infrastructure health monitoring. *Materials and Structures*, 31:259–266, 1998. (cited on page 115)
- [SAS98] E. Sayed-Ahmed and N. Shrive. A new steel anchorage system for post-tensioning applications using carbon fibre reinforced plastic tendons. *Canadian Journal of Civil Engineering*, 25(1):113–127, 1998. (cited on page 116)
- [SBKaS98] S.L. Semjonov, M.M. Bubnov, N.B. Kurinov, and a.G. Schebuniaev. Stability of mechanical properties of silica based optical fibres under  $\gamma$ -radiation. *RADECS 97. Fourth European Conference on Radiation and its Effects on Components and Systems*, pages 472–475, 1998. (cited on page 122)
- [SBM<sup>+</sup>12] O. Starkova, S.T. Buschhorn, E. Mannov, K. Schulte, and A. Aniskevich. Creep and recovery of epoxy/mwcnt nanocomposites. *Composites Part A: Applied Science and Manufacturing*, 43(8):1212 – 1218, 2012. (cited on page 117)
- [SC11] KM Shrestha and B. Chen. Aging coefficient, creep coefficient and extrapolating aging coefficient from short term test for sealed concrete. *Journal of Wuhan University of Technology–Materials Science Edition*, 26(1):154–159, 2011. (cited on page 59)
- [Sch80] G.W. Scherer. Stress-induced index profile distortion in optical waveguides. *Applied optics*, 19(12):2000–2006, 1980. (cited on page 80)
- [Sch95] M. Schwartz. *Brazing: for the engineering technologist*. Springer, 1995. (cited on page 134)
- [Sco94] J.H. Scofield. A Frequency-Domain Description of a Lock-in Amplifier. *Amer. J. Phys*, 62(2):129–133, 1994. (cited on page 214)

- [SCUS00] W. Schulz, J. Conte, E. Udd, and J. Seim. Static and dynamic testing of bridges and highways using long-gage fiber bragg grating based strain sensors. pages 79–86, 2000. (cited on page 115)
- [Sem93] S.L Semjonov. Reliability of Aluminium Coated Fibers at high temperature. *Proc. SPIE*, 2074:25–33, 1993. (cited on pages 85, 121)
- [Sen85] J.M. Senior. *Optical fiber communications: principles and practice*. Prentice-Hall international series in optoelectronics. Prentice/Hall International, 1985. (cited on page 158)
- [SG96] L Skuja and B Guttler. Detection of Interstitial Oxygen Molecules in SiO<sub>2</sub> Glass by a Direct Photoexcitation of the Infrared Luminescence of Singlet O<sub>2</sub>) and Raman study of -irradiated glasses. *Phys. Rev. Lett.*, 77(10), 1996. (cited on page 85)
- [SGC01] M. Shaw, R. Galeotti, and G. Coppo. Method of Fixing an Optical Fibre in a Laser Package. *Components*, pages 1441–1446, 2001. (cited on page 117)
- [SH92] F Schliep and R Hereth. Phase sensitive measurement technique for singlemode fibre directional couplers. *Electronics Letters*, 28(16):1538–1540, 1992. (cited on page 201)
- [SH96] D.L. Smith and D.W. Hoffman. Thin-film deposition: Principles and practice. *Physics Today*, 49:60, 1996. (cited on page 124)
- [SH98] B.R.I. Siebert and H. Henschel. Calculation of fast neutron dose in plastic-coated optical fibres. *IEEE Trans. Nucl. Sci*, 45(3):1570–1575, 1998. (cited on pages 91, 122)
- [SH03] S. Sandlin and A. Hokkanen. Embedding optical fibers in metal alloys. *Instrumentation & Measurement Magazine, IEEE*, 6(2):31–36, 2003. (cited on pages 132, 134)
- [She99] E. Sherara. Intelligent sensing for innovative bridges. *Journal of Intelligent Material Systems and Structures*, 10, 1999. (cited on pages 115, 168)

- [SHHK05] L. Skuja, M. Hirano, H. Hosono, and K. Kajihara. Defects in oxide glasses. *Physica Status Solidi*, 2(1):15–24, January 2005. (cited on pages 83, 85)
- [Sim13] Simmons. Mechanical Properties of Epoxy Resins, 2013. Available from <http://www.epoxyworktops.com/epoxy-resin/mech-properties.html/>. (cited on page 116)
- [SKRS06] S. Sandlin, T. Kinnunen, J. Ramo, and M. Sillanpaa. A simple method for metal re-coating of optical fibre bragg gratings. *Surface and Coatings Technology*, 201(6):3061–3065, December 2006. (cited on pages 122, 123)
- [SO97] R. Schenker and W. Oldham. Ultraviolet-induced densification in fused silica. *J. App. Physics*, 82:1065–1071, 1997. (cited on page 122)
- [SPKW76] American Welding Society, A.L. Phillips, W.H. Kearns, and C. Weisman. *Welding Handbook*. Number v. 2. American Welding Society, 1976. (cited on page 168)
- [SSO12] D. Sporea, A. Sporea, and C. Oproiu. Effects of hydrogen loading on optical attenuation of gamma-irradiated uv fibers. *J. Nucl. Mater.*, 423(13):142 – 148, 2012. (cited on page 86)
- [SSV93] A. Saetta, B. Schrefler, and R. Vitaliani. The carbonation of concrete and the mechanism of moisture, heat and carbon dioxide flow through porous materials. *Cement and Concrete Research*, 23(4):761 – 772, 1993. (cited on page 58)
- [Sta80] British Standard. BS 5896:1980. Specification for High tensile steel wire and strand for the prestressing of concrete, 1980. (cited on page 42)
- [Sta90] British Standard. BS 5400-4:1990. Steel, concrete and composite bridges, 1990. (cited on page 36)
- [SWP95] E. Snoeks, T. Weber, and A. Polman. MeV ion irradiation-induced creation and relaxation of mechanical stress in silica. *J. App. Physics*, 78(7):4723–4732, 1995. (cited on page 122)

- [TJC99] M.D. Todd, G.A. Johnson, and C.C. Chang. Passive, light intensity-independent interferometric method for fibre Bragg grating interrogation. *Elec. Lett.*, 35(22):784–786, 1999. (cited on pages 201, 240, 243)
- [TL93] HF Taylor and CE Lee. Sensing applications of fiber fabry perot interferometers embedded in composites and in metals. *ASME, NEW YORK, NY,(USA).*, 181:47–52, 1993. (cited on page 133)
- [TL96] Q. Tan and Y. Lee. Soldering technology for optoelectronic packaging. In *Electronic Components and Technology Conference, 1996. Proceedings., 46th*, pages 26–36. IEEE, 1996. (cited on page 117)
- [TMJ<sup>+</sup>09] U. Tiwari, V. Mishra, S.C. Jain, K. Kesavan, K. Ravisankar, N. Singh, GC Poddar, and P. Kapur. Health monitoring of steel and concrete structures using fibre bragg grating sensors. *Curr Sci*, 97:1539–42, 2009. (cited on page 168)
- [TMR<sup>+</sup>01] R C Tennyson, A A Mufti, S Rizkalla, G Tadros, and B Benmokrane. Structural health monitoring of innovative bridges in canada with fiber optic sensors. *Smart Materials and Structures*, 10(3):560, 2001. (cited on page 115)
- [TO00] J. Toribio and E. Ovejero. Composite microstructure of cold-drawn pearlitic steel and its role in stress corrosion behavior. *Journal of Materials Engineering and Performance*, 9:272–279, 2000. 10.1361/105994900770345917. (cited on page 40)
- [Tro98] J. Troska. Radiation effects in commercial off-the-shelf single-mode optical fibers. *Proc. SPIE*, 3440:112–119, 1998. (cited on pages 91, 94, 95)
- [TSB02] MD Todd, M Seaver, and F Bucholtz. Improved, operationally-passive interferometric demodulation method using  $3 \times 3$  coupler. *Electronics Letters*, 38(15):784–786, 2002. (cited on page 199)
- [TTQ12] Y. Tu, S.T. Tu, and Y.H. Qi. Thermal characteristics of silver-recoated regenerated grating sensors for high-temperature sensing. In *Proc. of SPIE Vol.*, volume 8421, pages 84215E–1, 2012. (cited on page 130)

- [UK 11] UK Health and Safety Executive: Office for Nuclear Regulation. Licence condition handbook. 2011. (cited on page 19)
- [UK 12] UK Government Department of Energy and Climate Change. Statistics — Energy consumption in the UK. 2012. (cited on page 1)
- [UK 13] UK Government Department of Energy and Climate Change. Statistics — Electricity: section 5, Energy Trends. 2013. (cited on page 1)
- [Uni08] United Nations: Economic and Social Affairs. World Population Prospects, The 2008 Revision Highlights. 2008. (cited on page 1)
- [VBA95] B. Valk, R.K. Baettig, and O. Anthamatten. Laser welding for fiber pigtailling with long-term stability and submicron accuracy. *Optical Engineering*, 34(9):2675–2682, 1995. (cited on page 168)
- [VBN+00] M. Van Uffelen, F. Berghmans, a. Nowodzinski, P. Jucker, B. Brichard, F. Vos, and M. Decreton. Fiber-optic link components for maintenance tasks in thermonuclear fusion environments. *1999 Fifth European Conference on Radiation and Its Effects on Components and Systems. RADECS 99*, pages 491–496, 2000. (cited on pages 90, 91, 93, 93, 94, 95)
- [VH11] F. Von Hippel. The radiological and psychological consequences of the Fukushima Daiichi accident. *Bulletin of the Atomic Scientists*, 67(5):27–36, 2011. (cited on page 27)
- [VHM95] G. A. Valaskovic, M. Holton, and G. H. Morrison. Parameter control, characterization, and optimization in the fabrication of optical fiber near-field probes. *Applied Optics*, 34(7):1215–1228, March 1995. (cited on page 124)
- [VHW10] J. Verbeke, C. Hagmann, and D. Wright. Simulation of Neutron and Gamma Ray Emission from Fission and Photofission, 2010. (cited on page 21)
- [Vis13] Vishay. Model 700 Portable Strain Gage Welding and Soldering Unit, 2013. Available from <http://www.vishaypg.com/docs/11302/700.pdf/>. (cited on page 169)

- [VMD09] X.H. Vu, Y. Malecot, and L. Daudeville. Strain measurements on porous concrete samples for triaxial compression and extension tests under very high confinement. *Journal of Strain Analysis for Engineering Design*, 44(8), 2009. (cited on page 37)
- [WAC02] M. Whelan, D. Albrecht, and A. Capsoni. Remote structural monitoring of the cathedral of como using an optical fiber bragg sensor system. pages 242–252, 2002. (cited on page 115)
- [Wan05] M Wandel. Attenuation in silica-based optical fibers: PhD Thesis, Industrial PhD Program (EF 954), 2005. (cited on page 83)
- [WCY06] Y. Wang, Y. Cui, and B. Yun. A Fiber Bragg Grating Sensor System for Simultaneously Static and Dynamic Measurements With a Wavelength-Swept Fiber Laser. *IEEE Phot. Tech. Lett.*, 18(14), 2006. (cited on page 196)
- [WDK<sup>+</sup>08] T. Wijnands, L. De Jonge, J. Kuhnenn, S. Hoeffgen, and U. Weinand. Optical Absorption in Commercial Single Mode Optical Fibers in a High Energy Physics Radiation Field. *IEEE Trans. Nucl. Sci.*, 55(4):2216–2222, 2008. (cited on pages 93, 98)
- [WH11] Y. Wang and H. Huang. Optical fiber corrosion sensor based on laser light reflection. *Smart Materials and Structures*, 20(8):085003, 2011. (cited on page 168)
- [Wil08] R.R. Willey. Using fence post designs to speed the atomic layer deposition of optical thin films. *Applied Optics*, 47(13):C9–C12, May 2008. (cited on page 123)
- [WYJ<sup>+</sup>01] C.Y. Wei, C. Ye, S. James, R. Tatam, and P. Irving. An experimental approach to quantify strain transfer efficiency of fibre bragg grating sensors to host structures. *13th International Conference on Composite Materials ICCM-13, Beijing, China*, 2001. (cited on page 184)
- [Yab05] A.D. Yablon. *Optical Fiber Fusion Splicing*. Springer Series in Optical Sciences. Springer, 2005. (cited on page 158)

- [YJRS09] Y. Yang, GD Janaki Ram, and BE Stucker. Bond formation and fiber embedment during ultrasonic consolidation. *Journal of Materials Processing Technology*, 209(10):4915–4924, 2009. (cited on page 168)
- [YK07a] H.J. Yoon and C.G. Kim. The mechanical strength of fiber bragg gratings under controlled uv laser conditions. *Smart materials and structures*, 16(4):1315, 2007. (cited on page 121)
- [YK07b] S. Youakim and V. Karbhari. An approach to determine long-term behavior of concrete members prestressed with FRP tendons. *Construction and Building Materials*, 21(5):1052–1060, May 2007. (cited on page 56)
- [YLS05] Y. K. Yu, D. W. Liaw, and R. K. Shiue. Infrared brazing inconel 601 and 422 stainless steel using the 70Au-22Ni-8Pd braze alloy. *Journal of Materials Science*, 40(13):3445–3452, July 2005. (cited on page 134)
- [ZC93] B.D. Zimmermann and R.O. Claus. Spatially multiplexed optical fiber time domain sensors for civil engineering applications. In *Applications of Fiber Optic Sensors in Engineering Mechanics*, pages 280–287. ASCE, 1993. (cited on page 115)
- [ZCZ11] Z. Zhu, Y. Chen, and Y. Zhang. The temperature sensitivity of fiber bragg gratings embedded in an al 6061 matrix by ultrasonic welding. *Journal of Intelligent Material Systems and Structures*, 22(18):2173–2179, 2011. (cited on page 168)
- [Zho03] Z. Zhou. An integrated FBG sensing system for bridge health monitoring. *International Workshop on Structural Health Monitoring , Stanford University*, 2003. (cited on pages 100, 114)
- [ZKRC10] T. Zhu, T. Ke, Y. Rao, and K. Chiang. Fabry-Perot optical fiber tip sensor for high temperature measurement. *Optics Communications*, 283(19):3683–3685, October 2010. (cited on page 100)
- [ZL04] Y. Zhao and Y. Liao. Discrimination methods and demodulation techniques for fiber bragg grating sensors. *Optics and Lasers in Engineering*, 41(1):1–18, 2004. (cited on pages 3, 195)

- [ZS02] G. Zhou and LM Sim. Damage detection and assessment in fibre-reinforced composite structures with embedded fibre optic sensors-review. *Smart Materials and Structures*, 11(6):925, 2002. (cited on page 116)
- [ZS06] H. Zhang and J. Senkara. *Resistance Welding: Fundamentals and Applications*. CRC/Taylor & Francis, 2006. (cited on page 169)
- [ZSB] A. Zikic, L. Smith, and G. Brodt. Smart fibre bragg grating feasibility retrofitting assessment in nuclear power plant structures. (cited on page 259)
- [ZZGF03] L. Zhao, Q. Zheng, J. Geng, and Z. Fang. Effect of friction in ferrules on compression tuning characteristics of fiber bragg gratings. *Optics & Laser Technology*, 35(7):559–562, 2003. (cited on page 132)